2018

UNDERSTANDING CHANGES TO GLACIER AND ICE SHEET GEOMETRY: THE ROLES OF CLIMATE AND ICE DYNAMICS

Caitlyn Elizabeth Florentine

UNDERSTANDING CHANGES TO GLACIER AND ICE SHEET GEOMETRY: THE ROLES OF CLIMATE AND ICE DYNAMICS

By

CAITLYN ELIZABETH FLORENTINE

Master of Science, Montana State University, Bozeman, MT, 2011
Bachelor of Arts, Colorado College, Colorado Springs, CO, 2007

Dissertation

presented in partial fulfillment of the requirements
for the degree of

Doctor of Philosophy
in Geosciences

The University of Montana
Missoula, MT

August, 2018

Approved by:

Scott Whittenburg, Dean of The Graduate School
Graduate School

Dr. Joel T. Harper, Chair
Department of Geosciences

Dr. Jesse V. Johnson
Department of Computer Science

Dr. Marco Maneta
Department of Geosciences

Dr. Toby W. Meierbachtol
Department of Geosciences

Dr. Johnnie N. Moore
Department of Geosciences

Florentine, Caitlyn, Ph.D., Summer 2018 *Geosciences*

Understanding Changes to Glacier and Ice Sheet Geometry: The Roles of Climate and Ice Dynamics

Chairperson: Dr. Joel T. Harper

Glacier and ice sheet geometry depend on climatic and ice dynamic processes that are coupled and often highly complex. Thus, partitioning and understanding the drivers of change to glacier and ice sheet geometry requires creative approaches.

Radiostratigraphy data document emergent layers in the ablation zone of western Greenland that emulate theoretical englacial flow paths. Yet true alignment between radar layers and the englacial flow field can be uncertain because these structures have travelled hundreds of km from their original point of deposition, have been shaped by ice deformation for millennia, and have been subjected to complex and three-dimensional ice motion across steep and rugged bedrock terrain. In Chapter 2 I address this problem. Using ice dynamics information from a thermomechanically coupled, higher order ice sheet model, in conjunction with an observationally based test built on principles of mass conservation, I demonstrate that real world effects do not disrupt alignment between targeted ablation zone emergent radar layers and the local, present-day ice flow field.

Topographically driven processes such as wind-drifting, avalanching, and shading, can sustain mountain glaciers situated in settings that are otherwise unsuitable for maintaining glacier ice. Local topography can thus disrupt the way regional climate controls glacier retreat, which limits insight into the climate representativeness of some mountain glaciers. In Chapters 3 and 4 I address this issue. Analyzing glaciological, geodetic, and meteorological data, I quantitatively demonstrate that the glacier-climate relationship at a retreating cirque glacier evolved as mass balance processes associated with local topography became more influential from 1950 to 2014. I then assess regional glacier area changes in the Northern Rockies from the Little Ice Age glacial maxima to the modern. I characterize terrain parameters at each glacier and estimate glacier thickness. Using these data and extremely simple models of ice mass loss I assess climatic, topographic, and glaciological drivers. Predictable factors like initial glacier size, aspect, and elevation only partly explain the observed pattern of glacier disappearance. This implies that less predictable and poorly resolved processes like avalanching and wind-drifting drive spatially complex patterns of glacier mass change across this mountain landscape.

TABLE OF CONTENTS

TABLE OF CONTENTS

TABLE OF CONTENTS

LIST OF FIGURES

LIST OF FIGURES

LIST OF FIGURES

Chapter 3

LIST OF FIGURES

LIST OF FIGURES

LIST OF FIGURES

LIST OF FIGURES

LIST OF TABLES

LIST OF TABLES

Chapter 4

ACKNOWLEDGEMENTS

The research presented in this dissertation would not have been possible without the expertise of my academic advisor, Dr. Joel Harper. He spent countless hours working on these projects, challenging my thinking, and pushing me to grow as a scientist. Dr. Johnnie Moore also dedicated substantial time and energy to ensuring that this research came to fruition. Dr. Jesse Johnson encouraged me to explore the edges of my quantitative reasoning capabilities. Dr. Toby Meierbachtol provided solid and timely advice, scientific and otherwise, when the going got tough.

Many bright and driven people within the University of Montana Group for Quantitative Study of Snow and Ice and Department of Geosciences have supported me and this work over the course of the last five years. Specifically, I would like to thank Dr. Doug Brinkerhoff, Dr. Sharon Bywater-Reyes, Jacob Downs, Ben Hills, Ellen Knappe, Nathan Maier, Dr. Hilary Martens, Patrick Wright, and the scientists at Geowomen's soup nights, who were supportive in critical ways at critical times.

Colleagues at the U.S. Geological Survey have provided key collaboration and community. I am particularly indebted to the Climate Change in Mountain Ecosystems research group and Glacier National Park for creating a space where I could think clearly, feel connected, and write.

The support of my family and friends was also instrumental. My dad, George Florentine, never once doubted my technical prowess and always encouraged me to pursue what I love. My mom, Deborah Helser, showed me how to integrate the stubbornness that research requires with the beauty that first drew me to glaciology. My brother, Kyle Florentine, was always willing to dissect the nitty gritty details, and big overarching themes, of work and life.

Psychoanalyst Vic Stampley helped me to develop an analytical framework for the interpersonal dimension of science and research. This allayed anxiety during my PhD and will continue to promote positive mental health throughout my career.

The mountains of Montana and the north woods of Wisconsin motivated and grounded me.

Finally, I acknowledge my partner, Cullen Fortney. His honest and committed approach to doing science at the laboratory bench inspired me. Knowing of his dependable, humble, and steady efforts at the hospital empowered me to organize and focus my own efforts in science. Plus, his sharp sense of humor and quick wit made me laugh when I needed to most.

CHAPTER 1

INTRODUCTION TO THE DISSERTATION

1. Background

Glacier and ice sheet change is compelling, both because it alters the landscape in dramatic and relatable ways (Popovich, 2017; Schiermeier, 2016), and because it has hydrologic consequences that affect irrigation, hydropower, and global sea level (Bolch et al., 2012; Moon et al., 2018; Sorg et al., 2012; Yi et al., 2017). Understanding glacier and ice sheet change requires process-based insight into the mechanics of these glacial systems. One fundamental way to gain such insight is to inspect changing glacier and ice sheet geometry.

The geometry of a glacier or an ice sheet is determined by the volume of ice mass involved, and by the distribution of that ice mass across the landscape. These are in turn defined by climate, which controls ice mass input and output at the surface boundary (i.e. surface mass balance), and ice dynamics, which control the flux of ice mass through space (Cuffey and Paterson, 2010; Hooke, 2005; Oerlemans, 2001; van der Veen, 2013). Neither of these sets of processes – surface mass balance or solid mass flux – operate independently (Figure 1).

Instead, climate, ice dynamics, and geometry of the glacier or ice sheet are intimately coupled. For example, climate sensitivity of a mountain glacier is strongly influenced by glacier geometry due to the so-called height-mass balance feedback; enhanced melt at the terminus of a glacier decreases its overall elevation distribution, which increases the surface area subjected to enhanced melt (Oerlemans, 2001). Similarly, thinning

sensitivity of outlet glaciers along the western Greenland ice sheet is strongly influenced by glacier geometry; in the studied region, advection dominates diffusion (i.e. Péclet numbers are high) where outlet glaciers are steep and thin, which limits the inland propagation of thinning initiated at the terminus (Felikson et al., 2017).

The interdependence of glacier geometry, climate, and ice dynamics can also lead to nonlinearities in the geometric response of glaciers to simple step-wise changes in climate. Simple models show that when the bed topography underlying a mountain glacier contains an overdeepening, i.e. reverse slope at the lip of an alpine cirque, then steady state geometry is bimodal, with modes distinguished by presence or absence of antecedent ice (Oerlemans, 1987).

This dissertation addresses scientific problems involving this type of complex interplay between glacier and ice sheet geometry, climate, and ice dynamics. To introduce broadly relevant concepts and to contextualize my research, here I define different components of glacier geometry and briefly explain glacier response time. I then provide an overview of dissertation chapters.

1.1 Components of glacier and ice sheet geometry

Glacier geometry may be described by one-, two-, or three-dimensional data. Ice volume (3D) is the most hydrologically relevant metric of glacier geometry, as ice volume can be directly converted to water mass given material (ice, snow, firn) densities. Glacier volume varies substantially depending on the glacier type, with ice sheets being the largest volumes of ice on Earth, e.g. the Greenland Ice Sheet is 2,990,000 km^3 (Moon et al., 2018). Small mountain glaciers are on the other end of Earth's ice volume

spectrum. For example, Sperry Glacier, a cirque type glacier in Glacier National Park in the Northern Rocky Mountains, is only ~0.03 km^3 (Brown et al., 2010). Determining glacier and ice sheet volume requires knowledge of glacier area and ice thickness. Ice thickness is determined via direct measurements from ice penetrating radar (e.g. Leuschen, 2011), and via interpolation from spatial statistics such as kriging or from applying principles of mass conservation (Morlighem et al., 2013).

The geometry of a glacier may also be described only by glacier surface area (2D). Using aerial and satellite imagery, glacier areas can be delineated in map-view (i.e. Latitude/Longitude, x/y) geographic space by tracing the boundaries of ice depicted in georeferenced imagery (Pfeffer et al., 2014). Glacier area data may be scaled to ice volume using physical relationships derived from dimensional analysis of continuum mechanics equations (Bahr et al., 1997, 2014).

The geometry of a glacier is most succinctly described by glacier length (1D). Although glacier length is only one dimensional, and therefore cannot be directly converted to glacier mass, this 1D metric of glacier geometry can nonetheless be related to glacier mass balance so that variations in glacier length (i.e. glacier retreat) may be interpreted in the context of climatic forcing (Leclercq and Oerlemans, 2012; Oerlemans, 1994, 2005; Roe et al., 2016).

Glacier geometry is not restricted to the glacier boundary, but also encompasses englacial structures. Englacial layers, i.e. glacier stratigraphy, are three dimensional structures but may be imaged in two dimensions using ice penetrating radar collected along cross-glacier transects. Radar waves transmitted at or above the glacier surface penetrate the ice, and are reflected by englacial layers due to contrasts in dielectric

permittivity caused by differing dust content, crystal structure, or layer density (Hempel et al., 2000). Given radar wave velocity (v), and measuring the two-way travel time (t) of radar wave returns, distance (d) to englacial structures may be solved for ($d=v \cdot t$). Thus, cross sectional images of the glacier are developed from radar data collected along transects, resulting in radargrams that depict bedrock, ice thickness, and englacial layers (Brown et al., 2017; Catania et al., 2008).

1.2 Response time

The time required for a glacier to achieve new equilibrium length after some climatically induced mass balance change is formally defined as the glacier response time. It is determined mathematically as the characteristic time required for a modelled glacier to adjust from one equilibrium state to the next. Adjustment is technically designated as the state where the glacier has achieved ($1 - e^{-1}$) of its length change, thus the response time is defined mathematically as the e-folding time (Leclercq and Oerlemans, 2012).

A simple approximation of glacier response time - formal derivation presented by Cuffey and Paterson (2010) - is to divide the average ice thickness by the ablation rate at the terminus, i.e. $H/\dot{a}$. According to this simplest approximation, the response time of the Greenland Ice Sheet (given H = 3000 m, $\dot{a}$ = 1 to 2 m yr^{-1}) is millennial while the response time of a temperate mountain glacier (given H = 150 to 300 m, $\dot{a}$ = 5 to 10 m yr^{-1}) is decadal (Cuffey and Paterson, 2010).

However, simplified and mathematical considerations of glacier response time must be reconciled with more complex and observed accounts of real world glacier change.

Observations of Greenland surface elevation change (Csatho et al., 2014), terminus position change (Nick et al., 2009), and speed change (Moon et al., 2012) document ice sheet responsiveness on time scales much shorter (seasons, years, decades) than the millennial response time. Bahr et al. (1998) show that, counter to what is predicted by the simple $H/\dot{a}$ approximation, the response time of a large glacier can be faster than that of a smaller glacier given reasonable glacier hypsometry and mass balance. Glacier length data from the North Cascades in North America and the Swiss Alps in Europe further emphasize the importance of hypsometry on glacier response, with low-sloping, long glaciers showing longer response times and steadier retreat with less fluctuation than steep, short glaciers (Barry, 2006).

Regardless of the precise lag between perturbation and glacier response, it is because of this fundamental behavior – where glacier geometry does not necessarily respond instantaneously to external perturbations – that glacier change signals are dampened relative to the higher frequency signals of interannual variations in climate. Consequently, except in special cases (Brinkerhoff et al., 2017), many glaciers are robust and straightforward indicators of climate change trends, integrating interannual noise yet still sensitively and directly linked to climate (Roe et al., 2016).

2. Overview of contents

In this dissertation I investigate climatic and ice dynamic drivers of glacier geometry changes in two very distinct settings. In Chapter 2, I focus on englacial structures of the ablation zone in the western Greenland Ice Sheet. In the remaining chapters, I focus on glacier geometry changes in the Northern Rocky Mountains. Chapter 2 has been

published in the journal Frontiers in Earth Science: Cryospheric Sciences (Florentine et al., 2018b), Chapter 3 has been published in the journal The Cryosphere (Florentine et al., 2018a), and Chapter 4 is in an advanced state approaching readiness for submission. Each of these papers uses observational data and simple models to address distinct scientific problems, and to draw three independent sets of interpretations and conclusions.

2.1 Greenland Ice Sheet ablation zone radiostratigraphy project overview

Ice within the Greenland Ice Sheet is comprised of stratigraphic layers deposited annually. The spacing of these layers is controlled by rates of supra-glacial accumulation (Waddington et al., 2007) and sub-glacial melt (Fahnestock et al., 2001), while layer slope and orientation is controlled by ice flow and deformation (Holschuh et al., 2017). Extensive ice penetrating radar surveys over the course of the last three decades have resulted in ice sheet wide documentation of Greenland's englacial stratigraphy, which has been used to deduce glaciologically useful information, such as the age structure of the ice sheet interior (Macgregor et al., 2015). Yet limitations to automatic layer tracing methods and radar signal attenuation (Legarsky and Gao, 2006) have precluded inspection of englacial layers in the ablation zone near the ice sheet margin.

In this dissertation, I present results from a detailed and multifaceted analysis of a dense network (500 m north-south spacing) of ablation zone englacial layers documented by NASA Operation IceBridge Multi-channel Coherent Depth Sounding Radar (MCoRDS) data (Leuschen, 2011). I trace layers using a semi-automated algorithm which side stepped the obstacles associated with automated layer tracing routines, enabling me to capture englacial geometry documented by relatively noisy

radiostratigraphy data. Traced radar layers are subsequently used in one alignment analysis that is entirely based on observational data. This analysis is complemented with three other analyses of the ice flow field based on model output from a thermomechanically coupled, higher order ice sheet model (Meierbachtol et al., 2015). Three appendices to the main body of the dissertation provide supporting information for this Greenland radiostratigraphy analysis.

2.2 Northern Rocky Mountain cirque glacier project overview

Mountain glaciers are linked to erosion and mountain landscape evolution (Harbor et al., 1988), alpine ecosystems (Cannone et al., 2012), mountain hazards (Richardson and Reynolds, 2000), and hydrology (Gabbi et al., 2012). Collectively, small (<1 km^2) mountain glaciers (i.e. cirque glaciers) contain enough frozen water that excluding them from total, global ice volume and mass estimates introduces up to 10% error (Bahr and Radić, 2012). So, understanding the response of small mountain glaciers to changing, warming climate has implications that extend beyond the discrete 10^0 km^2 scale of the individual icy landform.

Furthermore, cirque glaciers are an important part of the allure of U.S. National Parks in the Rocky Mountains (i.e. Rocky Mountain National Park and Glacier National Park), which draw millions of tourists and hundreds-of-millions of tourism dollars to the parks and surrounding areas every year (Grau, 2015). It is therefore worthwhile to understand the processes and climate linkages that control these particular mountain glaciers so that accurate, scientifically sound information can be communicated to the public.

Glacier mass balance (Clark et al., 2017) and glacier margin (Fagre et al., 2017; Fagre and Martin-Mikle, 2018) data enable inspection of processes that control cirque glacier geometry changes in the Northern Rocky Mountains. In this dissertation I leverage these and other data to quantify geometric and ice mass change on decadal and centennial time scales. This work elucidates the evolving and spatially complex relationship between cirque glaciers and regional climate.

3. References

Bahr, D. B., Meier, M. F., and Peckham, S. D. (1997). The physical basis of glacier volume-area scaling. J. Geophys. Res. 102, 20355–20362.

Bahr, D. B., Pfeffer, W. T., and Kaser, G. (2014). A review of volume-area scaling of glaciers. Rev. Geophys. 52, 522–555. doi:10.1002/2014RG000465.

Bahr, D. B., Pfeffer, W. T., Sassolas, C., and Meier, M. F. (1998). Response time of glaciers as a function of size and mass balance: 2. Numerical experiments. J. Geophys. Res. 103, 9783–9789.

Bahr, D. B., and Radić, V. (2012). Significant contribution to total mass from very small glaciers. Cryosphere 6, 763–770. doi:10.5194/tc-6-763-2012.

Barry, R. G. (2006). The status of research on glaciers and global glacier recession: A review. Prog. Phys. Geogr. 30, 285–306. doi:10.1191/0309133306pp478ra.

Bolch, T., Kulkarni, A., Kaab, A., Huggel, C., Paul, F., Cogley, J. G., et al. (2012). The State and Fate of Himalayan Glaciers. Science (80-.). 336, 310–314. doi:10.1126/science.1215828.

Brinkerhoff, D., Truffer, M., and Aschwanden, A. (2017). Sediment transport drives tidewater glacier periodicity. Nat. Commun. 8. doi:10.1038/s41467-017-00095-5.

Brown, J., Harper, J., and Humphrey, N. (2010). Cirque glacier sensitivity to 21st century warming: Sperry Glacier, Rocky Mountains, USA. Glob. Planet. Change 74, 91–98. doi:10.1016/j.gloplacha.2010.09.001.

Brown, J., Harper, J., and Humphrey, N. (2017). Liquid water content in ice estimated through a full-depth ground radar profile and borehole measurements in western Greenland. Cryosphere 11, 669–679. doi:10.5194/tc-11-669-2017.

Cannone, N., Diolaiuti, G., Guglielmin, M., and Smiraglia, C. (2012). Accelerating Climate Change Impacts on Alpine Glacier Forefield Ecosystems in the European Alps. Ecol. Appl. 18, 637–648.

Catania, G. A., Neumann, T. A., and Price, S. F. (2008). Characterizing englacial drainage in the ablation zone of the Greenland ice sheet. J. Glaciol. 54, 567–578. doi:10.3189/002214308786570854.

Clark, A. M., Fagre, D. B., Peitzsch, E. H., Reardon, B. A., and Harper, J. T. (2017). Glaciological measurements and mass balances from Sperry Glacier, Montana,

USA, years 2005-2015. Earth Syst. Sci. Data 9, 47–61. doi:10.5194/essd-9-47-2017.
Csatho, B. M., Schenk, A. F., van der Veen, C. J., Babonis, G., Duncan, K., Rezvanbehbahani, S., et al. (2014). Laser altimetry reveals complex pattern of Greenland Ice Sheet dynamics. Proc. Natl. Acad. Sci. 111, 18478–18483. doi:10.1073/pnas.1411680112.
Cuffey, K. M., and Paterson, W. S. B. (2010). The Physics of Glaciers. 4th ed. Oxford: Elsevier.
Fagre, D. B., and Martin-Mikle, C. J. (2018). A comprehensive inventory of maximum glacial extent in Glacier National Park during the peak of the Little Ice Age: U.S. Geological Survey data release. U.S. Geol. Surv. data release. Available at: https://doi.org/10.5066/P95YJ3CN.
Fagre, D. B., McKeon, L. A., Dick, L. A., and Fountain, A. G. (2017). Glacier margin time series (1966, 1998, 2005, 2015) of the named glaciers of Glacier National Park, MT, USA. U.S. Geol. Surv. data release.
Fahnestock, M., Abdalati, W., Joughin, I., Brozena, J., Gogineni, P., and Adbalati, W. (2001). High geothermal heat flow, basal melt, and the origin of rapid ice flow in central Greenland. Science (80-.). 294, 2338–2342. doi:10.1126/science.1065370.
Felikson, D., Bartholomaus, T. C., Catania, G. A., Korsgaard, N. J., Kjær, K. H., Morlighem, M., et al. (2017). Inland thinning on the Greenland ice sheet controlled by outlet glacier geometry. Nat. Geosci., 1–26. doi:10.1038/ngeo2934.
Florentine, C., Harper, J., Fagre, D., Moore, J., and Peitzsch, E. (2018a). Local topography increasingly influences the mass balance of a retreating cirque glacier. 1–27. doi:10.5194/tc-12-2109-2018.
Florentine, C., Harper, J., Johnson, J., and Meierbachtol, T. (2018b). Radiostratigraphy reflects the present-day, internal ice flow field in the ablation zone of western greenland. Front. Earth Sci. 6, 1–11. doi:10.3389/feart.2018.00044.
Gabbi, J., Farinotti, D., Bauder, A., and Maurer, H. (2012). Ice volume distribution and implications on runoff projections in a glacierized catchment. Hydrol. Earth Syst. Sci. 16, 4543–4556. doi:10.5194/hess-16-4543-2012.
Grau, K. (2015). 2014 Economic Contribution of Nonresident Travel Spending in Montana Travel Regions and Counties 2014 Economic Contribution of Nonresident Travel Spending in Montana Travel Regions and Counties.
Harbor, J. M., Hallet, B., and Raymond, C. F. (1988). A numerical model of landform development by glacial erosion. Nature 333, 347. Available at: http://dx.doi.org/10.1038/333347a0.
Hempel, L., Thyssen, F., Gundestrup, N., Clausen, H. B., and Miller, H. (2000). A comparison of radio-echo sounding data and electrical conductivity of the GRIP ice core. J. Glaciol. 46, 369–374. doi:10.3189/172756500781833070.
Holschuh, N., Parizek, B. R., Alley, R. B., and Anandakrishnan, S. (2017). Decoding ice sheet behavior using englacial layer slopes. Geophys. Res. Lett. 44, 5561–5570. doi:10.1002/2017GL073417.
Hooke, R. L. (2005). Principles of Glacier Mechanics. 2nd ed. Cambridge: Cambridge University Press.

Leclercq, P. W., and Oerlemans, J. (2012). Global and hemispheric temperature reconstruction from glacier length fluctuations. Clim. Dyn. 38, 1065–1079. doi:10.1007/s00382-011-1145-7.

Legarsky, J. J., and Gao, X. (2006). Internal layer tracing and age-depth relationship from the ice divide toward Jakobshavn, Greenland. IEEE Geosci. Remote Sens. Lett. 3, 471–475. doi:10.1109/LGRS.2006.877749.

Leuschen, C. (2011). IceBridge MCoRDS L1B Geolocated Radar Echo Strength Profiles, Version 2, Boulder, Colorado USA, NASA Snow and Ice Data Center Distributed Active Archive Center. doi:http://dx.doi.org/10.5067/90S1XZRBAX5N.

Macgregor, J. A., Fahnestock, M. A., Catania, G. A., Paden, J. D., Gogineni, S. P., Young, S. K., et al. (2015). Radiostratigraphy and age sturcture of the Greenland Ice Sheet. J. Geophys. Res. Earth Surf. 120, 212–241. doi:10.1002/2014JF003215.Received.

Meierbachtol, T. W., Harper, J. T., Johnson, J. V., Humphrey, N. F., and Brinkerhoff, D. J. (2015). Thermal boundary conditions on western Greenland: Observational constraints and impacts on the modeled thermomechanical state. J. Geophys. Res. Earth Surf. 120, 623–636. doi:10.1002/2014JF003375.

Moon, T., Ahlstrøm, A., Goelzer, H., Lipscomb, W., and Nowicki, S. (2018). Rising Oceans Guaranteed: Arctic Land Ice Loss and Sea Level Rise. Curr. Clim. Chang. Reports, 1–12. doi:10.1007/s40641-018-0107-0.

Moon, T., Joughin, I., Smith, B., and Howat, I. (2012). 21st-century evolution of Greenland outlet glacier velocities. Science 336, 576–578. doi:10.1126/science.1219985.

Morlighem, M., Rignot, E., Mouginot, J., Wu, X., Seroussi, H., Larour, E., et al. (2013). High-resolution bed topography mapping of Russell Glacier, Greenland, inferred from Operation IceBridge data. J. Glaciol. 59, 1015–1023. doi:10.3189/2013JoG12J235.

Nick, F. M., Vieli, A., Howat, I. M., and Joughin, I. (2009). Large-scale changes in Greenland outlet glacier dynamics triggered at the terminus. Nat. Geosci. 2, 110–114. doi:10.1038/ngeo394.

Oerlemans, J. (1987). "On the response of valley glaciers to climatic change," in Glacier Fluctuations and Climate Change, ed. J. Oerlemans, 353–373. doi:10.1017/CBO9781107415324.004.

Oerlemans, J. (1994). Quantifying Global Warming from the Retreat of Glaciers. Science (80-.). 264, 243–245. doi:10.1126/science.264.5156.243.

Oerlemans, J. (2001). Glaciers and Climate Change. Netherlands: A.A. Balkema Publishers.

Oerlemans, J. (2005). Extracting a Climate Signal from 169 Glacier Records. Science (80-.). 308, 675–677. doi:10.1126/science.1107046.

Pfeffer, W. T., Arendt, A. A., Bliss, A., Bolch, T., Cogley, J. G., Gardner, A. S., et al. (2014). The randolph glacier inventory: A globally complete inventory of glaciers. J. Glaciol. 60, 537–552. doi:10.3189/2014JoG13J176.

Popovich, N. (2017). Mapping 50 years of melting ice in Glacier National Park. New York Times.

Richardson, S. D., and Reynolds, J. M. (2000). An overview of glacial hazards in the Himalayas. Quat. Int. 65–66, 31–47. doi:10.1016/S1040-6182(99)00035-X.

Roe, G. H., Baker, M. B., and Herla, F. (2016). Centennial glacier retreat as categorical evidence of regional climate change. Nat. Geosci. 10, 95–99. doi:10.1038/ngeo2863.

Schiermeier, Q. (2016). The ice historians. Nature 535, 480–483. doi:10.1038/535480a.

Sorg, A., Bolch, T., Stoffel, M., Solomina, O., and Beniston, M. (2012). Climate change impacts on glaciers and runoff in Tien Shan (Central Asia). Nat. Clim. Chang. 2, 725–731. doi:10.1038/nclimate1592.

van der Veen, C. J. Van (2013). Fundamentals of Glacier Dynamics. 2nd ed. Boca Raton: Taylor & Francis.

Waddington, E. D., Neumann, T. A., Koutnik, M. R., Marshall, H. P., and Morse, D. L. (2007). Inference of accumulation-rate patterns from deep layers in glaciers and ice sheets. J. Glaciol. 53, 694–712. doi:10.3189/002214307784409351.

Yi, S., Heki, K., and Qian, A. (2017). Acceleration in the Global Mean Sea Level Rise: 2005–2015. Geophys. Res. Lett. 44, 11,905-11,913. doi:10.1002/2017GL076129.

Figures

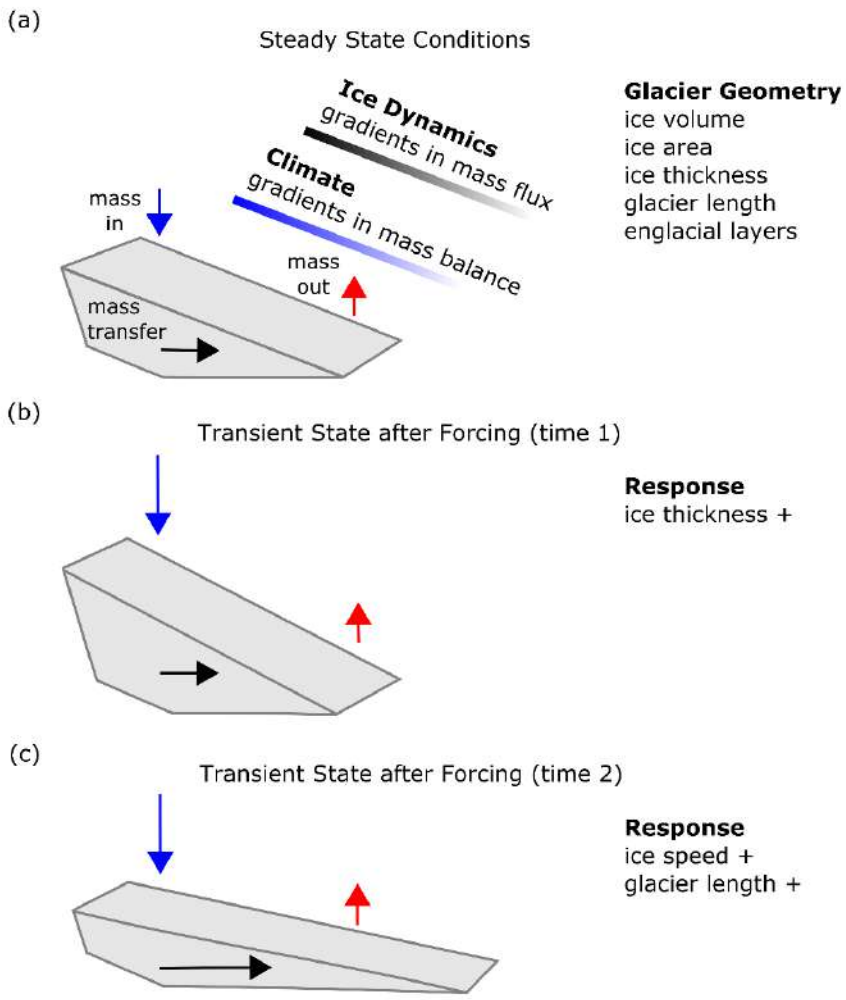

Figure 1. Ice geometry, climate, and ice dynamics are coupled in the glacier system, which can lead to geometric responses that are not straightforward or automatic. (a) Steady state conditions for a glacier in equilibrium with climate and ice dynamics. Mass is added at high elevations on the glacier, in the accumulation zone (blue arrow). Mass leaves the system at low elevations, in the ablation zone (red arrow). Mass is transferred via ice flow (black arrow). Components of glacier geometry that are subject to change given climate or ice dynamic forcings are listed. (b) Transient state after the glacier system has been subjected to some forcing (e.g. increased accumulation, big blue arrow). Glacier response now (time 1) is an increase in ice thickness. (c) Transient state in response to an increase in ice thickness. Glacier response now (time 2) is an increase in ice speed and glacier length.

CHAPTER 2

RADIOSTRATIGRAPHY REFLECTS THE PRESENT-DAY, INTERNAL ICE FLOW FIELD IN THE ABLATION ZONE OF WESTERN GREENLAND

Abstract:

Englacial radar reflectors in the ablation zone of the Greenland Ice Sheet are derived from layering deposited in the accumulation zone over past millennia. The original layer structure is distorted by ice flow toward the margin. In a simplified case, shear and normal strain incurred between the ice divide and terminus should align depositional layers such that they closely approximate particle paths through the ablation zone where horizontal motion dominates. It is unclear, however, if this relationship holds in western Greenland where complex bed topography, three dimensional ice flow, and historical changes to ice sheet mass and geometry since layer deposition may promote a misalignment between present-day layer orientation and the modern ice flow field. We investigate this problem using a suite of analyses that leverage ice sheet models and observational datasets. Our findings suggest that across a study sector of western Greenland, the radiostratigraphy of the ablation zone is closely aligned with englacial particle paths, and is not far departed from a state of balance. The englacial radiostratigraphy thus provides insight into the modern, local, internal flow field, and may serve to further constrain ice sheet models that simulate ice dynamics in this region.

1 Introduction

As ice sheets accumulate mass, surfaces are buried which then define discrete internal layers. Layer geometry is initially controlled by rates of surface accumulation, and further altered by internal deformation as ice flows away from the source. Buried surfaces have contrasting dielectric permittivity, which are revealed by ice penetrating radar due to discrete acid layers from volcanic aerosol deposition (Hempel et al., 2000; Millar, 1981), density contrasts, and differing crystal fabric orientation (Fujita et al., 1999). The hundreds of thousands of kilometers of airborne radar data collected over the Greenland Ice Sheet (GrIS) (Leuschen, 2011), document this internal architecture, the radiostratigraphy, thus providing insights into historical and current ice sheet conditions.

Radiostratigraphy has proven useful for a variety of glaciological investigations. For example, radargrams have been used to calculate historical accumulation rates (Karlsson et al., 2014; Waddington et al., 2007), illuminate strain history (MacGregor et al., 2016), characterize englacial drainage (Catania et al., 2008), quantify geothermal heat flux (Fahnestock, 2001) and constrain model estimates of basal motion (Holschuh and others, 2017). Studies utilizing radiostratigraphy for investigations of ice sheet dynamics have focused nearly exclusively on accumulation zones. This is in part because a small fractional area of the Greenland and Antarctic ice sheets experience net ablation, but is also because the continuity of radar reflectors tends to be poor near the margin where ice is thin, the surface is rough (Sime et al., 2014), and in the case of the GrIS, the steep and high relief basal topography (e.g. Lindbäck and others, 2014) often complicates radar reflections. Nevertheless, radiostratigraphy has potential to provide unique constraint on ice dynamics in the ablation zone of the GrIS.

Prior work suggests that original depositional layering becomes aligned with internal particle paths in the ablation zone of Barnes Ice Cap (Hudleston and Hooke, 1980), where the ice residence times are relatively short, i.e. thousands of years. Similarly, internal layers have been shown to be closely aligned with englacial streamlines in a numerical model of a synthetic accumulation zone, as long as horizontal ice flow is fast relative to vertical flow, and the ice is thick relative to the spacing of underlying bedrock peaks and troughs, i.e. the wavelength of bed roughness (Hindmarsh and others, 2006). The GrIS ablation zone indeed has a dominant component of horizontal motion, which is due to flow mainly by sliding (Ryser et al., 2014). Therefore, internal radar reflectors potentially reveal the englacial flow field of the GrIS ablation zone. Where radargrams are oriented tangent to the direction of ice flow, radar layers perhaps even approximate englacial streamlines.

Alternatively, the long residence time of ice in the GrIS implies that the climate, the ice geometry, and the flow field have all undergone substantial adjustments since ice now in the ablation zone was originally deposited near the divide. Layering in the ablation zone may be remnant structure, more related to the integration of transient historical conditions and upstream ice flow than to the present-day, local flow field. For example, we know that the southwest GrIS underwent km-scale retreat and thinning at the margins during the mid-Holocene (Simpson et al., 2009; van Tatenhove et al., 1996). Additionally, the bed topography and thinning ice in the ablation zone may further complicate the relationship between layering and ice flow. Uncertainty regarding the alignment between ablation zone radiostratigraphy and the englacial flow field casts

doubt on the utility of these data as an observational constraint on local, present-day ice dynamics.

Here we address the question of differences between englacial stratigraphy and the internal flow field by investigating the relationship between radar-detected layers in the western GrIS ablation zone and modern ice sheet conditions. A true comparison requires particle paths within the ice to be defined with perfect fidelity, but this is an unobservable entity. To manage this dilemma, we take the following approach to our analysis: 1) analyze the deformation field along a flowline to test for a characteristic pattern of strain that reorients depositional layering as it flows to the ablation zone; 2) compare model simulated isochrones and model simulated ice flow particle paths along a GrIS flowline; 3) compare particle paths and isochrones from ice flow simulations to observations of emergent radar layers documented in radiostratigraphy data; and finally, 4) employ an observation-based test for alignment between radar-detected internal geometry and the modern ice flow field using principles of mass conservation.

2 Methods

2.1 Study Area

We focus on the ablation zone of the Kangerlussuaq sector, a land-terminating section of the GrIS (Figure 1). The study region includes the widest ablation zone of the ice sheet, which extends ~100 km inland from the ice margin. The equilibrium line altitude (ELA) is at ~1530 m. a.s.l. according to recent in situ surface mass balance measurements (van de Wal et al., 2012). Below the ELA, surface mass balance is increasingly negative, with ablation at low elevations removing up to 4 m yr^{-1} (van de Wal et al., 2012). Recent

surface elevation lowering rates documented by 1992-2012 laser altimetry measurements are < 0.5 m yr^{-1} and are attributed predominantly to increasing melt rather than to changes in ice dynamics (Csatho et al., 2014). Ice velocity is variable in both space and time below the ELA, with spatial and seasonal patterns near the terminus roughly mirroring complex underlying bedrock topography (Jezek et al., 2013; Palmer et al., 2011). The seasonal and spatial mean speed of ice near the margin is ~100 m yr^{-1} (Joughin et al., 2010). Ice is roughly 1500 m thick near the ELA, but the region is incised by several deep bedrock troughs (Lindbäck et al., 2014). Thus the characteristic ice thickness near the margin is ~1000 m over bedrock troughs, and ~700 m over bedrock ridges.

2.2 Radiostratigraphy

A dense array of 40+ IceBridge flight lines was flown along this sector of the GrIS in 2011, providing radiostratigraphy data (Leuschen, 2011) for more than 2,000 km within the study area (Figure 1). The flight lines are oriented approximately along-flow. To represent radar data in geographic space we converted two-way travel time data to depth assuming that the wave speed in air and ice are 300 m μs^{-1} and 168 m μs^{-1} respectively. No firn correction was necessary as the data analyzed were within the ablation zone. In addition to the data processing already applied by Leuschen (2011), we further processed radar data by applying a logarithmic transformation, removing background noise, and applying a Hilbert transform to the raw power return data. This additional processing aided radiostratigraphy visualization.

Our observation-based test (described in Sect. 2.3.4) required englacial geometry provided by internal layers, so we digitally traced radar layers. Automated tracing

methods do not perform well in our near-margin study area (Legarsky and Gao, 2006). Nonetheless, we were able to successfully trace internal layers using a semi-automated method which combined visual inspection, user-defined picks, and data-driven interpolation. The interpolation algorithm matched user-defined picks to the nearest sample of the nearest radar trace. Vertical error (discerned by repeat picking along the same layer) was 16 m, which is comparable to the reported radar data depth accuracy of 13.6 m (Leuschen, 2011). Average horizontal error on traced layers was much larger (250 m), because the aspect ratio necessary for visualizing and tracing emergent layers favored vertical over horizontal resolution. We used the IceBridge ice surface and bed picks provided by Leuschen (2011).

2.3 Alignment Analyses

No single measure can reveal the relationship between radiostratigraphy and ice flow, because an observationally validated description of the internal flow field does not exist. We therefore investigate the geometry of the radiostratigraphy with regard to four separate aspects of the internal flow field, each described individually below.

2.3.1 Ice Deformation

To quantify ice deformation between the present-day ice divide and ablation zone, we analyzed the cumulative strain along a flowline (Figure 1). We define cumulative strain as time-integrated strain along a particle path. By computing cumulative strain, we assess the stretching and rotation of primary layering due to deformational processes. The deformation field was derived from a three dimensional, thermomechanically-coupled,

higher-order ice sheet model, representing a steady state instance of the model that is consistent with modern ice sheet geometry and velocity (Meierbachtol et al., 2015). The model assimilated surface velocity observations (Joughin et al., 2010), and used a numerical mesh shaped by high-resolution ($1km^2$) bedrock and ice surface data (Bamber et al., 2013). We calculated the cumulative strain rotating and elongating ice as it moves englacially from point of deposition in the interior, to emergence near the margin.
To visualize the accumulated strain, we considered a deforming unit ellipsoid that travels along a representative particle path. The unit ellipsoid started with equal length, width, and height at deposition. Subsequently, its dimensions and orientation were deformed by the magnitude and direction of cumulative principal strain. To assess the overall magnitude of total strain along particle path P1, we compute the natural octahedral unit shear (see Supplementary Material for computation details).

2.3.2 Simulating Isochrones and Particle Paths

To assess how the modelled internal ice flow field relates to englacial layers in the ablation zone, we simulated isochrones and particle paths using the same ice flow model (Meierbachtol et al., 2015) of the study region. The simulation reveals the geometric relationship between internal layers and streamlines in a flow field that is consistent with present-day ice sheet geometry and velocity. To simulate englacial particle paths, we followed a collection of particles through the modelled flow field, from deposition in the accumulation zone to emergence in the ablation zone. We employed a simple Lagrangian approach to particle tracking. This avoids the conditional instabilities associated with pure advection equations (Pattyn, 2002). In a Lagrangian coordinate system, particle

position is given by a set of simple ordinary differential equations, i.e. $\frac{dx}{dt} = u(x, y, z, t)$, where east-west longitudinal ice velocity is *u*, north-south transverse ice velocity is *v*, and vertical ice velocity is *w*. Each component of the velocity field (*u*,*v*,*w*) was defined by a thermomechanically-coupled model solution of ice flow, which accounted for higher order stresses and represented a steady state instance of ice dynamics (Meierbachtol et al., 2015). After applying a Gaussian filter to ensure smooth integration, we integrated velocity ($\frac{dx}{dt}, \frac{dy}{dt}, \frac{dw}{dt}$) to solve for particle position given by northing, easting, and elevation. Although the velocity field fed to the ode integrator was defined on a finite element mesh, particles were tracked in a pure Cartesian space. Particle paths were defined by particle positions at one year time steps through the ice flow field.

In order to simulate isochrones, we tracked particle age (*A*) by solving the simple ordinary differential equation $\frac{dA}{dt} = 1$, using the odeint solver from the scipy library (adapted from Hindmarsh, 1983). Particles were initiated with an age of zero years at the ice surface, so the surface boundary condition was $A(z=s)=0$. The age solution was therefore very simple: with each one year time step the ice particle was one year older (Pattyn, 2003). Finally, to quantify the spatial alignment of simulated isochrones and particle paths, we calculated the three-dimensional angle between short (~5 km long) isochrone and particle path segments.

2.3.3 Comparing Radiostratigraphy to Simulated Isochrones

To test for alignment between the observed and modelled internal ice flow field, we compare the pattern and geometry of radar-detected layers against simulated isochrones. The comparison shows whether or not observed internal layers (which have been

subjected to real world transience) agree with modelled layers (which are the product of a simulation with no transience). This comparison did not involve exact target matching of specific layers; such an exercise is precluded by simplification to the modelled domain. Furthermore, small errors in the modelled velocity field propagate during isochrone simulation, which does not compromise layer orientation and slope (e.g. Holschuh et al., 2017), but which can result in large errors on the absolute location of internal layers (Hindmarsh et al., 2009). We circumvent these issues by qualitatively comparing modelled isochrones to radiostratigraphy. The purpose of this comparison is to test of whether or not the structural pattern of layers produced by the modelled ice flow field reflects the englacial layers documented by radiostratigraphy.

2.3.4 Mass-conserving Ablation: An Observation-based Test

Lastly, we run a strictly observation-based test of the hypothesis that radar layers are parallel to englacial particle paths, independent of ice sheet model assumptions and parameters. This final analysis considers the relationship between observations of ice flow, surface melt, and internal layer geometry in the ablation zone. It assesses whether or not observed layers are consistent with the local flow field and present-day surface mass balance. The test involves the calculation of mass-conserving ablation rates. To explain the test, we first must inspect the ablation zone system.

Figure 2 depicts an along-flow cross section through an ice sheet ablation zone. In this dynamic system, ice is advected toward the margin. Meanwhile, ablation removes mass at the ice surface, increasing in magnitude as the surface elevation decreases. Englacial particles therefore travel pathways that eventually intersect the ice surface. Vertical

strain due to flux divergence will also remove (or add) ice between the particle and the ice surface along this emergent, englacial particle path. Because mass is conserved, ablation and ice flow may be related as:

$$-\frac{\eta}{\Delta t} = \bar{\dot{a}} + \bar{\dot{\varepsilon}}_{zz}\eta \quad (1)$$

where the overbars denote horizontal averages, and $-\frac{\eta}{\Delta t}$ is the average rate at which mass is lost along the emergent particle path. Within this term, Δt is a time step, defined by the length of the englacial particle path (*dx*) and the average ice speed along the layer ($\bar{v}$), and η is a fraction of the ice column. This rate of mass loss is attributable to the average rate of ablation along the layer ($\bar{\dot{a}}$) and the average flux divergence, i.e. the average rate of component thickness change due to vertical strain ($\bar{\dot{\varepsilon}}_{zz}\eta$). Basal melt is negligible compared to surface melt (Harper et al., 2016), and would only act to shift the entire near surface domain downward, so it is neglected. The formulation assumes a state of balance between modern velocity, geometry, and ablation, which is justified by laser altimetry measurements (Csatho et al., 2014) that show small surface elevation lowering rates (<0.5 m yr^{-1}) in our study area. Equation 1 is merely a rearranged expression of the conservation of mass equation commonly used in glaciology (see Supplementary Material), which involves only a fraction of the ice column as opposed to the full ice thickness.

IceBridge radiostratigraphy data document emergent internal layers that mimic the conceptualized englacial particle path depicted in Figure 2. If these radar layers do indeed approximate englacial particle paths, then the layers should provide geometry that balances with the ice flow field and local surface mass balance. To test this, we used satellite-derived velocity data and vertical strain rates derived therein (see Supplementary

Material) to define ice flow components ($\bar{v}$, $\bar{\dot{\varepsilon}}_{zz}$), and traced emergent radar layers to define geometric components (dx, η) of Equation (1). We then solved for the ablation rate required to conserve mass. Finally, we compared this radar-derived, mass-conserving (rMC) ablation rate to independent metrics of ablation provided by the regional climate model RACMO (see Supplementary Material) and K-transect measurements (van de Wal et al., 2012). We traced 113 along-flow emergent radar layer segments, used them to define geometry and ice flow terms, calculated rMC ablation rates, and finally compared rMC to RACMO and K-transect ablation.

In this system, mass is conserved on some characteristic time scale that is neither too short nor too long. For example, on the seasonal to interannual time step (too short), the ice geometry varies with winter snow accumulation and summer ablation, and velocity fields vary between days, seasons, and years (Bartholomew et al., 2011; Sole et al., 2013; Sundal et al., 2011). On a millennial time step (too long) the ice geometry varies due to climate-driven changes in ice volume (e.g. Alley et al., 2010). The critical averaging time step (Δt) is therefore many decades up to a century or two. This defines the time step of interest for our testing. We accordingly limit calculation of mass-conserving ablation rates to radar layers that define a time step of at least a century.

Solving for ablation enables us to leverage the obvious and simple relationship between elevation and ablation. Ablation rates derived from Equation (1) should be high magnitude at low elevation, and low magnitude at high elevation. Therefore, to vet radar-derived results, we analyzed the linear relationship between rMC ablation and elevation. If the magnitude and elevation trend of rMC ablation agrees well with independent metrics of melt (K-transect, MAR), then this would be evidence that radar layers act as

proxies of englacial particle paths (i.e. Figure 2). To explore the effect of using englacial particle paths that are instead departed from radiostratigraphy, we also solved for rMC ablation rates using hypothetical particle paths that dipped up to 3° degrees from the radar layer.

3 Results

3.1 Ice Deformation

Strain ellipsoids (Figure 3) illustrate englacial deformation along particle path P1 at 400 year snapshots. The pattern of principle strain for current ice sheet conditions is characterized predominantly by longitudinal (east-west) stretching and rotation onto horizontal. Englacial layers that start off as vertically stacked and equidimensional at the ice divide rotate and collapse 84° onto horizontal in the east-west direction, stretch in the east-west direction by 150%, compress in the north-south direction by 84%, and compress vertically by 67%. To uphold conservation of mass given the incompressibility of ice, the residual of principal strain components (i.e. $R = \varepsilon_1 + \varepsilon_2 + \varepsilon_3$) should be zero. The calculated principal strain along P1 had a mean residual of $\bar{R}$ = -8.39 x 10^{-6}. See Supplementary Material for visualizations of the deformed strain ellipsoid in the transverse vertical plane and map view, which further emphasize how ice deformation yields structures aligned with ice flow near the margin (Supplementary Figure 1). By 2800 yr the total strain was 2.84. The subhorizontal layers of the ablation zone therefore correspond to initially subhorizontal layering in the accumulation zone, but elements reaching the ablation zone have been rotated counter-clockwise (along flow) by nearly 90 degrees and stretched out one and a half times.

3.2 Simulated Isochrones and Particle Paths

Although we solved for 100 particle paths overall, here we focus our results on five representative particles spaced 30-120 km from the ice divide (Table 1, Figure 4). These particles travel pathways from different points of burial in the accumulation zone to emergence in the ablation zone. Particle P5 originates highest in the accumulation zone (30 km from the ice divide), and P1 starts lowest in the accumulation zone (120 km from the ice divide). P5 travels a path that extends deeper than that traveled by P1, and emerges at the ice surface at a lower elevation (< 500 m a.s.l.). P1 travels a shallower path, and emerges at a higher elevation (1,103 m a.s.l.).

In the accumulation zone, the ratio between vertical and horizontal flow is non uniform with progressively more vertical dominated flow toward the divide. Yet, as all particles approach the ELA (from Easting ~75-125 km), travel paths are dominated by horizontal flow. At the ELA, particles begin to experience complex flow, as the bed roughens and the ice thins. The ratio between vertical and horizontal flow varies from 1-10% in the ablation zone; in some sections the dominance of horizontal motion is disrupted as particles are advected hundreds of meters (i.e. 200-350 m) up and over bedrock peaks and ridges and then hundreds of meters down into bedrock troughs.

The age of ice at emergence across the ablation zone ranges from as young as 2 kyr to as old as 9 kyr. Ice that is 2 kyr old emerges at the surface about 30 km below the ELA. By 70 km below the ELA, about mid-way across the ablation zone, the ice is 4 kyr old at emergence. Here, ice that is at roughly three quarters ice depth, or ~500 m below the surface, is 9 kyr old.

High above the ELA, simulated isochrones and particle paths intersect. Yet, toward the ice sheet margin, the two align as the ice rotates, stretches laterally, and assumes mainly horizontal displacement. Quantitative assessment of this alignment is shown by the angles between linear segments of each (Figure 5). The initial angle between each particle path and the first isochrone (1 kyr) is variable. P5 is closely aligned (0.8°) with isochrone 1 kyr right away, while P2 is oriented more obliquely (5°). The final angle is also variable. P1 is only within 1.5° of alignment with the final isochrone it intersects (isochrone 3kyr), while P2-P5 are within 1° of parallel (of isochrones 4 kyr–9 kyr). Yet overall, the angle between simulated isochrones and particle paths decreases from the point of deposition to the point of emergence along P1, P2, P3, P4, and P5. Alignment only increases with distance from the divide, and time since deposition. By the 4 kyr time step, particle paths are misaligned by less than 1° from isochrones. The spatial relationship between internal layers and streamlines varies from sub-perpendicular near the ice divide to sub-parallel near the ice margin. In a flow field consistent with present-day ice sheet geometry and velocity, layers near the margin are aligned with the englacial flow field.

3.3 Isochrones and Radiostratigraphy

IceBridge radar data reveal clear internal layers that intersect the ice surface at elevations ranging from 900-1300 m a.s.l (e.g. Figure 6). Layering is easily observed in the upper half of the ice column. In the lower third of the ice column, and within ~20 km of the ice margin (i.e. Easting -228 km), virtually no layering is observed. This could be due to any combination of the following: (a) layering has been distorted by complex ice

flow beyond recognition; (b) much or all of the ice near the margin is temperate (Harrington et al., 2015); (c) signal scattering and off-nadir reflections are caused by complex bed topography; and/or (d) radar waves are attenuated by water in streams and the rotten cryoconite layer at the surface, so that low power returns associated with basal layer reflectors are lost.

Modelled isochrones show good agreement with radar layers in terms of orientation and relative position (Figure 7). Both show emergent layers between elevations of 900 and 1300 m a.s.l., and between Eastings of -177 km and -195 km. Both show layers that drape topography. This qualitative agreement indicates that real-world internal layers are consistent with the modelled internal flow field. Layers depicted in IceBridge radiostratigraphy that have been shaped by past transience are comparable to layers that have been shaped by a simulation of present-day ice flow.

3.4 Mass-conserving Ablation

IceBridge flight lines are oriented within 1° of the mean ice flow direction up glacier of Easting -210 km. Down-glacier of this cutoff an obliquely-oriented bedrock trough and the Russell Glacier outlet divert ice flow. However, the easternmost sections of IceBridge radargams (e.g. Figure 6) document two dimensional cross sections of ice flow. Radar flight lines essentially follow flowlines above 800 m a.s.l. and thereby can be used for the mass conservation analysis outlined by Figure 2 and in Sect. 2.3.4. Particle path lengths delineated by the 113 traced radar layers are tens of kilometers (i.e. 8.20 km to 34.3 km). The average ice velocity along these layers ranges from 59.3 m yr^{-1} to 120 m yr^{-1}, so that the characteristic time steps are century-scale (100 years to 327 years). The average

vertical strain rates are on the order of 10^{-3} yr^{-1} (i.e. -2.2 x 10^{-3} yr^{-1} to +2.4 x 10^{-3} yr^{-1}), and the fractions of the ice column are hundreds of meters, so that flux divergence along the particle path adds and subtracts tens of centimeters. Median values are shown in Table 2.

Mass-conserving ablation rates, derived from radar layers and observational data on ice flow, increased with decreasing elevation (Figure 8). The rMC ablation showed a statistically significant trend with elevation ($p < 0.01$, $r^2 = 0.952$), consistent with RACMO ($p < 0.01$, $r^2 = 0.958$). The median of rMC ablation was -1.36 +/- 0.37 m yr^{-1} (n=113), also consistent with RACMO (median = -1.81 +/- 0.74 m yr^{-1}, n=113). The magnitude of rMC ablation rates were furthermore consistent with in situ measurements of ablation from the K-transect at similar elevations (mean = -1.16+/- 0.55 m yr^{-1}, n=3).

In contrast, our analysis shows that if particle path slopes were just a few degrees off from radar layers, then the corresponding rMC ablation rates would overestimate comparable RACMO melt. Figure 8c demonstrates how a particle path dipping 1°, 2°, and 3° from the traced radar layer would result in substantial increases in the fraction of the ice column used to calculated rMC ablation. As Equation 1 and Figure 8b show, rMC ablation and the fraction of the ice column are linearly related. Particle paths merely a few degrees departed from the radar layer yield mass conserving ablation rates that are more than 100% off from ablation reported by RACMO and the K-transect. Layers imaged by ablation zone radiostratigraphy balanced optimally with present-day data on ice flow and surface mass balance when treated as direct proxies of englacial particle paths.

4 Discussion

The salient result of our analyses is that the flow field along our western GrIS transect transforms primary layer structures deposited in the accumulation zone into a layer structure in the ablation zone that is aligned with the horizontal direction of ice flow. The depositional layer spacing is not necessarily preserved, however, due to flux divergence during margin-ward flow. Particle flow paths are normal to layering at the divide, oblique to layering along the flanks of the accumulation zone, and parallel to layering below the equilibrium line. A cross section of the radiostratigraphy in the ablation zone that is oriented parallel to the direction of ice flow therefore reveals layer orientation that is representative of local englacial streamlines. This contrasts with other ice sheet circumstances, where folded (Siegert et al., 2004) and disturbed (Rippin et al., 2006) layers are inconsistent with present-day conditions, and have been shown to be remnant structures of past flow that have little relation to the local, modern flow field.

Each of our analyses relies upon modern instances of ice sheet mass balance, geometry, and velocity. We have not explicitly accounted for past or ongoing transience. However, on the time scale of recent years to decades this region has thinned on the order of tens of centimeters per year (Csatho et al., 2014; Helm et al., 2014), likely due to increased surface melt (Fettweis et al., 2011). On the millennial time scale, geologic (van Tatenhove et al., 1996) and modeling (Simpson et al., 2009) studies imply that the ice margin retreated on the order of tens of kilometers ~4 kyr ago, which was assumed to be accompanied by changes to the geometry of the remaining ice sheet. In fact, the scale of mid-Holocene retreat in this area is seemingly greater than other marginal areas (Simpson et al., 2009). This apparent discrepancy between past transience in ice sheet geometry,

and our analyses that imply the radiostratigraphy is consistent with a modern snapshot of the ablation zone, must somehow be reconciled.

Why do these modern ablation and velocity datasets balance against the emergent layer structure? The answer likely is in the characteristic length scale used in our mass conservation analysis. It is associated with a displacement time constant of centuries. Decadal period imbalances therefore could have been lost to centennial-scale diffusion, which would imply that the recently measured 0.5 m yr^{-1} rate of surface elevation lowering (Csatho et al., 2014) has not been constant over recent decades. Alternatively, sustained ablation changes on the century time scale could have been compensated by velocity changes, e.g. more melt accompanied by more ice delivered from up-stream would dampen the rate of ice sheet thinning and geometric change. It seems that transience on the millennial time scale, including the readvance and thickening of ice in this region (Huybrechts, 1994), has achieved a geometry that is representative of a balanced condition.

Our findings suggest that model solutions that assimilate modern data and assume balance between those fields (e.g. Brinkerhoff et al., 2011; Meierbachtol et al., 2015) could perhaps also utilize radiostratigraphy as an observational constraint on ice dynamics. In particular, layer structure perhaps serves as a unique indicator of local basal boundary conditions. For example, layers that steepen down flow that are not draping underlying bed bumps may indicate that the ice is flowing over a slippery then sticky spot on the bed (Holschuh et al., 2017). Provided that the challenges posed by poor radar data continuity near the ice sheet margin are overcome, radar layers parallel to ice flow may aid modeling efforts, by, as cited in this example, constraining estimates of frictional

anomalies at the bed (Holschuh et al., 2017). However, the isochrones associated with a steady state model solution of this region are not necessarily representative of the true age of the ice, since the ice sheet has not likely maintained its current geometry for as long as residence times associated with the current geometry. Furthermore, it is important to note that our analysis focused on a study area where modern transience is small, i.e. <0.5 m yr^{-1} surface elevation lowering, relative to other areas, such as GrIS marine-terminating outlet glaciers, where ice thinning up to many meters per year has been recorded (Csatho et al., 2014). The treatment of radar layers as consistent with present-day, local conditions is not necessarily supported for those areas.

Our analysis reduces the uncertainty surrounding ablation zone radiostratigraphy and its relationship to the englacial flow field within the analyzed reach, but has not eliminated the need for scrutiny interpreting radar geometry elsewhere in the GrIS ablation zone. Within the analyzed, western GrIS study area, we reject the hypothesis that internal layers reflect past transience and distal conditions strongly enough to disrupt alignment with the modern, local ice flow field. Our results point to local bed topography as being a primary driver of layer slope in the ablation zone, and imply that climate change impacts on the ice sheet have much less effect on these englacial structures. The flow field representativeness of the radiostratigraphy in the ablation zone will be maintained under a changing climate as long as the ice traveling below the ELA has undergone sufficient elongation with ~90° of rotation; conditions that are apparently difficult to disrupt. However, we did not formally probe the sensitivity of this result. Doing so would require an experiment wherein surface mass balance and ice flow fields were perturbed and resultant transience in internal structure and geometry tracked.

Questions regarding exactly what magnitude and character of transience are required to interrupt this alignment remain open, to be addressed by future work.

5 Conclusions

Ice in the GrIS ablation zone was initially deposited millennia ago, and since has traveled englacially through a complex and three dimensional flow field. We knew that in an idealized setting, and for the smaller and simpler Barnes Ice Cap (Hudleston and Hooke, 1980), emergent englacial layers, viewed parallel to the direction of ice flow, were closely aligned with local englacial streamlines. However, given the transience associated with GrIS long residence times, and the uncertain deformation associated with GrIS complex flow, it was unclear whether the internal layers imaged along the flanks of the GrIS were indicative of local and modern ice flow conditions, or of conditions up-ice or from millennia ago.

We used a multifaceted approach to address this problem, employing four distinct analyses of ice dynamics and englacial layer structure along western GrIS flowline. Each of our analyses, simulation and observation alike, supports the conclusion that radiostratigraphy in this southwest sector of the GrIS reveal englacial streamlines. Furthermore, our analyses suggest that radar layers may be interpreted as reflecting the present-day, local flow field rather than transient conditions inherited from past ice flow. This is a somewhat counterintuitive conclusion, given the imbalanced state of mass loss of the GrIS overall (Hanna et al., 2013), the likely history of retreat and readvance of this area of the GrIS in particular (Simpson et al., 2009; van Tatenhove et al., 1996), and the ongoing surface elevation thinning in this region due to increasing surface melt (Csatho

et al., 2014; Helm et al., 2014). Yet, promisingly, the radiostratigraphy we analyzed seems to have the potential to serve as a unique and powerful observational constraint on ice sheet models that simulate modern ice dynamics.

6 Acknowledgements

Co-authors on this paper are Joel Harper, Jesse Johnson, and Toby Meierbachtol. This work was funded by the NSF grant number PP-ANS 0909495 and NASA grant number NNX11AM12A. CF was supported by a grant from the Montana Space Grant Consortium. In the early stages of this project Dr. Michelle Koutnik of the University of Washington provided CF with insightful advice and model output regarding the interpretation of internal layers. Dr. Joel Brown wrote the original semi-automated layer tracing script which CF adopted and adapted.

7 References

Bamber, J. L., Griggs, J. A., Hurkmans, R. T. W. L., Dowdeswell, J. A., Gogineni, S. P., Howat, I., et al. (2013). A new bed elevation dataset for Greenland. Cryosph. 7, 499–510. doi:10.5194/tc-7-499-2013.

Bartholomew, I. D., Nienow, P., Sole, A., Mair, D., Cowton, T., King, M. A., et al. (2011). Seasonal variations in Greenland Ice Sheet motion: Inland extent and behaviour at higher elevations. Earth Planet. Sci. Lett. 307, 271–278. doi:10.1016/j.epsl.2011.04.014.

Brinkerhoff, D. J., Meierbachtol, T. W., Johnson, J. V., and Harper, J. T. (2011). Sensitivity of the frozen/melted basal boundary to perturbations of basal traction and geothermal heat flux : Isunnguata Sermia, Western Greenland.

Catania, G. A., Neumann, T. A., and Price, S. F. (2008). Characterizing englacial drainage in the ablation zone of the Greenland ice sheet. J. Glaciol. 54, 567–578. doi:10.3189/002214308786570854.

Csatho, B. M., Schenk, A. F., van der Veen, C. J., Babonis, G., Duncan, K., Rezvanbehbahani, S., et al. (2014). Laser altimetry reveals complex pattern of Greenland Ice Sheet dynamics. Proc. Natl. Acad. Sci. 111, 18478–18483. doi:10.1073/pnas.1411680112.

Fettweis, X., Tedesco, M., van den Broeke, M., and Ettema, J. (2011). Melting trends over the Greenland ice sheet (1958–2009) from spaceborne microwave data and regional climate models. Cryosph. 5, 359–375. doi:10.5194/tc-5-359-2011.

Fujita, S., Maeno, H., Uratsuka, S., Furukawa, T., Mae, S., Fujii, Y., et al. (1999). Nature of radio echo layering in the Antarctic Ice Sheet detected by a two-frequency experiment. J. Geophys. Res. Solid Earth 104, 13013–13024. doi:10.1029/1999JB900034.

Hanna, E., Navarro, F. J., Pattyn, F., Domingues, C. M., Fettweis, X., Ivins, E. R., et al. (2013). Ice-sheet mass balance and climate change. Nature 498, 51–59. doi:10.1038/nature12238.

Harper, J. T., Hubbard, A., Ruskeeniemi, T., Claesson Liljedahl, L., Kontula, A., Hobbs, M., et al. (2016). The Greenland Analogue Project : Data and Processes. SKB Rep. R-14-13, 387.

Harrington, J. A., Humphrey, N. F., and Harper, J. T. (2015). Temperature distribution and thermal anomalies along a flowline of the Greenland ice sheet. Ann. Glaciol. 56, 98–104. doi:10.3189/2015AoG70A945.

Helm, V., Humbert, A., and Miller, H. (2014). Elevation and elevation change of Greenland and Antarctica derived from CryoSat-2. Cryosphere 8, 1539–1559. doi:10.5194/tc-8-1539-2014.

Hempel, L., Thyssen, F., Gundestrup, N., Clausen, H. B., and Miller, H. (2000). A comparison of radio-echo sounding data and electrical conductivity of the GRIP ice core. J. Glaciol. 46, 369–374. doi:10.3189/172756500781833070.

Hindmarsh, A. (1983). "ODEPACK, a Systematized Collection of ODE Solvers," in Scientific Computing, ed. R. Stepleman (Elsevier).

Hindmarsh, R. C. A., Leysinger Vieli, G. J. M. C., and Parrenin, F. (2009). A large-scale numerical model for computing isochrone geometry. Ann. Glaciol. 50, 130–140. doi:10.3189/172756409789097450.

Hindmarsh, R. C. A., Leysinger Vieli, G. J. M. C., Raymond, M. J., and Gudmundsson, G. H. (2006). Draping or overriding: The effect of horizontal stress gradients on internal layer architecture in ice sheets. J. Geophys. Res. Earth Surf. 111. doi:10.1029/2005JF000309.

Holschuh, N., Parizek, B. R., Alley, R. B., and Anandakrishnan, S. (2017). Decoding ice sheet behavior using englacial layer slopes. Geophys. Res. Lett. 44, 5561–5570. doi:10.1002/2017GL073417.

Hudleston, P. J., and Hooke, R. L. (1980). Cumulative deformation in the Barnes Ice Cap and implications for the development of foliation. Tectonophysics 66, 127–146.

Huybrechts, P. (1994). The Present Evolution of the Greenland Ice Sheet: An Assessment by Modelling. Glob. Planet. Change 9, 39–51.

Jezek, K., Wu, X., Paden, J., and Leuschen, C. (2013). Radar mapping of Isunnguata Sermia, Greenland. J. Glaciol. 59, 1135–1146. doi:10.3189/2013JoG12J248.

Joughin, I., Smith, B. E., Howat, I. M., Scambos, T., and Moon, T. (2010). Greenland flow variability from ice-sheet-wide velocity mapping. J. Glaciol. 56, 415–430. doi:10.3189/002214310792447734.

Karlsson, N. B., Bingham, R. G., Rippin, D. M., Hindmarsh, R. C. A., Corr, H. F. J., and Vaughan, D. G. (2014). Constraining past accumulation in the central Pine Island Glacier basin, West Antarctica, using radio-echo sounding. J. Glaciol. 60, 553–562. doi:10.3189/2014JoG13J180.

Legarsky, J. J., and Gao, X. (2006). Internal layer tracing and age-depth relationship from the ice divide toward Jakobshavn, Greenland. IEEE Geosci. Remote Sens. Lett. 3, 471–475. doi:10.1109/LGRS.2006.877749.

Leuschen, C. (2011). IceBridge MCoRDS L1B Geolocated Radar Echo Strength Profiles, Version 2, Boulder, Colorado USA, NASA Snow and Ice Data Center Distributed Active Archive Center. doi:http://dx.doi.org/10.5067/90S1XZRBAX5N.

Lindbäck, K., Pettersson, R., Doyle, S. H., Helanow, C., Jansson, P., Savstrup Kristensen, S., et al. (2014). High-resolution ice thickness and bed topography of a land-terminating section of the Greenland Ice Sheet. Earth Syst. Sci. Data Discuss. 7, 129–148. doi:10.5194/essdd-7-129-2014.

MacGregor, J. A., Colgan, W. T., Fahnestock, M. A., Morlighem, M., Catania, G. A., Paden, J. D., et al. (2016). Holocene deceleration of the Greenland Ice Sheet. Science 351, 590–593. doi:10.1126/science.aab1702.

Meierbachtol, T. W., Harper, J. T., Johnson, J. V., Humphrey, N. F., and Brinkerhoff, D. J. (2015). Thermal boundary conditions on western Greenland: Observational constraints and impacts on the modeled thermomechanical state. J. Geophys. Res. Earth Surf. 120, 623–636. doi:10.1002/2014JF003375.

Millar, D. H. M. (1981). Radio-echo layering in polar ice sheets and past volcanic activity. Nature 292, 441–443.

Palmer, S., Shepherd, A., Nienow, P., and Joughin, I. (2011). Seasonal speedup of the Greenland Ice Sheet linked to routing of surface water. Earth Planet. Sci. Lett. 302, 423–428. doi:10.1016/j.epsl.2010.12.037.

Pattyn, F. (2002). Ice-flow characteristics over a rough bedrock: implications for ice-core interpretation. Polar Meteorol. Glaciol. 16, 42–52.

Pattyn, F. (2003). A new three-dimensional higher-order thermomechanical ice sheet model: Basic sensitivity, ice stream development, and ice flow across subglacial lakes. J. Geophys. Res. 108, 2382. doi:10.1029/2002JB002329.

Rippin, D. M., Siegert, M. J., Bamber, J. L., Vaughan, D. G., and Corr, H. F. J. (2006). Switch-off of a major enhanced ice flow unit in East Antarctica. Geophys. Res. Lett. 33, 1–6. doi:10.1029/2006GL026648.

Ryser, C., L̂hi, M. P., Andrews, L. C., Hoffman, M. J., Catania, G. A., Hawley, R. L., et al. (2014). Sustained high basal motion of the Greenland ice sheet revealed by borehole deformation. J. Glaciol. 60, 647–660. doi:10.3189/2014JoG13J196.

Siegert, M. J., Welch, B., Morse, D., Vieli, A., Blankenship, D. D., Joughin, I., et al. (2004). Ice flow direction change in interior West Antarctica. Science 305, 1948–51. doi:10.1126/science.1101072.

Sime, L. C., Karlsson, N. B., Paden, J. D., and Prasad Gogineni, S. (2014). Isochronous information in a Greenland ice sheet radio echo sounding data set. Geophys. Res. Lett. 41, 1593–1599. doi:10.1002/2013GL057928.

Simpson, M. J. R., Milne, G. A., Huybrechts, P., and Long, A. J. (2009). Calibrating a glaciological model of the Greenland ice sheet from the Last Glacial Maximum to present-day using field observations of relative sea level and ice extent. Quat. Sci. Rev. 28, 1631–1657. doi:10.1016/j.quascirev.2009.03.004.

Sole, A., Nienow, P., Bartholomew, I., Mair, D., Cowton, T., Tedstone, A., et al. (2013). Winter motion mediates dynamic response of the Greenland Ice Sheet to warmer summers. Geophys. Res. Lett. 40, 3940–3944. doi:10.1002/grl.50764.

Sundal, A. V., Shepherd, A., Nienow, P., Hanna, E., Palmer, S., and Huybrechts, P. (2011). Melt-induced speed-up of Greenland ice sheet offset by efficient subglacial drainage. Nature 469, 521–524. doi:10.1038/nature09740.

van de Wal, R. S. W., Boot, W., Smeets, C. J. P. P., Snellen, H., van den Broeke, M. R., and Oerlemans, J. (2012). Twenty-one years of mass balance observations along the K-transect, West Greenland. Earth Syst. Sci. Data 4, 31–35. doi:10.5194/essd-4-31-2012.

van Tatenhove, F. G., van Der Meer, J. J., and Koster, E. A. (1996). Implications for Deglaciation Chronology from New AMS Age Determinations in Central West Greenland. Quat. Res. 45, 245–253. doi:10.1006/qres.1996.0025.

Waddington, E. D., Neumann, T. A., Koutnik, M. R., Marshall, H. P., and Morse, D. L. (2007). Inference of accumulation-rate patterns from deep layers in glaciers and ice sheets. J. Glaciol. 53, 694–712. doi:10.3189/002214307784409351.

Zwally, H. J., Giovinetto, M. B., Beckley, M. A., and Saba, J. L. (2017) Antarctic and Greenland Drainage Systems, GSFC Cryospheric Sciences Laboratory, at http://icesat4.gsfc.nasa.gov/cryo_data/ant_grn_drainage_systems.php.

Figures

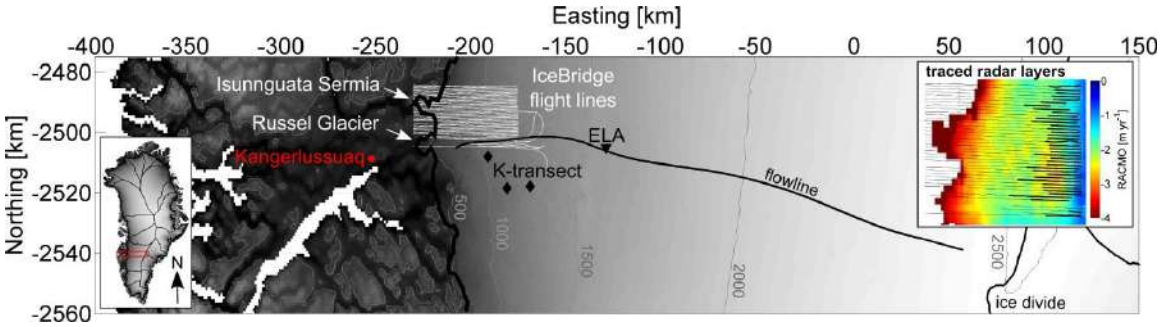

Figure 1. Study area in western Greenland. Shown with ice surface elevation contours in meters above sea level (gray lines and shading; data by Bamber et al., 2013) and the ice divide (thick white line; data by Zwally et al., 2012). Inset shows the location of the study area (red) within context of the entire Greenland Ice Sheet. This and all subsequent figures use geographic coordinates in polar stereographic projection (true latitude 70^0, central meridian -45^0). The outlet glaciers Isunnguata Sermia and Russell Glacier are indicated (white arrows). Location of IceBridge flightlines (thin white lines), K-transect surface mass balance sites (black diamonds), the modeled ice flowline (black line), and the Equilibrium Line Altitude (ELA; black triangle), are also shown. The extents of traced radar layers used to calculate radar-derived mass conserving (rMC) ablation rates are shown on the zoomed inset of IceBridge flightlines (bold black lines), plotted over surface mass balance output from the regional climate model RACMO (gridded, colored cells; data by Noël et al., 2016).

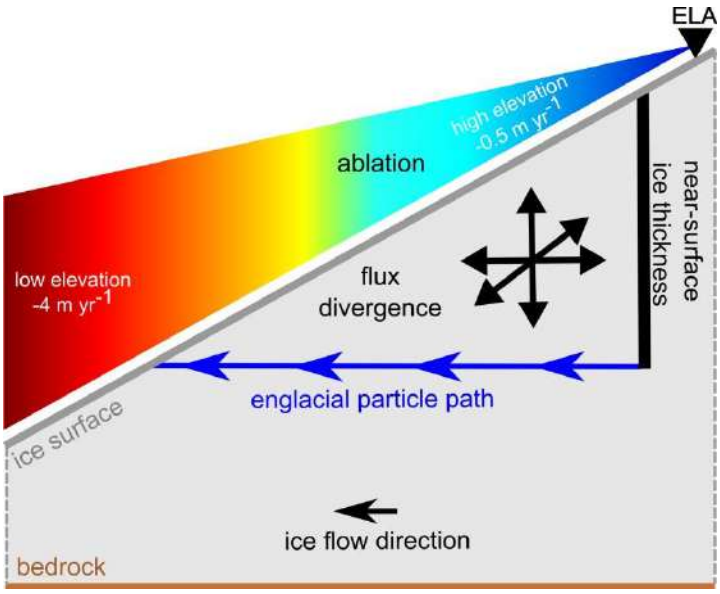

Figure 2. Schematic shows an along-flow cross section of the ablation zone, illustrating mass conservation below the ELA.

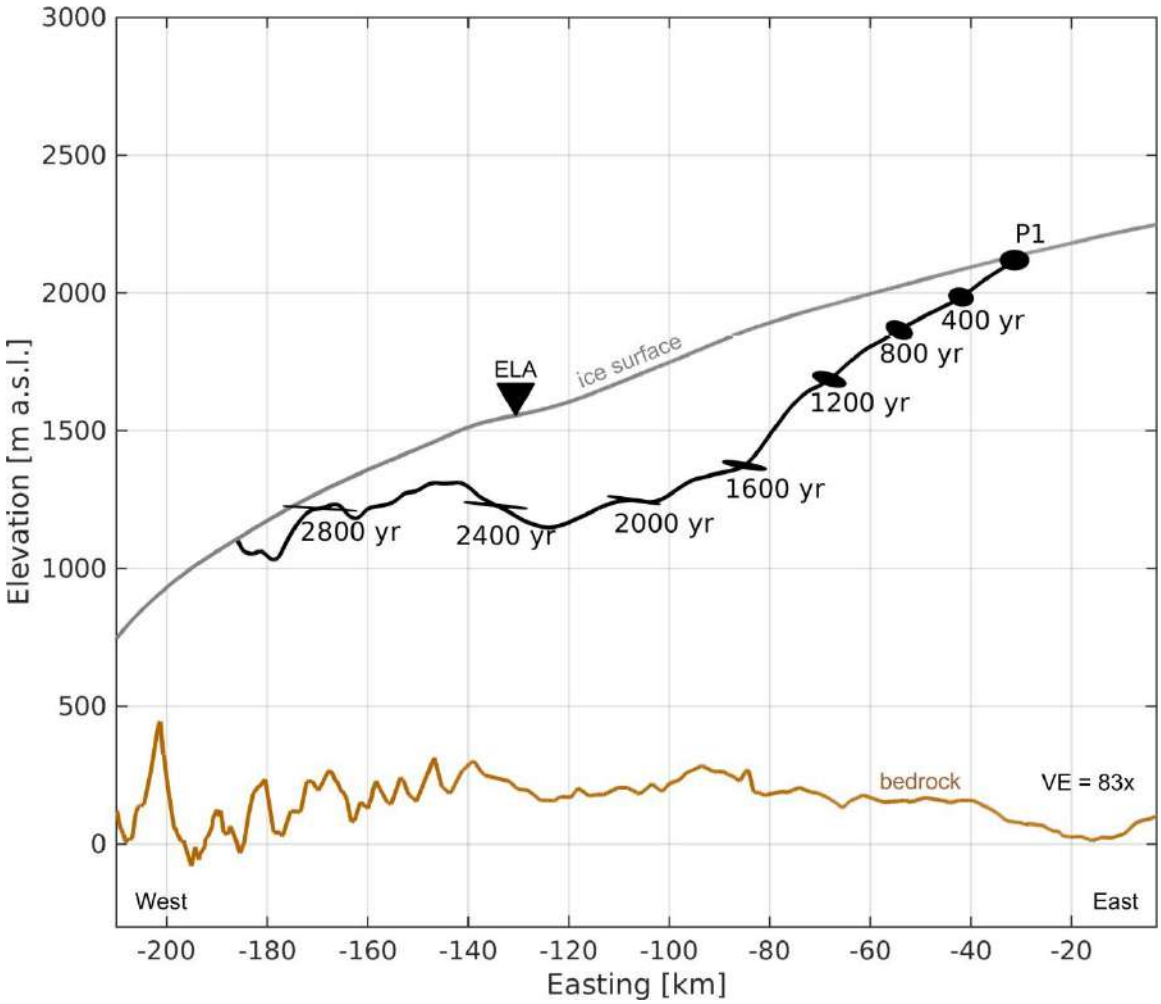

Figure 3. Ice deformation results. The deforming strain ellipsoids are shown along particle path P1 (black line) at 400 year snapshots. The ice surface (gray line), bed (brown line), and the ELA (black triangle) are also shown.

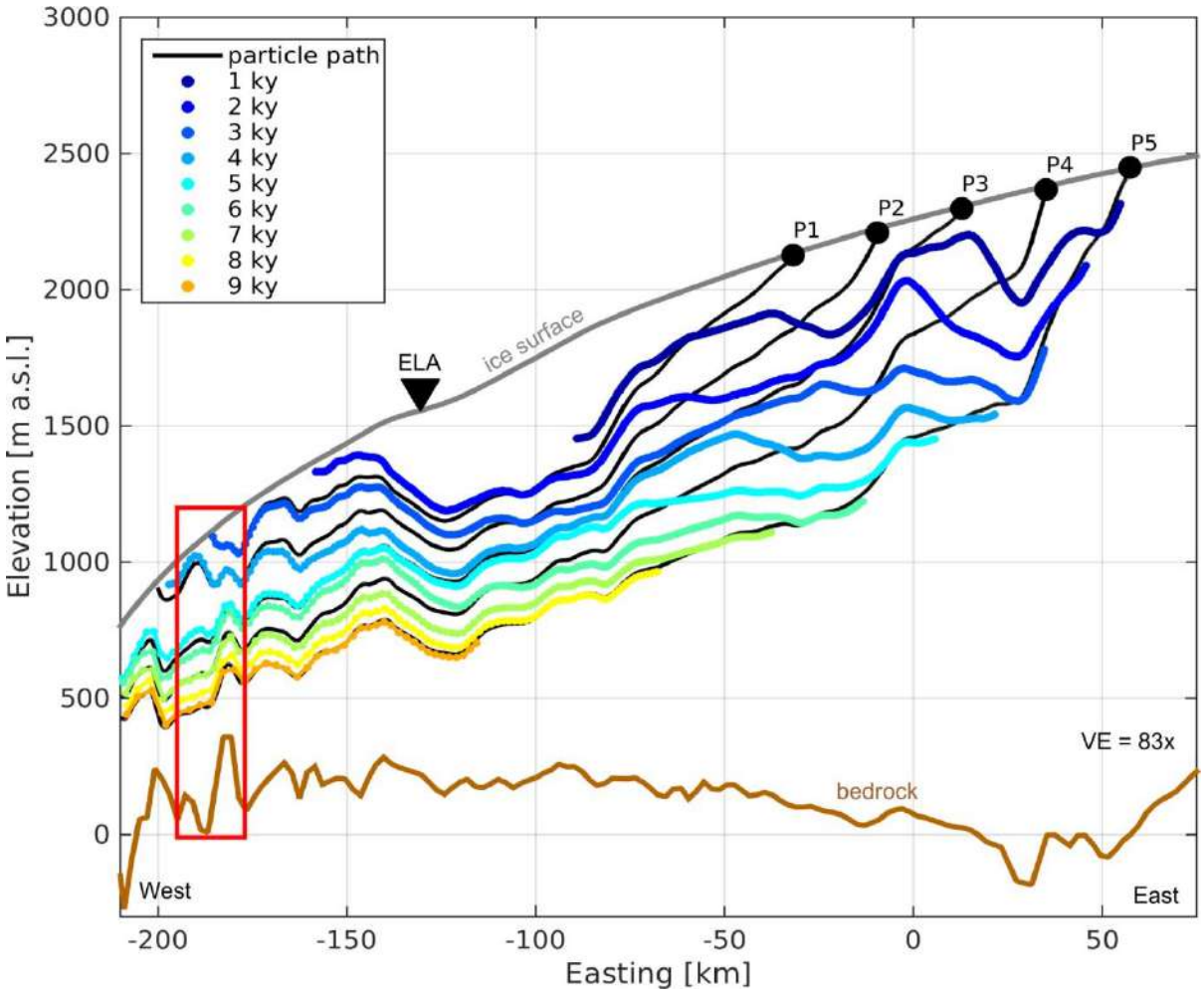

Figure 4. Simulation results. Simulated isochrones (colored lines: blue to orange, youngest to oldest) and particle paths (black lines) are shown from burial in the accumulation zone to emergence in the ablation zone. Note that due to the aspect ratio, vertical motion is exaggerated 83x. Ice surface (gray line), bed (brown line), and the ELA (black triangle) are also shown. The extent of Figure 7 is indicated (red box). There is a third dimension (Northing) to these results which is not shown here.

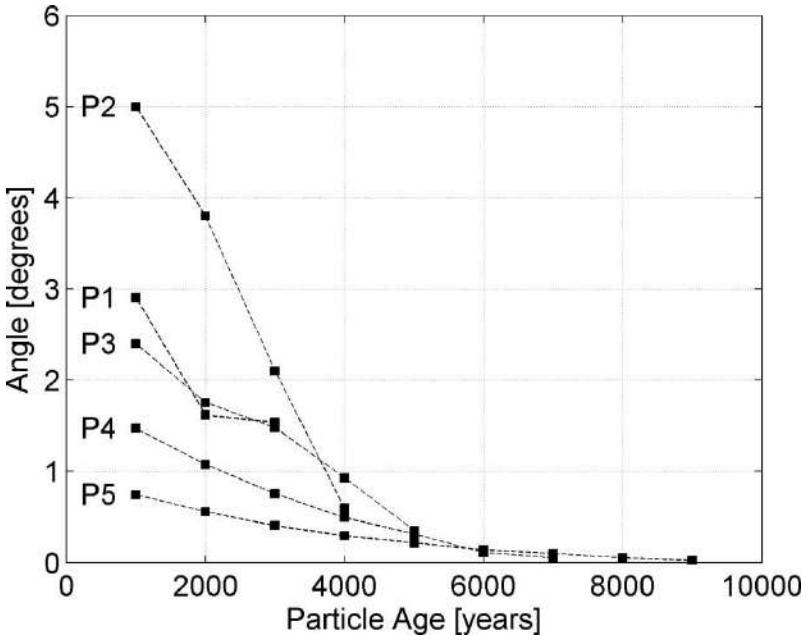

Figure 5. The angle between simulated isochrones and particle paths P1-P5. Results are shown as particles age from deposition near the ice divide (age 0), to emergence near the ice sheet margin.

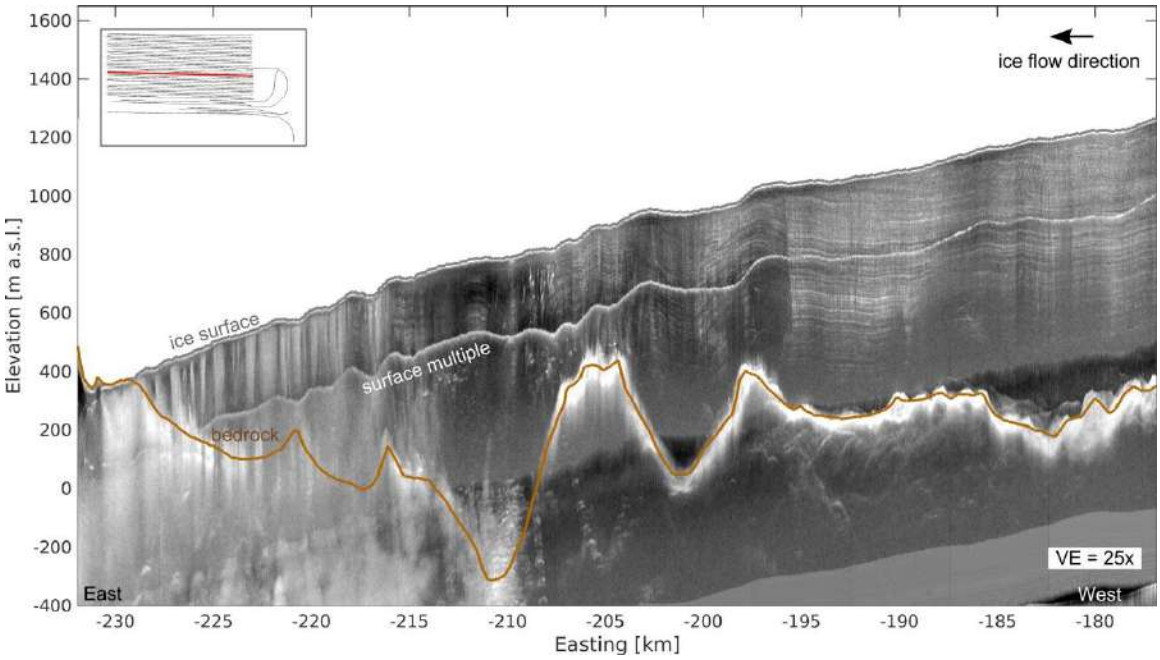

Figure 6. IceBridge radargram showing internal layers along an ablation zone cross section. Ice flow is West to East. Ice surface (thin black line) and bed (brown line) picked from the radar data are shown. The thick bold white reflector at ~1/3 ice depth is a surface multiple, an artifact of airborne radar depth sounding (data by Leuschen, 2011). Inset shows map view of IceBridge flight lines, with the extent of this radargram highlighted (red).

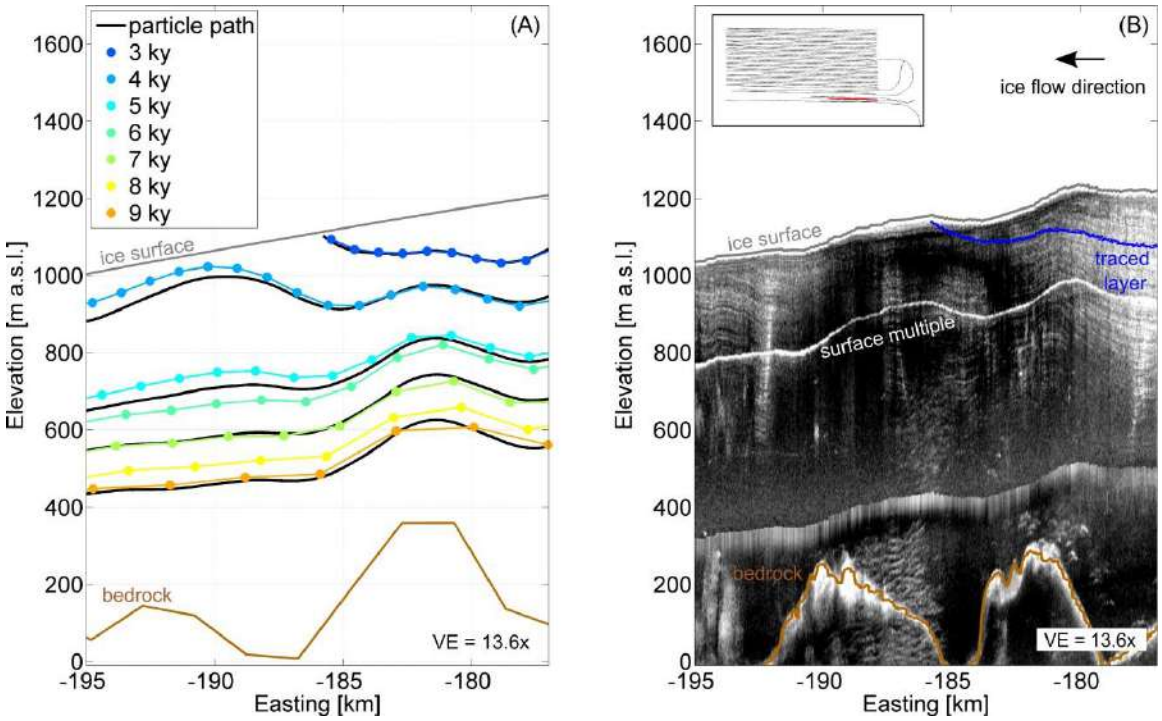

Figure 7. Comparison between simulation and observation. (A) Simulated isochrones (colored lines: blue to orange, youngest to oldest) and englacial particle paths (black lines), and (B) observed internal layers in IceBridge radiostratigraphy (Leuschen, 2011), with one traced radar layer shown (blue line). The ice surface (gray line), bed (brown line), and surface multiple are as in Figure 6. Inset shows map view of IceBridge flight lines, with the extent of this radargram segment highlighted (red).

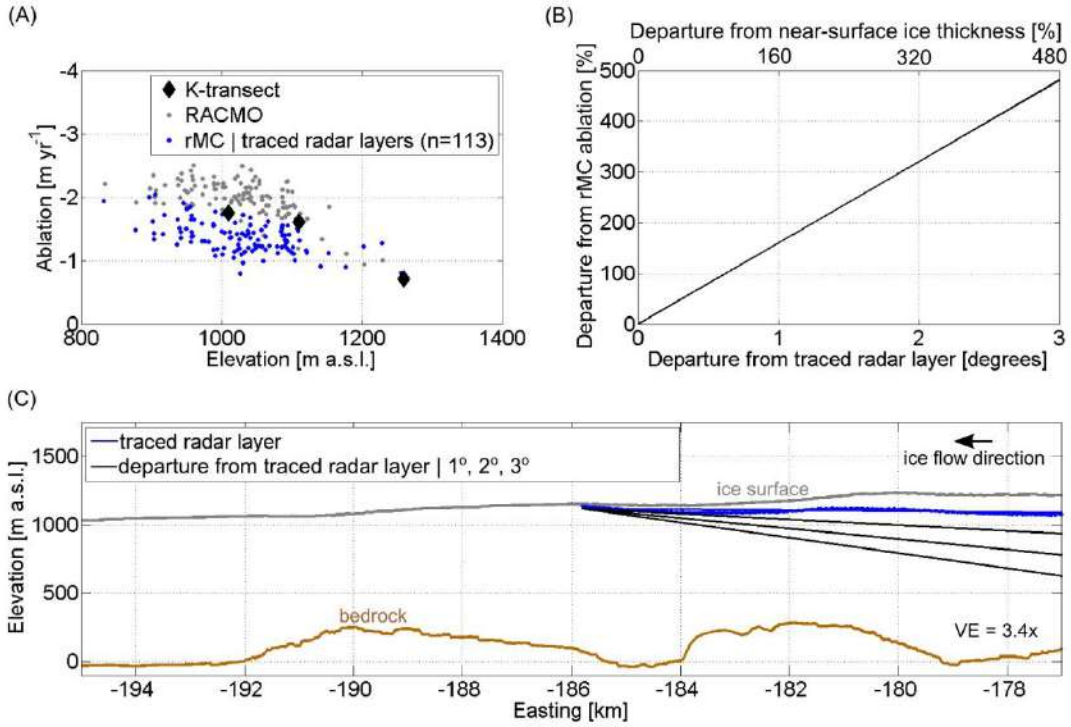

Figure 8. (A) Radar-derived, mass-conserving (rMC) ablation rates (blue dots), K-transect in situ observations (black diamonds), and regional climate model RACMO output (gray dots) plotted against elevation. (B) Plot shows the effect of using englacial particle paths that are departed from radar layers. The fraction of the ice column (top x-axis) increases as departure from the traced radar layer (bottom x-axis) increases. Increased fractions of the ice column result in increased ablation rates (y-axis). Departures are expressed relative to the traced radar layer shown in (C). (C) Along-flow cross section showing IceBridge ice surface (black line), bed (brown line), and traced radar layer (blue line), presented the same as in Figure 6 but without the complete radiostratigraphy and with less vertical exaggeration. Hypothetical particle paths dipping 1°, 2°, and 3° from the traced radar layer (dashed black lines) are also shown.

Tables

Starter Particle	Easting [km]	Northing [km]	Elevation [m a.s.l.]	Distance from Divide [km]
P1	-31.9	-2524.4	2117	120
P2	-9.6	-2528.0	2199	98
P3	12.8	-2531.6	2288	75
P4	35.1	-2535.2	2357	52
P5	57.4	-2538.8	2438	30

Table 1. Initial coordinates, elevation, and distance from the ice divide of simulated particles.

Variable	Symbol	Median
Particle path length	Δx	14,756 +/- 250 m
Fraction of the ice column	η	211 +/- 16 m
Average velocity	$\bar{v}$	100 +/- 4.8 m yr^{-1}
Average vertical strain rate	$\bar{\dot{\varepsilon}}_{zz}$	1.20×10^{-4} +/- 0.025 yr^{-1}
Average radar-derived mass conserving ablation	$\bar{\dot{a}}$	-1.36 +/- 0.37 m yr^{-1}
Average RACMO ablation	$\bar{\dot{a}}$	-1.81 +/- 0.74 m yr^{-1}

Table 2. Median of observational data used to calculate radar-derived, mass conserving (rMC) ablation rates. Median rMC and RACMO ablation also listed. Average refers to the spatial average along traced layers.

Supplementary Material

Radiostratigraphy reflects the present-day, internal ice flow field in the ablation zone of western Greenland

Caitlyn Florentine*, Joel Harper, Jesse Johnson, Toby Meierbachtol

*** Correspondence:** Caitlyn Florentine, caitlyn.florentine@umontana.edu

1 Supplementary Methods: Ice Deformation

This section outlines details on instantaneous strain, cumulative strain, principal strain, and total strain calculations.

1.1 Ice Velocity and Strain Rate

The modelled velocity field is comprised of three components: longitudinal (u), transverse (v), and vertical (w). The model domain is on a Cartesian coordinate system where longitudinal is east-west, transverse is north-south, and vertical is up-down with respect to sea level. Normal strain rates are defined as the spatial gradient of ice flow in the direction of ice flow, so that normal strain rates in the longitudinal direction are defined as $\dot{\varepsilon}_{xx} = \frac{\partial u}{\partial x}$, in the transverse direction as $\dot{\varepsilon}_{yy} = \frac{\partial v}{\partial y}$, and in the vertical direction as $\dot{\varepsilon}_{zz} = \frac{\partial w}{\partial z}$. Shear strain rates along a vertical plane extending in the longitudinal direction are defined as $\dot{\varepsilon}_{xz} = \frac{1}{2}\left(\frac{\partial u}{\partial z} + \frac{\partial w}{\partial x}\right)$, along a vertical plane extending in the transverse direction as $\dot{\varepsilon}_{yz} = \frac{1}{2}\left(\frac{\partial v}{\partial z} + \frac{\partial w}{\partial y}\right)$, and along a horizontal plane as $\dot{\varepsilon}_{xy} = \frac{1}{2}\left(\frac{\partial u}{\partial y} + \frac{\partial v}{\partial x}\right)$ (Hooke, 2005). These were computed on the entire numerical mesh from the Meierbachtol et al. (2015) study, using the finite element solver software

FEniCS. The deformation tensor of ice is symmetric (van der Veen, 2013). Thus these six components of normal and shear strain rates provided the full strain rate tensor.

1.2 Finite and Cumulative Strain

Approximating strain by taking instantaneous strain rate on a time step (i.e. $\dot{\varepsilon}_{xy}\,\Delta t$) does not accurately resolve large strains (Cuffey and Patterson, 2010), such as those incurred between the ice divide and the margin. Therefore, we calculated finite strain from deposition to emergence. Finite, or logarithmic strain, is defined as (Hooke, 1998):

$$\varepsilon = \ln(1 + \dot{\varepsilon}\,\Delta t) \qquad \text{(I)}$$

We compute finite strain on 1 year time steps along P1 (Fig.3), and sum to find cumulative strain.

1.3 Principal Cumulative Strain

We solved for the eigenvalues and eigenvectors of the cumulative strain tensor to solve for the principal magnitude and direction of cumulative strain at each time step along the modelled particle path.

1.4 A Metric of Total Strain: Natural Octahedral Unit Shear

Cumulative normal strain components (ε_{xx}, ε_{yy}, ε_{zz}) are used to calculate cumulative natural octahedral unit shear (Hooke, 1998), which is a useful metric of total strain:

$$\gamma_{oc} = \frac{2}{3}\left[\left(\varepsilon_{xx} - \varepsilon_{yy}\right)^2 + \left(\varepsilon_{yy} - \varepsilon_{zz}\right)^2 + \left(\varepsilon_{zz} - \varepsilon_{xx}\right)^2 \right]^{\frac{1}{2}} \qquad \text{(II)}$$

2 Supplementary Methods: Mass-conserving Ablation

2.1 Relation to Canon

The vertically-integrated continuity relation is (Cuffey and Paterson, 2010):

$$\frac{\partial H}{\partial t} = \dot{a} - \nabla \cdot \vec{q} \tag{III}$$

Where $\frac{\partial H}{\partial t}$ represents the rate of ice thickness change, $\dot{a}$ represents the surface mass balance, and the remaining term represents divergence in ice flux. Ice flux is $\vec{q} = \bar{U}H$, where the full ice thickness (bed to surface) is *H*, and the vertical average of ice flow is $\bar{U} = \langle \bar{u}_x, \bar{u}_y \rangle$. Expanded, this flux divergence term is:

$$\nabla \cdot \vec{q} = H\left(\frac{\partial \bar{u}_x}{\partial x} + \frac{\partial \bar{u}_y}{\partial y}\right) + \bar{u}_x \frac{\partial H}{\partial x} + \bar{u}_y \frac{\partial H}{\partial y} \tag{IV}$$

Plugging this expansion back into the first equation, and assuming ice flow is aligned with the x-coordinate, yields another commonly-used expression of the continuity equation (der Veen, 2009):

$$\frac{\partial H}{\partial t} = \dot{a} - \left[H\left(\frac{\partial \bar{u}_x}{\partial x} + \frac{\partial \bar{u}_y}{\partial y}\right) + u_x \frac{\partial H}{\partial x}\right] \tag{V}$$

Part of the first bracketed term on the right hand side can be simplified using the assumption of incompressibility, i.e. $\left(\frac{\partial \bar{u}_x}{\partial x} + \frac{\partial \bar{u}_y}{\partial y}\right) = -\frac{\partial \bar{u}_z}{\partial z} = -\bar{\dot{\varepsilon}}_{zz}$. The last bracketed term represents advection of ice thickness gradients.

Now we apply this canonical equation to the geometry represented by emergent layer radiostratigraphy in Figure 2. Rather than consider the full ice thickness, we consider a fraction of the ice column, so H becomes η. We consider surface mass balance averaged along the particle path, thus $\dot{a}$ becomes $\bar{\dot{a}}$. In the near-surface, where our analysis is

restricted, we assume that $\bar{U} = U_{sfc}$, and that subsequently $-\bar{\dot{\varepsilon}}_{zz} = -\dot{\varepsilon}_{zz\_sfc}$. We consider vertical strain averaged along the particle path, thus $-\dot{\varepsilon}_{zz\_sfc}$ becomes $-\bar{\dot{\varepsilon}}_{zz}$, where now the overbar refers to a horizontal average. In a steady state system, time-dependent rates of change are zero so $\frac{\partial H}{\partial t} = 0$. We consider a steady state because observations of $\frac{\partial H}{\partial t}$ in the study area are small (Csatho et al., 2014). These substitutions yield:

$$0 = \bar{\dot{a}} - \left[\eta(-\bar{\dot{\varepsilon}}_{zz}) + u_x \frac{\partial \eta}{\partial x}\right] \quad \text{(VI)}$$

We consider discrete rather than continuous changes in geometry along the particle path thus $\partial\eta$ becomes $\Delta\eta$ and ∂x becomes Δx. The change in fraction of the ice column is equal to the negative of the initial fraction of the ice column, because $\eta_1 = \eta$ at the start point, and $\eta_2 = 0$ at the point of emergence, i.e. $\Delta\eta = \eta_2 - \eta_1 = -\eta$. We consider the average velocity along the particle path length thus, $u_x = \bar{v}$. Assigning this final substitution, the term $u_x \frac{\partial \eta}{\partial x}$ reduces it to $\bar{v}\frac{-\eta}{\Delta x}$ which is $-\frac{\eta}{\Delta t}$. Rearranging terms yields the equation used in our method:

$$-\frac{\eta}{\Delta t} = \bar{\dot{a}} + \bar{\dot{\varepsilon}}_{zz}\eta \quad \text{(VII)}$$

2.2 Velocity Data

Surface ice velocities derived from interferometric synthetic aperture radar (InSAR) satellite data for the winter of 2007 to 2008 are available for the study area at 500 m grid cell resolution (Joughin et al., 2010). We used these observational data to define the average ice speed ($\bar{v}$) along each traced radar layer. The direction of ice velocity was parallel to the flight lines. Comparing these velocity data to another satellite-derived

velocity dataset (Rignot and Mouginot, 2012), we found the two to differ by <6% along IceBridge flight lines. This is similar to the observational error (~5%; Table 2).
We acknowledge that our use surface velocity observations to define englacial particle travel at depth does not precisely resolve englacial particle speed, but assert that the difference is negligible. Every radar layer analyzed was near-surface, at ice depths <15% of the total ice thickness. Regardless of the mode of motion (i.e. sliding or deformation), ice at such a near-surface depth travels at speeds similar to surface ice (Cuffey and Paterson, 2010).

2.3 Vertical Strain Rate Data

A vertical strain rate field is given by the conservation of mass, assuming incompressibility, i.e. $\dot{\varepsilon}_{zz} = -(\dot{\varepsilon}_{xx} + \dot{\varepsilon}_{yy})$. When velocity observational errors are propagated through this vertical strain rate calculation, errors are an order of magnitude greater than the vertical strain rate itself, i.e. error ~ 0.01 yr^{-1} where $\dot{\varepsilon}_{zz}$ ~ 0.001 yr^{-1}. This is a common problem when differentiating discrete data. To address this issue, we smoothed velocity data using a linear convolution at a smoothing window of 4500 m, as it optimized the trade-off between spatial resolution of the velocity field, and magnitude of propagated error through the vertical strain rate calculation (Fig. S2, Supplement). Longitudinal ($\dot{\varepsilon}_{xx}$) and transverse ($\dot{\varepsilon}_{yy}$) strain rates were calculated from the convolved velocity data at a corresponding length scale of 4500 m.

2.4 Ablation Data: K-transect and RACMO

In situ melt surface mass balance data are available for 1990-2010 at K-transect sites within the study area (van de Wal et al., 2012). Modelled annual surface mass balances

are available at 1 km^2 grid cell resolution from the regional climate model RACMO (Noël et al., 2016). We calculated average ablation rates for RACMO output on a 20 year, modern interval that corresponds with K-transect data (1990-2010). These data are not an exhaustive account or inter-comparison between the many available GrIS regional climate models. However, we assume K-transect data and RACMO output encapsulate ablation measurement uncertainty, spatial variability, and interannual variability characteristic of modern (recent decades) methods and conditions.

2.5 Propagation of Error

To honor uncertainties associated with the data used to define each term (η , Δx, $\bar{v}$, and $\bar{\dot{\varepsilon}}_{zz}$) in Eq. (1), we propagate observational error according to a Taylor series expansion, given by,

$$F_{error} = \sum_i \left[\frac{\partial F}{\partial \alpha_i} \alpha_{ierror}\right]^2 \quad \text{(VIII)}$$

where F is the function, α is each input variable (*i*) in the function, and error is denoted by subscript.

Supplementary Figures

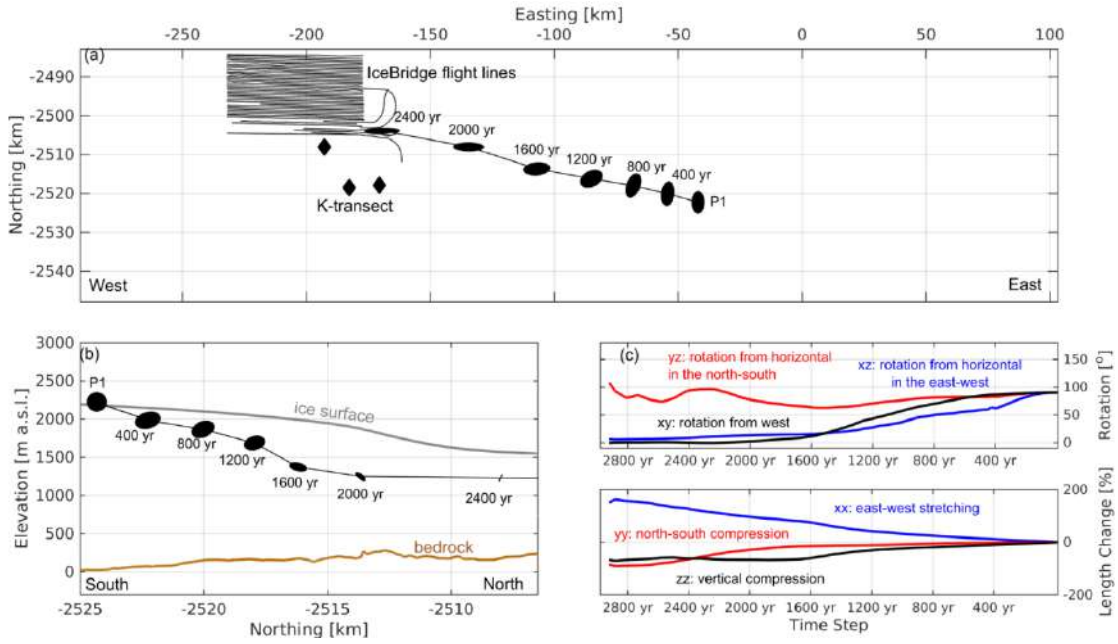

Figure S1. Ice deformation results show (a) deforming strain ellipsoids in map view, plotted with IceBridge flight lines (black lines) and K-transect sites (black diamonds) for spatial context; (b) deforming strain ellipsoids along a transverse (north-south) cross section, showing the ice surface (gray line) and bed (brown line); and (c) rotation and stretching incurred from deposition to time step 2800 yr along particle path P1 (Fig.3).

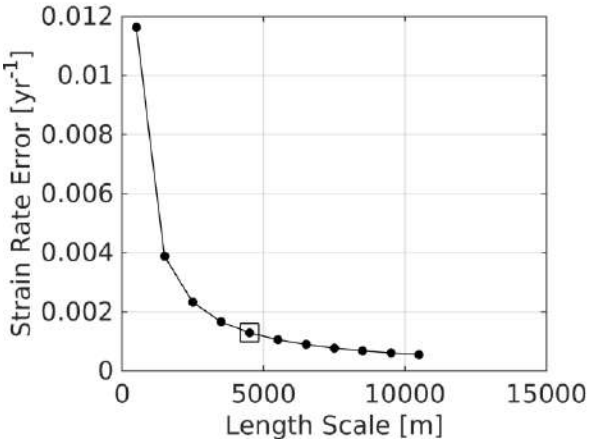

Figure S2. Average error for vertical strain rates calculated on different length scales. This curve was used to determine the optimal smoothing window (4500 m, boxed) for convolving velocity data and computing strain rates.

CHAPTER 3

LOCAL TOPOGRAPHY INCREASINGLY INFLUENCES THE MASS BALANCE OF A RETREATING CIRQUE GLACIER

Abstract:

Local topographically driven processes, such as wind drifting, avalanching, and shading, are known to alter the relationship between the mass balance of small cirque glaciers and regional climate. Yet partitioning such local effects from regional climate influence has proven difficult, creating uncertainty in the climate representativeness of some glaciers. We address this problem for Sperry Glacier in Glacier National Park, USA using field-measured surface mass balance, geodetic constraints on mass balance, and regional climate data recorded at a network of meteorological and snow stations. Geodetically derived mass changes between 1950-1960, 1960-2005, and 2005-2014 document average mass change rates during each period at -0.22$\pm$0.12 m w.e. yr^{-1}, -0.18$\pm$0.05 m w.e. yr^{-1}, and -0.10$\pm$0.03 m w.e. yr^{-1}. A correlation of field-measured mass balance and regional climate variables closely (i.e. within 0.08 m w.e. yr^{-1}) predicts the geodetically measured mass loss from 2005-2014. However, this correlation overestimates glacier mass balance for 1950-1960 by +1.18$\pm$0.92 m w.e. yr^{-1}. Our analysis suggests that local effects, not represented in regional climate variables, have become a more dominant driver of the net mass balance as the glacier lost 0.50 km^2 and retreated further into its cirque.

1 Introduction

Glaciers are sensitive indicators of climate (Dyurgerov and Meier, 2000; Roe et al., 2016) because ice mass gains are ultimately controlled by winter precipitation, and ice mass losses are ultimately controlled by radiation and air temperature during summer. However, prior studies of small (i.e. <0.5 km^2) mountain glaciers, which are often located in cirques, show that local topographic effects, including avalanching, wind drifting, and shading, enhance winter mass gains or mediate summer mass losses (e.g. Hock, 2003; Kuhn, 1995; Laha et al., 2017). These topographically driven mass balance processes complicate the relationship between regional climate and cirque glacier surface mass balance.

Such complications have been documented in high relief areas worldwide. Analysis from Montasio Occidentale Glacier in the Italian Julian Alps demonstrated that avalanche-fed, shaded glaciers can exist at low elevations otherwise climatically unsuitable for the persistence of glacier ice (Carturan et al., 2013). Analysis from a network of on-ice automatic weather stations on a cirque glacier in the French Pyrenees concluded that topographic effects may exert more control on surface energy budgets - and thereby melt - than regional lapse rates in air temperature and moisture (Hannah et al., 2000). The small glaciers of the North American Rocky Mountains have also been shown to have a disrupted, complex relationship to regional climate. In Colorado, glacier mass balance at very small (<0.2 km^2) glaciers showed no statistically significant correlation to winter precipitation during the 20^{th} century, suggesting that winter mass inputs were not connected to regional winter precipitation in a straightforward, linear manner (Hoffman et al., 2007). This result instead implied the importance of processes

driven by local topography, including snow avalanching and wind drifting. In the Canadian Rockies, an inventory of nearly 2,000 glaciers showed that while larger glaciers retreated during the last half of the 20th century, very small glaciers did not change (DeBeer and Sharp, 2007). A follow-up analysis showed that the stability of these very small (<0.4 km^2) glaciers was closely related to their topographically favorable setting (DeBeer and Sharp, 2009).

Because local topography can substantially influence the mass balance of small and sheltered mountain glaciers, it follows that as glaciers retreat further toward cirque headwalls, the direct control of regional climate on glacier mass balance should diminish, and local processes should become more influential (e.g. Haugen et al., 2010). That said, direct mass balance data from Andrews Glacier, an east-facing <0.2-km^2 glacier in Colorado, exhibited a strong correlation (r = -0.93) between summer temperature and net annual balance (Hoffman et al., 2007), despite enhanced accumulation via wind drifting and avalanching during the winter: glacier mass losses during summer outweighed the extra snow provided by topographically driven snow redistribution. Mechanistically, this could be because Andrews Glacier is small enough to have a diminished katabatic boundary layer at its surface, leaving the glacier sensitive to ambient summer temperatures (Carturan et al., 2015). Regardless, this example shows that regional climate can remain the primary driver of net mass balance, even when local topography plays a strong role.

This paper examines the time evolution of the partitioning between regional climate and local influences on glacier mass balance of a glacier retreating into its cirque. Since 1966, Sperry Glacier, Montana has reduced in area by 40% and retreated 300 m (Fagre et

al., 2017). We hypothesize that during a recent interval (2005-2014), as a larger proportion of the glacier surface has become sheltered by its cirque headwall, the relationship between specific mass balance and regional climate is quantifiably distinct from that during mid-century (1950-1960), when the glacier extended further downslope from its cirque headwall. To test this hypothesis, we leverage a field measured (glaciological) surface mass balance record and repeat geodetic mass balances.

2 Study area

Sperry Glacier (48.623° N, -113.758° W) sits just west of the Continental Divide, occupying a cirque that abuts the 2,801 m high Gunsight Peak, and is roughly in the center of Glacier National Park (GNP), Montana (Fig. 1a). A bedrock headwall, crested by a ridgeline that runs 2 km toward the northeast from Gunsight Peak (Fig. 1b), rises 100-300 m above Sperry Glacier (Fig. 2). This headwall is 0.17 km^2 in area, and has slopes between 50° to near vertical. A sub-ridge extends 500 m toward the north, bordering the glacier's western margin (labelled west ridge in Fig. 1b). Between the headwall and this sub-ridge, Sperry Glacier has a 40° ramp extending to the top of Gunsight Peak, so that some ice overlaps the ridge (Fig. 1b). A cornice that can be 10-20 m high develops every winter along this topmost section of the glacier (Fig. 2). A distinctive bergschrund separates the top 50-150 m of the glacier from the main ice body (Fig. 2). The terrain in front of Sperry Glacier is relatively low angle (<15°). Moraines located 1 km from the ice terminus (Fig. 2) indicate that in the geologically recent past, the glacier covered most of a topographic bench now bare of ice. These moraines were likely deposited when the glacier was at its Little Ice Age maximum extent (Carrara, 1989). Historical photographs and analysis from 1914 (Alden, 1914) show ice once

covered 3.24 km^2. Since that time Sperry Glacier has steadily retreated, decreasing in area to 1.58 km^2 in 1938 (Johnson, 1980), and to 0.80 km^2 in 2015 (Fagre et al., 2017).

3 Methods

3.1 Elevation data

Modern Digital Elevation Models (DEMs) of Sperry Glacier and adjacent terrain were derived from National Technical Means imagery collected in 2005 and DigitalGlobe Worldview imagery collected in 2014. These DEMs were generated by Fahey (2014), and are the same data as used by Clark et al. (2017). Both images were collected in September, when glacier mass is at an assumed annual minimum, on 02 September 2005 and 07 September 2014 respectively. The DEMs were generated with SOCET SET® software, which uses photogrammetric methods to extract terrain data from imagery (Zhang, 2006). Grid cell resolution was 5 m. The absolute accuracy of the DEM with respect to an independent vertical datum was 3.05 m in the horizontal and 7.54 m in the vertical. The precision of the DEM was 0.44 m and 0.47 m in the horizontal and vertical respectively.

U.S. Geological Survey (USGS) topographic maps at 6.1 m (20 ft) contour resolution were available for Sperry Glacier for 1950 and 1960 (Johnson, 1980). These maps were originally created using aerial photography and Kelsh plotter techniques, guided by 13 plane table bench marks. Both maps document elevation near the assumed September glacier mass minimum, on 01 September 1950 and 08 September 1960. We digitized these historic elevation data by first manually tracing scanned maps to produce digitized contours, and then interpolating digitized contours using a natural neighbor interpolation tool (ESRI, 2014; Sibson, 1981). Grid cell resolution was 5 m. We found that the historic

elevation data from the original Johnson maps from 1950 and 1960 were 56 m lower than the modern vertical datum due to the authors' sea level datum assumption. We remedied this error by adding 56 m to the 1950 and 1960 DEMs.

3.2 Geodetic mass balance and DEM co-registration

The 1950 and 1960 DEMs did not require co-registration because they were originally mapped using a common vertical datum and spatial reference frame. We co-registered the 2005 and 2014, and the 1960 and 2005, DEMs following universal co-registration methods outlined by Nuth and Kääb (2011). The method used a statistical approach that minimized vertical differences over stable (i.e. not prone to landslide/rockfall), vegetation-free, snow-free, and low-sloping ($< 30^0$) bedrock (Fig. S1, Supplement). After co-registration, the root mean squared error of elevation differences over stable bedrock improved from 8.43 m to 6.91 m for the 1960 and 2005 DEMs, and from 2.48 m to 2.01 m for the 2005 and 2014 DEMs. The mean of bedrock elevation differences after co-registration was effectively zero, i.e. $< 10^{-15}$ m, but differences over individual pixels still ranged from -42 m to +83 m for the 1960 and 2005 DEMs and -15 to +14 m for the 2005 and 2014 DEMs (Fig. S2, Supplement). These large differences tended to occur over steep terrain, and are included in our elevation error estimate.

Glacier margin data for 2005 and 2014, used to clip DEMs to glacier extent, were derived from aerial and satellite imagery (i.e. Fig. 1b) and ground-based GPS surveys of the glacier terminus. We defined 1950 and 1960 glacier margin data by digitally tracing the glacier from the same historic topographic maps by Johnson (1980).

We generated a record of geodetic mass balance for Sperry Glacier, given by:

$$B_a = \frac{\Delta V}{A}\left(\frac{\rho_i}{\rho_w}\right), \quad (1)$$

where B_a is the specific surface mass balance expressed in meters of water equivalent, ΔV is the change in glacier volume (determined from DEM data described in Sect. 3.1), ρ_i is the density of ice, ρ_w is the density of water (1000 kg m^{-3}), and A is the average of initial and final glacier area. To convert volume to mass, we adopted the approximation outlined by Huss (2013), and assigned ice density as $\rho_i = 850 \pm 60$ kg m^{-3}.

3.3 Geodetic mass balance assessment

There are three main sources of uncertainty in our geodetic mass balance calculation: elevation errors that affect the volume calculation, density errors which affect the volume to density conversion, and map coverage errors that affect the historic geodetic mass balance.

3.3.1 Elevation change uncertainty

After co-registering DEMs, elevation error on the geodetic mass balance was estimated by analyzing elevation differences over stable bedrock terrain. Because error tends to be greater over steep terrain at high elevations, we analyzed error by 50-m elevation band, rather than in bulk across the entire DEM. The quantity of stable bedrock points varied from 14,472 in the lowest elevation band to 1,825 points in the highest elevation band. We used standard error propagation, as applied in previous geodetic mass balance studies (Ruiz et al., 2017; Thomson et al., 2017), given by:

$$E\Delta h_i = \frac{\sigma_{dh}}{\sqrt{N_{eff}}}, \quad (2)$$

where $E\Delta h_i$ is the mean elevation error for a 50-m elevation band (i) that spans the glacier, σ_{dh} is the standard deviation of elevation differences over stable bedrock for the

elevation band, and N_{eff} is the number of independent values within the elevation band. This in turn is given by:

$$N_{eff} = \frac{N_{tot} \cdot P}{2 \cdot d} \quad (3)$$

where N_{tot} is the total number of pixels (grid cells), P is pixel size, and d is the distance of spatial autocorrelation (100 m), estimated from variogram analysis (Smith et al., 2018). We then summed elevation error across the glacier surface, weighting the error by the ratio of the glacier surface covering that elevation band.

3.3.2 Density uncertainty

We followed the convention outlined by Huss (2013) and used a constant density of ρ_i= 850±60 kg m^{-3} to convert glacier volume change to mass, which was derived from a suite of empirical firn densification experiments, and is appropriate for geodetic mass balance calculations where the time intervals considered are longer than 5 years, the volume change is nonzero, and the mass balance gradient is stable. These conditions are satisfied for Sperry Glacier because (a) geodetic mass balance periods are 10 years (1950-1960), 45 years (1960-2005), and 9 years (2005-2014) long, (b) glacier volume changes were nonzero, and (c) glaciological measurements show that mass balance gradients were relatively constant during 2005-2014, i.e. 0.004-0.019 m w.e. m^{-1} for winter and 0.003-0.011 m w.e. m^{-1} for summer (Clark et al., 2017). The ±60 kg m^{-3} density error amounted to < 8% error on geodetic mass balances.

We assumed that elevation and density errors were independent, and therefore summed them quadratically to solve for the total error on the geodetic mass balance, given by:

$$E_t = \sqrt{E\Delta h^2 + E\rho^2} \quad (4)$$

where $\boldsymbol{E\Delta h}$ is elevation error, $\boldsymbol{E\rho}$ is density error, and $\boldsymbol{E_t}$ is the total error in m w.e. on the geodetic mass balance.

3.3.3 Map coverage errors

The historic maps used to derive 1950 and 1960 DEMs are missing the upper section of the glacier. Historic photos verify that in the mid-20th century Sperry Glacier extended to the top of Gunsight Peak, as it does today. To enable consistent geodetic mass balance calculation for the entirety of Sperry Glacier, we filled in elevation change over this missing section (Fig. 3) using modern 2005-2014 results. We opted for this remedy, rather than the alternative of truncating 2005-2014 data, in order to be consistent with glaciological data, which were generated for the entire glacier surface including the upper section. By using modern elevation change rate results to infill missing historic data, we assumed that the rate of mass change in that area near the cirque headwall was the same through the study interval (1950-2014). Given that we had no way to test the validity of this assumption, and to ensure it did not fundamentally alter geodetic mass balance results, we also computed results for the truncated glacier (Table S1, Table S2, Supplement). The difference between the truncated and infilled geodetic mass balance was $\leq$0.04 m w.e. yr^{-1} for both 1950-1960 and 1960-2005 (Table S2, Supplement), which is less than the accounted geodetic mass balance error (0.05 m w.e. yr^{-1} for 1950-1960, 0.12 m w.e. yr^{-1} for 1960-2005) (see section 4.1). Infilling data for the missing upper section therefore does not alter geodetic mass balance results beyond the reported uncertainty bounds.

3.4 Glaciological mass balance

Sperry Glacier has been the focus of a USGS intensive glacier mass balance monitoring program since 2005. Therefore, glaciological mass balance measurements of seasonal mass gains and losses at Sperry Glacier are available from the year 2005 onward (Clark et al., 2017). We used these data, measured in the field according to standard mass balance protocols (Kaser et al., 2003; Ostrem and Brugman, 1999) to define specific, conventional (Cogley et al., 2011) winter and summer glacier mass balance from 2005-2014. We also analyzed point balance data collected along a longitudinal transect (stakes in Figure 1; data from Clark et al. 2017) to inspect mass balance gradients at Sperry Glacier. To correct for bias in the raw, specific glaciological balances reported by Clark et al. (2017), we performed calibration as outlined by Zemp et al. (2013). The results of this calibration, which utilized the 2005-2014 geodetic mass balance calculated in this study to correct the absolute magnitude of annual and summer glaciological balances without losing seasonal/annual variability (Zemp et al., 2013), are reported in Table 1. Such calibration ensures that systematic errors in the glaciological method are rectified and englacial and subglacial mass changes not measured at surface stakes are accounted. Details on this calibration are provided in the Supplement.

3.5 Mass balance and climate regressions

Employing annual glaciological measurements (Clark et al., 2017), we defined a functional relationship (i.e. linear regression) between 2005-2014 specific surface mass balance and regional climate. Regional climate was defined by data on winter peak snow water equivalent (SWE) and summer positive degree days (PDD). Climate data from

2005-2014 were used to define the regressions, and climate data from 1950-2005 were used to apply the regressions back in time.

3.5.1 Meteorological and snow data

The Global Historical Climatology Network provides historic temperature data for Kalispell, Montana located approximately 50 km southwest of Sperry Glacier (Figure 1). There are closer meteorological stations, but these had short and incomplete records. For example, average daily temperatures were recorded at Sperry Glacier for most (83%) summer days from 2005-2013 (Baker et al., 2018). To assess the representativeness of Kalispell temperature data relative to the glacier site, we compared this shorter, discontinuous record with the longer, continuous Kalispell record. Temperatures measured at Kalispell are highly representative of regional climate as reflected by gridded values from North American Regional Reanalysis output (Supplement, Fig. S3a). Kalispell is located at an elevation of 901 m, which is 1554 m lower than the average elevation across Sperry Glacier in 2005-2014. We therefore applied a lapse rate correction of -5.57 °C km^{-1}, calculated using 7 years of temperature measurements from a meteorological station at Sperry Glacier (Figure 1b), to correct for the elevation difference. Comparison of lapse-rate-corrected temperatures derived from the Kalispell meteorological station with the 7-year record of in situ July, August, September temperatures measured at the Sperry Glacier meteorological station (Fig. 1b) yielded no statistically significant difference at the 99% confidence interval ($p<0.01$), and the distribution of residuals was normal.

The Kalispell record reports continuous daily average air temperatures back to 1950 for the melt season summer months. We follow the convention defined by previous GNP melt modelling (Clark et al., 2017) and confine the Sperry Glacier melt season to July, August, and September. Glaciological observations suggest that although May and June can be warm enough to generate melt at Sperry Glacier, the deep snowpack is not necessarily warmed with pore space filled to saturation, and therefore melt does not necessarily run off the glacier.

Because the glacier terminus increased in elevation from 1950-2014, the surface of Sperry Glacier was on average 35 m lower in elevation during 1950-1960, and 21 m lower in elevation during 1960-2005. We accounted for these changes in elevation by adjusting the lapse rate correction accordingly for each time period. The effect of this accounting was small, resulting in -0.16°C and -0.12°C changes to average summer temperature, and cumulatively -24 °C day and -14 °C day changes to PDD. Ultimately, correcting for elevation changes at Sperry Glacier corresponded to cm-scale changes to the mass balance regression.

Data from the Natural Resources Conservation Service at five nearby snow course sites (Desert Mountain, 1707 m; Piegan Pass, 1676 m; Marias Pass, 1600 m; Mount Allen, 1737 m; and Mineral Creek, 1219 m) and one adjacent Snow Telemetry (SNOTEL) site (Flattop Mountain, 1921 m) provide SWE data for locations within a 50-km radius of Sperry Glacier (Fig.1a). Temperature data are also recorded at the Flattop Mountain site. SWE is recorded monthly at snow course sites, via manual measurement, whereas SWE is recorded daily at SNOTEL sites via transducer measurements from a snow pillow. The 1950-2014 period is long enough to encompass meso-scale changes in

atmospheric flow patterns, which elsewhere have been shown to have an important impact on winter accumulation and glacier mass balance (e.g. Huss et al., 2010). The peak SWE data we analyzed have been shown to reflect such meso-scale, decadal shifts in snow (McCabe and Dettinger, 2002; Pederson et al., 2011; Selkowitz et al., 2002). Based on an analysis of the historical snow data from the region against observations from Sperry Glacier, we chose to use Mount Allen snow data for our mass balance regression. We found high correlation coefficients ($r^2 \geq 0.939$) for each of the seven datasets analyzed (Table S3, Supplement). The highest correlation was with Flattop Mountain SNOTEL ($r^2 = 0.990$), but at this station consistent snow data only go back to 1970. The second highest correlation ($r^2 = 0.973$), for a snow record that started prior to 1950 and so encompassed the geodetic record, was Mount Allen.

3.5.2 Regression analysis

To quantify the glacier-climate relationship for 2005-2014, we fit a linear regression between 2005-2014 climate data (x: PDD, SWE) and glaciological mass balance (y: b_s, b_w) data. We forced the best-fit line through the origin so that zero PDD and zero SWE equated to zero melt and zero accumulation, respectively. The linear combination of the two seasonal linear equations was thus:

$$B_a = m_s\,(PDD) + m_w(SWE) \quad (5)$$

where B_a is the specific annual balance, m_s is the summer proportionality factor, m_w is the winter proportionality factor, PDD is summer positive degree days, i.e. the sum of the average temperatures of days above 0 °C during the melt season, and SWE is peak winter snow water equivalent. We solved for the proportionality factors using an ordinary least squares, one parameter linear regression.

The linear regression only provides a best estimate of the mass balance of Sperry Glacier. To discern how dependable this estimate was, we considered the 95% confidence interval on each seasonal linear regression. Knowing that the true proportionality factor (i.e. slope of the best fit line) fell somewhere within the upper and lower bounds, we used the upper and lower confidence intervals to compute maximum and minimum possible mass balances. This accounting accommodated uncertainty due to (a) the discrepancy between snow and meteorological station locations and Sperry Glacier, (b) assuming that seasonal melt is largely driven by net available shortwave radiation and that PDD is a reasonable proxy for this, and (c) assuming that the summer melt season is limited to July, August, and September (JAS). To test the sensitivity of our results to this last assumption, we computed a summer linear regression using May, June, July, August, and September (MJJAS) PDD. Ultimately, the median difference between mass balance values produced by the MJJAS versus JAS regressions was just 0.04 m w.e. yr^{-1}.

The linear regression quantifies the 2005-2014 relationship between Sperry Glacier and regional climate, and is fixed with respect to this time. Yet we have hypothesized that this relationship changed as the glacier retreated. By fixing the proportionality factors m_s and m_w to the modern glacier-climate relationship, and then forcing this modern regression with historic climate data, we test our hypothesis that the glacier-climate relationship changed as the glacier retreated.

3.6 Shading, avalanching, and wind-drifting

Attributing the hypothesized change in the glacier-climate relationship to the increasing influence of local topographic effects requires inspection of topographically

influenced processes at Sperry Glacier. To assess topographic shading, we used the Solar Area Radiation tool (ESRI, 2014) to calculate cumulative insolation received across Sperry Glacier during the melt season months of July, August, and September in 2014, when the glacier was smaller, steeper, and more shaded, versus 1950, when the glacier was larger, flatter, and less shaded. This hemispherical viewshed algorithm (Fu and Rich, 2002) calculated radiation based on an upward-looking sky map for every grid cell within our 2014 DEM, the seasonal progression of the position of the sun relative to Earth, a fixed atmospheric transmissivity, topographic shading, latitude, elevation, slope, and aspect. To qualitatively assess avalanching and wind-drifting snow processes, we examined field observations, historic photographs, and field-measured mass balance data collected by Clark et al. (2017).

4 Results

4.1 Retreat, thinning, and negative mass balance

Sperry Glacier has decreased from 1.30 km^2 in 1950, to 1.23 km^2 in 1960, to 0.86 km^2 in 2005, to 0.80 km^2 in 2014 (Table 2). During the mid-20^{th} century the glacier extended onto relatively flat (<15° slope) bedrock terrain, therefore the lower portion of the glacier was relatively low angle. As a result, between 1950 and 2014, despite nearly 0.5 km of retreat, the glacier terminus only receded upward by 56 m in elevation. The loss of this northwest-oriented, low-sloping terminus resulted in a steepening of the glacier's median slope by 9^0, and a rotation of the glacier's median aspect toward the north by 11^0**.** Elevation change across the glacier surface is generally similar in its spatial pattern, but not magnitude, during 1950-1960, 1960-2005, and 2005-2014 (Fig. 3a, c, e). Thinning

occurred across the lower portion, but is most pronounced at the terminus. The upper elevations of the glacier thickened from 1960-2005 and 2005-2014, but at rates less than +1 m yr^{-1} (Fig. 3). The magnitude of thinning near the terminus is distinct for each period. Terminus thinning rates from 1950-1960 were up to -2.5 m yr^{-1} (Fig. 3b), whereas terminus thinning rates from 1960-2005 (Fig. 3d) and 2005-2014 (Fig. 3f) were smaller than -1.5 m yr^{-1}. No development of debris cover at the glacier terminus that might explain this decreased thinning rate is evident. The magnitude of thickening was likewise distinct between periods, with 1950-1960 showing a bulge near the glacier's middle (approximately 2500 m), growing at nearly +1 m yr^{-1} (Fig. 3b).

Despite differences in the magnitude of elevation change, the hypsometry of the glacier remained similar in 1950, 1960, 2005, and 2014. Sperry Glacier lost 50 m of ice at the glacier terminus during the 1960-2005 interval which agrees with the average amount of thinning (52.4 m) reported for glaciers in the Canadian Rockies for the same period (Clarke et al., 2017). Commensurate with its area loss and thinning, the glacier also lost volume. Geodetic mass balance results show Sperry Glacier shrank by -3.33×10^6 m^3 from 1950-1960, -11.3×10^6 m^3 from 1960-2005, and -0.90×10^6 m^3 from 2005-2014 (Table 3). It lost -2.83×10^9 kg of mass from 1950-1960, -9.68×10^9 kg from 1960-2005, and -0.76×10^9 kg from 2005-2014 (Table 1). The rate of mass change at Sperry Glacier was -0.22 ± 0.12 m w.e. yr^{-1} from 1950-1960, -0.18 ± 0.05 m w.e. yr^{-1} from 1960-2005, and -0.10 ± 0.03 m w.e. yr^{-1} from 2005-2014 (Table 3). The glacier is near balance, but slightly losing mass.

4.2 Glacier-climate relationship

Linear regressions show strong ($r^2 > 0.97$), statistically significant ($p < 0.03$) correlation between climate and glaciological data (Fig. 4). The model therefore effectively defines a functional relationship between glacier mass balance and regional climate for 2005-2014. The regressions correlate warmer summers to more negative summer mass balance ($r^2 = 0.978$), and snowier winters to more positive winter mass balance ($r^2 = 0.973$). From the regression results, the proportionality factor for winter (m_w), which scales snow course data on peak SWE to winter glaciological measurements, is 2.99. The proportionality factor for summer (m_s), which scales meteorological data on PDD to summer glaciological measurements, is -0.004 m w.e. $°C^{-1} \cdot day^{-1}$.

We used climate data to apply the linear regression back in time to 1950 (Figure 5). Average PDD during 1950-1960 was 709 ± 53 °C ·day, which was virtually the same as average PDD during 1960-2005 (717 ± 86 °C · day). Summer PDD then showed a 41 °C · day increase to an average of 758 ± 75 °C · day during 2005-2014, although this increase was well within interannual variability. Snow data show that on average, SWE decreased from 1.31 ± 0.26 m w.e. in 1950-1960, to 1.08 ± 0.32 m w.e. in 1960-2005, to 0.95 ± 0.25 m w.e. in 2005-2014, although these step decreases are likewise within the range of interannual variability. The step change in peak SWE during the mid-1970s is consistent with other regional SWE records (Fig. S3b, Supplement), and has been interpreted as a result of a modal change in the Pacific decadal oscillation, a pattern of ocean climate variability which is closely tied to peak SWE in this region (McCabe and Dettinger, 2002; Pederson et al., 2011; Selkowitz et al., 2002). Generally, PDD and SWE in 1950-1960 compared to 2005-2014 seem to differ. To quantitatively assess the difference, we

performed simple t-tests. T-test results showed that the lower (higher) average SWE (PDD) during 2005-2014 differed statistically from 1950-1960 SWE (PDD) at $p < 0.01$, $\alpha = 0.99$ ($p < 0.15$, $\alpha = 0.85$). This evidence supports the notion that 2005-2014 had relatively dry winters and warm summers compared to 1950-1960.

Nevertheless, geodetic results show that average mass change rates at Sperry Glacier for 2005-2014 (-0.10 $\pm$ 0.03 m w.e. yr^{-1}) and 1950-1960 (-0.22 $\pm$ 0.12 m w.e. yr^{-1}) were comparable, i.e. within error bounds. This differs drastically from mass balance results derived from the regression, which include many years of net mass gain during the mid-20th century (Fig. 5). Sufficient individual years are positive during the mid-20th century to yield positive averages from 1950-1960 and 1960-2005, at +0.98 ± 0.83 m w.e. yr^{-1} and +0.34 ± 0.75 m w.e. yr^{-1} respectively. However, confidence intervals from the linear regression model suggest the possibility of a negative average during 1960-2005. Conversely, error on the 1950-1960 mass balance include only positive averages, i.e. glacier thickening and mass gain. The 1950-1960 mass gain predicted by the regression (+0.98 ± 0.83 m w.e. yr^{-1}) is distinctly at odds with the 1950-1960 geodetic mass balance of -0.22 ± 0.12 m w.e. yr^{-1}.

4.3 Local controls on surface mass balance

The amount of potential clear sky radiation available for specific summer melt at Sperry Glacier decreased by 118,605 kJ m^{-2} (approximately 15 W m^{-2}) from 1950-2014, likely due to steepening of the glacier surface, and a greater proportion of the glacier becoming shaded. Given the heat of fusion for ice (334 kJ m^{-2}), this energy deficit translates to 0.36 m w.e. less potential melt for the summer melt season averaged over the

entire glacier, driven only by changes in the relative influence of local effects (i.e. shading, steepening), independent of climate. Field observations show that the rock headwall extending above Sperry Glacier (Fig. 2) contributes high frequency, low volume, loose avalanches (Fig. 6b), and that the cornice above the bergschrund often breaks in the spring, subsequently triggering localized slab avalanches that extend 500 m down from the crest of the ridge to an elevation of 2460 m. (Fig. 6c). Historic aerial photographs show that a prominent ridge of wind-drifted snow consistently develops at lower elevations in the basin (Fig. 6a). Field-measured mass balance data showing highly variable snow accumulation provide evidence of wind effects. Accumulation ranges from 0.00 m w.e. in wind scoured areas, where seasonal snowpack had been stripped down to bare ice, up to more than 5 m w.e. in wind loaded areas (Clark et al., 2017).

Field-measured point data (n=551), taken along stakes from the terminus toward the headwall of the glacier (Clark et al., 2017), show the impact of these local effects (shading, avalanching, wind drifting) on the mass balance elevation gradient (Fig. 7c). Toward the glacier terminus, at elevations lower than 2475 m, the mass balance gradient of winter accumulation is 10×10^{-4} m w.e. $(m)^{-1}$. Toward the glacier head, at elevations above 2475 m, the mass balance gradient of winter accumulation is an order of magnitude higher at 150×10^{-4} m w.e. $(m)^{-1}$. The elevation gradients shown by summer ablation measurements show a similar inflection (Fig. 7c). At elevations higher than 2475 m, where the glacier is steeper and more shaded, the melt gradient rate increases eightfold from 6.6×10^{-4} m w.e. $(m)^{-1}$ to 53×10^{-4} m w.e. $(m)^{-1}$.

5 Discussion

Our results reveal that the drivers of mass balance at Sperry Glacier evolved as the glacier retreated. Specifically, the strong correlation between modern-era field and climate data poorly predicts the 1950-1960 geodetically derived mass balance (Fig. 5c) and documents a change in the relationship between regional climate and rates of ice mass loss.

It seems that Sperry Glacier became less reflective of the regional climate as it retreated. Geodetic results compared to regional climate data show that Sperry Glacier lost less area-averaged mass from 2005-2014 (-0.10 ± 0.03 m w.e. yr^{-1}) than from 1950-1960 (-0.22 ± 0.12 m w.e. yr^{-1}) despite the 2005-2014 period being characterized by warmer summers and lower precipitation winters. Glacier elevation changes reflect both surface mass balance and ice flow processes (Cuffey and Paterson, 2010). However, if we were to attribute geodetic results solely to surface mass balance, then our results (Fig. 3) suggest that the equilibrium line altitude remained relatively constant from 1950-2014 despite climate warming. Thus as Sperry Glacier retreated, its accumulation area ratio (Cogley et al., 2011) increased. With an increased fraction of the glacier remaining snow-covered throughout the melt season, the average glacier albedo increases (Naegeli and Huss, 2017). Such time changes in glacier albedo must have affected the summer proportionality factor, i.e. the amount of area averaged melt relative to regional summer temperature, which in part explains the discrepancy between the linear regression and the 1950-1960 mass balance (Fig.5c).

We had hypothesized that the discrepancy between the regression and the historic mass balance would be attributable to avalanching, wind drifting, and shading becoming

relatively more influential as the glacier retreated. Glaciological measurements provide direct evidence of these effects, as the mass balance gradient at Sperry Glacier has two distinct components reflecting regional and local drivers (Fig. 7c). For example, the winter mass balance gradient at elevations below 2475 m, 10×10^{-4} m w.e. $(m)^{-1}$, falls within the range of regional SWE lapse rates, $6.2\text{-}10.4 \times 10^{-4}$ m w.e. $(m)^{-1}$, reported in a study of snow accumulation in northwest Montana (Gillan et al., 2010). The stark increase (to 150×10^{-4} m w.e. $(m)^{-1}$) in winter mass balance gradient at higher elevations is consistent with enhanced snow accumulation reported for so-called "drift" glaciers located below the regional equilibrium line altitude in Colorado, where winter accumulation from local effects was four to eight times regional snow accumulation (Outcalt and MacPhail, 1965). Field-measured summer data at high elevations are sparse, but these summer point balances also show a sudden steepening of the summer mass balance gradient above 2475 m (Fig. 7c), likely because these high reaches of the glacier are shaded by the headwall.

Our linear regression results fall short of elucidating what drove the change in the relationship between climate variables and Sperry Glacier. Therefore, we used glaciological measurements in one final, complementary analysis to assess the impact of the time-changing glacier hypsometry and the local and regional mass balance gradients on the glacier's total mass balance. We applied field-measured mass balance gradients to the hypsometry of Sperry Glacier in 2014 and 1950 (Fig. 7a,b black bars), first using only the regional gradient (Fig. 7c dotted lines) and then using the regional plus local gradients (Fig. 7c solid lines). This demonstrates that without local effects, given the 1950 glacier hypsometry, specific surface mass balance would be -1.04 m w.e. Similarly, without local

effects, given the 2014 glacier hypsometry, specific surface mass balance would be -0.96 m w.e. Thus, in theory, the hypothetical mass balance response of the 1950 and 2014 glaciers would be roughly similar when forced only by regionally determined gradients. However, when the local mass balance gradients are applied, the balance for 1950 increased by 37% to -0.66 m w.e., and for 2014 by 57% to -0.41 m w.e. These results demonstrate that local mass balance processes have apparently played a strong role at Sperry Glacier since 1950, and that role strengthened as the glacier retreated.

The impact of topographic effects is not evenly partitioned between seasonal components. The differences between the solid and dotted lines in Figure 7b and Figure 7d illustrate local effects: suppression of summer melt (light red area), surplus in winter accumulation (light blue area), and net mass balance enhancement (light gray area). We find that winter local effects (i.e. the surplus in winter accumulation due to avalanching and wind loading) account for 79% of the discrepancy between the mass balance defined by regional mass balance gradients alone versus that defined by both regional and local gradients. Summer local effects (i.e. the mediation in summer melt due to shading) accounted for 21% of the discrepancy. This analysis supports the interpretation that the altered mass balance response we have documented, wherein the glacier had a less negative balance in 2005-2014 despite less favorable regional climate conditions, is driven by the increasing influence of local effects rather than just the changing glacier hypsometry. Here we have examined the time evolution of local effects in bulk. To quantitatively partition the mass impact of discrete processes, future work could assess the evolution in geographic parameters for wind (e.g. Winstral et al., 2002) and avalanche (e.g. Carturan et al., 2013) effects.

Sperry Glacier's increasing sensitivity to local mass balance drivers is consistent with studies of 20th century glacier change elsewhere in the Rocky Mountains (DeBeer and Sharp, 2009), and is commensurate with modeled projections of future changes to cirque glaciers in the Swiss Alps. For example, although 25% of 1133 individual very small (<0.5 km^2) glaciers are projected to disappear as soon as the next 25 years, 67 glaciers (6%) are projected to maintain more than half of their area through at least 2050 (Huss and Fischer, 2016). The persistence of these select glaciers, which are located at lower elevation than the regional equilibrium line altitude, signals the sometimes strong influence of local mass balance drivers. Despite local effects allowing some glaciers to persist for a few more decades, categorical evidence of world-wide glacier retreat in response to 20th century warming (Roe et al., 2016) suggests that local mass balance drivers do not interrupt the synchronicity of glacier response to climate change on global, century-long scales. Indeed, very small (<0.2 km^2) glaciers in Colorado showed a strong annual mass balance response to 20th century summer temperatures despite being heavily influenced by winter topographic effects (Hoffman et al., 2007). Thus, the evolving relationship between climate and mass balance demonstrated by Sperry Glacier reveals the complexity in interpreting glacier changes in Glacier National Park and at small cirque glaciers elsewhere on Earth, but does not preclude the reality of a climate that is trending toward conditions that mandate glacier disappearance.

6 Conclusion

Analysis of a 64-year record of glacier mass change against meteorological and snow data demonstrates that the relationship between regional climate variables and Sperry

Glacier is evolving through time. By assessing geodetic mass measurements, regional climate data, and field measured mass balance, we deduced that this shift was caused by local drivers related to topography becoming increasingly influential as the cirque glacier retreated. Our results therefore emphasize the importance of accounting for spatially complex, local topographic processes in projections of 21st century mountain glacier change. These effects can exert substantial and time-changing control on the mass balance of retreating cirque glaciers, are likely highly variable from glacier to glacier, and must therefore be carefully considered and treated in interpretations and projections of cirque glacier change.

7 Acknowledgements

Co-authors on this paper are Joel Harper, Dan Fagre, Johnnie Moore, and Erich Peitzsch. This work was funded by the Climate and Land Use Change mission area of the U.S. Geological Survey. CF received funding from the Jerry O'Neal National Park Service Student Fellowship.

8 References

Alden, C.: Glaciers of Glacier National Park, U.S. Dep. Inter., 48(Washington, D.C.), 1914.

Baker, E. H., O'Neel, S., Fagre, D. B., Whorton, E. N., Sass, L. C., McNeil, C. J., Peitzsch, E. H., Clark, A. M., Florentine, C. E. and McGrath, D.: USGS Benchmark Glacier Mass Balance and Project Data: 1966-2016: U.S. Geological Survey data release, 2018.

Carrara, P. E.: Late Quaternary Glacial and Vegetative History of the Glacier National Park Region, Montana, U.S. Geological Survey Bulletin 1902, U.S. Department of the Interior, Washington D.C., 1989.

Carturan, L., Baldassi, G. A., Bondesan, A., Calligaro, S., Carton, A., Cazorzi, F., Dalla Fontana, G., Francese, R., Guarnieri, A., Milan, N., Moro, D. and Tarolli, P.: Current Behaviour and Dynamics of the Lowermost Italian Glacier (Montasio Occidentale, Julian Alps), Geogr. Ann. Ser. A Phys. Geogr., 95(1), 79–96, doi:10.1111/geoa.12002, 2013.

Carturan, L., Cazorzi, F., De Blasi, F. and Dalla Fontana, G.: Air temperature variability over three glaciers in the Ortles-Cevedale (Italian Alps): Effects of glacier fragmentation, comparison of calculation methods, and impacts on mass balance modeling, Cryosphere, 9(3), 1129–1146, doi:10.5194/tc-9-1129-2015, 2015.

Clark, A. M., Fagre, D. B., Peitzsch, E. H., Reardon, B. A. and Harper, J. T.: Glaciological measurements and mass balances from Sperry Glacier, Montana, USA, years 2005-2015, Earth Syst. Sci. Data, 9(1), 47–61, doi:10.5194/essd-9-47-2017, 2017.

Cogley, J. G., Hock, R., Rassmussen, L. A., Arendt, A. A., Bauder, A., Braithwaite, R. J., Jansson, P., Kaser, G., Moller, M., Nicholson, L. and Zemp, M.: Glossary of mass balance and related terms, IHP-VII Technical Documents in Hydrology No. 86, IACS Contribution No. 2, UNESCO-IHP, Paris., 2011.

Cuffey, K. M. and Patterson, W. S. B.: The Physics of Glaciers, 4th ed., Elsevier, Oxford., 2010.

DeBeer, C. M. and Sharp, M. J.: Recent changes in glacier area and volume within the southern Canadian Cordillera, Ann. Glaciol., 46, 215–221, doi:10.3189/172756407782871710, 2007.

DeBeer, C. M. and Sharp, M. J.: Topographic influences on recent changes of very small glaciers in the monashee mountains, British Columbia, Canada, J. Glaciol., 55(192), 691–700, doi:10.3189/002214309789470851, 2009.

Dyurgerov, M. B. and Meier, M. F.: Twentieth century climate change: Evidence from small glaciers, PNAS, 97(4), 1406–1411, 2000.

ESRI: ArcGIS Desktop: Release 10.3.1, 2014.

Fagre, D. B., McKeon, L. A., Dick, L. A. and Fountain, A. G.: Glacier margin time series (1966, 1998, 2005, 2015) of the named glaciers of Glacier National Park, MT, USA, U.S. Geol. Surv. data release, 2017.

Fu, P. and Rich, P. M.: A geometric solar radiation model with applications in agriculture and forestry, Comput. Electron. Agric., 37(1–3), 25–35, doi:10.1016/S0168-1699(02)00115-1, 2002.

Gillan, B. J., Harper, J. T. and Moore, J. N.: Timing of present and future snowmelt from high elevations in northwest Montana, Water Resour. Res., 46(1), 1–13, doi:10.1029/2009WR007861, 2010.

Hannah, D. M., Gurnell, A. M. and McGregor, G. R.: Spatio-temporal variation in microclimate, the surface energy balance and ablation over a cirque glacier, Int. J. Climatol., 20(7), 733–758, doi:10.1002/1097-0088(20000615)20:7<733::AID-JOC490>3.0.CO;2-F, 2000.

Haugen, B. D., Scambos, T. A., Pfeffer, W. T. and Anderson, R. S.: Twentieth-century Changes in the Thickness and Extent of Arapaho Glacier, Front Range, Colorado, Arctic, Antarct. Alp. Res., 42(2), 198–209, doi:10.1657/1938-4246-42.2.198, 2010.

Hock, R.: Temperature index melt modelling in mountain areas, J. Hydrol., 282(1–4), 104–115, doi:10.1016/S0022-1694(03)00257-9, 2003.

Hoffman, M. J., Fountain, A. G. and Achuff, J. M.: 20th-century variations in area of cirque glaciers and glacierets, Rocky Mountain National Park, Rocky Mountains, Colorado, USA, Ann. Glaciol., 46, 349–354, doi:10.3189/172756407782871233, 2007.

Huss, M.: Density assumptions for converting geodetic glacier volume change to mass change, Cryosph., 7(1), 219–244, doi:10.5194/tcd-7-219-2013, 2013.

Huss, M. and Fischer, M.: Sensitivity of Very Small Glaciers in the Swiss Alps to Future Climate Change, Front. Earth Sci., 4(April), 1–17, doi:10.3389/feart.2016.00034, 2016.

Huss, M., Hock, R., Bauder, A. and Funk, M.: 100-year mass changes in the Swiss Alps linked to the Atlantic Multidecadal Oscillation, Geophys. Res. Lett., 37(10), 1–5, doi:10.1029/2010GL042616, 2010.

Johnson, A.: Grinnell and Sperry Glaciers, Glacier National Park, Montana: A record of vanishing ice, Geol. Surv. Open-File Rep., 1180, 1–29, 1980.

Kaser, G., Fountain, A., Jansson, P., Heucke, E. and Knaus, M.: A manual for monitoring the mass balance of mountain glaciers, UNESCO, 137, 2003.

Kuhn, M.: The mass balance of very small glaciers, Zeitschrift fur Gletscherkd. und Glazialgeol., 31, 171–179, 1995.

Laha, S., Kumari, R., Singh, S., Mishra, A., Sharma, T., Banerjee, A., Nainwal, H. C. and Shankar, R.: Evaluating the contribution of avalanching to the mass balance of Himalayan glaciers, , 1–17, doi:10.1017/aog.2017.27, 2017.

McCabe, G. J. and Dettinger, M. D.: Primary Modes and Predictability of Year-to-Year Snowpack Variations in the Western United States from Teleconnections with Pacific Ocean Climate, J. Hydrometeorol., 3(1), 13–25, doi:10.1175/1525-7541(2002)003<0013:PMAPOY>2.0.CO;2, 2002.

Naegeli, K. and Huss, M.: Sensitivity of mountain glacier mass balance to changes in bare-ice albedo, Ann. Glaciol., 58(75), 119–129, doi:10.1017/aog.2017.25, 2017.

Nuth, C. and Kääb, A.: Co-registration and bias corrections of satellite elevation data sets for quantifying glacier thickness change, Cryosphere, 5(1), 271–290, doi:10.5194/tc-5-271-2011, 2011.

Ostrem, G. and Brugman, M.: Glacier Mass Balance Measurements: A Manual for Field and Office Work, Minist. Supply Serv. - Environ. Canada Norweigian Water Energy Adm., 224, 1991.

Outcalt, S. J. and MacPhail, D. D.: A survey of Neoglaciation in the Front Range of Colorado, University of Colorado Press, Boulder, CO., 1965.
Pederson, G. T., Gray, S. T., Ault, T., Marsh, W., Fagre, D. B., Bunn, A. G., Woodhouse, C. A. and Graumlich, L. J.: Climatic controls on the snowmelt hydrology of the northern Rocky Mountains, J. Clim., 24(6), 1666–1687, doi:10.1175/2010JCLI3729.1, 2011.
Roe, G. H., Baker, M. B. and Herla, F.: Centennial glacier retreat as categorical evidence of regional climate change, Nat. Geosci., 1(December), doi:10.1038/ngeo2863, 2016.
Ruiz, L., Berthier, E., Viale, M., Pitte, P. and Masiokas, M. H.: Recent geodetic mass balance of Monte Tronador glaciers, northern Patagonian Andes, Cryosphere, 11(1), 619–634, doi:10.5194/tc-11-619-2017, 2017.
Selkowitz, D. J., Fagre, D. B. and Reardon, B. A.: Interannual variations in snowpack in the Crown of the Continent Ecosystem, Hydrol. Process., 16(18), 3651–3665, doi:10.1002/hyp.1234, 2002.
Sibson, R.: A Brief Description of Natural Neighbor Interpolation, in Interpolating Multivariate Data, pp. 21–36, John Wiley & Sons, New York., 1981.
Smith, M. J., Goodchild, M. F. and Longley, P. A.: Geospatial Analysis: A Comprehensive Guide to Principles Techniques and Software Tools, Sixth., 2018.
Thomson, L. I., Zemp, M., Copland, L., Cogley, J. G. and Ecclestone, M. A.: Comparison of geodetic and glaciological mass budgets for White Glacier, Axel Heiberg Island, Canada, J. Glaciol., 63(237), 55–66, doi:10.1017/jog.2016.112, 2017.
Winstral, A., Elder, K. and Davis, R. E.: Spatial Snow Modeling of Wind-Redistributed Snow Using Terrain-Based Parameters, J. Hydrometeorol., 3(5), 524–538, doi:10.1175/1525-7541(2002)003<0524:SSMOWR>2.0.CO;2, 2002.
Zemp, M., Thibert, E., Huss, M., Stumm, D., Rolstad Denby, C., Nuth, C., Nussbaumer, S. U., Moholdt, G., Mercer, A., Mayer, C., Joerg, P. C., Jansson, P., Hynek, B., Fischer, A., Escher-Vetter, H., Elvehøy, H. and Andreassen, L. M.: Reanalysing glacier mass balance measurement series, Cryosphere, 7(4), 1227–1245, doi:10.5194/tc-7-1227-2013, 2013.
Zhang, B.: Towards a higher level of automation in softcopy photogrammetry: NGATE and LiDAR processing in SOCET SET®, in GeoCue Corporation 2nd Annual Technical Exchange Conference, p. 32, Nashville, Tennessee., 2006.

Figures

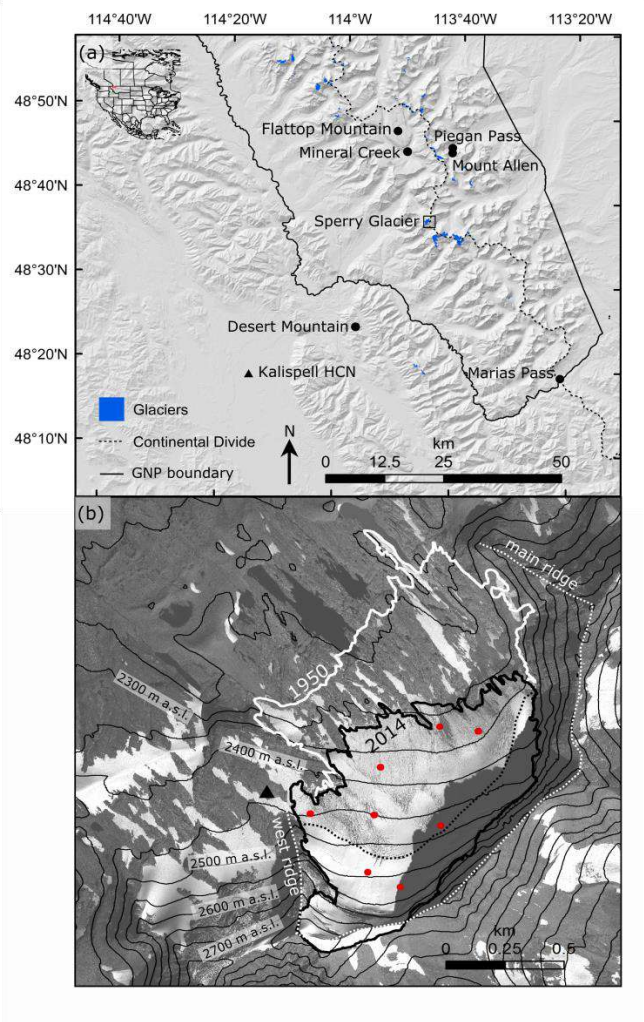

Figure 1. (a) Study area in the U.S. Northern Rocky Mountains, located just south of the USA-Canada border, as indicated by the red box on the inset map. The 39 named glaciers within and near Glacier National Park (GNP) are shown (blue). The continental divide (dashed black line), GNP boundaries (solid black line), the location of Sperry Glacier (small box), Kalispell Historical Climate Network (HCN) meteorological station (black triangle), and snow measurement sites (black circles), are also shown. (b) Worldview imagery from 07 September 2014 depicts Sperry Glacier with the 1950 (white line) and 2014 (black line) glacier margins shown. The approximate seasonal snow line (dotted black line) and the *main ridge that defines the crest of the cirque headwall above Sperry Glacier, as well as the west ridge which bounds Sperry Glacier (dotted white line), are also depicted. Elevation (m) above sea level (a.s.l.) is represented by thin black contour lines. Stakes where glaciological measurements were made are shown (red) as is the Sperry Glacier meteorological station (black triangle).*

Figure 2. Sperry Glacier on 01 September 2009. Arrow points to the north. Note low-sloping proglacial terrain. In 1950 and 1960, the glacier extended onto this relatively flat ground. Gunsight Peak is indicated by the black star. The west ridge, headwall, cornice, bergschrund, and moraines discussed in the text are labeled. Photograph credit: USGS Climate Change in Mountain Ecosystem photograph archives.

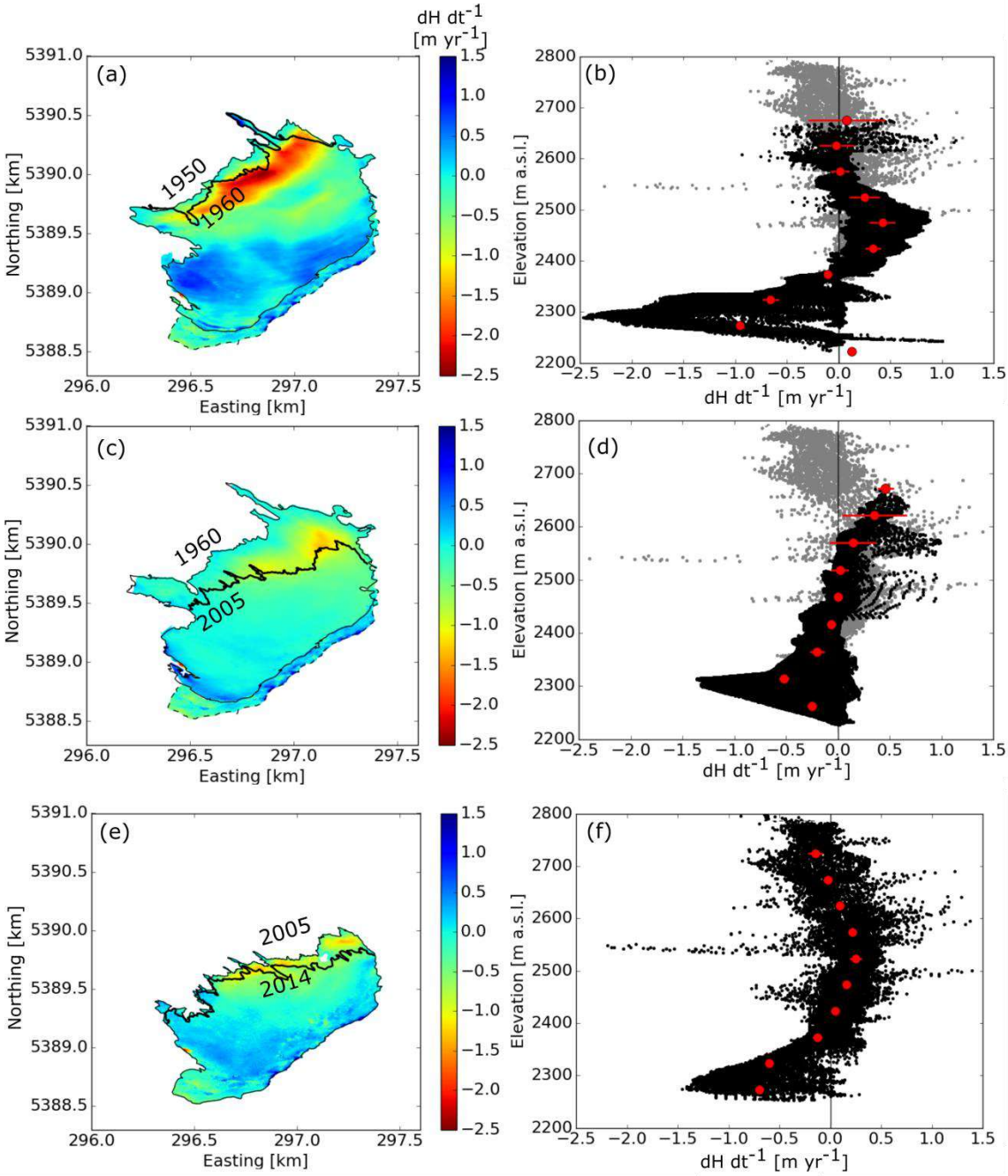

Figure 3. Elevation change over Sperry Glacier from (a,b) 1950-1960, (c,d) 1960-2005, and (e,f) 2005-2014. Left column shows elevation change across the glacier surface, and right column shows hypsometry of elevation change. Black dots on the hypsometry figures (b,d,f) indicate individual pixels, red dots indicate elevation band means, and horizontal red bars indicate elevation band mean errors. Error is mostly smaller than, and therefore obscured by, the red dot. The missing upper section is delineated by the dotted line in (a) and (c). Data from 2005-2014 were used to fill in this missing section. These 2005-2014 infill data are indicated by the gray dots in (b) and (d).

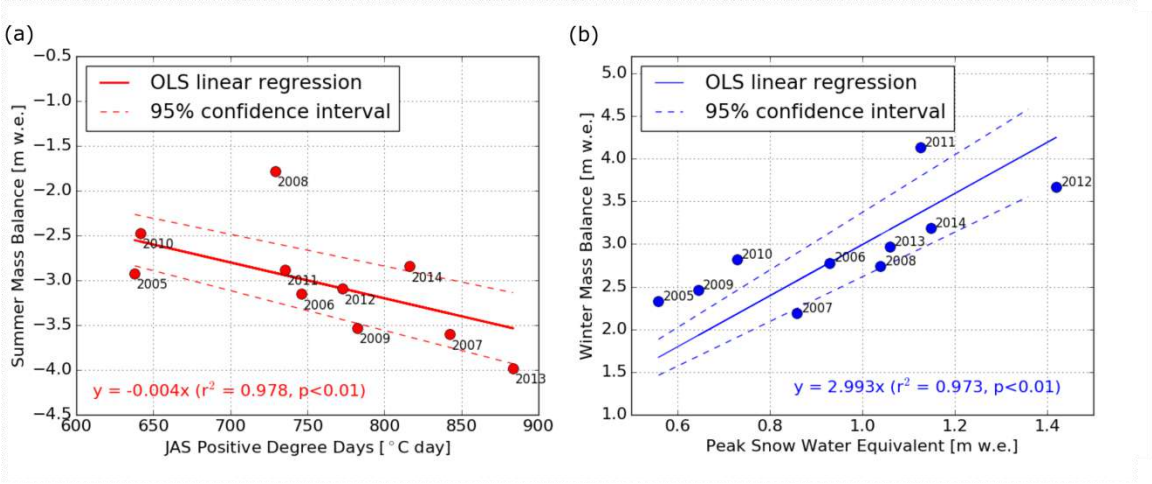

Figure 4. Ordinary least squares (OLS) linear regressions between climate data and glaciological mass balance for 2005-2014. (a) Summer, i.e. July, August, September (JAS), positive degree days versus summer mass balance. The linear regression is shown in red text and is plotted (solid red line). The 95% confidence interval on the regression is also shown (dotted red lines). (b) Peak snow water equivalent (SWE) versus winter mass balance. SWE data are from the Mount Allen snow course. The linear regression is shown in blue text and is plotted (sold blue line). The 95% confidence interval on the regression is also shown (dotted blue lines).

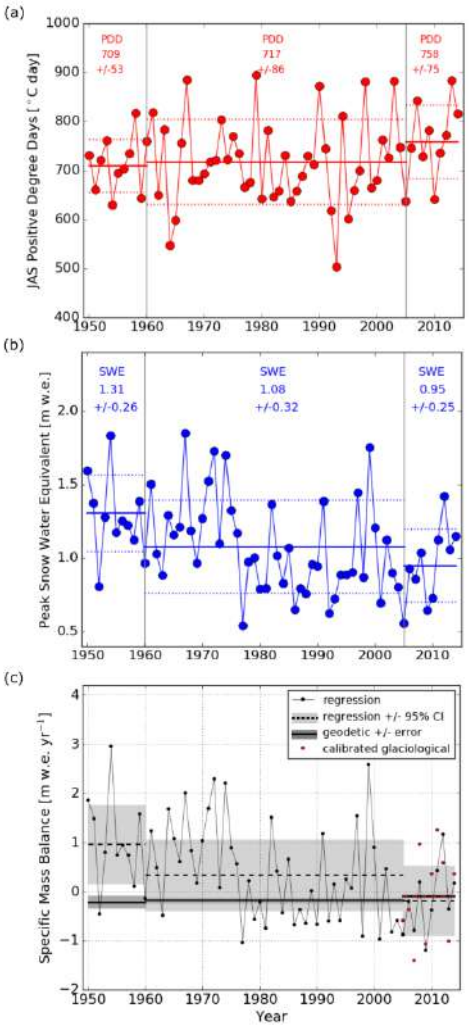

Figure 5. Annual climate data for 1950-2014 and comparison of regression and geodetic mass balance results. (a) Positive degree days (PDD) calculated from the Kalispell Historical Climate Network summer, i.e. July, August, September (JAS), temperature data, adjusted for elevation by the standard lapse rate. (b) Peak snow water equivalent (SWE), calculated from Mount Allen snow course data. Mean (solid line) and one standard deviation (dashed line) of PDD and SWE for each geodetic mass balance interval (1950-1960, 1960-2005, 2005-2014) are plotted and reported in text with standard deviation. (c) Regression results for annual mass balance (black dots, thin black line) are shown, as are regression results for the average mass balance from 1950-1960, 1960-2005, 2005-2014 black dotted lines). Calibrated, annual glaciological balances are shown (red dots), as is the average of this glaciological balance from 2005-2014 (red dotted line). Errors, set by confidence intervals on the linear regression, are also shown (light gray boxes). Geodetic mass balances for 1950-1960, 1960-2005, and 2005-2014 are plotted (horizontal black lines) with errors (dark gray boxes).

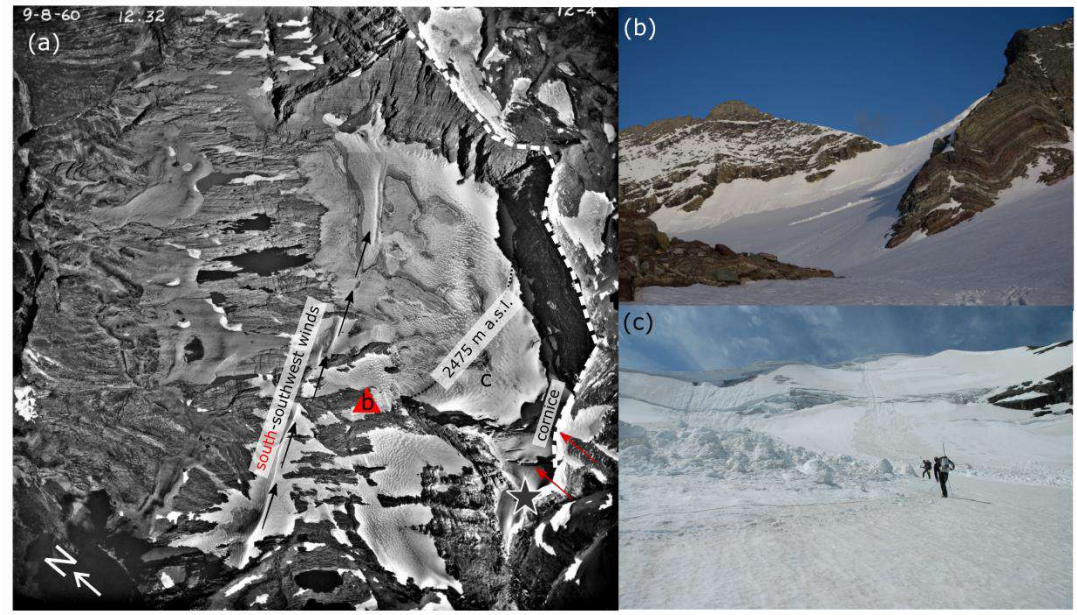

Figure 6. Snow avalanches and wind drifted snow at Sperry Glacier. (a) Aerial photograph of Sperry Glacier taken on 8 September 1960 shows a prominent ridge of wind drifted snow that is evidence of southwest winds in the basin (black arrows), is shown. The cornice that is evidence of south winds (red arrows) is labeled. Sperry Glacier meteorological station is shown (red triangle) and the approximate elevation (2475 m a.s.l.) above which the winter and summer mass balance gradients change is drawn. The photograph also shows the glacier lapping over the top of Gunsight Peak (black star) at the highest elevation of the ridge (dotted white line). Photograph credit: USGS Climate Change in Mountain Ecosystem photograph archives. (b) Sperry Glacier in June, 2010. Snow sluffing and loose avalanches off the headwall are depicted. Photograph was taken from the Sperry Glacier meteorological station, labelled "b" in (a). Photograph credit: Joel Harper. (c) Sperry Glacier in June, 2006. Cornice collapse (on the left) often causes a localized slab avalanche. Loose avalanche depicted on the right. Photograph credit: USGS Climate Change in Mountain Ecosystem photograph archives. Photograph was taken from the approximate location labelled "c" in (a).

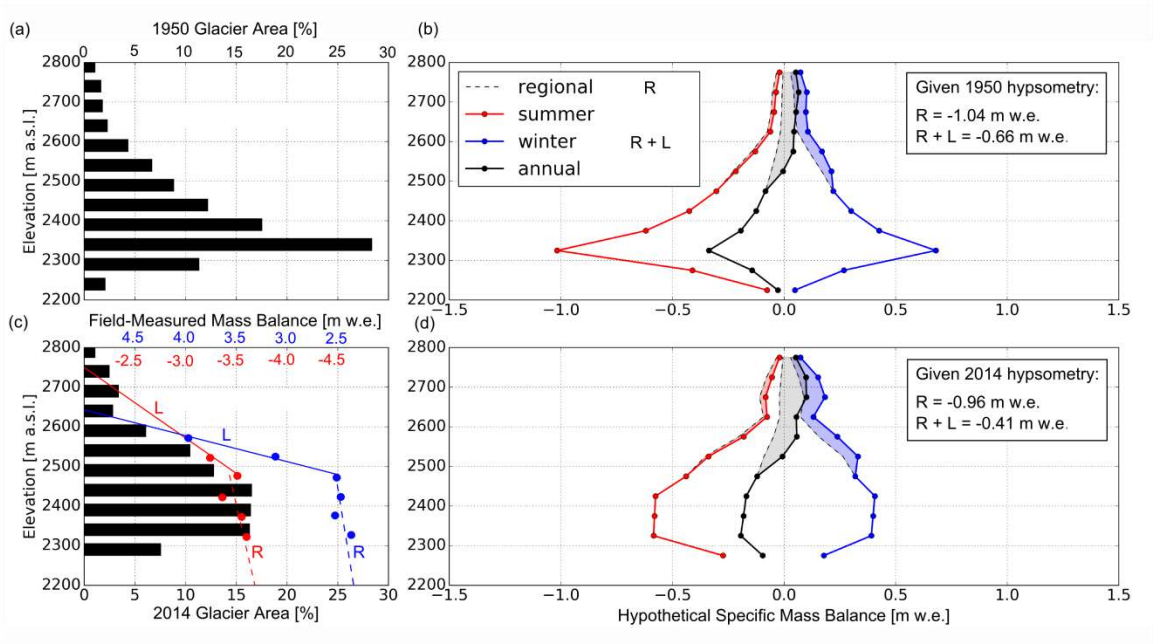

Figure 7. Parsing local from regional mass balance drivers. (a) Hypsometry of the 1950 glacier, presented in 50-m elevation bands (black bars). (b) Sperry Glacier hypothetical mass balance, as it varies with elevation, given 1950 glacier hypsometry and mass balance gradients. Solid lines show the summer (red), winter (blue), and annual (black) balances calculated using field-measured local (L) and regional (R) mass balance gradients shown in (c). Dotted black lines show the same but excluding L at high elevations, i.e. using R only. (c) Hypsometry of the 2014 glacier surface (black bars), and mass balance gradients measured at Sperry Glacier (red and blue dots and lines). The mean of 2005-2014 summer (red dots) and winter (blue dots) point mass balances, measured at stakes sites, are plotted against the average elevation of the 50-m elevation band wherein the stake was located. Lower elevation (< 2475 m) mass balance gradients reflect regional (R) mass balance gradients for melt (dashed red line) and snow water equivalent (SWE) (dashed blue line). Higher elevation (> 2475 m) mass balance gradients reflect local (L) mass balance gradients for melt (dotted red line) and SWE (dotted blue line). (d) Sperry Glacier hypothetical mass balance as shown in (b), but given 2014 glacier hypsometry.

Tables

	Summer Balance (m w.e.)	Winter Balance (m w.e.)	Annual Balance (m w.e.)	AAR
2005	-2.92	+2.33	-0.59	34%
2006	-3.15	+2.78	-0.37	-
2007	-3.60	+2.19	-1.41	-
2008	-1.78	+2.74	+0.96	-
2009	-3.53	+2.46	-1.07	46%
2010	-2.47	+2.82	+0.35	48%
2011	-2.88	+4.13	+1.25	-
2012	-3.09	+3.67	+0.58	-
2013	-3.98	+2.97	-1.01	36%
2014	-2.84	+3.19	+0.35	-

Table 1: Area-averaged glaciological mass balance values used in this study. Winter balances are as reported by Clark et al. (2017). Summer and annual balances are the result of calibration against the 2005-2014 geodetic mass balance, accomplished following the calibration steps outlined by Zemp et al. (2013). Accumulation area ratio (AAR) as reported by Clark et al. (2017) is listed for years when the seasonal snowline was mapped.

	DEM Source	Area (km^2)	Median Elevation (m)	Median Slope (°)	Median Aspect (°)
01 Sept 1950	USGS Topographic Map 1:6,000	1.30	2317	15	315 NNW
08 Sept 1960	USGS Topographic Map 1:6,000	1.23	2325	17	315 NNW
02 Sept 2005	National Technical Means Imagery	0.86	2425	22	326 NW
07 Sept 2014	National Technical Means Imagery	0.80	2444	24	326 NW

Table 2: Digital elevation model (DEM) specifications and glacier elevation results. Acquisition dates for the original imagery used to derive elevation data are listed.

	Net Volume Change	Net Mass Change	Elevation Error	Density Error	Total Error	Geodetic Mass Balance
	ΔV	ΔM	$E\Delta h$	$E\rho$	E_t	$dH\ dt^{-1}$
	($m^3 \times 10^6$)	($kg \times 10^9$)	(m w.e.)	(m w.e.)	(m w.e.)	(m w.e. yr^{-1})
1950-1960	-3.33	-2.83	1.20	0.18	1.22	-0.22 ± 0.12
1960-2005	-11.3	-9.68	2.16	0.68	2.27	-0.18 ± 0.05
2005-2014	-0.90	-0.76	0.26	0.06	0.27	-0.10 ± 0.03

Table 3: Geodetic mass balance results. Net changes in volume (ΔV) and mass (ΔM) on Sperry Glacier from 1950-1960, 1960-2005, and 2005-2014 are listed. Uncertainties due to elevation error ($E\Delta h$) and density ($E\rho$) are listed, as are total errors (E_t). Geodetic mass balances ($dH\ dt^{-1}$) are listed with uncertainty defined by total error, expressed as a rate.

Supplement contents:

- Details on the glaciological mass balance calibration
- Figure S1
- Figure S2
- Figure S3
- Table S1
- Table S2
- Table S3

Glaciological mass balance calibration

We defined the annual glaciological balance as the sum ($B_{a.sum}$) of the site index summer (B_s) and winter (B_w) balances reported by Clark et al. (2017). We calibrated annual and summer balances using the following steps, defined in the calibration section of the Zemp et al. (2013) reanalysis procedure.

First, we calculated the centred glaciological balance (β_t), which is the deviation from the mean glaciological balance ($\bar{B}_{a.sum}$) for 2005-2014. This term captured interannual variability documented by glaciological data:

$$\beta_t = B_{a.sum} - \bar{B}_{a.sum} \quad \text{(S1)}$$

Next, we used this centered glaciological balance and the geodetic mass balance ($\bar{B}_{a.geodetic}$) to calculate the calibrated annual balance ($B_{a.cal}$):

$$B_{a.cal} = \beta_t + \bar{B}_{a.geodetic} \quad \text{(S2)}$$

Finally, we calculated the calibrated summer balance:

$$B_{s.cal} = B_{a.cal} - B_w \quad \text{(S3)}$$

These calibrated summer and annual balances are reported in Table 1.

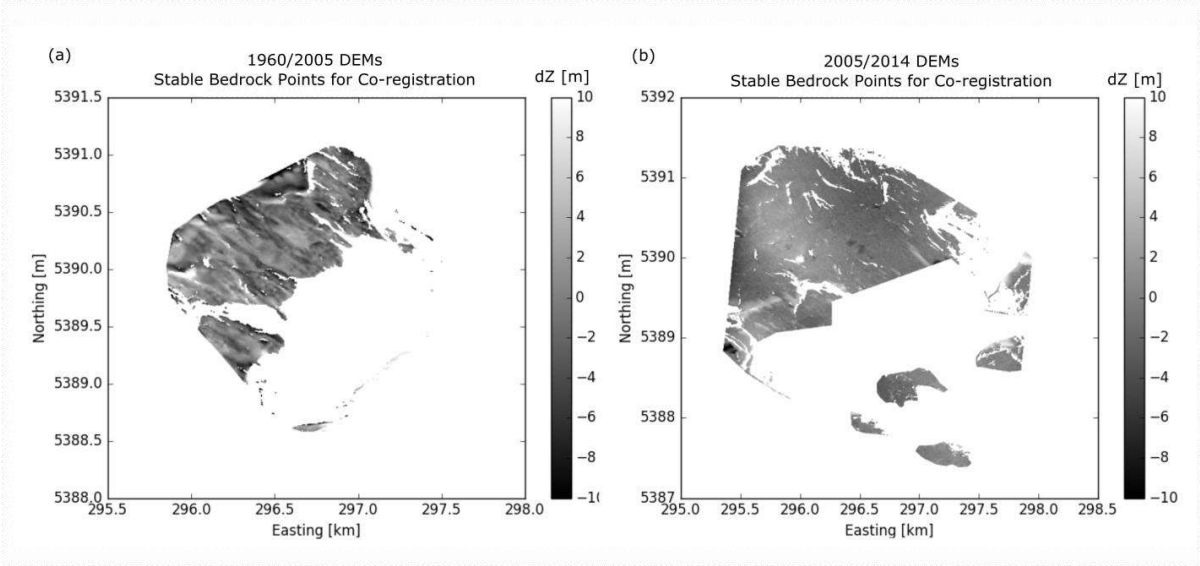

Figure S1: Elevation differences over the stable bedrock used for DEM co-registration are shown on a forced -10 m to 10 m scale. The full suite of elevation differences over stable bedrock terrain is shown in Figure S2.

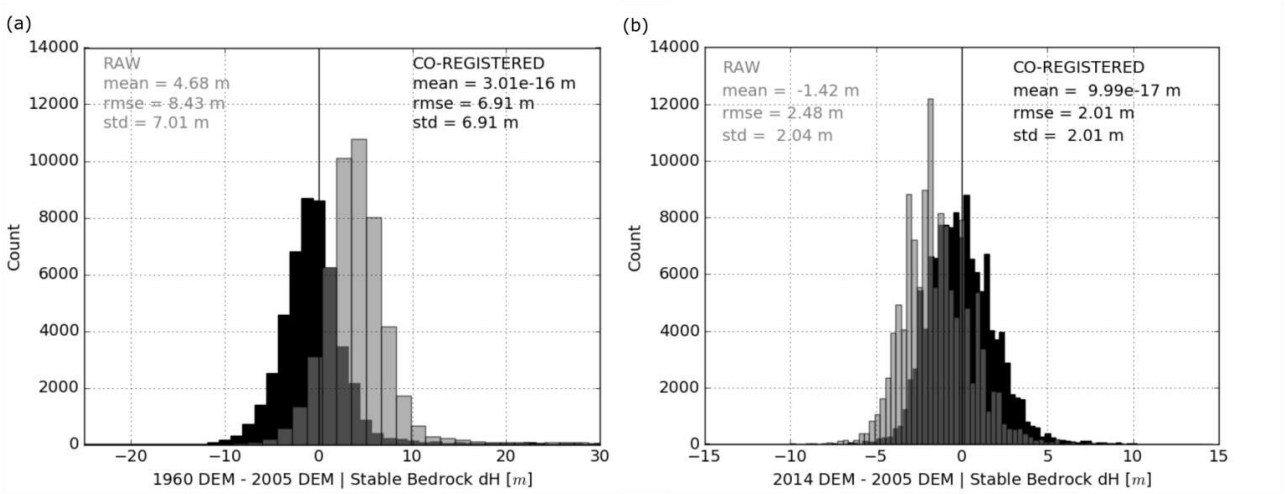

Figure S2: Elevation differences over stable bedrock terrain before (gray bars) and after (black bars) co-registration of the (a) 1960/2005 and (b) 2005/2014 DEMs. Plots show the magnitude (x-axis) and pixel count (y-axis) of elevation differences over stable bedrock terrain that is low-sloping (< 30°), and free of vegetation, snow, and ice. Text on the plots reports mean, root mean square error (rmse), and standard deviation (std) of these elevation differences for the raw (gray text) and co-registered (black text) results. The number of pixels used for co-registration for 1960/2005 (n = 23,951) was fewer than for 2005/2014 (n = 127,440) due to the 2005 and 2014 DEMs covering more bedrock terrain. Dark gray bars are an artefact of light gray bar transparency.

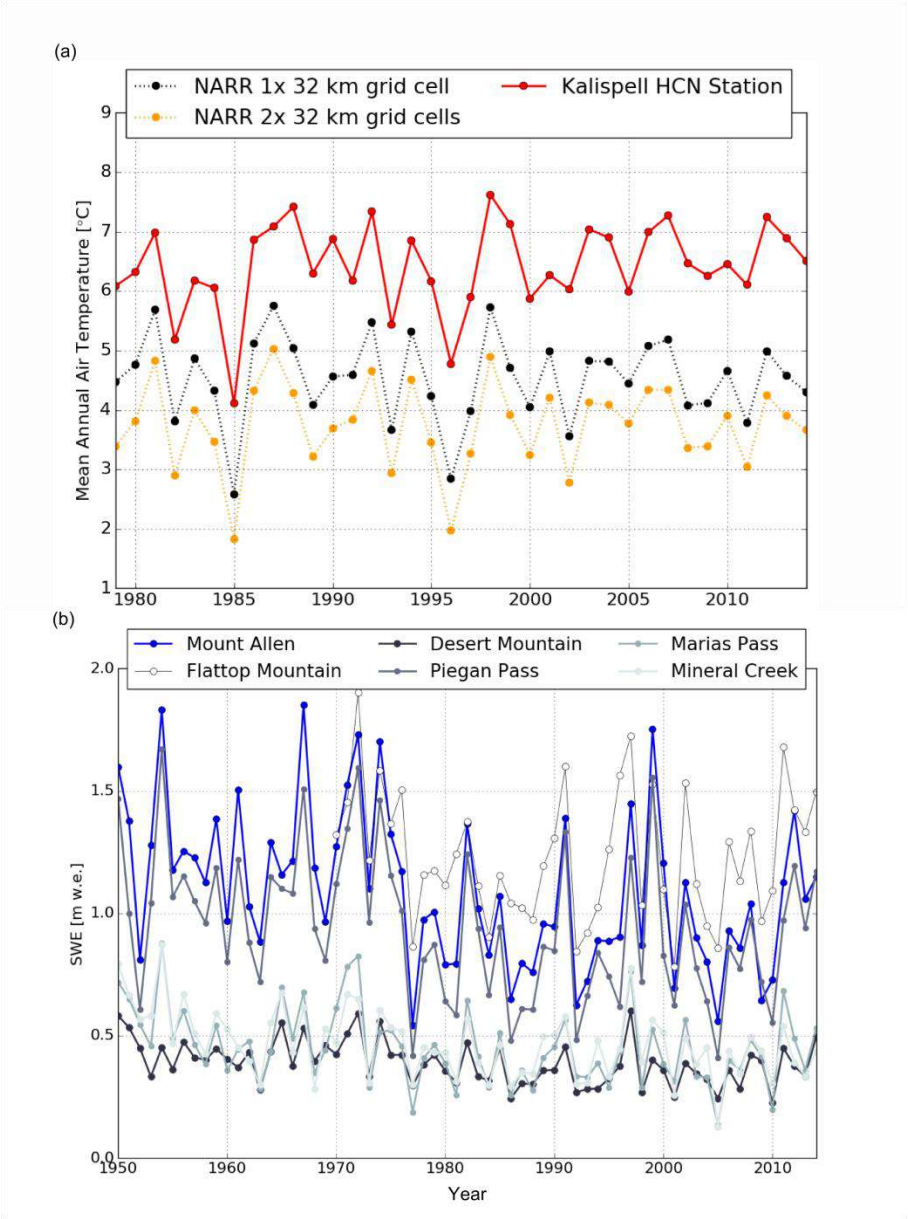

Figure S3: Auxiliary meteorological and snow data. (a) Mean annual air temperatures measured (solid lines) at the Kalispell Historical Climate Network (HCN) station (red) compared with mean annual air temperatures according to North American Regional Reanalysis output (dotted lines) for a single 32-km grid cell containing the Kalispell station (black), and two 32-km grid cells containing the Kalispell station and Sperry Glacier (yellow). (b) Annual peak SWE data for six snow stations in the study area. Station details listed in Table S3.

	Area	Difference from Full Glacier Results		Median Elevation	Difference from Full Glacier Results	
	(m^2 x 10^6)	(m^2 x 10^6)	(%)	(m a.s.l.)	(m a.s.l.)	(%)
1950 DEM	1.16	-0.14	-11	2305	-12	-0.5
1960 DEM	1.10	-0.13	-12	2310	-15	-0.7

Table S1: Digital elevation model (DEM) results for the truncated glacier. Differences from the full glacier results (see Table 2), where 2014 elevations were used to fill in the missing upper section, are also reported.

	Net Volume Change	Difference from Full Glacier Results		Net Mass Change	Difference from Full Glacier Results		Mass Change Rate	Difference from Full Glacier Results	
	ΔV			ΔM			$dH\ dt^{-1}$		
	($m^3 \times 10^6$)	($m^3 \times 10^6$)	(%)	(kg x 10^9)	(kg x 10^9)	(%)	(m w.e. yr^{-1})	(m w.e. yr^{-1})	(%)
1950-1960	-3.54	-0.21	-6	-3.00	-0.17	-6	-0.26	-0.04	-18
1960-2005	-12.3	-1.00	-9	-10.5	-0.82	-9	-0.21	-0.03	-17

Table S2: Geodetic mass balance results for the truncated glacier. The net change in volume (ΔV) and mass (ΔM) are listed, as are mass change rates ($dH\ dt^{-1}$). Differences from full glacier results, where 2005-2014 values were used to fill in the missing upper section, are also reported.

Site	Measurement	r^2	m_w (unitless)	Distance (km)	Elevation (m)	First Year
Sperry Glacier	-	1	1	0	2450	-
Flattop Mountain	SNOTEL	0.990	2.32	~15	1920	1970
Mount Allen	Snow Course	0.973	2.99	~14	1737	1922
Desert Mountain	Snow Course	0.960	7.93	~27	1707	1937
Piegan Pass	Snow Course	0.959	3.28	~14	1676	1922
Marias Pass	Snow Course	0.939	6.68	~46	1600	1934
Mineral Creek	Snow Course	0.945	7.24	~13	1219	1939

Table S3: Snow data that were assessed, but not used in the linear regression. The type of snow measurement site and correlation coefficients (r^2) between glaciological winter mass balance and peak SWE measured at the snow measurement site for 2005-2014 are listed. Winter proportionality factors (m_w), calculated using 2005-2014 glaciological winter balance data; map distance from Sperry Glacier, snow measurement site elevation, and start of the historical record of the snow data (First Year) are also listed. The dash (-) indicates not measured.

CHAPTER 4

EVALUATING DRIVERS OF GLACIER CHANGE SINCE THE LITTLE ICE AGE IN THE NORTHERN ROCKY MOUNTAINS

Abstract:

Changes in glacier ice coverage in response to centennial/decadal scale climate forcings are spatially complex and non-uniform across mountain range landscapes. To investigate the drivers of this spatial complexity in the northern Rocky Mountains, USA, we analyze glacier area changes from the Little Ice Age (LIA) glacial maxima at approximately the mid-19th century to the modern. Glacier area data reconstructed from moraine tracing show that at the LIA glacial maxima there were 147 glaciers in the study area, ranging from 0.01 to 4.97 km^2. Every single LIA glacier decreased in area and 98 (67%) of the small (<1.5 km^2) LIA glaciers disappeared over the course of the 20th century. However, although all LIA glaciers that vanished were small, not every small LIA glacier disappeared. Considering decision tree algorithm results trained on glacier and terrain parameters, along with simple stability assessments based on estimated LIA ice thicknesses, we find that the predictable factors of initial glacier size and elevation cannot perfectly explain the observed pattern of glacier disappearance. Our results instead promote a more nuanced understanding: on the centennial time scale, glaciers remained coupled to regional climate (i.e. every glacier retreated) and change was grossly predictable based on initial glacier size (i.e. the biggest LIA glaciers persisted), but topographic effects (e.g. avalanching) modulated glacier change at small (<1.5 km^2) glaciers more than did regional lapse rates (i.e. elevation).

1 Introduction

As climate becomes less favorable for maintaining glacier ice across a mountain landscape, a complex pattern of change can result from the spatially heterogeneous processes that drive glacier mass balance. Glacier hypsometry and ice volume exert a first order control on how glacier mass and the spatial footprint of a glacier change in response to climate perturbations (Cuffey and Paterson, 2010; Oerlemans, 2001). However, local topography can strongly affect accumulation and ablation processes of small (10^{-1} to 10^{0} km^2) mountain glaciers (Carrivick et al., 2015; Florentine et al., 2018; Hughes, 2010; Kuhn, 1995), such that glacier retreat can be highly variable for proximal glaciers situated in topographically favorable versus unfavorable settings (Debeer and Sharp, 2009). Thus, the spatial pattern of ice change across mountain ranges is not necessarily expected to be uniform or to coincide perfectly with the primary factors that control local climatic conditions such as elevation and aspect. This complexity muddles the relationship between mountain glaciers and climate.

Comparing reconstructions of the areal extent of mountain glaciers at the end of the Little Ice Age glacial maxima more than a century ago (Matthews and Briffa, 2005) to the areal extent of glaciers today provides an opportunity to investigate the spatially complex drivers of glacier change across mountain landscapes. Such comparison directly documents glacier area change on an individual, glacier by glacier basis (Knoll et al., 2009; Lucchesi et al., 2014; Qiao and Yi, 2017). In turn, glacier volume and mass change may be estimated from glacier area data using geometric inferences based on the yield strength of ice (Kerschner et al., 1999; Knoll et al., 2009). Furthermore, pairing glacier change data with quantitative assessment of local terrain factors enables insight into

topographically controlled mass balance processes (i.e. shading, avalanching, wind-drifting) (DeBeer and Sharp, 2009).

In this paper we compare reconstructed LIA glacier areal extents (Fagre and Martin-Mikle, 2018) to modern (21st century) glacier areal extents (Fagre et al., 2017) in and near Glacier National Park (GNP) in the northern Rocky Mountains. Our goal is to elucidate spatially varying factors driving change to glacier ice masses across this mountain landscape to better understand glacier-climate relationships. First, we analyze glacier area change. Next, we define and assess terrain parameters that approximate topographically driven mass balance processes and use these results to train a decision tree algorithm that determines rank orders for the relative importance of different controls (i.e. initial glacier area, elevation, avalanching, etc.). Finally, we estimate glacier thickness and consider simple physical constraints on melt (i.e. elevation lapse rates) to evaluate the expected stability of LIA glaciers based on initial ice mass and elevation distribution, and then compare this to the observed pattern of disappearance. Our work provides insight into the relative control of predictable factors like elevation and initial glacier size, versus less predictable (and unresolved) factors like snow avalanching and wind drifting.

2 Study area

The mountainous terrain of GNP is characterized by glacially carved valleys, cirques, horns, and arêtes (Figure 1). During the period of cooling associated with the Little Ice Age (16th to 19th centuries) GNP glaciers advanced (Carrara, 1989) and deposited distinct moraines, distinguishable as centuries (and not millennia) young because of the sharply crested morphology and lack of vegetative cover. Tree ring dates of 1860 and 1859 from

just inside the Jackson and Agassiz Glacier moraines indicate that these glaciers reached their LIA maximum extent in the mid-19th century (Carrara and McGimsey, 1981). Today there are 39 named glaciers within and near GNP (Fagre et al., 2017), all of which are paired with LIA moraines located tens to hundreds of m downslope from the modern glacier terminus (e.g. Figure 2).

3 Data and methods

To ensure a complete and consistent inventory of glaciers present on the modern, 21st century landscape, we inspected 39 named glacier margins in and near GNP derived from 2015 WorldView imagery (Fagre et al., 2017), and complimented these data with 17 additional unnamed glaciers identified during a systematic inventory of 2005 National Agriculture Imagery Program (NAIP) imagery. We distinguished glaciers from perennial snow fields using the following criteria: glaciers had to be a cohesive body identifiable as bare ice in late summer imagery once seasonal snow had melted. Our inspection of the 39 named glaciers resulted in exclusion of Baby, Boulder, Harris, Herbst, Hudson, Siyeh, and Two Ocean Glaciers. Ultimately, our complete inventory of modern GNP glacier margins totaled 49 (32 named glaciers, 17 additional unnamed glaciers). The areal extent of LIA glaciers was provided by the moraine-derived dataset created by Fagre and Martin-Mikle (2018).

To enable comparison of LIA and modern glaciers, we use 10 m National Elevation Dataset (NED) as a digital elevation model (DEM), in conjunction with the glacier margin data described above, to define LIA and modern glacier area, median glacier elevation, median glacier slope, and median glacier aspect. Aspect and slope were

calculated using an algorithm written in python (Christopher Nuth, personal communication) like that applied in ArGIS software (ESRI, 2014). Median values are reported for each glacier as these reflect the central tendency of the spatial field and require no assumption of the distribution of values across the glacier, which is likely not normally distributed. We note that median elevation may be a reasonable approximation of the equilibrium line altitude (ELA), because if the glacier accumulation area ratio (AAR, the ratio of the accumulation area to the ablation area) were 0.5, then the median elevation would be the ELA. An AAR of 0.5 falls within typical AAR for small cirque glaciers (0.44 ± 0.07) and valley-filling glaciers (0.6) (Colucci, 2016; Murray and Locke, 1989).

Our use of modern elevation data to quantify glacier elevation is a source of uncertainty because modern surface elevations do not reflect the surface of LIA glacier ice. LIA glacier results are therefore characteristic of the terrain occupied by the LIA glacier, rather than a precise report of the actual LIA glacier surface.

3.1 Terrain parameters

Ultimately our goal was to assess the relative control of predictable factors like initial glacier ice mass and regional lapse rates against local, unresolved factors like avalanching, wind-drifting, and shading. To address the former, we analyzed LIA glacier area as a proxy for initial glacier ice mass, and median glacier elevation as a proxy for temperature and thus sensible heat flux. To address the latter, we analyzed terrain parameters for LIA glacier shading, avalanching, and wind drifting that act as proxies for topographically driven mass balance processes. These parameters are not independent.

Therefore, we calculated Spearman's rank correlation coefficients to quantify and understand relationships between parameters. We limit terrain parameterization to small (<1.5 km^2) glaciers, as our results show that larger LIA glaciers persisted without exception (see section 4 Results) and therefore do not evoke the same suspicion that persistence depended on anything other than initial glacier size.

3.1.1 Radiation

We define incoming solar radiation (W m^{-2}) across each glacier to approximate shading. The Solar Area Radiation tool (ESRI, 2014) was used to calculate potential clear sky radiation during melt season months, defined as July, August, and September (Clark et al., 2015; Florentine et al., 2018). This hemispherical viewshed algorithm (Fu and Rich, 2002) accounts for the seasonal progression of the sun, a fixed atmospheric transmissivity, latitude, as well as topographic shading, elevation, slope, and aspect based on NED data. We computed radiation across the terrain footprint of every small LIA glacier, and then reported the median value. Thus, if most grid cells across the glacier were shaded, then the radiation index for that glacier was a low magnitude W m^{-2} value. The assumption of clear sky, without accounting for the effect of clouds, is a source of uncertainty.

3.1.2 Avalanching

Avalanche starting zone areas on glacier headwalls acted a proxy for snow mass input by slab avalanching. We first delineated headwalls, and then computed starting zones on each headwall as the area where slope was greater than 30° (and therefore likely to slide),

and less than 60° (and therefore likely to accumulate sufficient snow for slab development). Glacier headwalls were delineated by drawing headwall margins perpendicular to bedrock elevation contours (70 m contour intervals) above the glacier. Headwall designation was restricted to only the bedrock area above the main ice body, i.e. headwalls did not include bedrock above narrow (tens of meters) ledges of ice that extended off the main glacier.

We also computed an avalanche interception index for the likelihood that the glacier surface intercepted and retained avalanched snow, defined as the ratio between the slope of the headwall and the slope of the glacier surface:

$$I = \frac{\alpha_h}{\alpha_g} \quad (1)$$

where α_h is the median headwall slope, $\alpha_g$is the median glacier slope, and I is the avalanche interception index. An index greater than one indicated that the slope of the glacier was flatter than the slope of the headwall, and thus the glacier had better potential for avalanche interception.

Finally, we computed an index for the likelihood of snow sluffing off headwalls. Not all snow redistributed onto a glacier surface by avalanche activity occurs via slab avalanching. Often continual sluffing off steep headwalls occurs during or soon after storms. Observations from Sperry Glacier provide evidence for this more frequent, sluffing avalanche activity (Florentine et al., 2018). We used headwall slope as a proxy for avalanche sluffing, where steep headwalls were assumed to lead to high sluffing activity.

3.1.3 Wind

Finally, we computed a wind exposure index to approximate scouring versus loading of snow across the glacier surface. We leveraged previous work that developed an empirically determined wind parameter (Winstral et al., 2002), based on the maximum upwind slope relative to the dominant, seasonally averaged, regional wind direction. This study found that defining the wind parameter across the 100 m length scale optimized agreement between parameterized wind drift and observed snow depths measured at 504 points across an ~1 km^2, high elevation study area in the Colorado Rocky Mountains (Winstral et al., 2002).

The dominant wind direction in GNP is from the southwest (i.e. 225°), as shown by analysis of 20th century GNP climatology (Finklin, 1986) and meteorological data from a high elevation weather station in GNP: wind direction measured at an off-ice meteorological station adjacent to Sperry Glacier (elevation ~2450 m) between 2014 and 2016 was 219$\pm$65° (Erich Peitzsch, personal communication). We therefore calculated the maximum upwind slope as:

$$\alpha = \tan^{-1}\frac{v}{h} \quad (2)$$

where vertical relief to the highest point within 100 m to the SW is v, horizontal ground distance to the highest point is h, which together define the maximum upwind slope, i.e. the wind exposure index (α). We report the median wind exposure across each LIA glacier. Hence if most grid cells across the glacier were sheltered from SW winds, then the index was a high magnitude, positive angle.

3.2 Glacier thickness

Interpreting glacier area as a proxy for ice mass is limiting, because glaciers with identical area can have distinct ice volume (and therefore mass) due to differing ice thicknesses. To address this limitation, we use glaciological principles to estimate ice thickness across LIA glaciers, which we later use in our analysis to define an index for the relative stability of LIA glaciers (i.e. which glaciers were massive and thick versus which glaciers were spread thinly across the landscape).

Following methods used in other paleoclimate and cirque glacier studies (Kerschner et al., 1999; Knoll et al., 2009; Kull and Grosjean, 2000; Sanders et al., 2010), we apply the approximation that basal shear stress is balanced by driving stress. We therefore assume that ice within every LIA glacier flowed, which is supported by the moraines that were deposited by every LIA glacier. Further, we assume stress to be equal to the approximate yield strength of temperate ice, 100 kPa (Cuffey and Paterson, 2010; Nye, 1959). Applying the simple slab model, which sets glacier surface slope parallel to bed slope, enables us to estimate ice thickness:

$$h = \frac{\tau_b}{\rho g \sin\theta} \quad (3)$$

where h is the estimated ice thickness consistent with 100 kPa at each DEM grid cell across the glacier footprint, given 100 kPa as the yield strength of ice (τ_b) (Cuffey and Paterson, 2010), 900 kg m^{-3} as the density of ice (ρ), 9.81 m s^{-2} as acceleration due to gravity (g), and glacier slope (α) at every DEM grid cell across the glacier footprint. The method agreed well with measurements available for one modern GNP glacier. It yielded an average ice thickness for modern Sperry Glacier of 38 m, which is within 3 m of the 35 m average ice thickness estimated from ice penetrating radar (Brown et al., 2010).

4 Results

LIA glaciers in GNP were not long valley glaciers (Figure 1). At the LIA there were 147 cirque glaciers, individually <5 km^2 in area (Figure 3), but collectively comprising 59.65 km^2 of ice coverage in and near GNP. By the beginning of the 21st century, only 49 modern glaciers remained, meaning that 98 glaciers disappeared. Modern glaciers cover 75% less area, at 15.13 km^2 of ice coverage. Consistent with previous work showing predominantly northeast-facing aspects of cirque glaciers in the Northern Rocky Mountains (Graf, 1976), our results show that modern glacier aspects range from NW (287°) to SE (136°). This range was wider for LIA glaciers (252° to 154°) which had more southerly and westerly exposures. The median elevation of LIA glaciers was 2185 m, which is only 98 m lower than the median elevation of modern glaciers. Further, the elevation range of LIA and modern glaciers overlaps (Figure 4). The elevation shift of GNP glaciers from the LIA to now was thus not nearly as dramatic as the hundreds of m depression of the glaciation threshold typical for the Pleistocene Last Glacial Maximum (Locke, 1990; Porter, 1977).

Inspecting area change at LIA glaciers, we found strong correlation between initial (LIA) glacier area (r^2=0.98, $p<0.01$) and glacier area change: big LIA glaciers lost more area than did small LIA glaciers (Figure 5a). The relative area changes of the nine biggest (>1.5 km^2) LIA glaciers (Agassiz, Sperry, Jackson, Blackfoot, Grinnell, Kintla, Pumpelly, Harrison, and Rainbow) varied from 45 to 83% (Figure 5a; Figure 6). The relative area loss of the small LIA glaciers that persisted varied from 9 to 90% (Figure 5b).

All LIA glaciers that disappeared were smaller than 1.5 km^2 (Figure 7a). Of the 138 LIA glaciers in this small size class, 71% (n=98) disappeared and 29% (n=40) persisted. Comparing terrain parameters, we found that LIA glaciers that disappeared tended to have smaller avalanche starting zones (Figure 7e) (Table 2). T-tests run on parameters that had normal distributions showed significant differences at the 95% confidence interval ($p<0.05$) between elevation and radiation (Figure 7b and Figure 7c). LIA glaciers that disappeared tended to be lower in elevation and more shaded (Figure 8b). The range of wind exposure at LIA glaciers that disappeared was wider than at LIA glaciers that persisted (Figure 7d). Some LIA glaciers that disappeared were in highly wind scoured locations (Figure 8a).

Spearman correlation coefficients show that there is a strong ($r>0.6$) monotonic relationship between radiation and elevation (+0.65), and radiation and headwall slope (-0.77). These results quantify the relationships between terrain parameters: high elevation glaciers are more exposed to clear sky insolation because less terrain interrupts the skyline extending above the glacier (Debeer and Shap, 2009), and glaciers at the base of steep headwalls tend to be shaded.

5 Discussion

Similar to LIA glacier reconstructions in the Julian Alps and South Tyrol, Italy (Colucci, 2016; Knoll et al., 2009), our results show that the northern Rocky Mountain LIA ice masses were cirque glaciers, like modern GNP glaciers only larger. Cirque glaciers tend to be characterized by anomalous accumulation from wind-drifting and avalanching of snow (Kuhn, 1995), and to be heavily affected by local topography

(Hoffman et al., 2007). Cirque glaciers therefore do not always demonstrate classic accumulation/ablation area zoning. Instead of following an elevation contour, the cirque glacier ELA, which separates the accumulation and ablation zone, can run parallel to the headwall ridge (e.g. Sperry Glacier in GNP; Florentine et al., 2018).

Hence, given that all LIA glaciers analyzed in this study qualify as cirque glaciers <5 km^2, topographically driven mass balance processes must have driven some portion of the observed glacier change across this mountain landscape. Our subsequent analyses attempt to tease out whether these local topographic effects ultimately controlled, or merely modulated, LIA glacier response to 20^{th} century climate change.

5.1 Large versus small changes of the big glaciers

Because all LIA glaciers in and near GNP were cirque-type, these glaciers were less subject to rapid terminus retreat than would be expected for valley-type glaciers with more extended area altitude distributions (Oerlemans, 2001). Nonetheless, area altitude distribution (i.e. glacier hypsometry) still partly explains the relative area loss on big cirque glaciers. For example, Sperry Glacier lost a large (79%) proportion of its area, likely because >30% of the glacier was distributed at low elevation (Figure 9b).

The differing area loss of 52% at Harrison Glacier and 70% at the adjacent Blackfoot Glaciers (Figure 6e and Figure 6h) is not necessarily explained by hypsometry, as these glaciers had similar LIA area altitude distribution (Figure 9e and Figure 9h). Instead, the different relative area loss is probably explained by different initial area aspect distribution. Median aspect at Blackfoot Glacier rotated 43° from northeasterly (75°) at the LIA to more northerly (32°) at the modern (Table 1; Figure 4), as areas situated at the

base of west-facing headwalls melted and were lost (Figure 6e). Meanwhile, Harrison Glacier only departed 1° from its LIA median aspect (Table 2; Figure 4). Big glacier area loss thus fits well with expected, predictable drivers of glacier change, i.e. elevation and aspect.

5.2 Small glaciers that vanished

LIA glaciers that disappeared were generally small (Figure 7a). Subjected to climate change from the LIA to modern, which included 20th century increase in maximum temperature of 1.13° C in this region (Pederson et al., 2010), locations where many very small (median size of LIA glaciers that disappeared was 0.07 km^2) glaciers were sustained during the LIA became inviable for hosting glacier ice. Many very small LIA glaciers melted completely, which is consistent with the expected, predictable condition of initial glacier size controlling glacier change.

5.3 Why did some small LIA glaciers persist?

Our results underscore the fundamental control of glacier size on glacier disappearance. However, not all small (<1.5 km^2) LIA glaciers vanished. This could potentially be explained if small LIA glaciers that persisted were thick glaciers that were relatively more stable, merely due to greater initial mass. Furthermore, select small LIA glaciers could have persisted if these glaciers were located at high, cold elevations. To test whether the pattern of GNP glacier disappearance is simply explained by initial glacier size and elevation we use two independent analyses: classification and regression tree (CART) based on terrain parameters, and stability indices based on ice thickness.

5.3.1 Classification tree

First, we used 10-fold cross validation to run CART analysis on terrain parameters. The tree was trained on the binary designation of LIA glacier disappearance versus persistence for 80% (n=119) of the available 147 LIA glaciers. It showed 79% accuracy when tested on the remaining 20% (n=28) of the data (Table 4), i.e. the tree accurately predicted disappearance/persistence for 22 of the 28 glaciers in the test data set.

CART results show that initial glacier area exerts the strongest control on whether LIA glaciers persisted versus disappeared (Figure 10). However, after initial glacier size, avalanche starting zone area and radiation distinguish glacier disappearance versus persistence. Radiation is strongly correlated with elevation (+0.65), but the avalanche starting zone parameter is not strongly correlated (i.e. r<0.60) with any other parameter. This suggests that while initial glacier size was a paramount control on ice persistence versus disappearance, it was local factors (avalanche starting zone) rather than regional lapse rates (elevation) that next determined whether small glaciers vanished.

5.3.2 Stability index

Second, using LIA ice thickness estimates and modern mass balance measurements from Sperry Glacier (Clark et al., 2017) we developed a stability index. This index constituted a first order assessment of how difficult it would be to melt each LIA glacier:

$$SI = \frac{h_g / \dot{a}_g}{\bar{h} / \dot{a}} \quad (5)$$

where the stability index (SI) is determined by the time required to ablate the estimated median LIA glacier thickness (h_g) at an assigned ablation rate scaled to glacier elevation

($\dot{a}_g$), normalized by the time required to melt the average LIA glacier thickness ($\bar{h}$) at the assigned ablation rate ($\dot{a}$). Thus, thin, low elevation LIA glaciers had small stability indices.

The mean annual mass balance measured on-ice at an elevation of 2338 m on Sperry Glacier from 2005 to 2014 was -1.08 m yr^{-1}, which we approximate as -1 m yr^{-1} and apply as the assigned ablation rate ($\dot{a}$) (Clark et al., 2017). The annual mass balance elevation gradient measured at Sperry Glacier was -3.4×10^{-4} m m^{-1} (Clark et al., 2017; Florentine et al., 2018). We scaled -1 m yr^{-1} to elevation using this measured gradient, which resulted in glacier assigned ablation rates ($\dot{a}_g$) that ranged from -0.88 to -1.21 m yr^{-1}.

Stability index results (Figure 11) provide an account of the expected pattern of glacier disappearance given one regional mass loss rate, scaled for the predictable and known control of elevation. This stability analysis does not correctly differentiate observed glacier disappearance, i.e. Figure 11 does not show all red dots exclusively clustering toward the thin glaciers and low stability index corner of the plot. This result corroborates our decision tree results, namely that in this small (<1.5 km^2) size class, glacier persistence was not purely a function of initial ice volume. Instead, glacier persistence was some function of size and other processes that are not captured by regional lapse rates.

6 Conclusions

Topographic effects complicate mountain glacier response to regional climate change. Our evaluation of glacier retreat in the northern Rocky Mountains since the LIA glacial

maxima supports this point. However, we found that although topographic effects played an important role in driving the spatially heterogeneous pattern of glacier change, these effects did not entirely decouple glaciers from climate. Instead we found that on the centennial time scale, regional changes, likely related to the broad scale global climate warming, dominantly forced glacier change. However, our results simultaneously pointed to the modulating effects of local, topographically driven mass balance processes, as the observed occurrences of glacier persistence versus disappearance could not be perfectly explained or predicted based on initial glacier size and elevation.

7 Acknowledgements

We acknowledge the contributions of Lisa McKeon to this work. She shared important glacier insights, honed by her years of field work in Glacier National Park, openly and generously. Co-authors on this paper are Joel Harper, Dan Fagre, Chelsea Martin-Mikle, and Adam Clark. CF, DF, and JH conceptualized the study. JH and DF contributed to writing. CM aided interpretation of the LIA glacier area dataset. AC created the modern, unnamed glacier area dataset.

8 References

Bahr, D. B. and Radić, V.: Significant contribution to total mass from very small glaciers, Cryosphere, 6(4), 763–770, doi:10.5194/tc-6-763-2012, 2012.

Bahr, D. B., Meier, M. F. and Peckham, S. D.: The physical basis of glacier volume-area scaling, J. Geophys. Res., 102(B9), 20355–20362, 1997.

Bahr, D. B., Pfeffer, W. T. and Kaser, G.: A review of volume-area scaling of glaciers, Rev. Geophys., 52, 522–555, doi:10.1002/2014RG000465, 2014.

Beamer, J. P., Hill, D. F., McGrath, D., Arendt, A. and Kienholz, C.: Hydrologic impacts of changes in climate and glacier extent in the Gulf of Alaska watershed, Water Resour. Res., 53(9), 7502–7520, doi:10.1002/2016WR020033, 2017.

Carrara, P. E.: Late Quaternary Glacial and Vegetative History of the Glacier National Park Region, Montana, U.S. Geological Survey Bulletin 1902, U.S. Department of the Interior, Washington D.C., 1989.

Carrivick, J. L., Berry, K., Geilhausen, M., James, W. H. M., Williams, C., Brown, L. E., Rippin, D. M. and Carver, S. J.: Decadal-Scale Changes of the ??denwinkelkees, Central Austria, Suggest Increasing Control of Topography and Evolution Towards Steady State, Geogr. Ann. Ser. A Phys. Geogr., 97(3), 543–562, doi:10.1111/geoa.12100, 2015.

Clark, A. M., Harper, J. T., Fagre, D. B. and Fagre, D. B.: Glacier-Derived August Runoff in Northwest Montana Glacier-derived August runoff in northwest Montana, Arctic, Antarct. Alp. Res., 47(1), 1–16, doi:10.1657/AAAR0014-033, 2015.

Colucci, R. R.: Geomorphic influence on small glacier response to post-Little Ice Age climate warming: Julian Alps, Europe, Earth Surf. Process. Landforms, 41(9), 1227–1240, doi:10.1002/esp.3908, 2016.

Cuffey, K. M. and Patterson, W. S. B.: The Physics of Glaciers, 4th ed., Elsevier, Oxford., 2010.

DeBeer, C. M. and Sharp, M. J.: Topographic influences on recent changes of very small glaciers in the monashee mountains, British Columbia, Canada, J. Glaciol., 55(192), 691–700, doi:10.3189/002214309789470851, 2009.

ESRI: ArcGIS Desktop: Release 10.3.1, 2014.

Fagre, D. B. and Martin-Mikle, C. J.: A comprehensive inventory of maximum glacial extent in Glacier National Park during the peak of the Little Ice Age: U.S. Geological Survey data release, U.S. Geol. Surv. data release [online] Available from: https://doi.org/10.5066/P95YJ3CN, 2018.

Fagre, D. B., McKeon, L. A., Dick, L. A. and Fountain, A. G.: Glacier margin time series (1966, 1998, 2005, 2015) of the named glaciers of Glacier National Park, MT, USA, U.S. Geol. Surv. data release, 2017.

Finklin, A. I.: A climatic handbook for Glacier National Park-- with Data for Waterton Lakes National Park, Gen. Tech. Rep. INT-GTR-204, (July), 1986.

Florentine, C., Harper, J., Fagre, D., Moore, J. and Peitzsch, E.: Local topography increasingly influences the mass balance of a retreating cirque glacier, , (March), 1–27, doi:10.5194/tc-12-2109-2018, 2018.

Fu, P. and Rich, P. M.: A geometric solar radiation model with applications in agriculture and forestry, Comput. Electron. Agric., 37(1–3), 25–35, doi:10.1016/S0168-1699(02)00115-1, 2002.
Graf, W. L.: Cirques as Glacier Locations, , 8(1), 79–90, 1976.
Hoffman, M. J., Fountain, A. G. and Achuff, J. M.: 20th-century variations in area of cirque glaciers and glacierets, Rocky Mountain National Park, Rocky Mountains, Colorado, USA, Ann. Glaciol., 46, 349–354, doi:10.3189/172756407782871233, 2007.
Hughes, P. D.: Little Ice Age glaciers in the Balkans: Low altitude glaciation enabled by cooler temperatures and local topoclimatic controls, Earth Surf. Process. Landforms, 35(2), 229–241, doi:10.1002/esp.1916, 2010.
Kerschner, H., Ivy-Ochs, S. and Schlüchter, C.: Paleoclimatic interpretation of the early Late-glacial glacier in the Gschnitz valley, central Alps, Austria, Ann. Glaciol., 28, 135–140, doi:10.3189/172756499781821661, 1999.
Knoll, C., Kerschner, H., Heller, A. and Rastner, P.: A GIS-based reconstruction of little ice age glacier maximum extents for South Tyrol, Italy, Trans. GIS, 13(5–6), 449–463, doi:10.1111/j.1467-9671.2009.01173.x, 2009.
Kuhn, M.: The mass balance of very small glaciers, Zeitschrift fur Gletscherkd. und Glazialgeol., 31, 171–179, 1995.
Kull, C. and Grosjean, M.: Late Pleistocene climate conditions in the north Chilean Andes drawn from a climate glacier model, J. Glaciol., 45(155), 622–632 [online] Available from: http://www.ingentaconnect.com/content/igsoc/jog/2000/00000046/00000155/art00008%5CnC:%5CUsers%5CAlfonso%5CDocuments%5CPhD%5CReview%5Cs8.pdf, 2000.
Locke, W. W.: Late Pleistocene glaciers and the climate of western Montana, U.S.A., Arct. Alp. Res., 22(1), 1–13 [online] Available from: http://www.jstor.org/stable/1551716 ., 1990.
Lucchesi, S., Fioraso, G., Bertotto, S. and Chiarle, M.: Little Ice Age and contemporary glacier extent in the Western and South-Western Piedmont Alps (North-Western Italy), J. Maps, 10(3), 409–423, doi:10.1080/17445647.2014.880226, 2014.
Matthews, J. and Briffa, K.: The ' Little Ice Age ': Re-Evaluation of an Evolving Concept, Geogr. Ann. Ser. A, …, 87(1), 17–36, doi:10.1111/j.0435-3676.2005.00242.x, 2005.
Murray, D. R. and Locke, W. W.: Dynamics of the late Pleistocene Big Timber glacier, Crazy Mountains, Montana, USA, J. Glaciol., 35(120), 183–190, doi:10.3189/S0022143000004470, 1989.
Nye, J. W.: The Motion of Ice Sheets and Glaciers, J. Glaciol., 3, 493–507, 1959.
Oerlemans, J.: Glaciers and Climate Change, A.A. Balkema Publishers, Netherlands., 2001.
Porter, S. C.: Present and past glaciation thresholds in the Cascade Range, Washington, USA: Topographic and climatic controls, and paleoclimatic implications, J. Glaciol., 18(78), 101–116, 1977.
Qiao, B. and Yi, C.: Reconstruction of Little Ice Age glacier area and equilibrium line attitudes in the central and western Himalaya, Quat. Int., 444, 65–75, doi:10.1016/j.quaint.2016.11.049, 2017.

Sakai, A. and Fujita, K.: Contrasting glacier responses to recent climate change in high-mountain Asia, Sci. Rep., 7(1), 1–8, doi:10.1038/s41598-017-14256-5, 2017.
Sanders, J. W., Cuffey, K. M., Macgregor, K. R., Kavanaugh, J. L. and Dow, C. F.: Dynamics of an alpine cirque glacier, Am. J. Sci., 310(8), 753–773, doi:10.2475/08.2010.03, 2010.
Veettil, B. K., Wang, S., Simões, J. C., Ruiz Pereira, S. F. and de Souza, S. F.: Regional climate forcing and topographic influence on glacier shrinkage: eastern cordilleras of Peru, Int. J. Climatol., 38(2), 979–995, doi:10.1002/joc.5226, 2018.
Winstral, A., Elder, K., and Davis, R. E. (2002). Spatial Snow Modeling of Wind-Redistributed Snow Using Terrain-Based Parameters. *J. Hydrometeorol.* 3, 524–538. doi:10.1175/1525-7541(2002)003<0524:SSMOWR>2.0.CO;2.

Figures

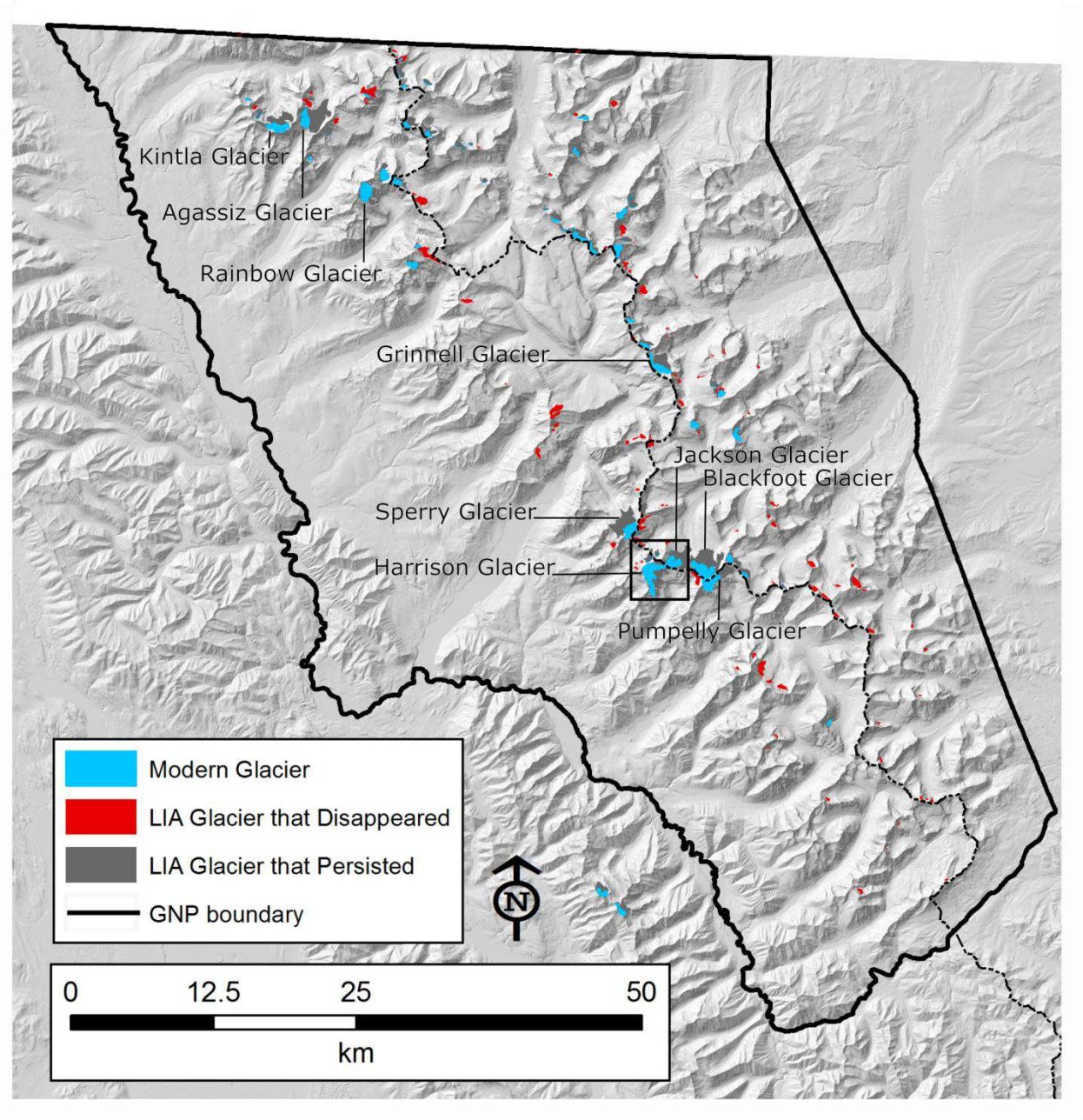

Figure 1. Map of the study area showing Little Ice Age (LIA) and modern (21st century) glaciers. LIA glaciers that disappeared are shown in red, LIA glaciers that persisted are shown in gray, and modern glaciers are shown in blue. The boundary of Glacier National Park (GNP) is delineated (black line), as is the continental divide (dashed black line). Extent of Figure 8 is outlined by the black box, and the nine LIA glaciers >1.5 km^2 are labeled.

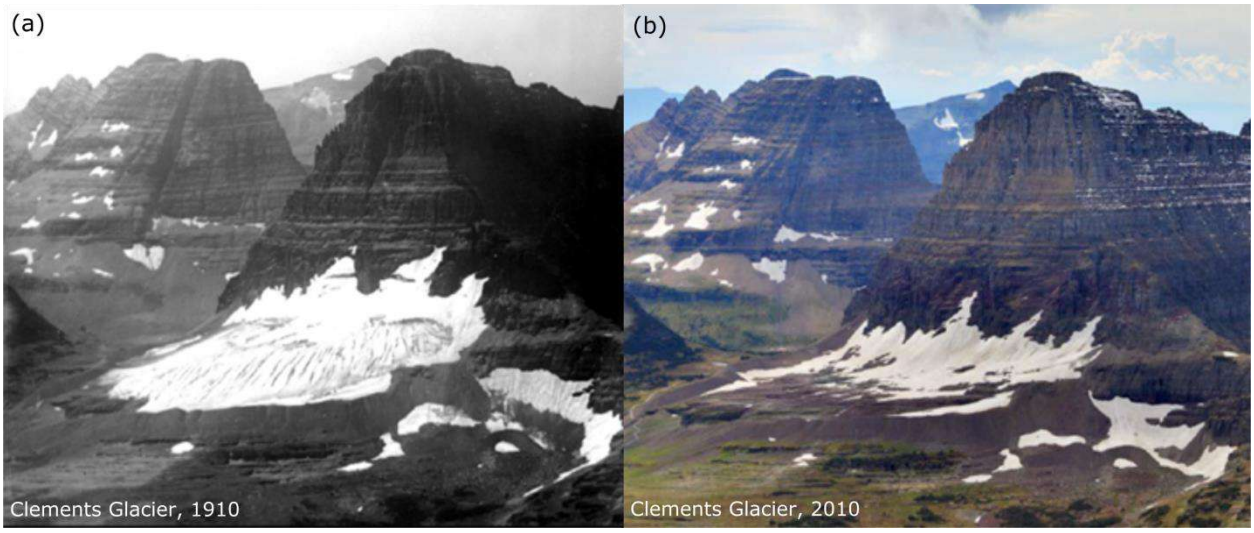

Figure 2. Example of LIA moraines. (a) East-facing Clements Glacier in 1910 (Source: Glacier National Park archives). (b) The site of Clements Glacier in 2010. Seasonal snow is visible, but glacier ice here has disappeared (Source: USGS Climate Change in Mountain Ecosystems archive).

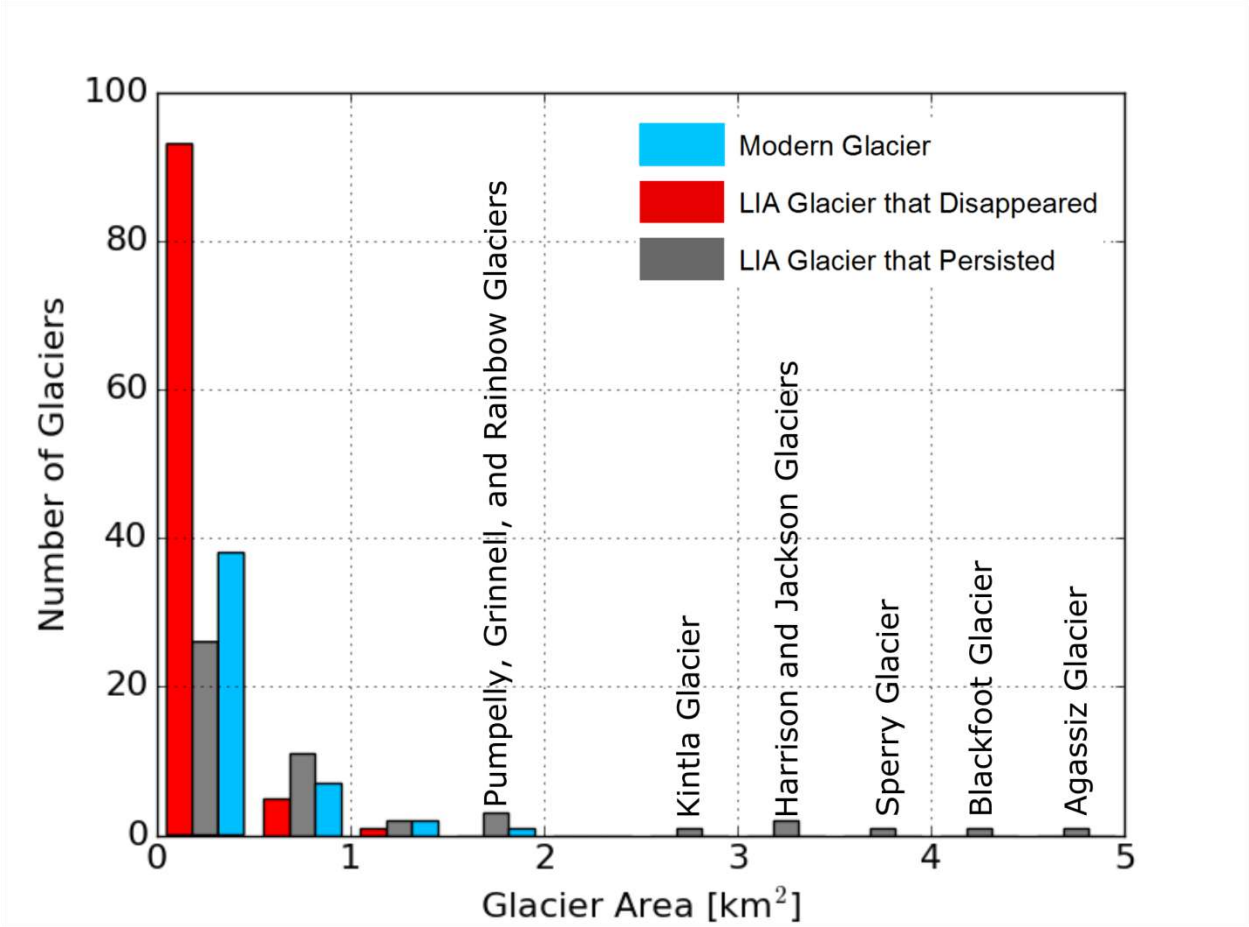

Figure 3. Bar plot showing the size distribution of Little Ice Age (LIA) and modern glaciers. Data for LIA glaciers that disappeared are shown in red (n=98), data for LIA glaciers that persisted are shown in gray (n=49), and data for modern glaciers are shown in blue (n=49). Size classes are grouped by 0.5 km^2 increments. Big (>1.5 km^2) LIA glaciers are named. There is only one modern glacier (Harrison Glacier) bigger than 1.5 km^2.

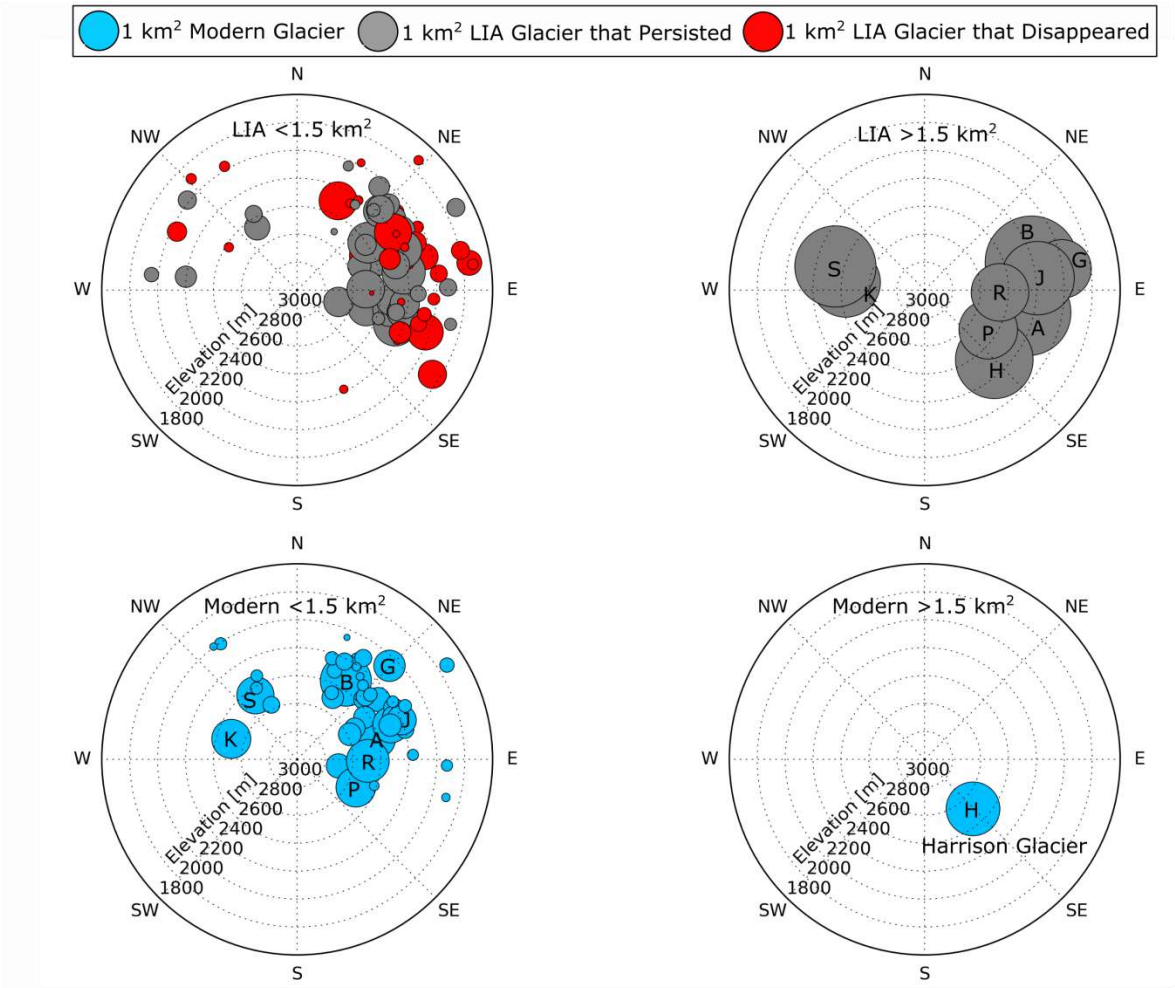

Figure 4. Glacier aspect and elevation plotted on rose diagrams, separated by size class (<1.5 km^2 on the left, >1.5 km^2 on the right) and time (LIA on the top, modern on the bottom). High elevation glaciers plot toward the center and low elevation glaciers plot toward the edge. LIA glaciers that disappeared are plotted in red, LIA glaciers that persisted are plotted in gray, and modern glaciers are plotted in blue, all scaled to size relative to the 1 km^2 circles shown in the legend.

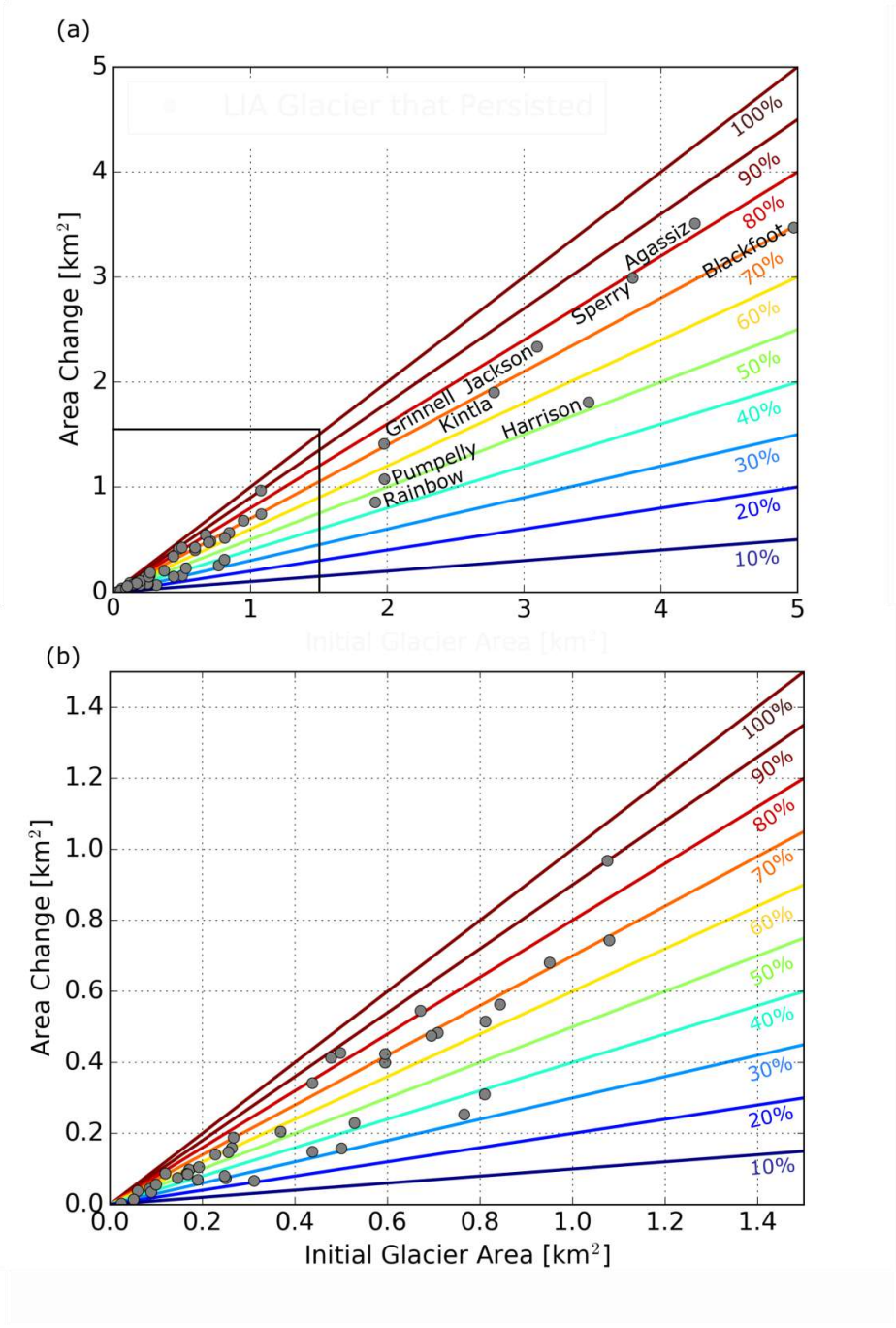

Figure 5. Glacier area change for the 98 LIA glaciers that persisted. (a) Glaciers plot as gray dots by initial LIA glacier area on the x-axis, and glacier area change (LIA area minus modern area) on the y-axis. Relative area change is illustrated by colored lines ranging from 100% (darkest red) to 10% change (darkest blue). Big LIA glaciers > 1.5 km^2 are named. (b) Same as in (a) but only showing small (<1.5 km^2) LIA glaciers.

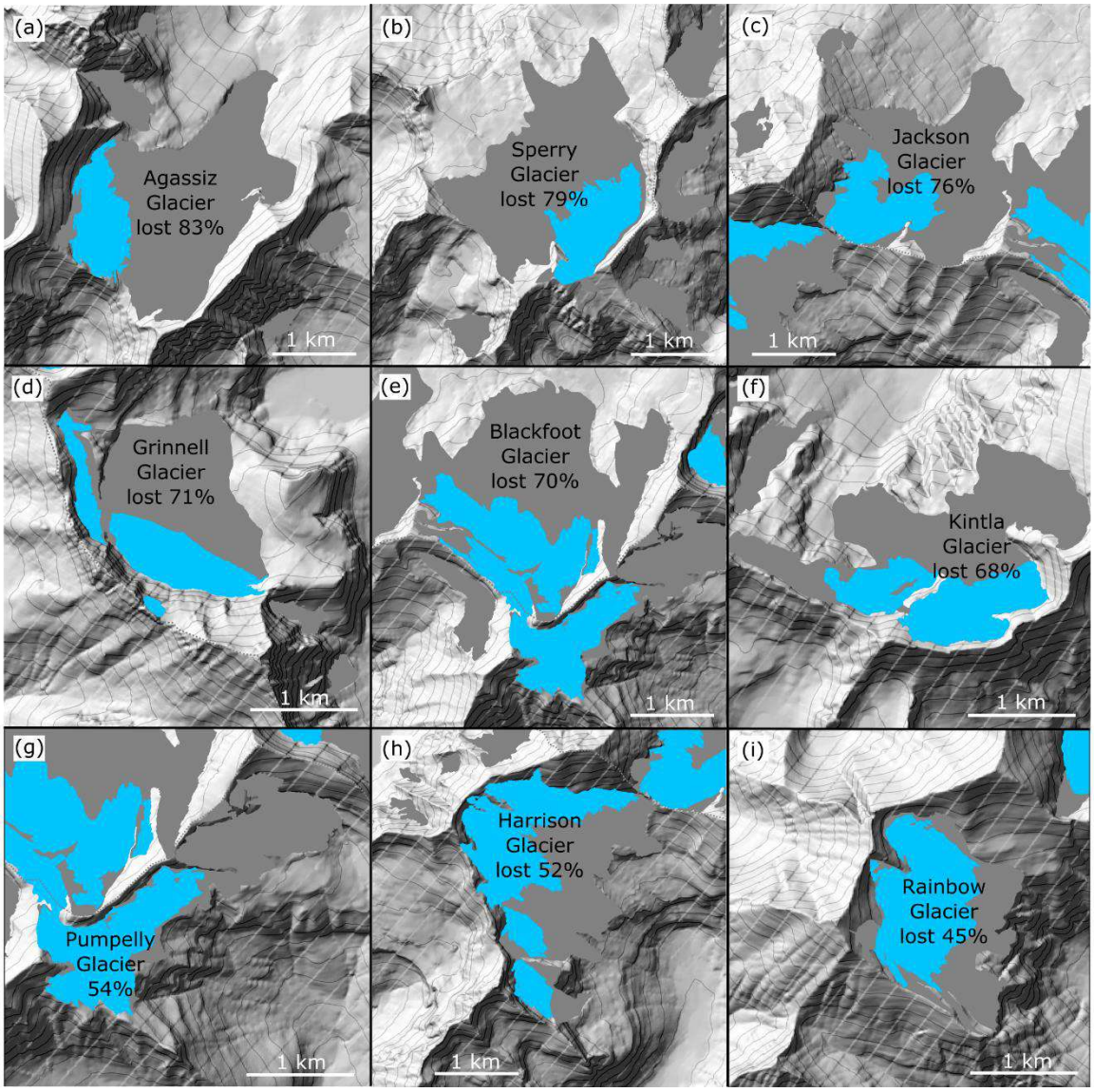

Figure 6. Glacier area change for the nine big (>1.5 km^2) Little Ice Age (LIA) glaciers. Hillshade and elevation contours derived from the National Elevation Dataset are shown beneath LIA glacier (gray) and modern glacier (blue) areas.

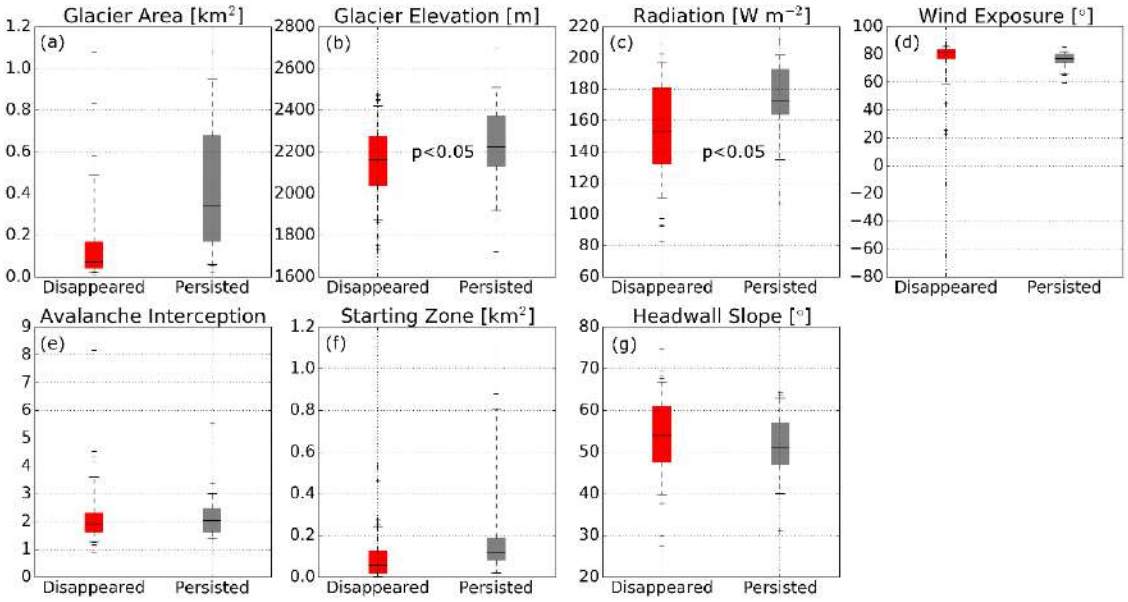

Figure 7. Boxplots of terrain parameters for small (<1.5 km^2) LIA glaciers. Data for the subset of LIA glaciers that disappeared (n=98) are shown in red, and for the subset of LIA glaciers that persisted (n=49) are shown in gray. Boxes extend from the 25th to 75th percentile values, whiskers extend from the 5th to 95th percentile values, and the black horizontal line denotes the median value. (a) Glacier area in km^2, (b) glacier median elevation in m, (c) median radiation across the glacier in W m^{-2}, (d) median wind exposure across the glacier in degrees, (e) avalanche interception index, (f) avalanche starting zone in km^2, (g) and median headwall slope in degrees. T-test results are reported for the parameters (i.e. elevation and radiation) that were normally distributed and that showed statistical differences ($p<0.05$) at the 95% confidence interval between LIA glaciers that disappeared and LIA glaciers that persisted.

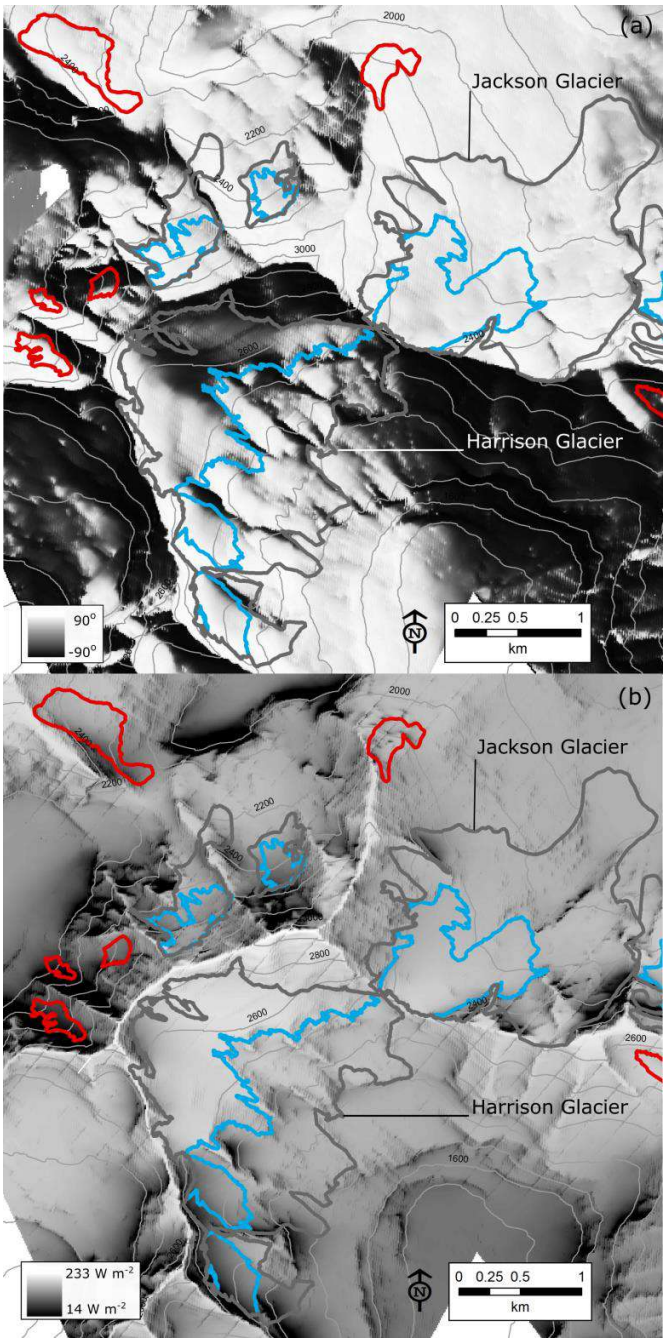

Figure 8. Radiation and wind exposure results for the area near Jackson and Harrison Glaciers. Little Ice Age (LIA) glaciers that disappeared are outlined in red, LIA glaciers that persisted are outlined in gray, and modern glaciers are outlined in blue. (a) Wind exposure results show areas exposed to southwest winds as dark (and therefore likely to be wind scoured), and areas sheltered from southwest winds (and therefore likely to be wind loaded) as light. (b) Clear sky radiation results show areas that receive high amounts of radiation as light and low amounts of radiation (shaded) as dark.

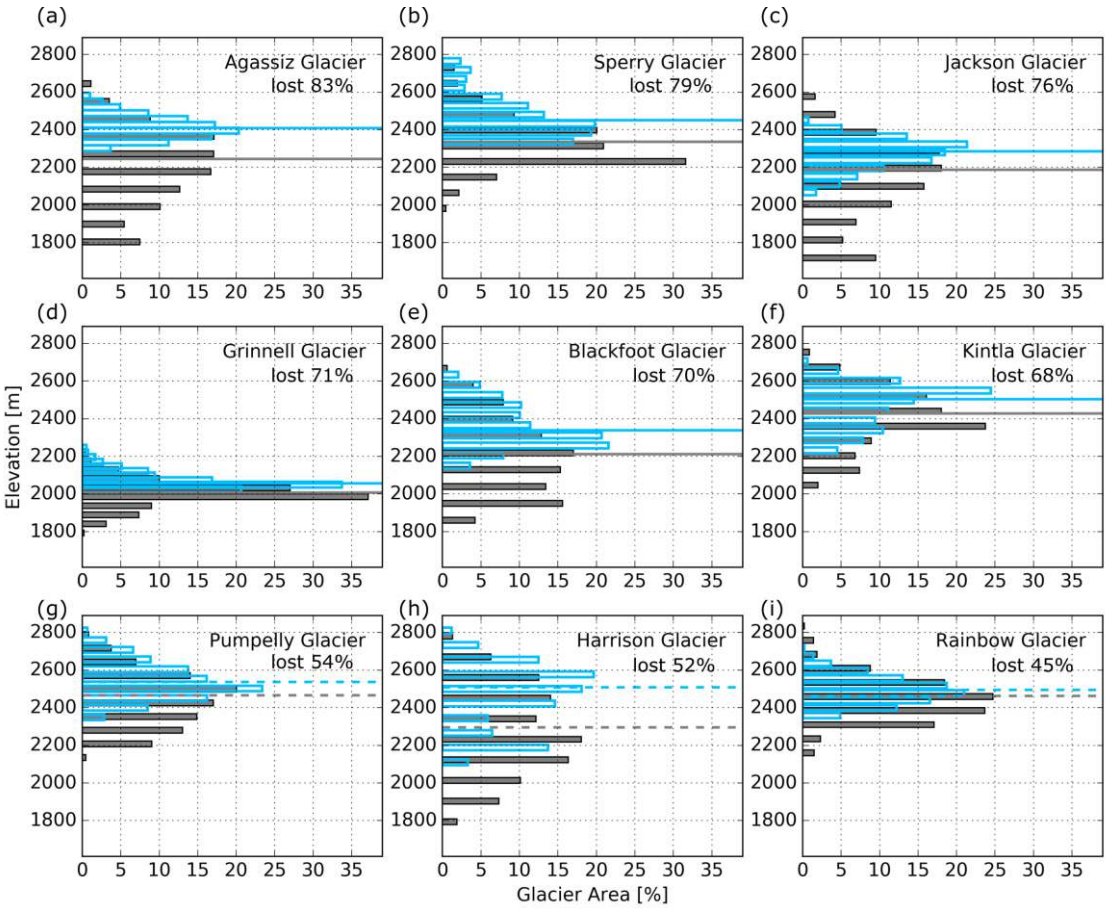

Figure 9. Elevation distribution of big (LIA area >1.5 km^2) glaciers. LIA glacier hypsometry is plotted in gray, and modern glacier hypsometry is plotted in blue. Percentage area loss is noted, and each glacier is named. Median glacier elevation at the LIA is plotted as a horizontal gray line, and median glacier elevation at the modern is plotted as a horizontal blue line. Median elevation lines are dotted for the three glaciers (Pumpelly, Harrison, and Rainbow) that lost less than 55% area. Median elevations for these nine glaciers are reported in Table 1.

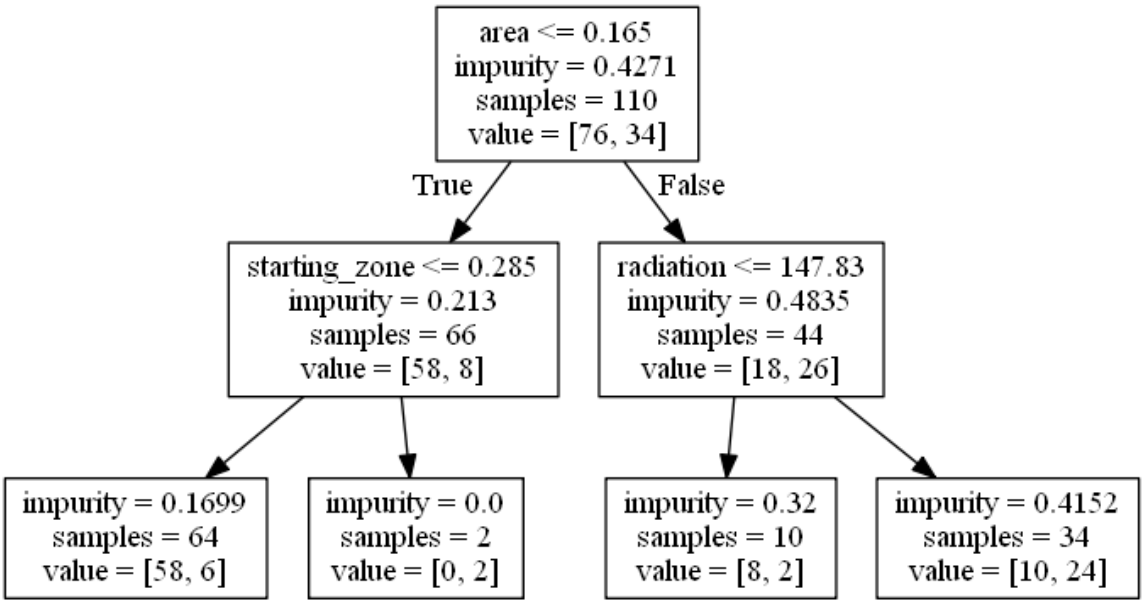

Figure 10. Classification and regression tree (10-fold cross validated), trained on LIA glacier disappearance (True) and persistence (False) for a training subset (n=119) of the small (<1.5 km^2) LIA glaciers. The impurity value reflects the Gini cost function used to evaluate splits in the dataset. Impurity = 0.0 indicates a perfect split. Samples indicate the number of glaciers in each node. Values indicates the number of true samples (LIA glaciers that disappeared) and the number of false samples (LIA glaciers that persisted) within each node. Glacier area ("area") and avalanche starting zone ("starting_zone") are reported in km^2. Radiation is reported in W m^{-2}.

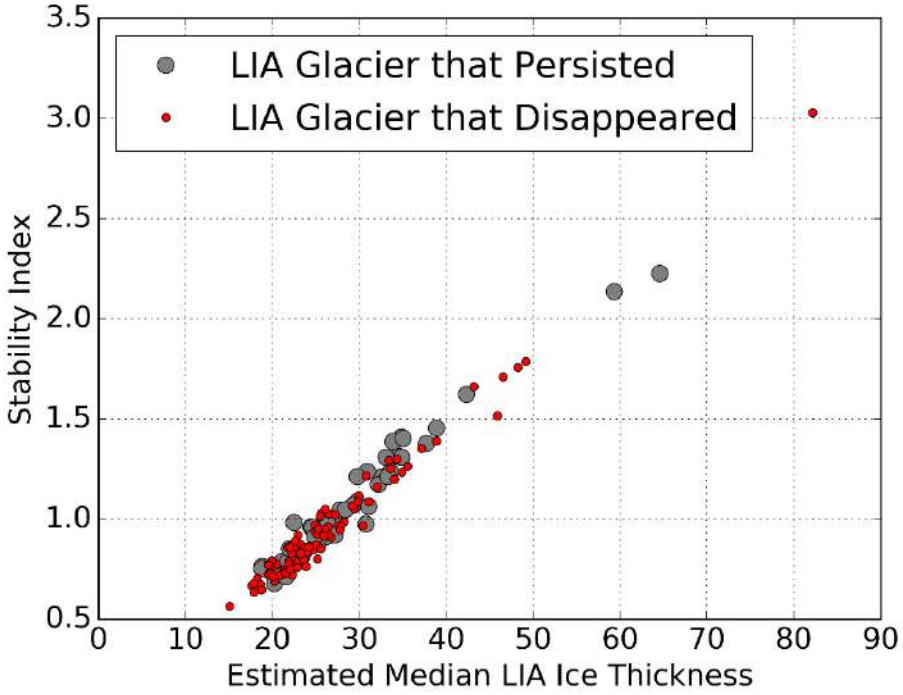

Figure 11. Estimated median LIA glacier ice thickness versus stability index (described in the text). LIA glaciers that disappeared are plotted in red, and LIA glaciers that persisted are plotted in gray. This plot shows that a uniform melt rate, scaled only by elevation, cannot explain the observed pattern of LIA glacier disappearance.

Tables

	Median Elevation			Median Aspect		
	LIA [m]	Modern [m]	Δ [m]	LIA [°]	Modern [°]	Δ [°]
Agassiz Glacier	2244	2408	+164	102	76	26 to N
Sperry Glacier	2336	2450	+213	285	327	42 to N
Jackson Glacier	2187	2285	+98	84	70	14 to N
Grinnell Glacier	2007	2057	+50	81	45	36 to N
Blackfoot Glacier	2211	2338	+127	75	32	43 to N
Kintla Glacier	2429	2505	+76	276	287	11 to N
Pumpelly Glacier	2465	2537	+72	122	115	7 to N
Harrison Glacier	2296	2508	+212	135	136	1 to S
Rainbow Glacier	2463	2493	+30	92	91	1 to N

Table 1. Elevation and aspect of the big (>1.5 km^2) LIA glaciers. Median glacier elevation and median glacier aspect are listed for each LIA and modern glacier. Changes (Δ) in median elevation and median aspect from the LIA to modern are also listed.

		Predictable Controls			Topographic Controls			
		Elevation	Area	Av Start	Av Int	H Slope	Radiation	Wind
		m	km^2	m^2	unitless	°	$W\ m^{-2}$	°
LIA Disapp. n=98	Median	2162	0.07	0.06	1.93	54	153	81
	Std	172	0.19	0.09	0.92	9	31	20
	Max	2476	1.08	0.53	8.16	75	209	87
	Min	1729	0.01	0.00	0.88	27	62	-65
LIA Persisted n=49	Median	2227	0.31	0.12	2.04	51	174	77
	Std	194	0.30	0.27	0.74	8	24	6
	Max	2694	1.08	1.08	5.53	64	212	85
	Min	1721	0.02	0.00	1.27	31	107	59
	p-val	<0.05					<0.05	

Table 2. Parameter statistics for small (<1.5 km^2) LIA glaciers. T-test results are reported for the parameters (i.e. elevation and radiation) that were normally distributed and that showed statistical differences ($p<0.05$) at the 95% confidence interval between LIA glaciers that disappeared and LIA glaciers that persisted.

	Elevation	Area	Radiation	Wind	Av Int	H Slope	Av Start
Elevation	1.00	0.17	**0.65**	-0.18	-0.28	-0.44	-0.24
LIA Area		1.00	0.47	-0.60	0.23	-0.28	0.59
Radiation			1.00	-0.53	-0.18	**-0.77**	0.17
Wind				1.00	-0.21	0.30	-0.48
Av Int					1.00	0.50	-
H Slope						1.00	-0.31
Av Start							1.00

Table 3. Spearman correlation coefficients computed for LIA glacier parameters (n=147). Only statistically significant ($p<0.05$) correlations are reported. Strong correlations ($r>0.60$) are in bold.

		Observed (n=28)	
		Disappeared (n=18)	Persisted (n=10)
Predicted	Disappeared	**17**	5
	Persisted	1	**5**

Table 4. Confusion matrix for 10-fold cross validated classification tree shown in Figure 10. Bold values indicate correct prediction. The tree was 79% accurate (22 out of 28 predictions correct) when applied to the 28-glacier test sample.

APPENDIX A

RADIOSTRATIGRAPHY TRACED LAYERS

This appendix acts as repository for figures showing east-west running Operation IceBridge (OIB) radargrams by Leuschen (2001) with traced radar layers. Figures for this Appendix and Appendices C and B are presented from north to south, titled by OIB transect number, with #1 being the northernmost flightline depicted in Figure 1 of Chapter 1. OIB names are listed in Table 1. Layer tracing, radar data processing, and plotting were performed according to methods outlined in the main text. IceBridge ice surface (gray) and bedrock (brown) are plotted, as are traced layers (blue). The white line approximately half way through the ice columns is a surface multiple, an artifact from radar data collection. Coordinates for this Appendix and for Appendices B and C are in polar stereographic projection (true latitude 70°, central meridian -45°).

Leuschen, C. (2011). IceBridge MCoRDS L1B Geolocated Radar Echo Strength Profiles, Version 2, Boulder, Colorado USA, NASA Snow and Ice Data Center Distributed Active Archive Center. doi:http://dx.doi.org/10.5067/90S1XZRBAX5N.

OIB #	OIB Name
01	Data_20110416_02_005
02	Data_20110413_02_004
03	Data_20110413_02_008
04	Data_20110413_02_012
05	Data_20110416_02_007
06	Data_20110413_02_016
07	Data_20110413_02_020
08	Data_20110413_02_024
09	Data_20110416_02_011
10	Data_20110413_02_028
11	Data_20110413_03_003
12	Data_20110413_03_007
13	Data_20110416_02_015
14	Data_20110413_03_011
15	Data_20110413_03_015
16	Data_20110413_03_019
17	Data_20110416_03_019
18	Data_20110413_02_002
19	Data_20110413_02_006
20	Data_20110413_02_010
21	Data_20110413_02_014
22	Data_20110413_02018
23	Data_20110413_02_022
24	Data_20110413_02_026
25	Data_20110416_02_009
26	Data_20110413_02_030
27	Data_20110413_03_005
28	Data_20110413_03_009
29	Data_20110416_02_013
30	Data_20110413_03_013
31	Data_20110413_03_017
32	Data_20110413_03_021
33	Data_20110416_02_017
34	Data_20110408_20_001
35	Data_20110408_21_001
36	Data_20110408_22_001
37	Data_20110416_02_021 – No layers traced
38	Data_20110408_20_005
39	Data_20110408_21_005
40	Data_20110408_22_004
41	Data_20110416_02_025

Table 1. Operation IceBridge (OIB) flightline numbers and names.

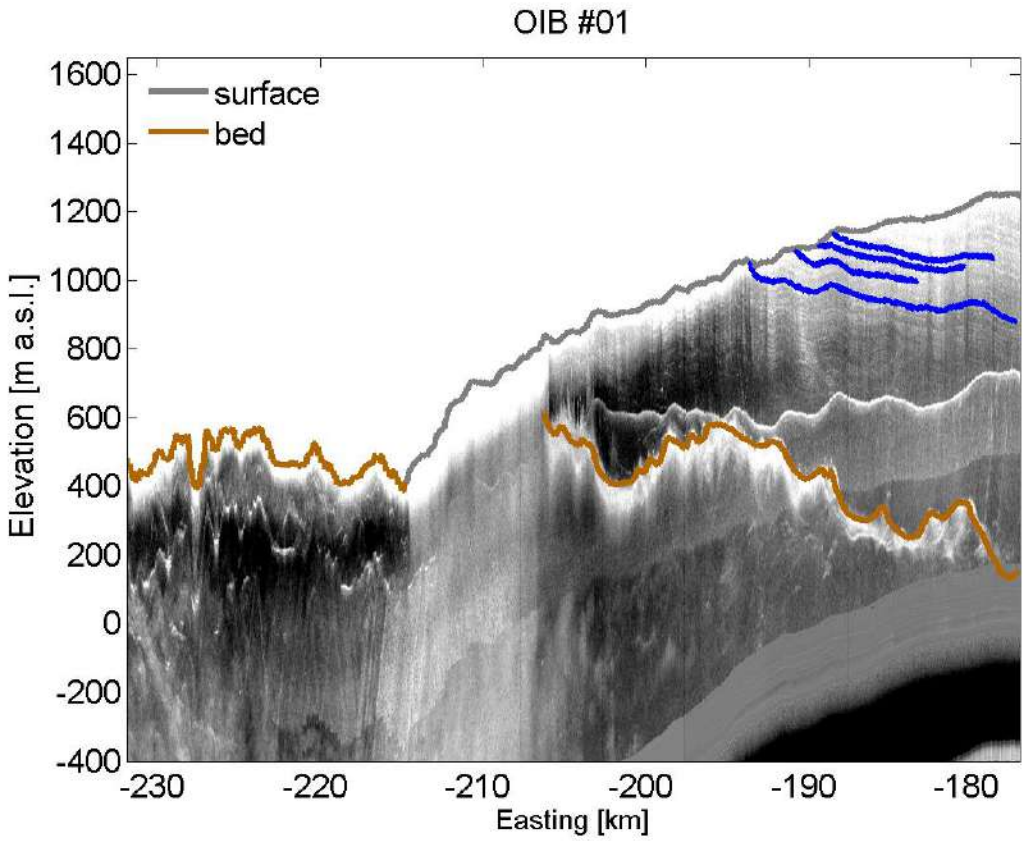
OIB #01
surface
bed
1600
1400
1200
1000
800
600
400
200
0
-200
-400
Elevation [m a.s.l.]
-230
-220
-210
-200
-190
-180
Easting [km]

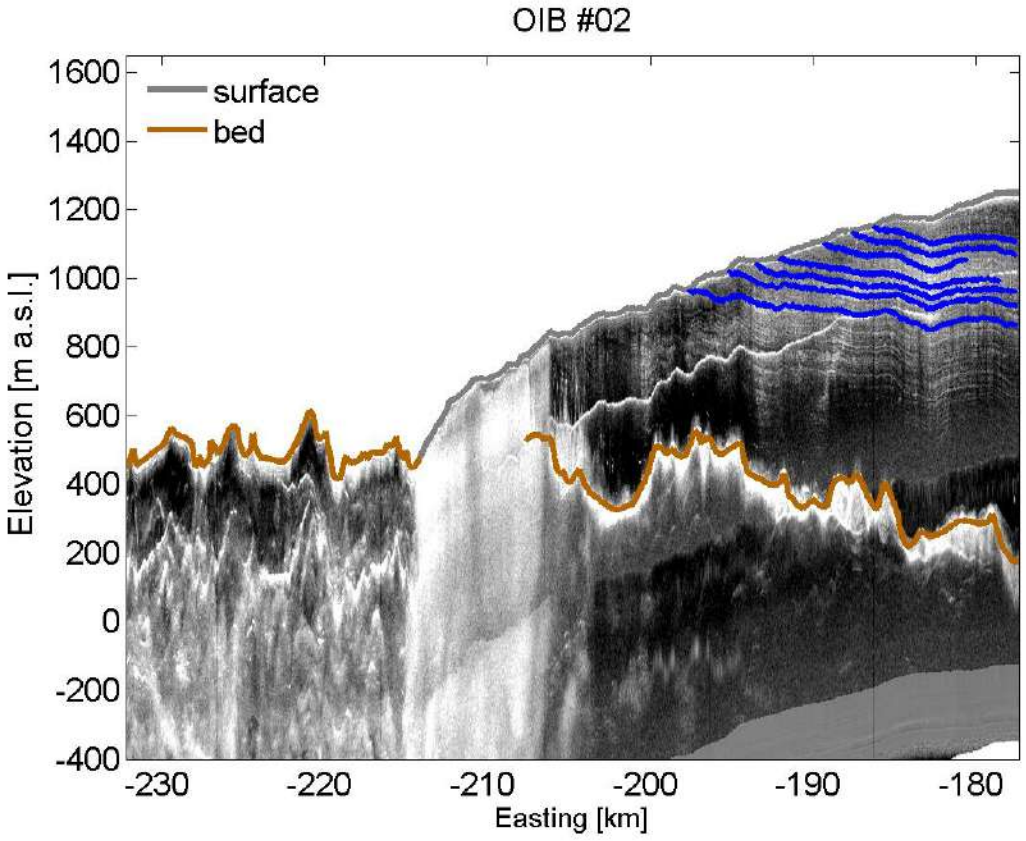
OIB #02
surface
bed
1600
1400
1200
1000
800
600
400
200
0
-200
-400
Elevation [m a.s.l.]
-230
-220
-210
-200
-190
-180
Easting [km]

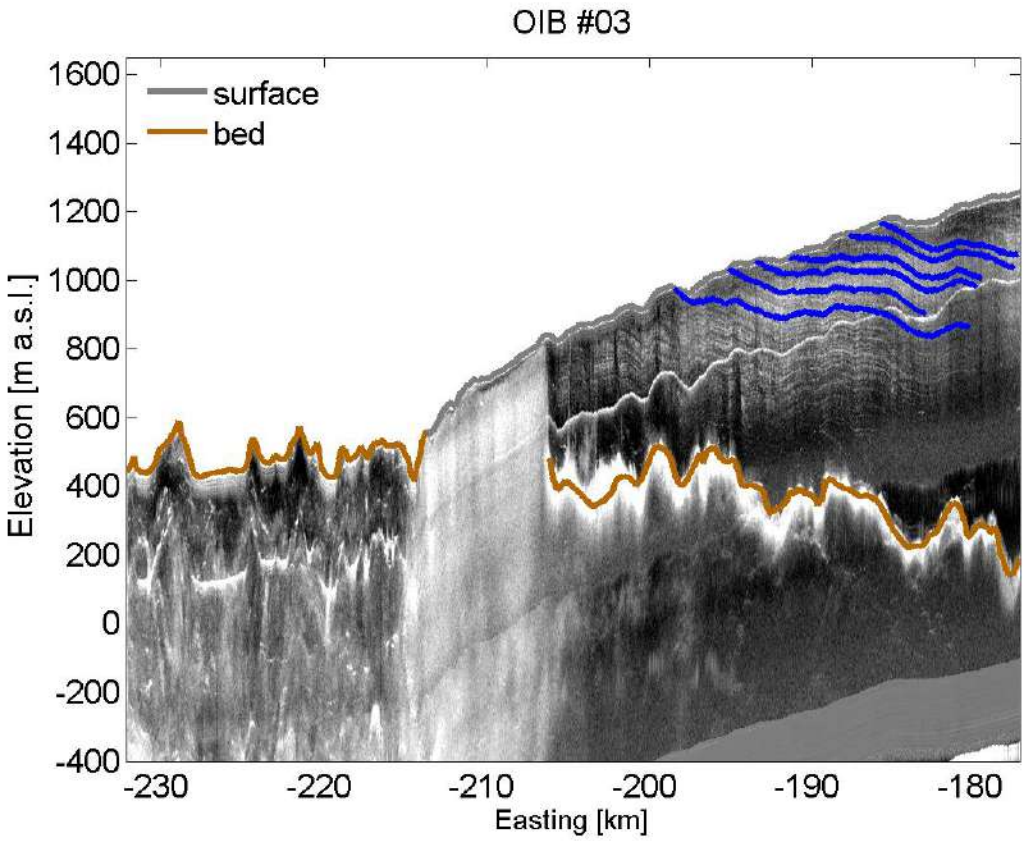
OIB #03
surface
bed
1600
1400
1200
1000
800
600
400
200
0
-200
-400
Elevation [m a.s.l.]
-230
-220
-210
-200
-190
-180
Easting [km]

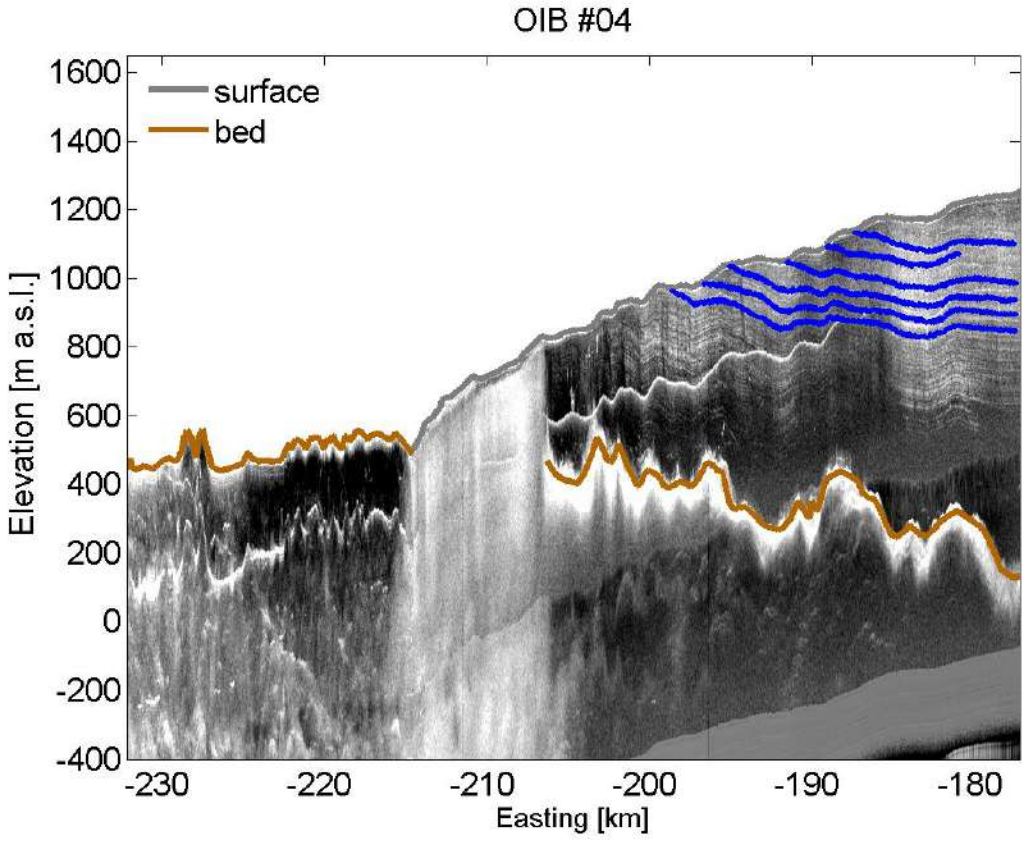
OIB #04
surface
bed
1600
1400
1200
1000
800
600
400
200
0
-200
-400
Elevation [m a.s.l.]
-230
-220
-210
-200
-190
-180
Easting [km]

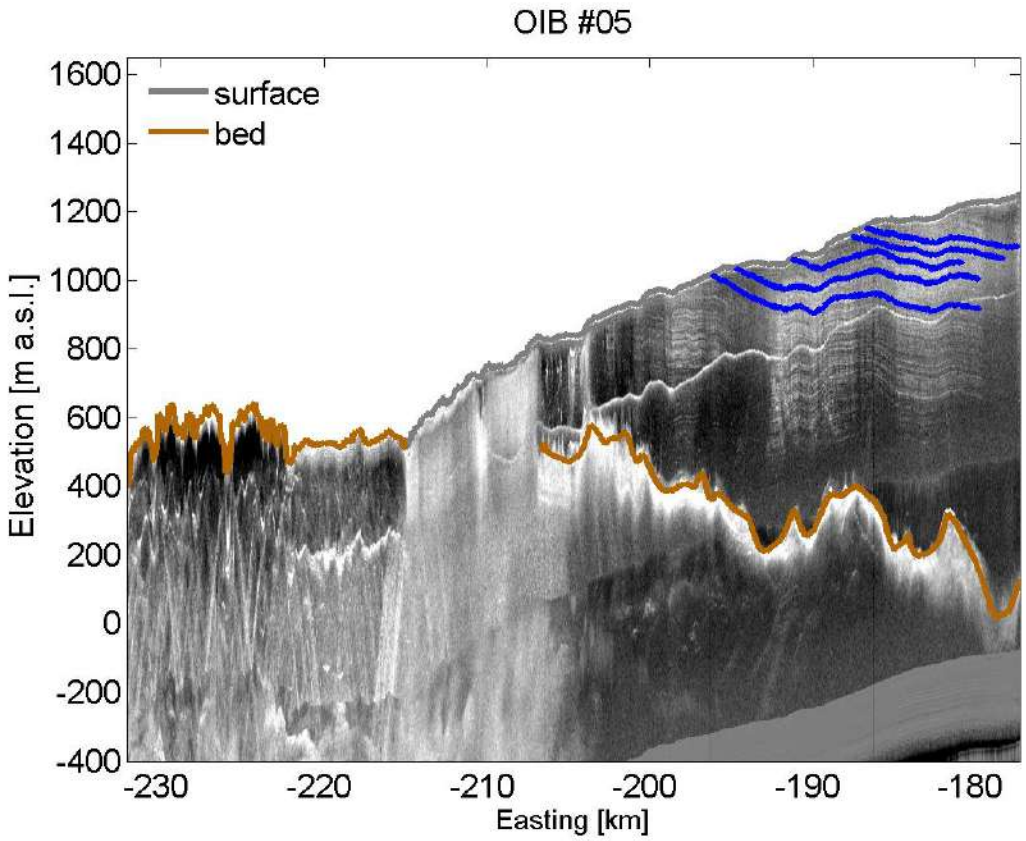
OIB #05
surface
bed
1600
1400
1200
1000
800
600
400
200
0
-200
-400
Elevation [m a.s.l.]
-230
-220
-210
-200
-190
-180
Easting [km]

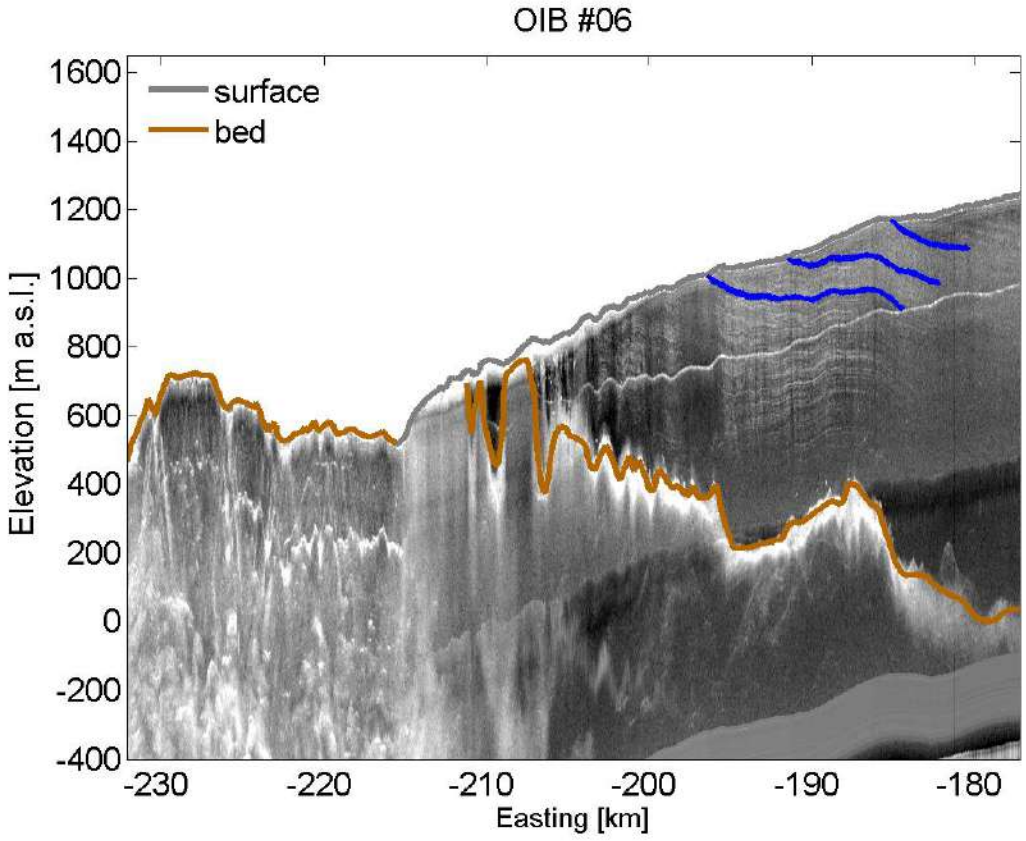
OIB #06
surface
bed
1600
1400
1200
1000
800
600
400
200
0
-200
-400
Elevation [m a.s.l.]
-230
-220
-210
-200
-190
-180
Easting [km]

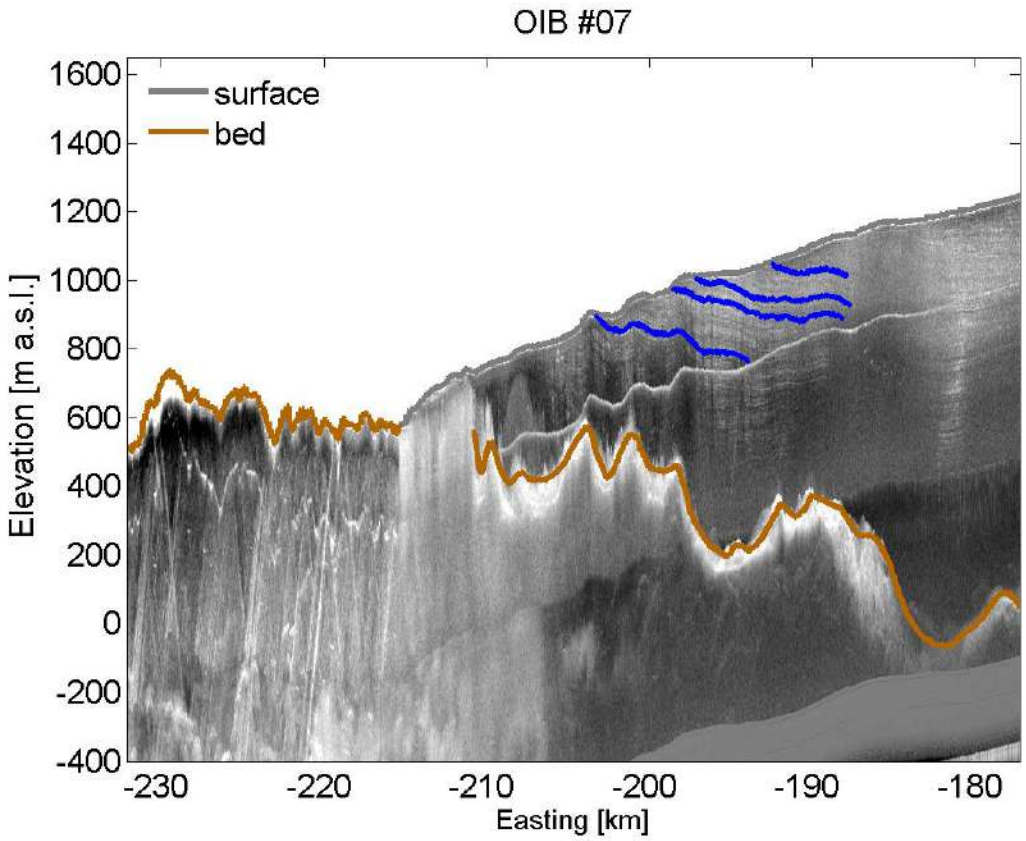
OIB #07
surface
bed
1600
1400
1200
1000
800
600
400
200
0
-200
-400
Elevation [m a.s.l.]
-230
-220
-210
-200
-190
-180
Easting [km]

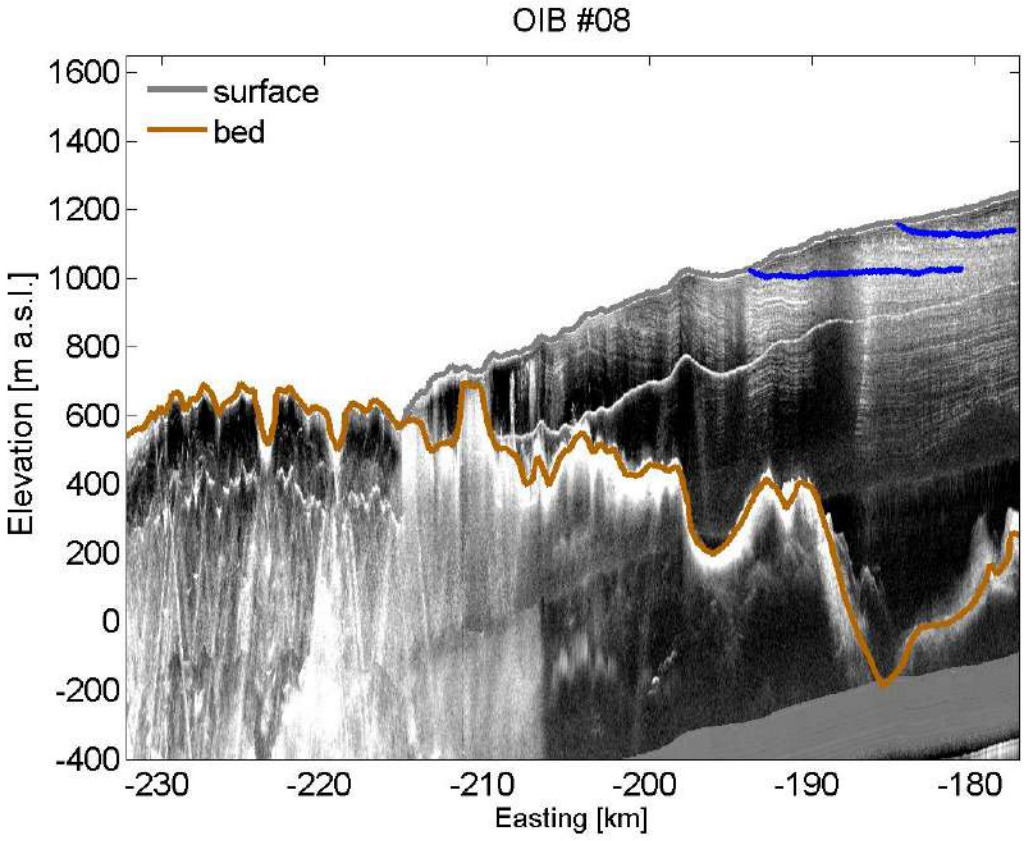
OIB #08
surface
bed
1600
1400
1200
1000
800
600
400
200
0
-200
-400
Elevation [m a.s.l.]
-230
-220
-210
-200
-190
-180
Easting [km]

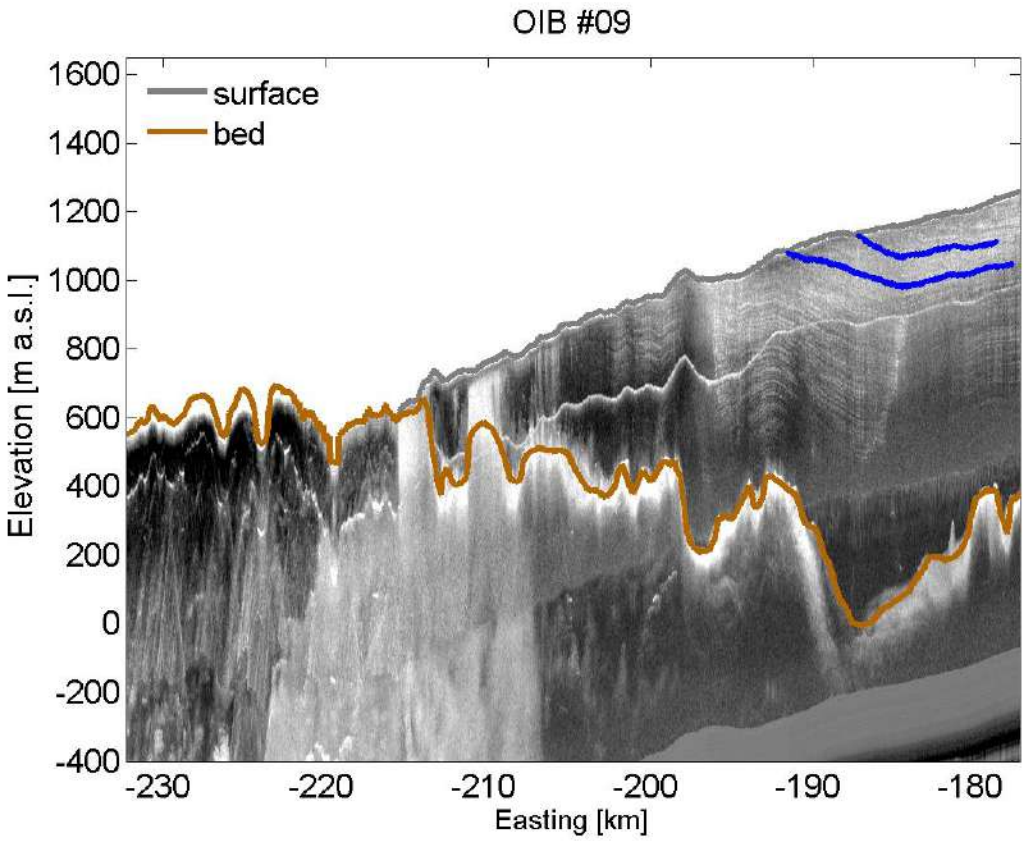
OIB #09
surface
bed
1600
1400
1200
1000
800
600
400
200
0
-200
-400
Elevation [m a.s.l.]
-230
-220
-210
-200
-190
-180
Easting [km]

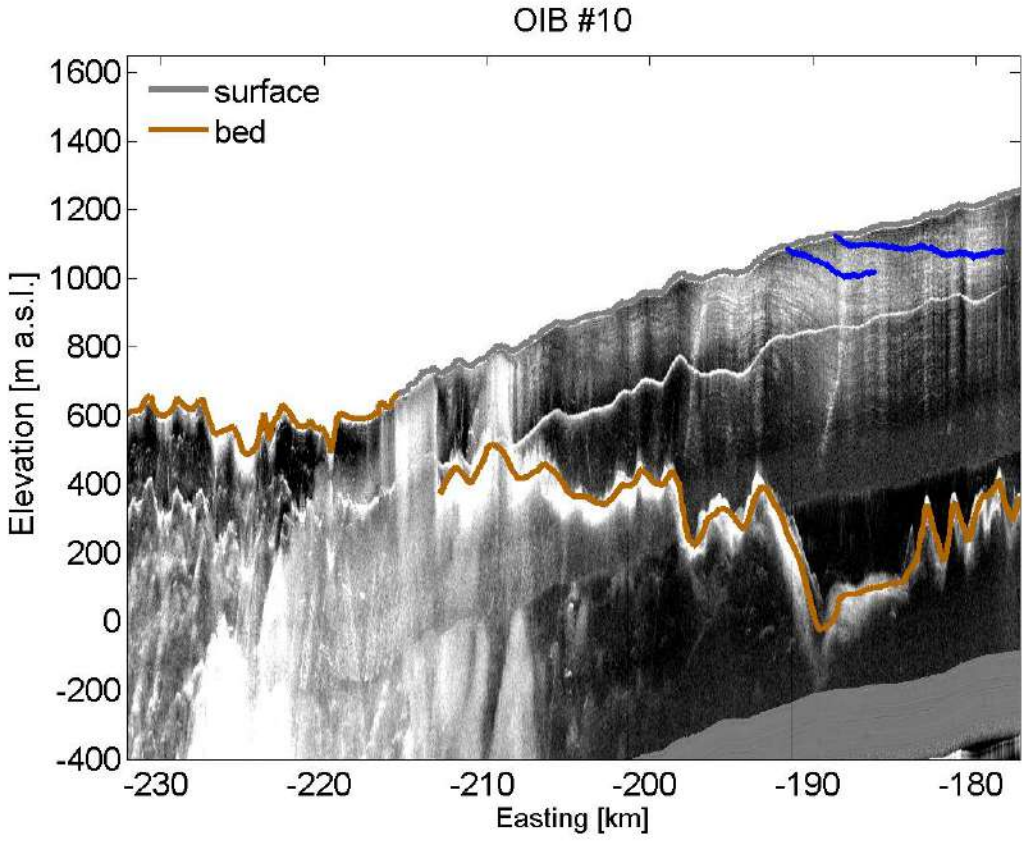
OIB #10
surface
bed
1600
1400
1200
1000
800
600
400
200
0
-200
-400
Elevation [m a.s.l.]
-230
-220
-210
-200
-190
-180
Easting [km]

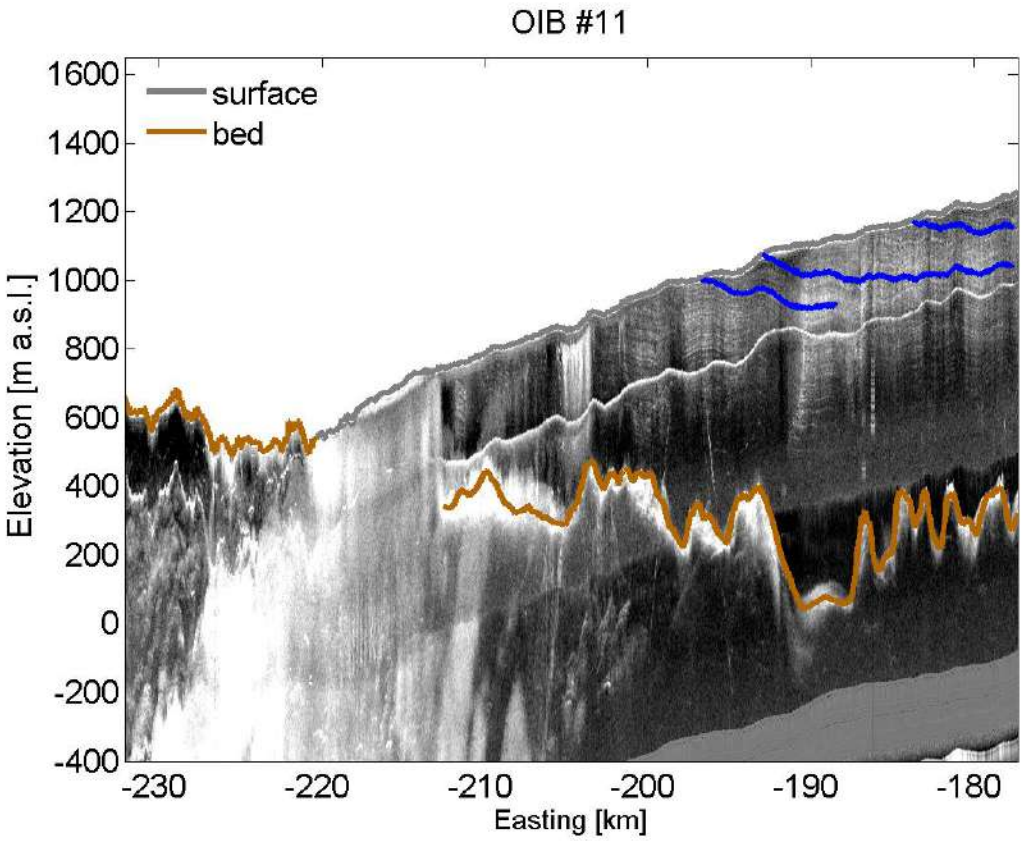
OIB #11
surface
bed
1600
1400
1200
1000
800
600
400
200
0
-200
-400
Elevation [m a.s.l.]
-230
-220
-210
-200
-190
-180
Easting [km]

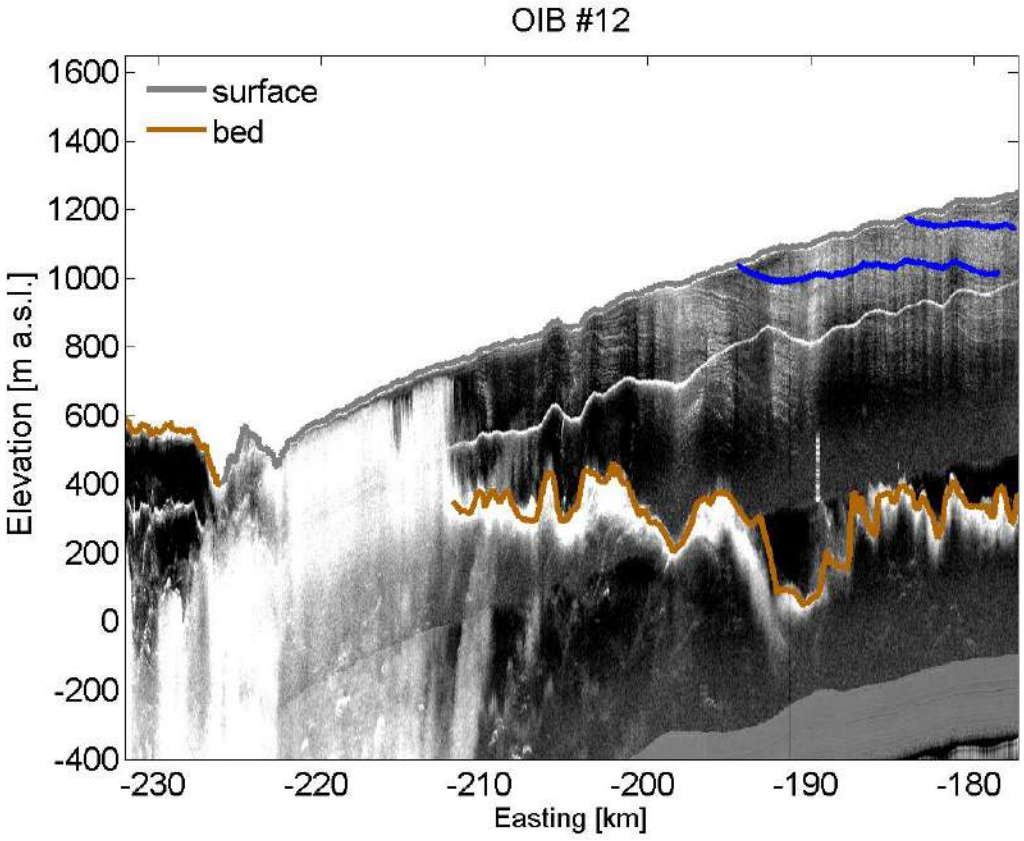
OIB #12
surface
bed
1600
1400
1200
1000
800
600
400
200
0
-200
-400
Elevation [m a.s.l.]
-230
-220
-210
-200
-190
-180
Easting [km]

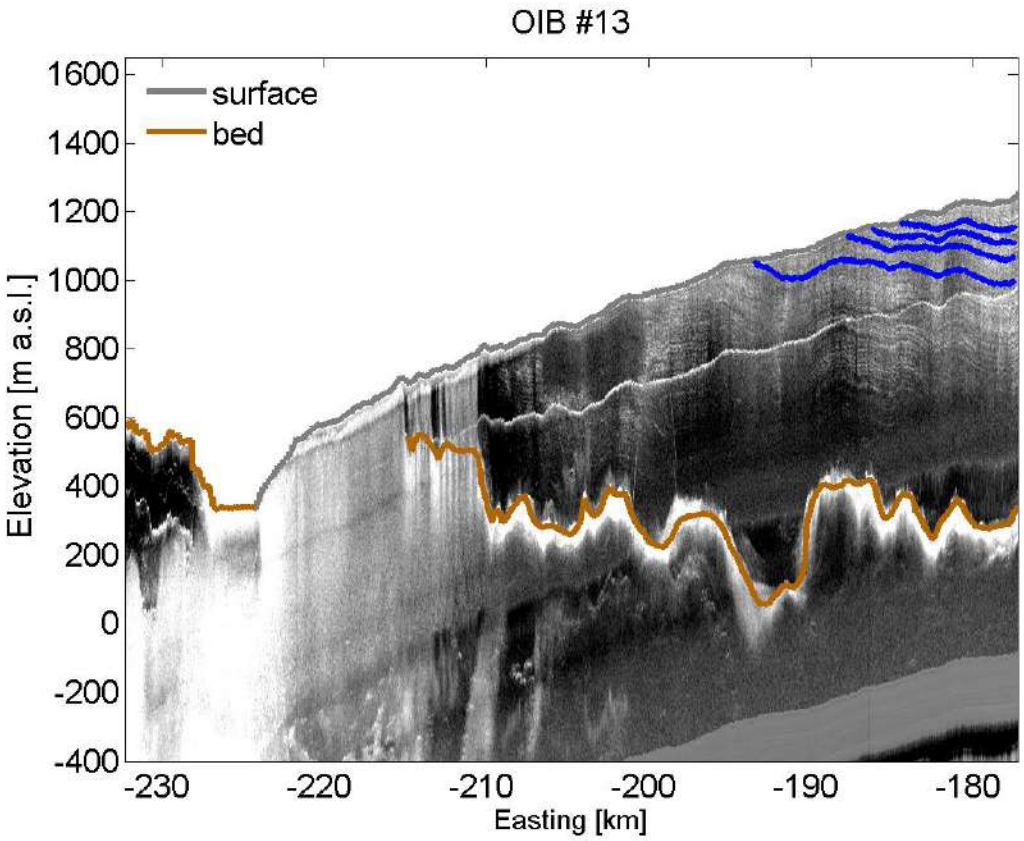
OIB #13
surface
bed
1600
1400
1200
1000
800
600
400
200
0
-200
-400
Elevation [m a.s.l.]
-230
-220
-210
-200
-190
-180
Easting [km]

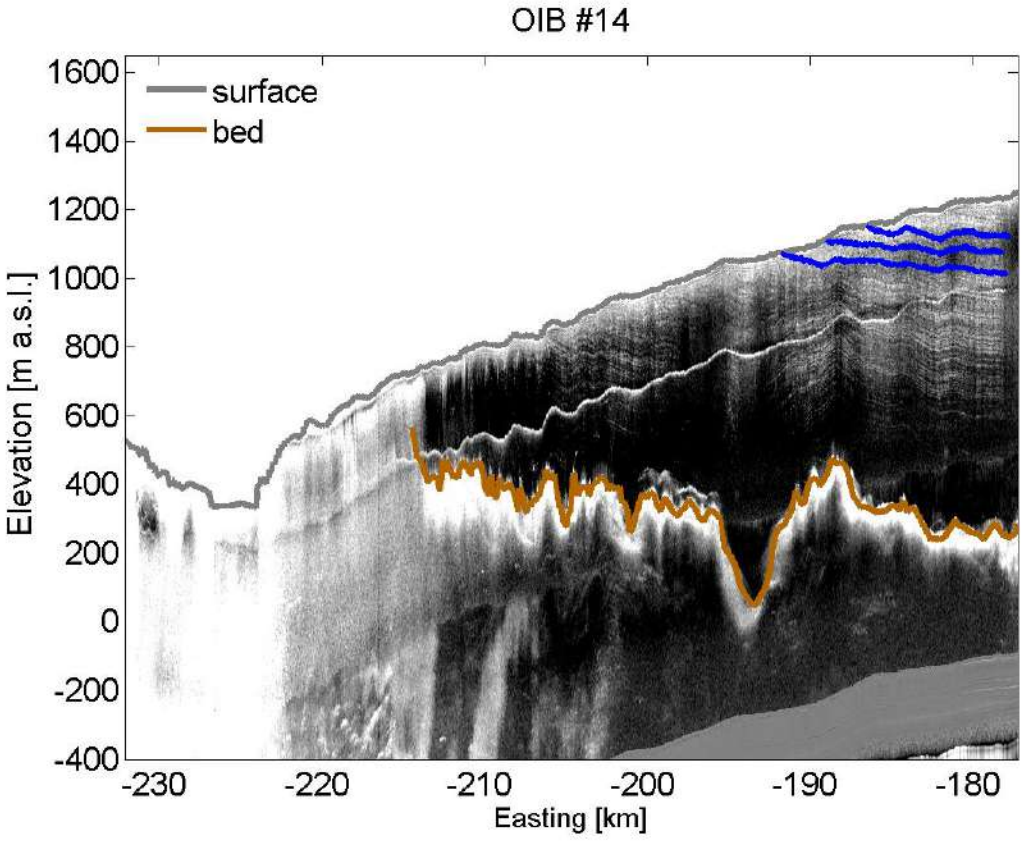
OIB #14
surface
bed
1600
1400
1200
1000
800
600
400
200
0
-200
-400
Elevation [m a.s.l.]
-230
-220
-210
-200
-190
-180
Easting [km]

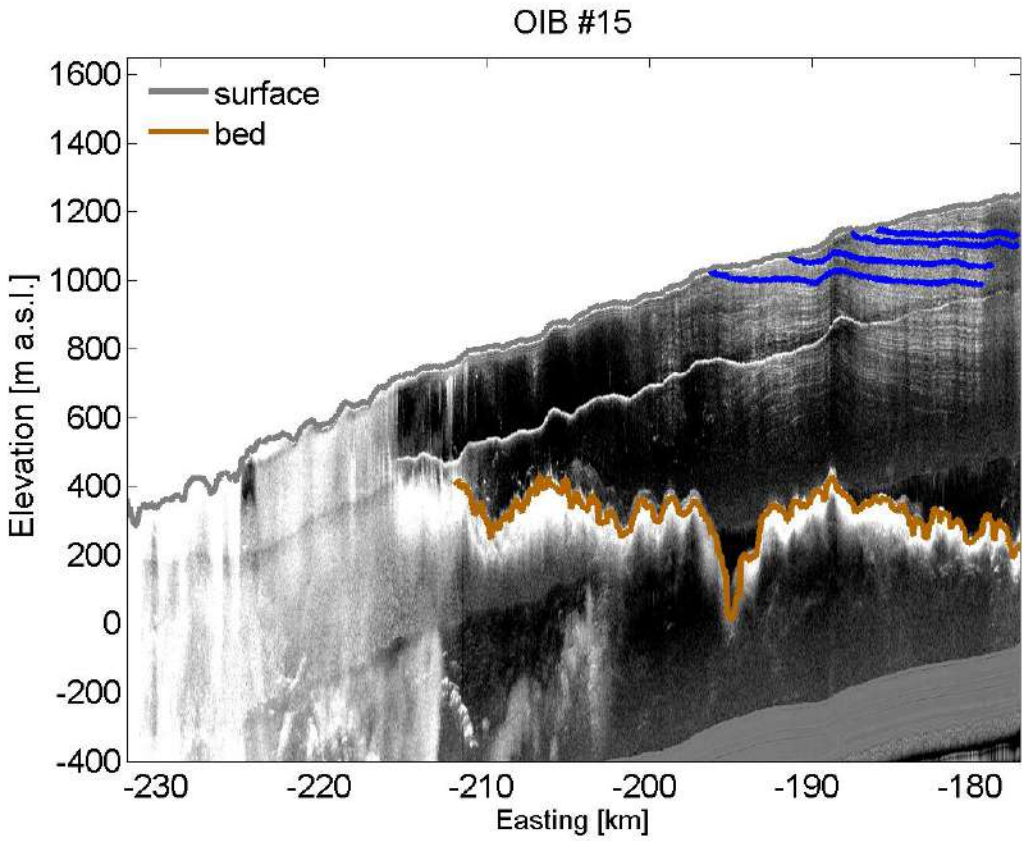
OIB #15
surface
bed
1600
1400
1200
1000
800
600
400
200
0
-200
-400
Elevation [m a.s.l.]
-230
-220
-210
-200
-190
-180
Easting [km]

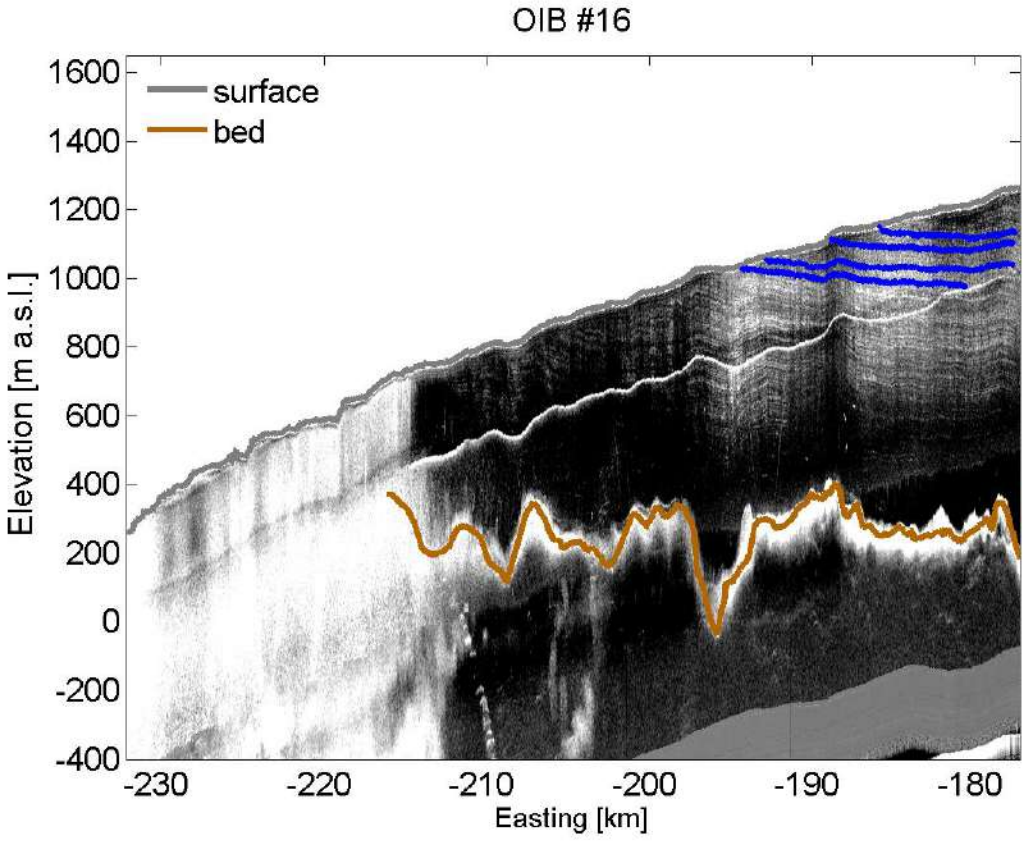
OIB #16
surface
bed
1600
1400
1200
1000
800
600
400
200
0
-200
-400
Elevation [m a.s.l.]
-230
-220
-210
-200
-190
-180
Easting [km]

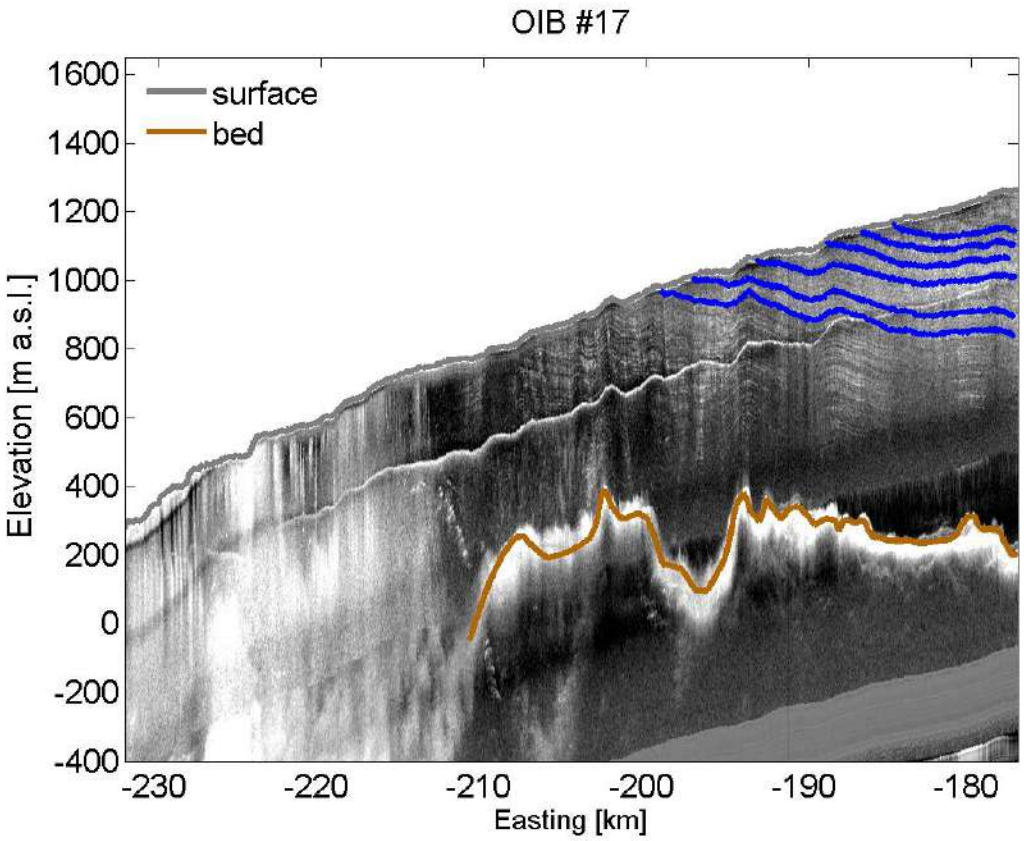
OIB #17
surface
bed
1600
1400
1200
1000
800
600
400
200
0
-200
-400
Elevation [m a.s.l.]
-230
-220
-210
-200
-190
-180
Easting [km]

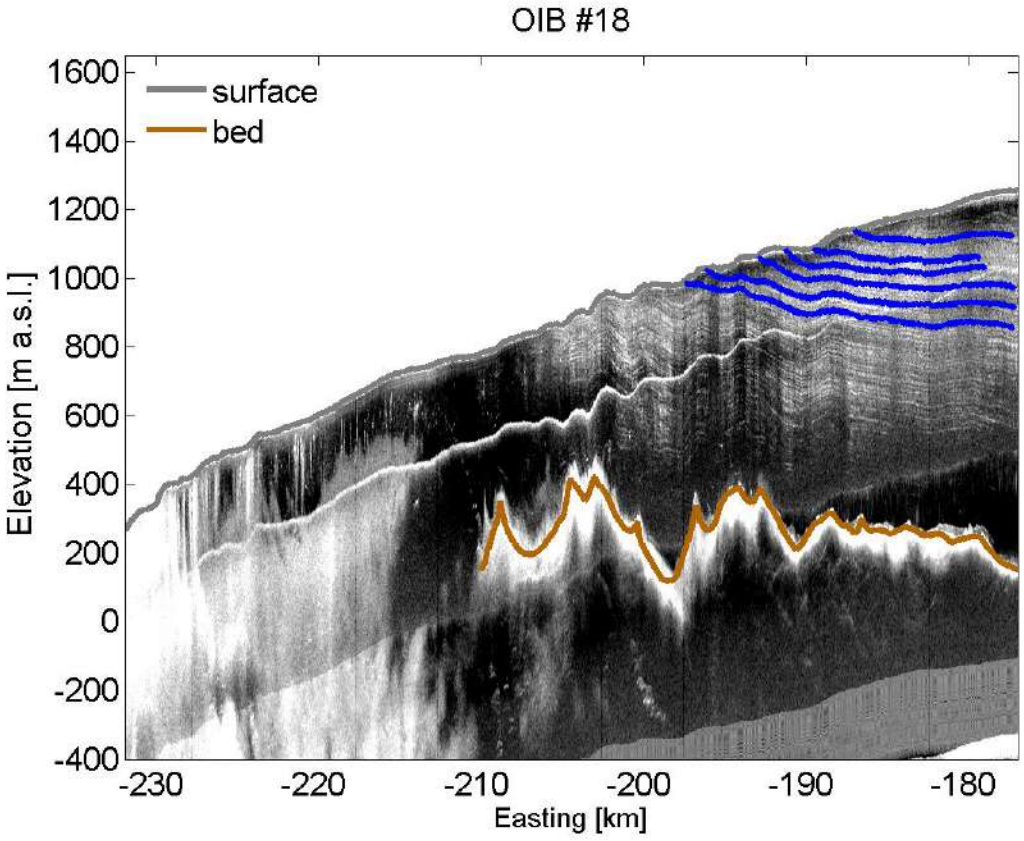
OIB #18
surface
bed
1600
1400
1200
1000
800
600
400
200
0
-200
-400
Elevation [m a.s.l.]
-230
-220
-210
-200
-190
-180
Easting [km]

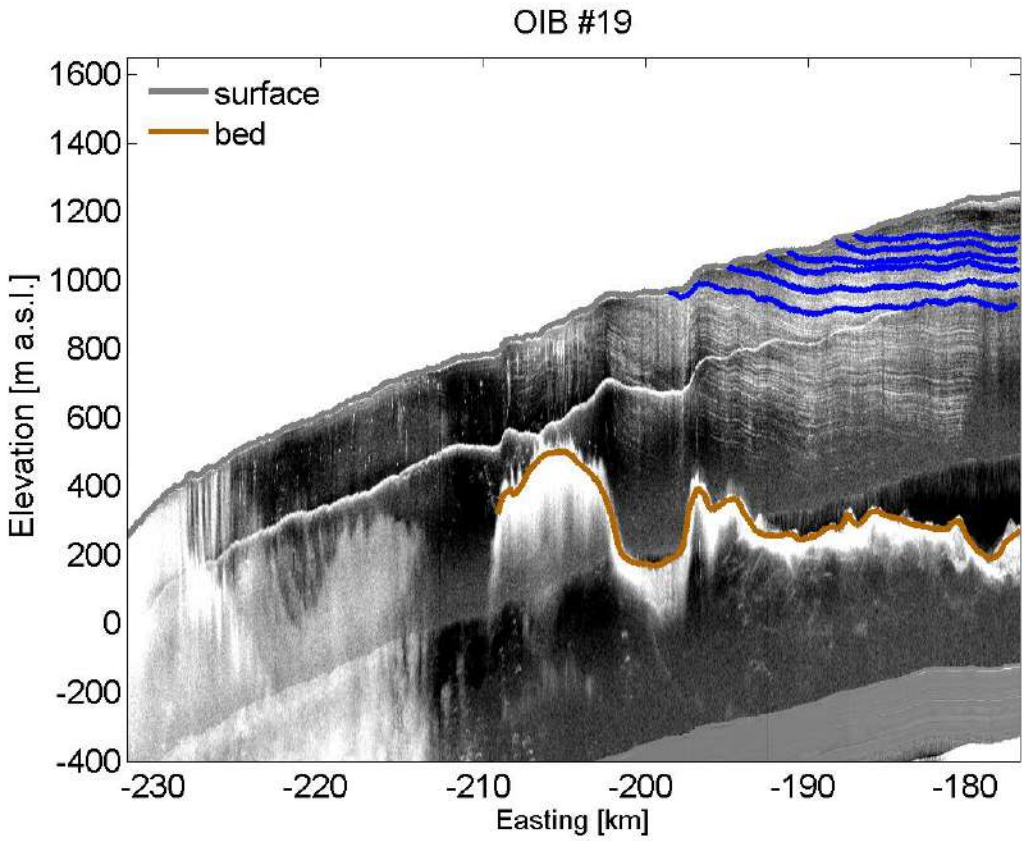
OIB #19
surface
bed
1600
1400
1200
1000
800
600
400
200
0
-200
-400
Elevation [m a.s.l.]
-230
-220
-210
-200
-190
-180
Easting [km]

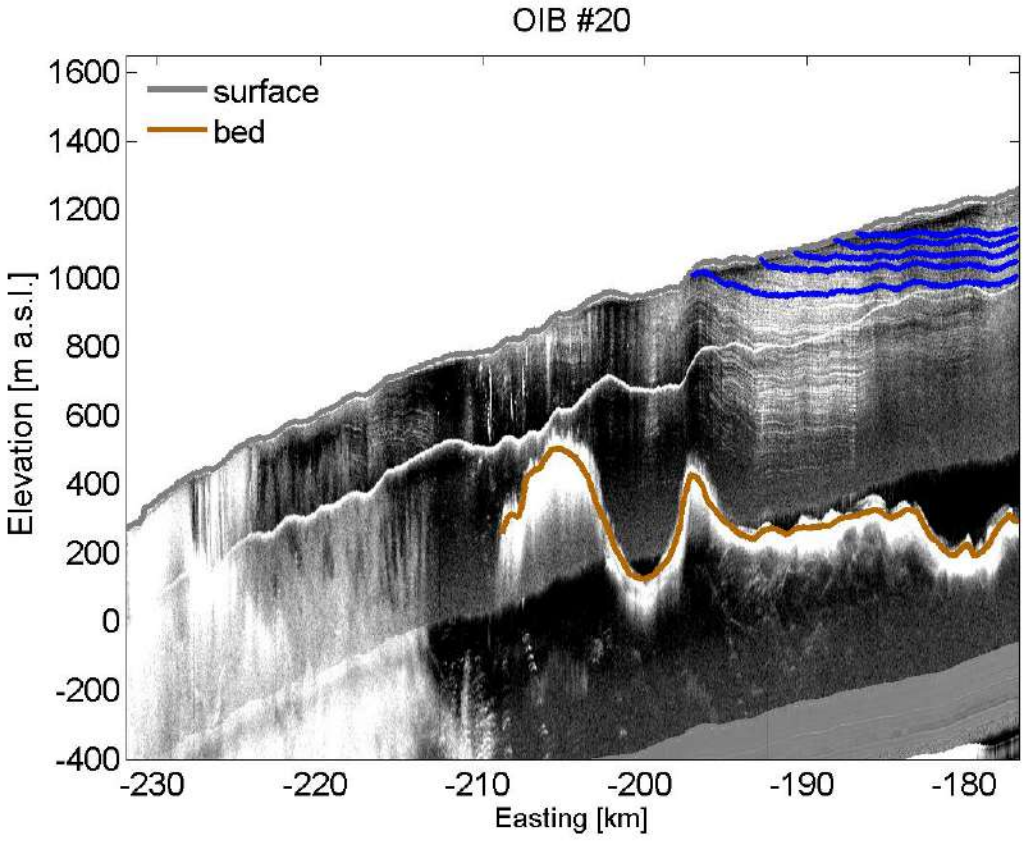
OIB #20
surface
bed
1600
1400
1200
1000
800
600
400
200
0
-200
-400
Elevation [m a.s.l.]
-230
-220
-210
-200
-190
-180
Easting [km]

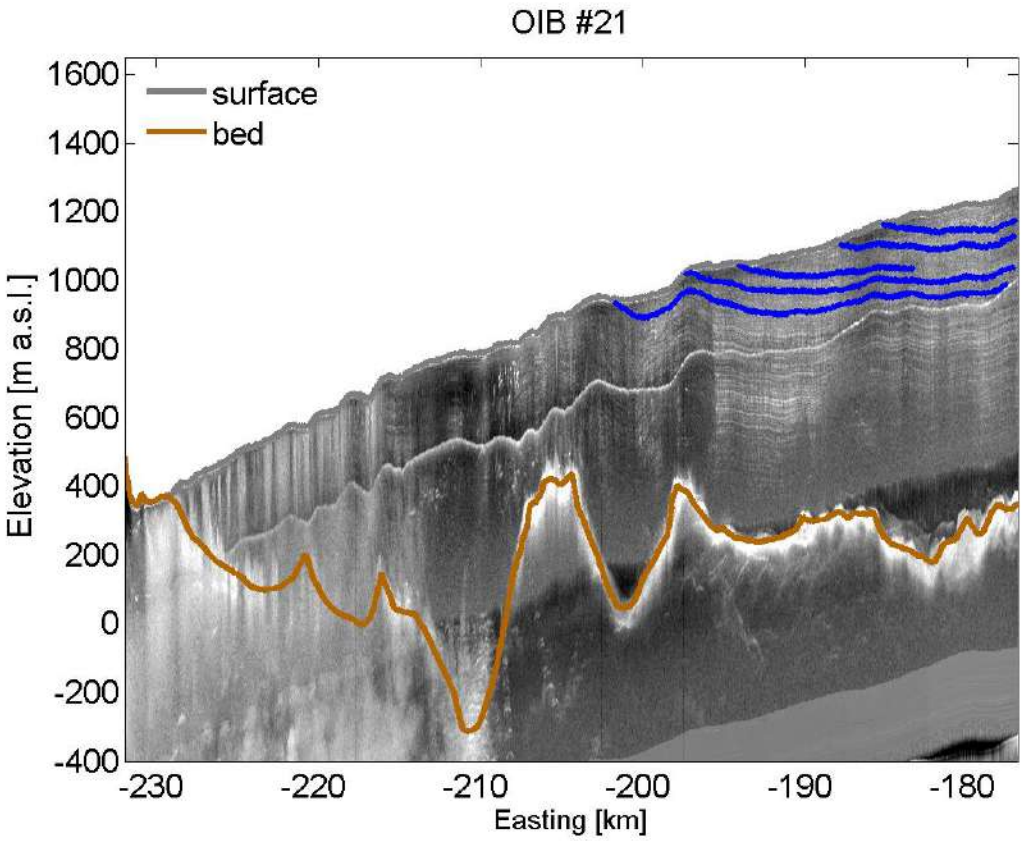
OIB #21
surface
bed
1600
1400
1200
1000
800
600
400
200
0
-200
-400
Elevation [m a.s.l.]
-230
-220
-210
-200
-190
-180
Easting [km]

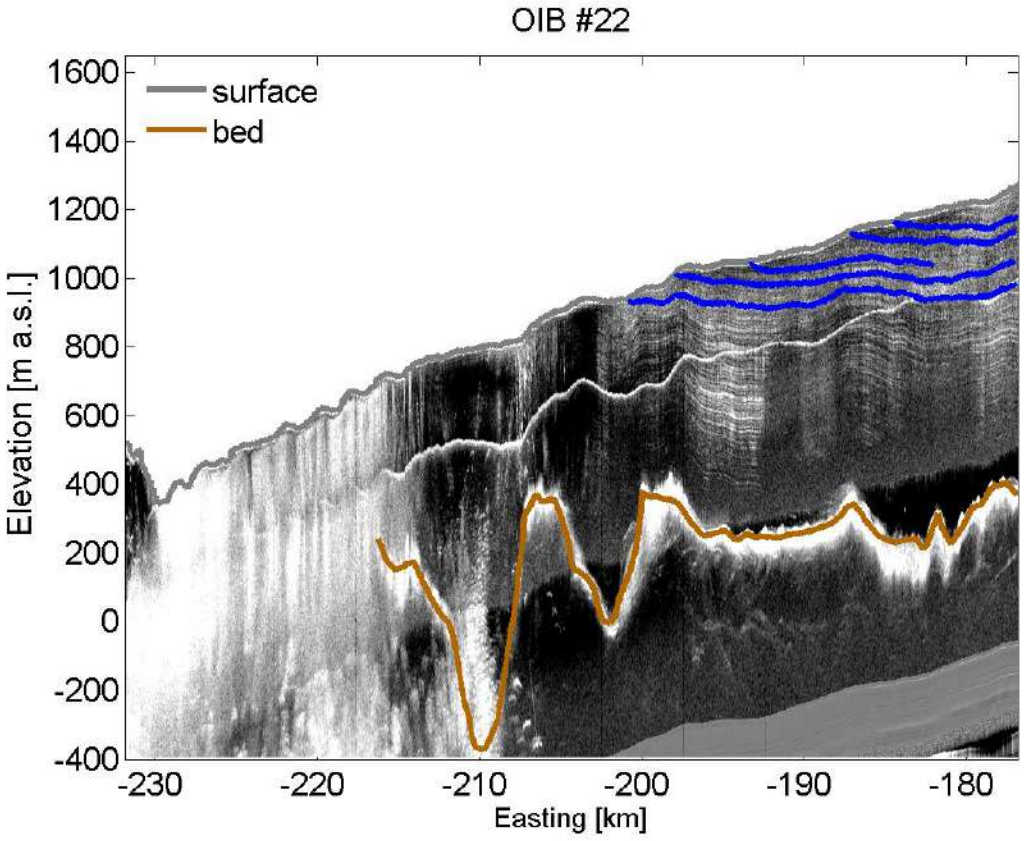
OIB #22
surface
bed
1600
1400
1200
1000
800
600
400
200
0
-200
-400
Elevation [m a.s.l.]
-230
-220
-210
-200
-190
-180
Easting [km]

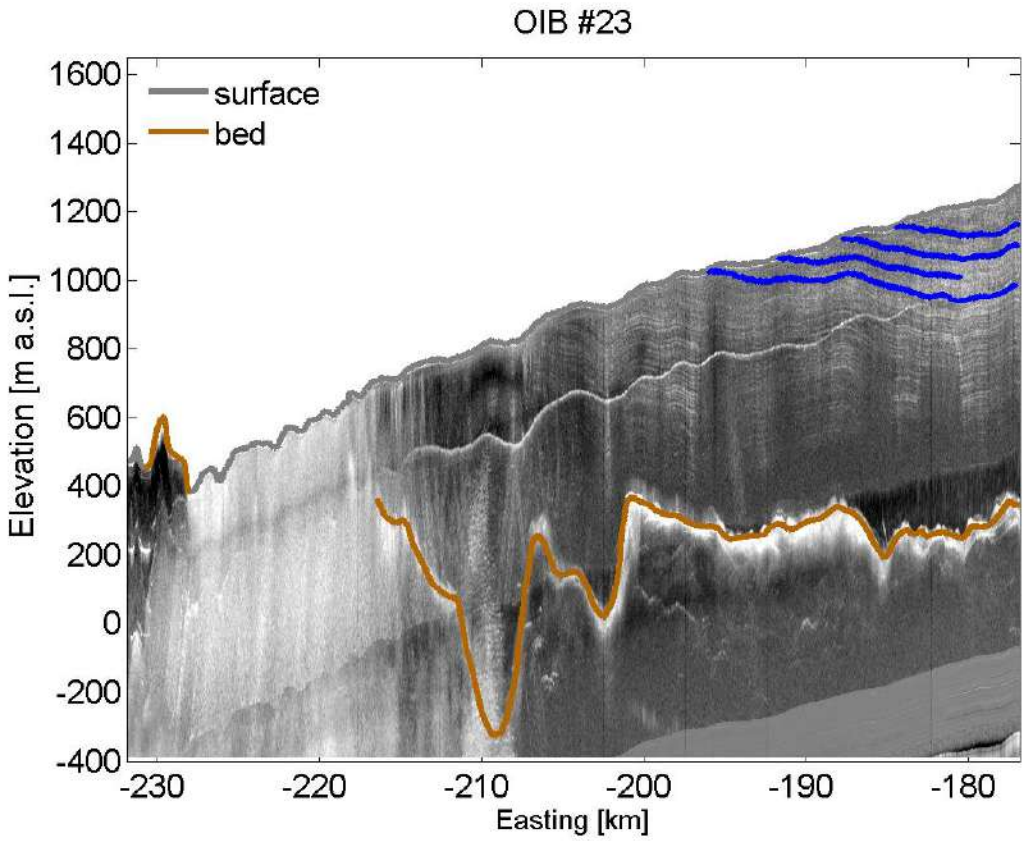
OIB #23
surface
bed
1600
1400
1200
1000
800
600
400
200
0
-200
-400
Elevation [m a.s.l.]
-230
-220
-210
-200
-190
-180
Easting [km]

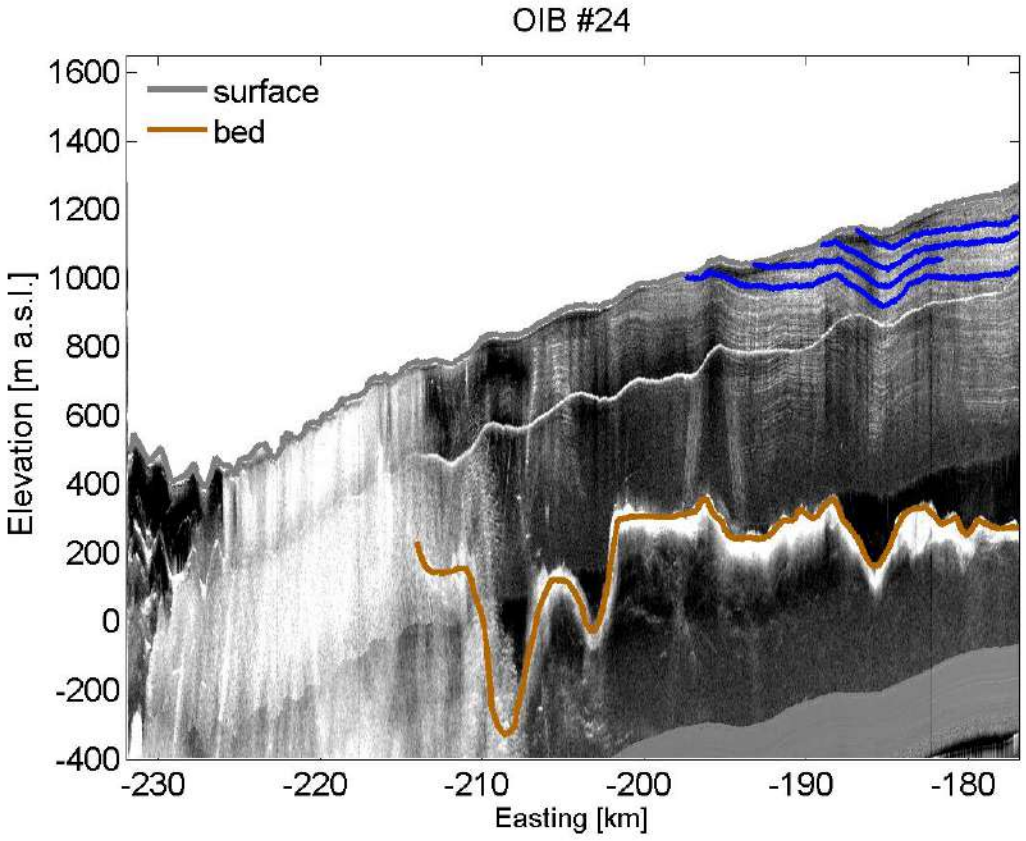
OIB #24
surface
bed
1600
1400
1200
1000
800
600
400
200
0
-200
-400
Elevation [m a.s.l.]
-230
-220
-210
-200
-190
-180
Easting [km]

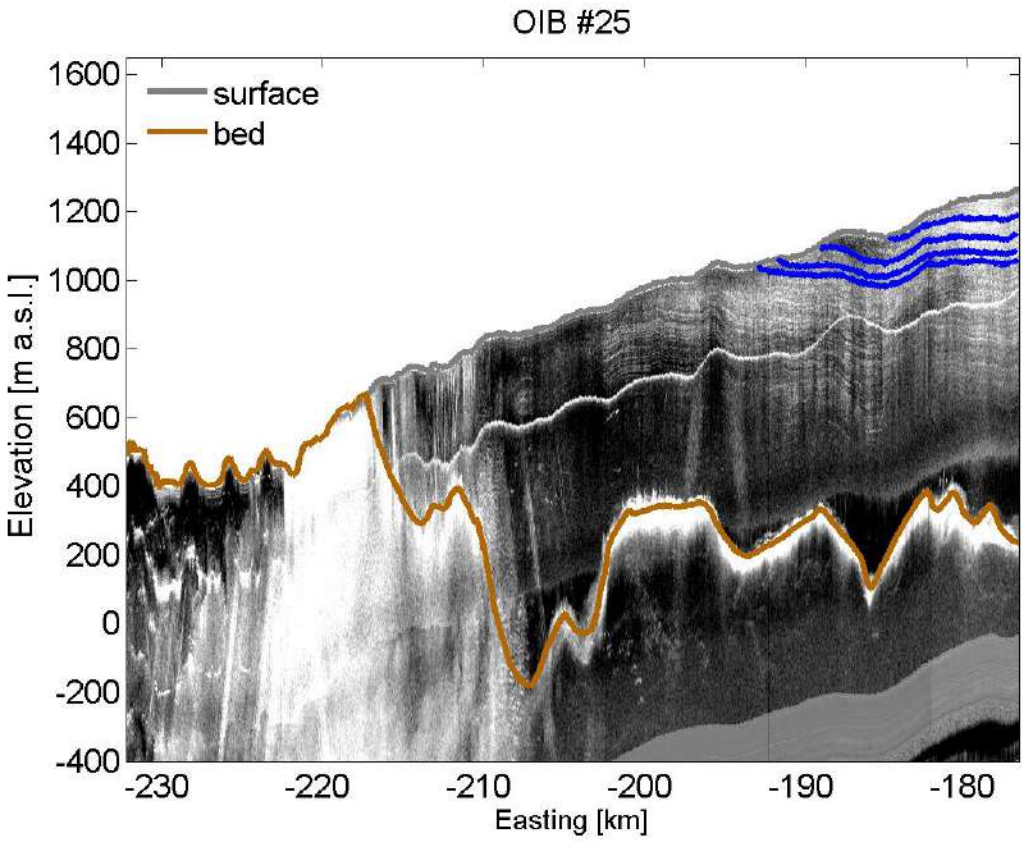
OIB #25
surface
bed
1600
1400
1200
1000
800
600
400
200
0
-200
-400
Elevation [m a.s.l.]
-230
-220
-210
-200
-190
-180
Easting [km]

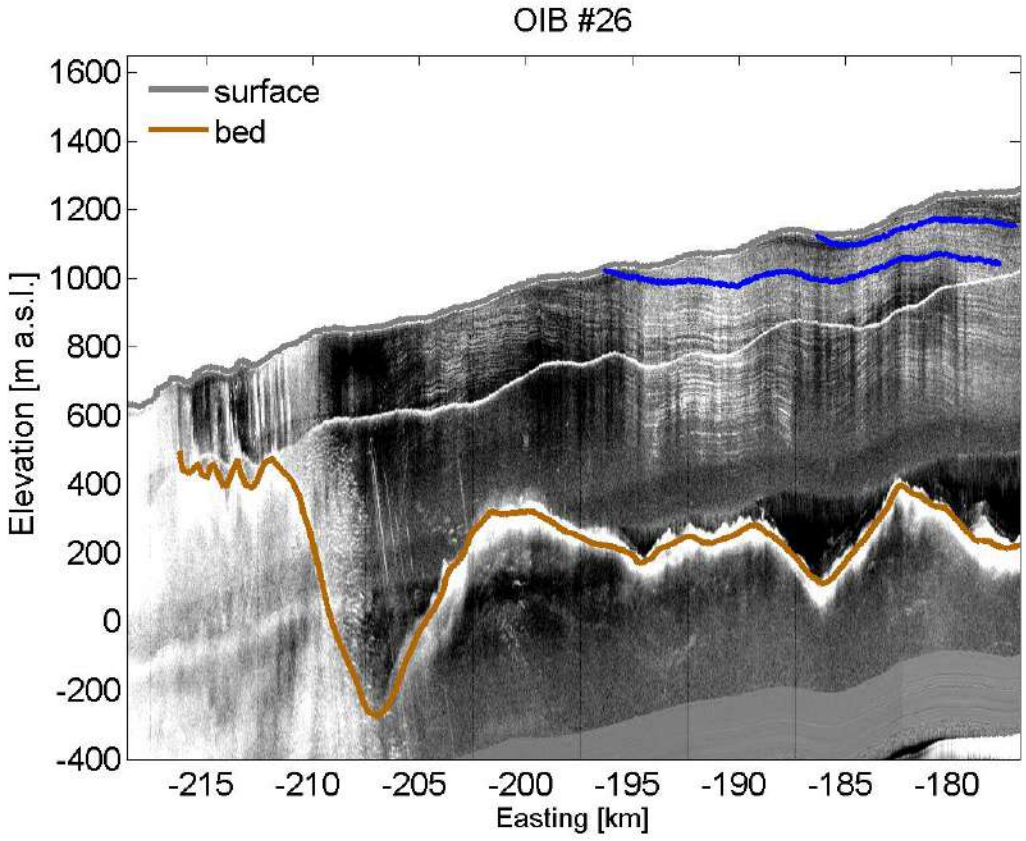
OIB #26
surface
bed
1600
1400
1200
1000
800
600
400
200
0
-200
-400
Elevation [m a.s.l.]
-215
-210
-205
-200
-195
-190
-185
-180
Easting [km]

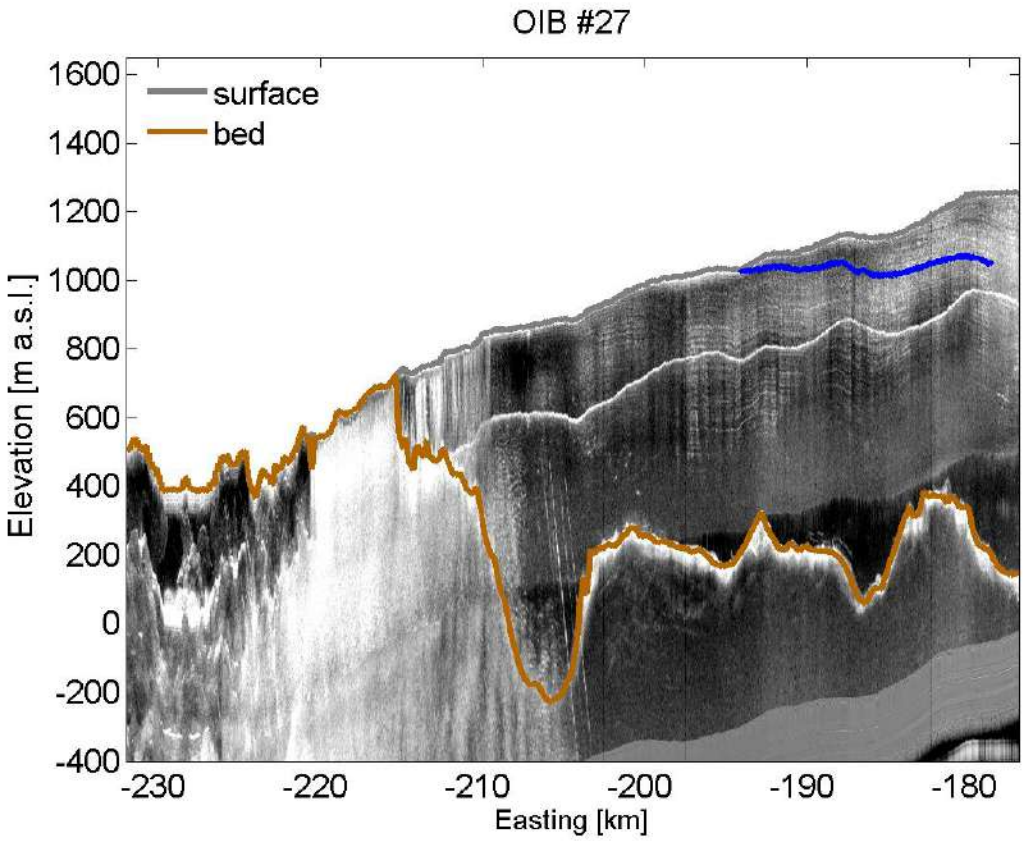
OIB #27
surface
bed
1600
1400
1200
1000
800
600
400
200
0
-200
-400
Elevation [m a.s.l.]
-230
-220
-210
-200
-190
-180
Easting [km]

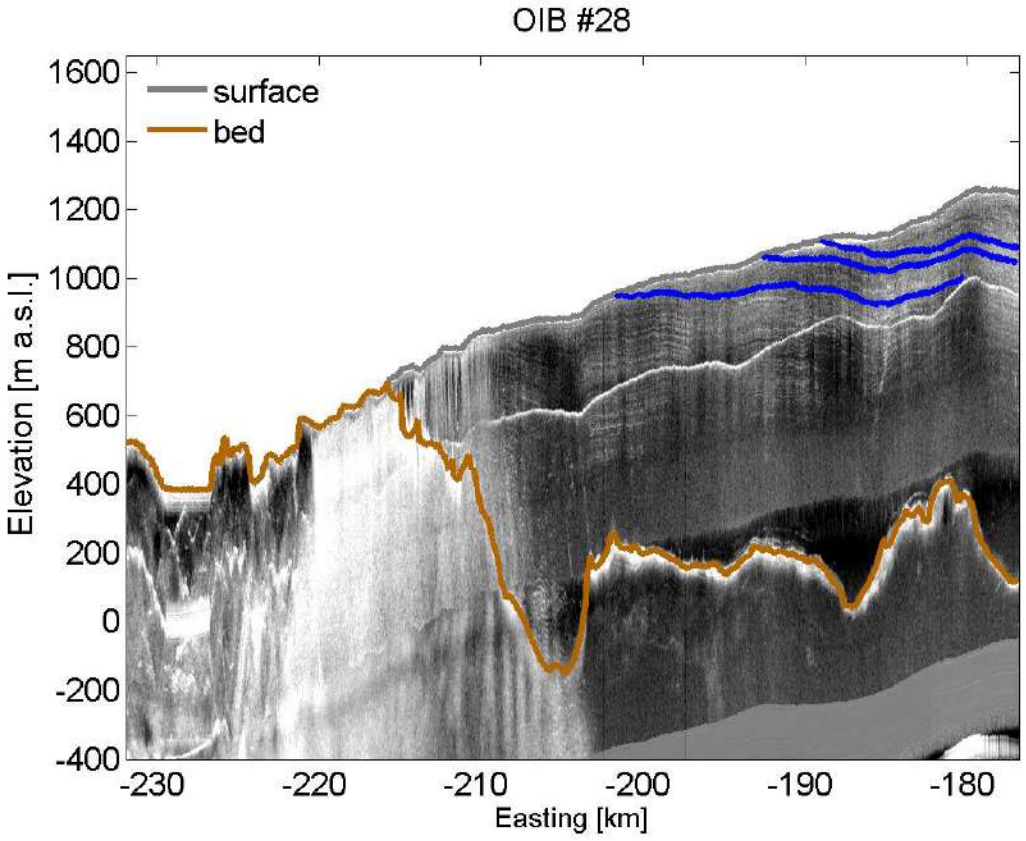
OIB #28
surface
bed
1600
1400
1200
1000
800
600
400
200
0
-200
-400
Elevation [m a.s.l.]
-230
-220
-210
-200
-190
-180
Easting [km]

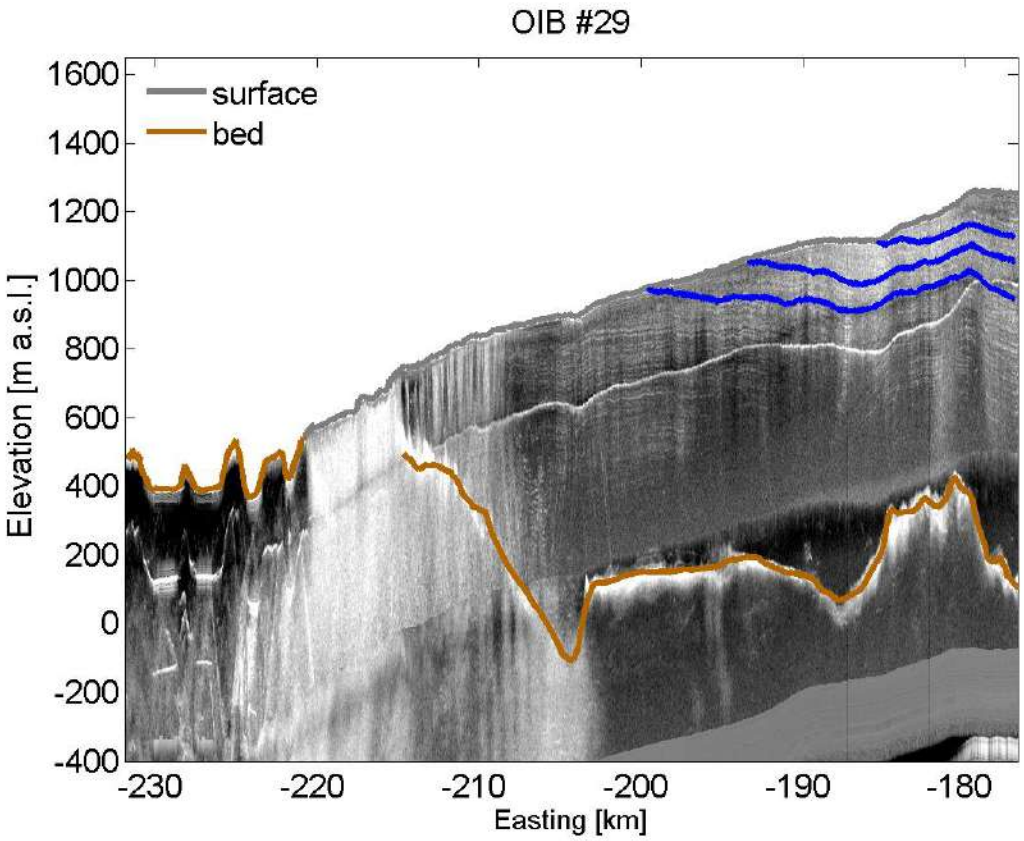
OIB #29
surface
bed
1600
1400
1200
1000
800
600
400
200
0
-200
-400
Elevation [m a.s.l.]
-230
-220
-210
-200
-190
-180
Easting [km]

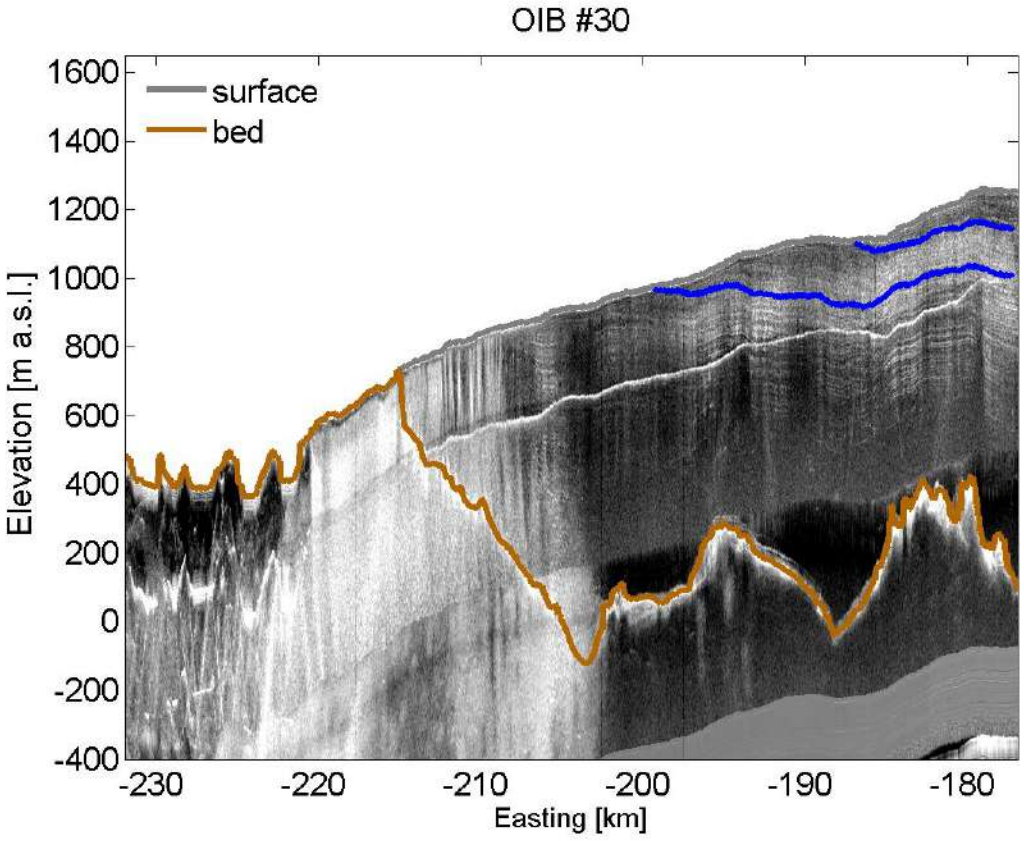
OIB #30
surface
bed
1600
1400
1200
1000
800
600
400
200
0
-200
-400
Elevation [m a.s.l.]
-230
-220
-210
-200
-190
-180
Easting [km]

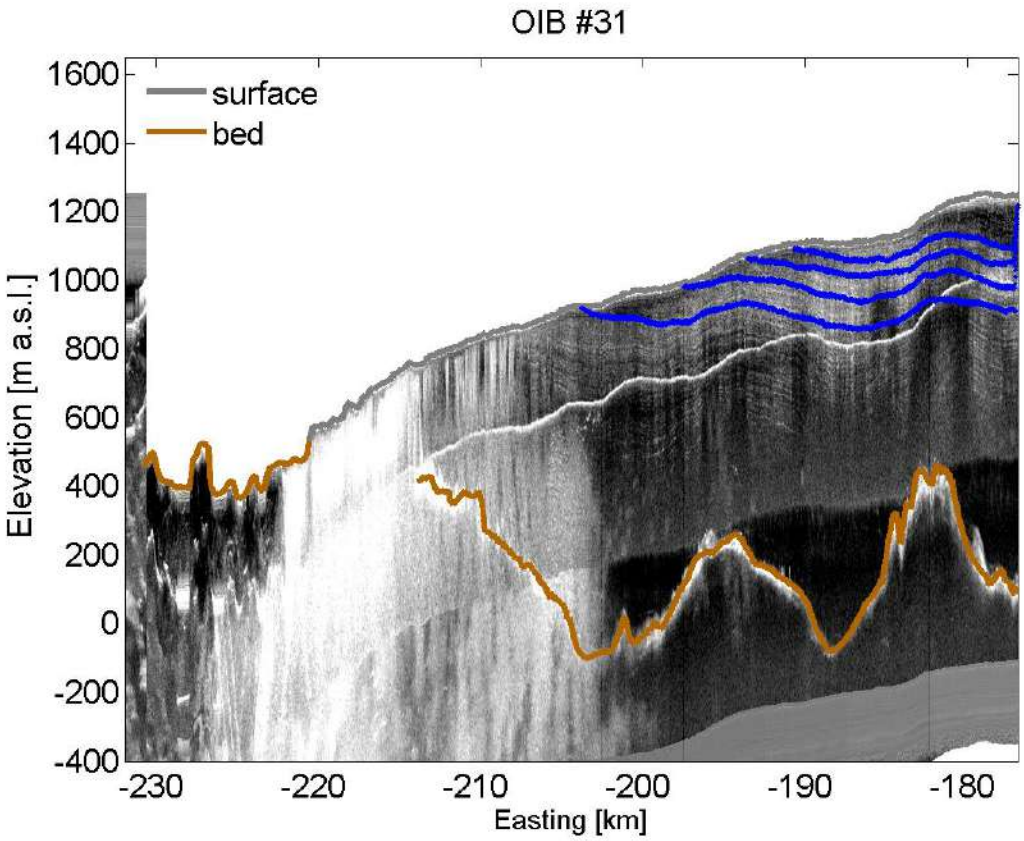
OIB #31
surface
bed
1600
1400
1200
1000
800
600
400
200
0
-200
-400
Elevation [m a.s.l.]
-230
-220
-210
-200
-190
-180
Easting [km]

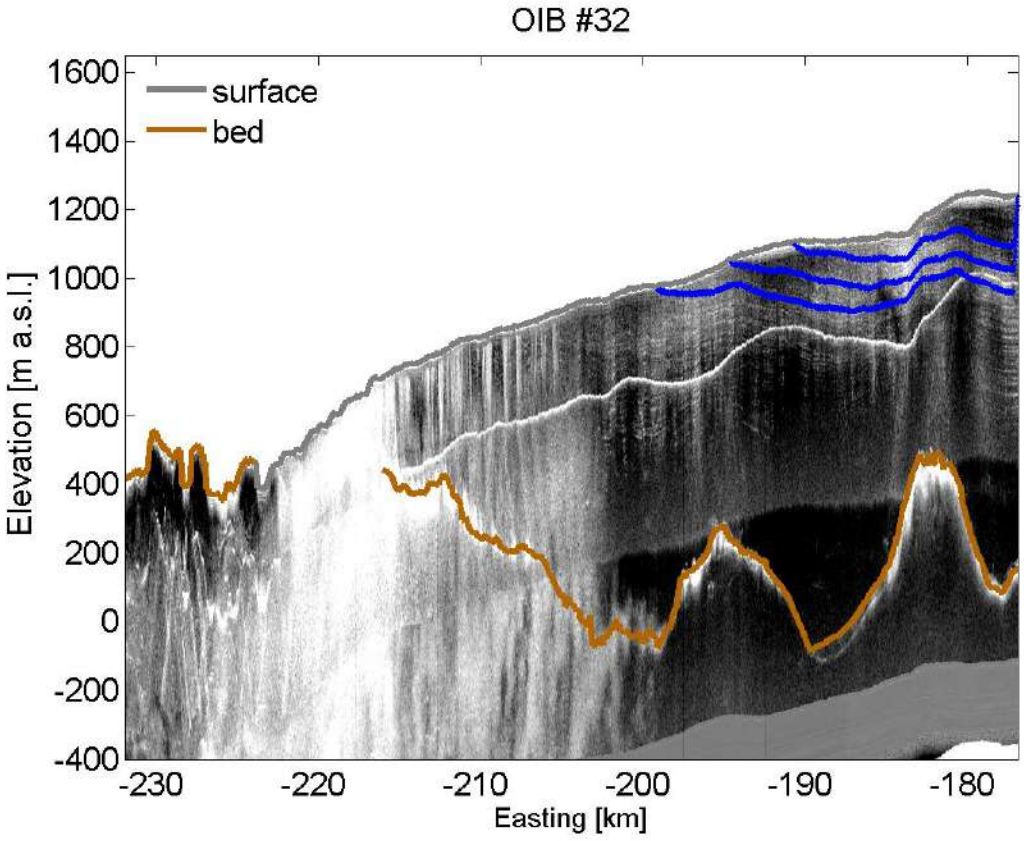
OIB #32
surface
bed
1600
1400
1200
1000
800
600
400
200
0
-200
-400
Elevation [m a.s.l.]
-230
-220
-210
-200
-190
-180
Easting [km]

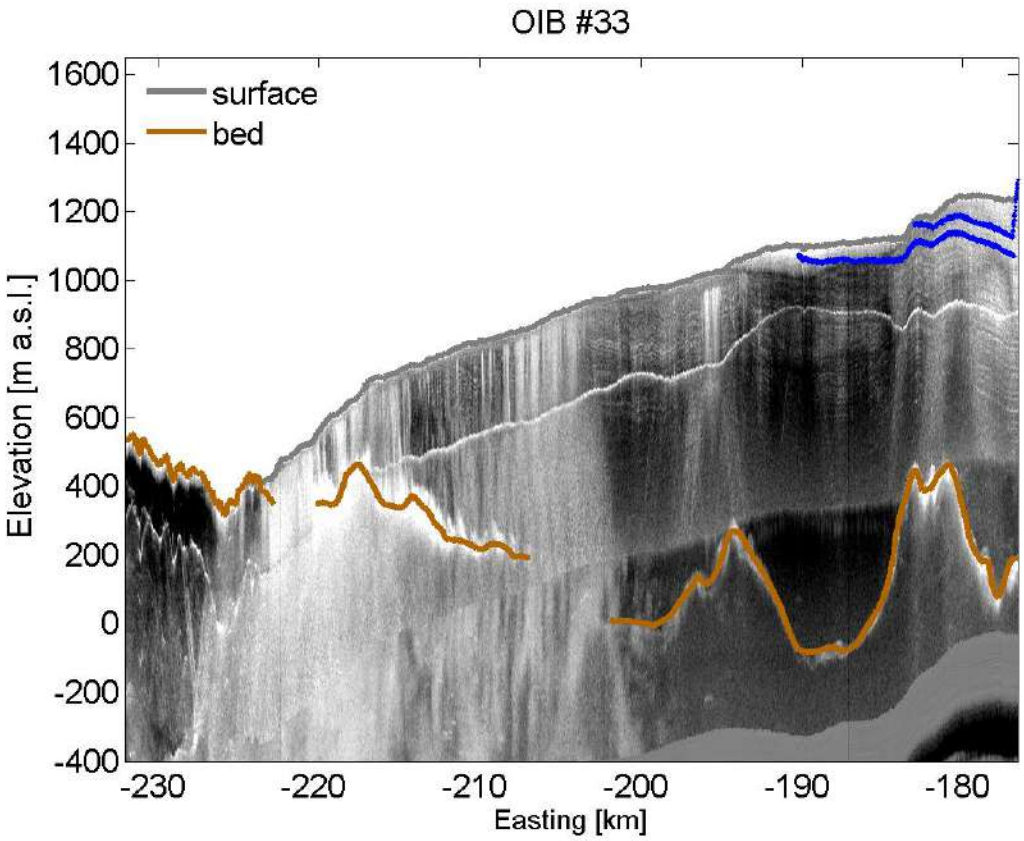
OIB #33
surface
bed
1600
1400
1200
1000
800
600
400
200
0
-200
-400
Elevation [m a.s.l.]
-230
-220
-210
-200
-190
-180
Easting [km]

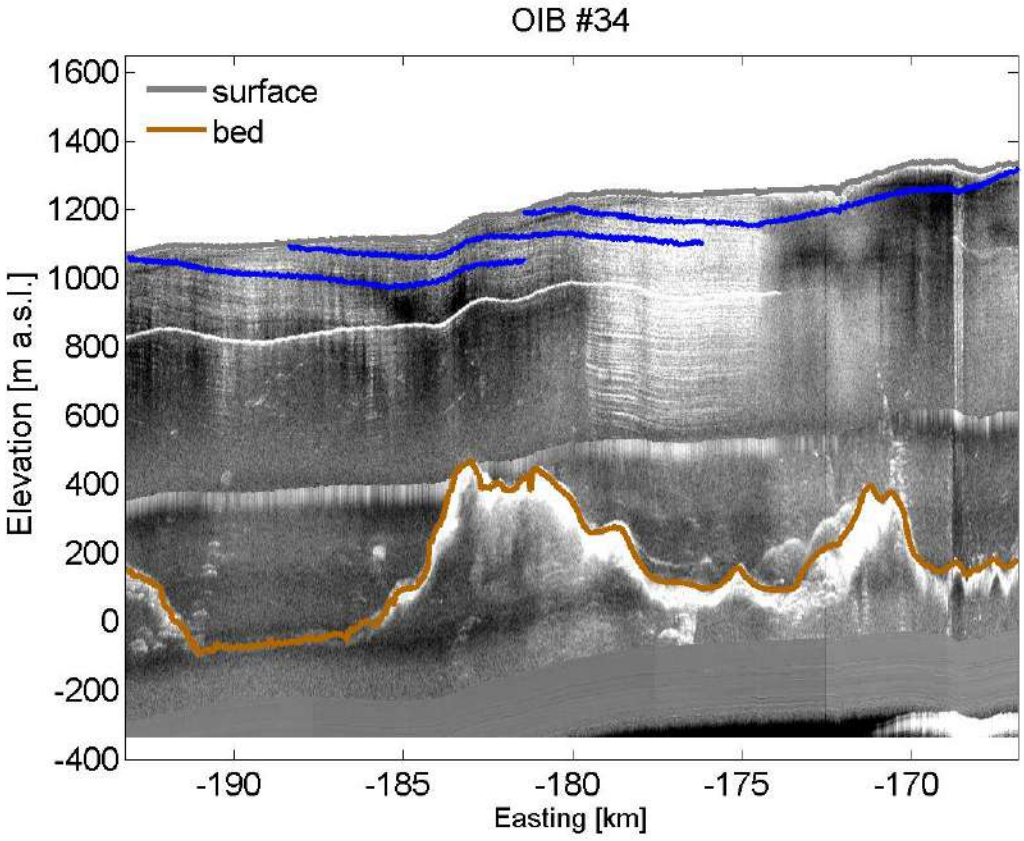
OIB #34
surface
bed
1600
1400
1200
1000
800
600
400
200
0
-200
-400
Elevation [m a.s.l.]
-190
-185
-180
-175
-170
Easting [km]

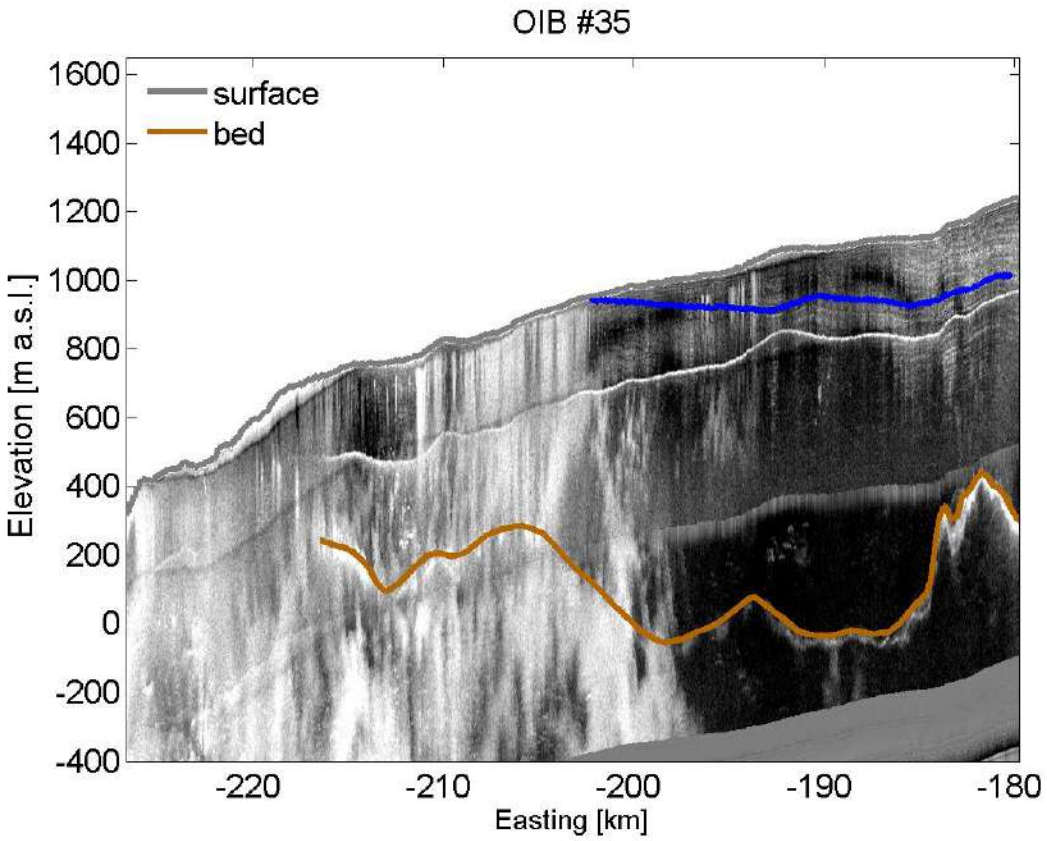
OIB #35
surface
bed
1600
1400
1200
1000
800
600
400
200
0
-200
-400
Elevation [m a.s.l.]
-220
-210
-200
-190
-180
Easting [km]

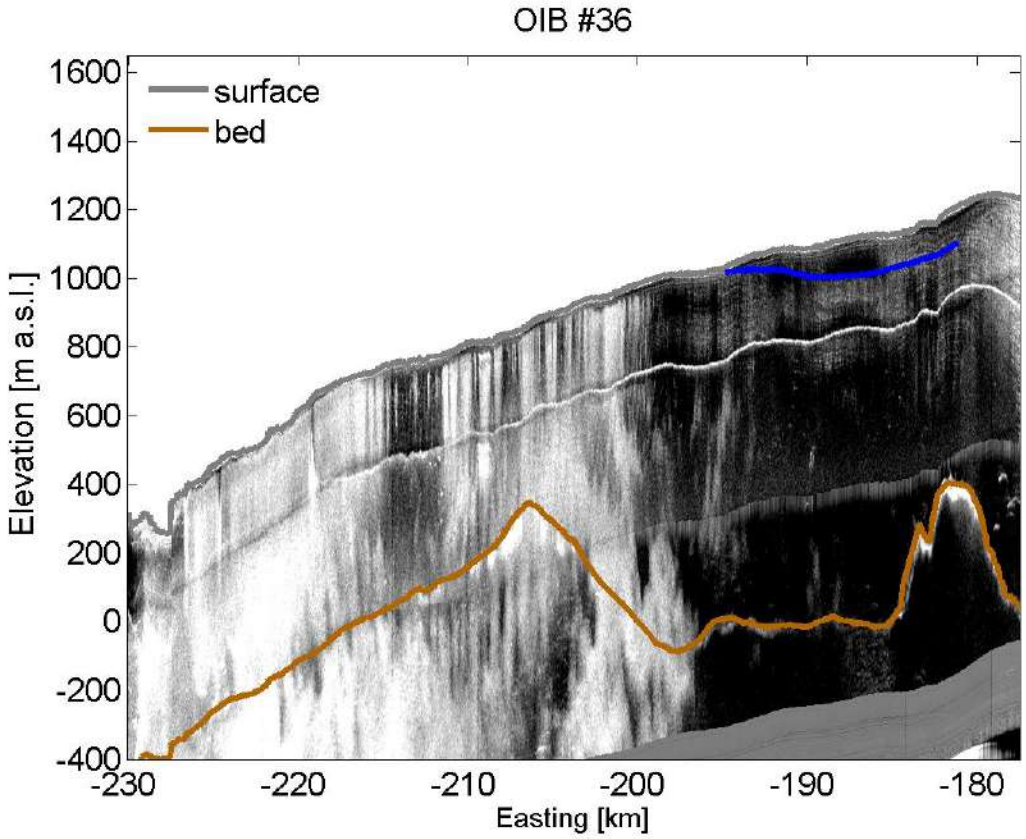
OIB #36
surface
bed
1600
1400
1200
1000
800
600
400
200
0
-200
-400
Elevation [m a.s.l.]
-230
-220
-210
-200
-190
-180
Easting [km]

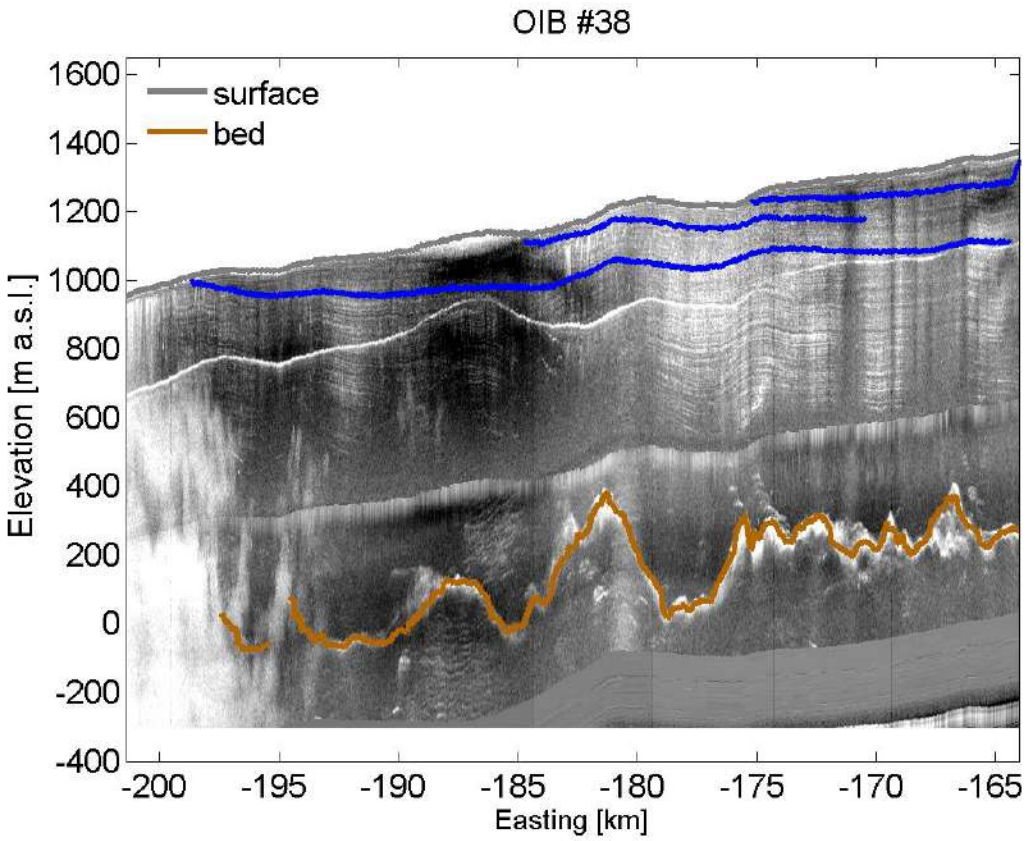
OIB #38
surface
bed
Elevation [m a.s.l.]
1600
1400
1200
1000
800
600
400
200
0
-200
-400
-200
-195
-190
-185
-180
-175
-170
-165
Easting [km]

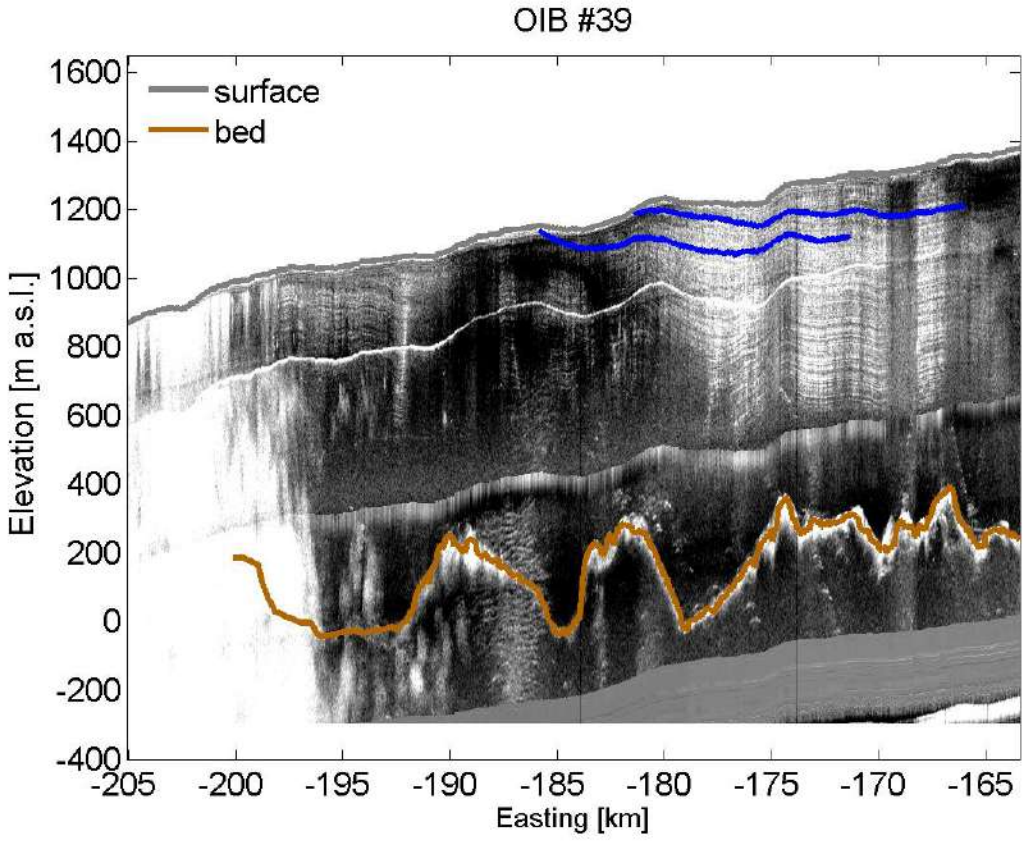
OIB #39
surface
bed
Elevation [m a.s.l.]
1600
1400
1200
1000
800
600
400
200
0
-200
-400
-205
-200
-195
-190
-185
-180
-175
-170
-165
Easting [km]

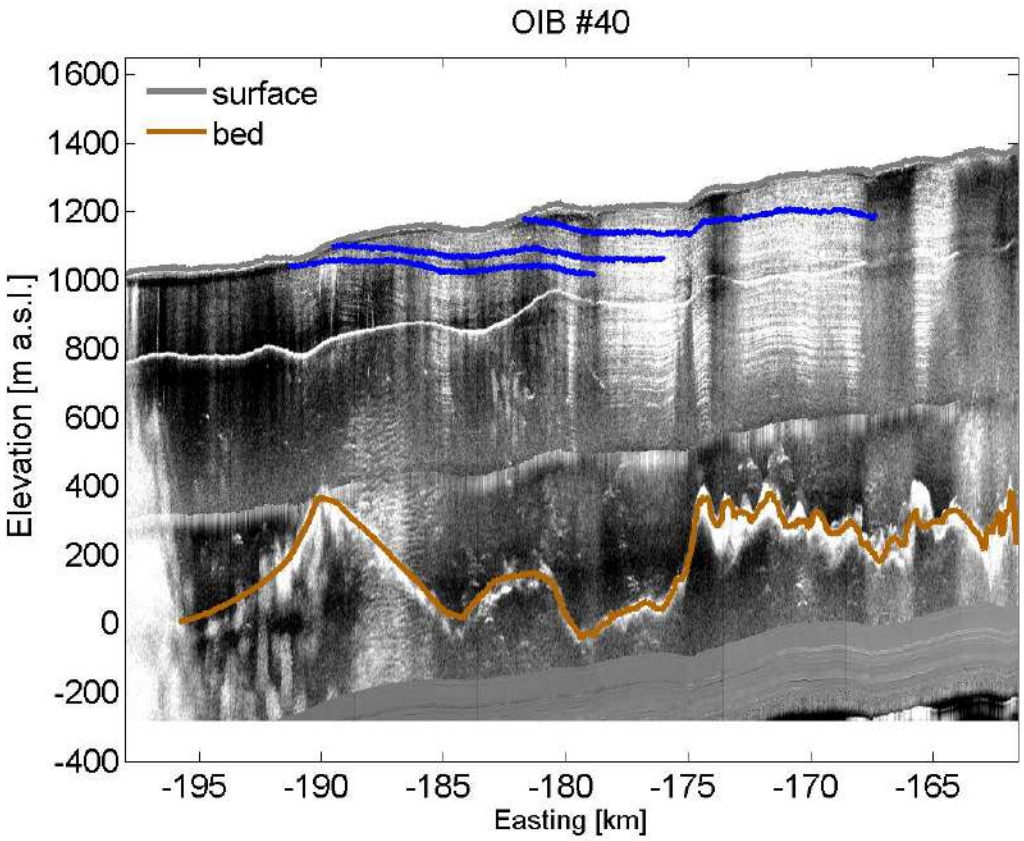
OIB #40
surface
bed
Elevation [m a.s.l.]
1600
1400
1200
1000
800
600
400
200
0
-200
-400
-195
-190
-185
-180
-175
-170
-165
Easting [km]

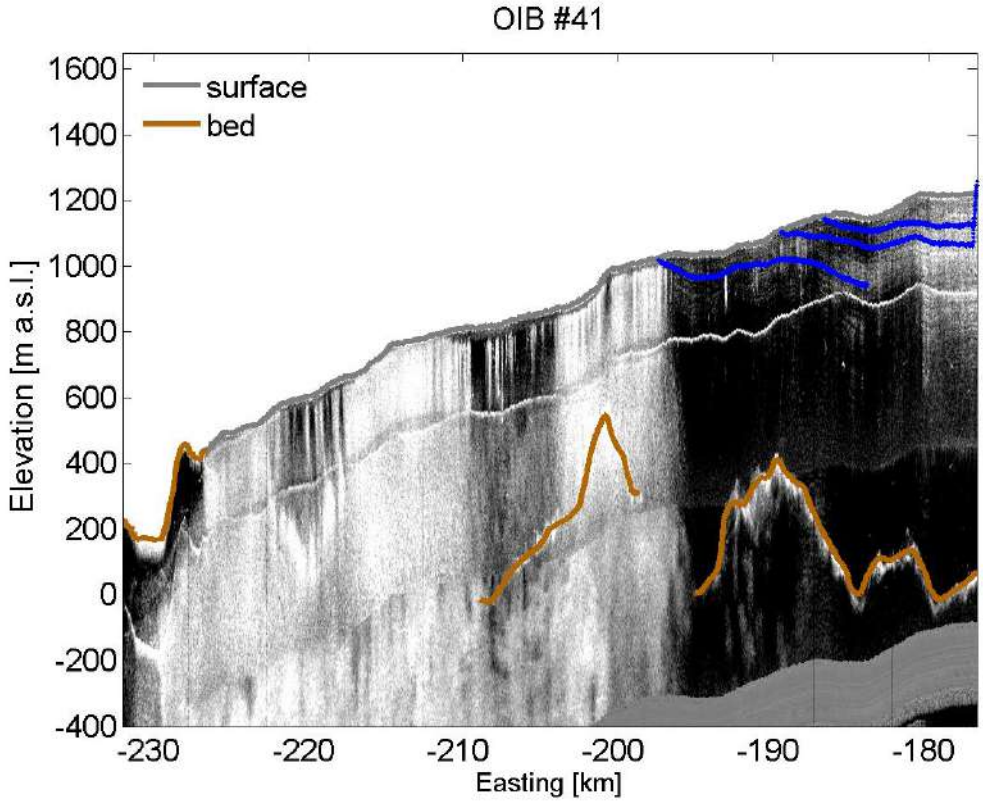
OIB #41
surface
bed
Elevation [m a.s.l.]
1600
1400
1200
1000
800
600
400
200
0
-200
-400
-230
-220
-210
-200
-190
-180
Easting [km]

APPENDIX B

RADIOSTRATIGRAPHY CONTINUITY INDEX

This appendix presents continuity indices for the east-west running Operation Ice Bridge (OIB) radargrams analyzed in Chapter 1. The continuity index is a quantitative metric that defines radar layer continuity for every trace along a radargram, outlined by Karlsson et al. (2012) as:

$$\psi = \frac{1}{2\Delta r N} \sum_{i=n_i}^{n_N} |P_{i+1} - P_{i-1}|$$

where P_i is the radar data power in decibels (dB) at point i, and Δr is the depth in meters (m), N is a subset of samples taken vertically through the ice column (i.e. radar trace), n is the number of samples (i.e. points) within the trace. The maximum continuity index value calculated for radar data collected along each transect is reported in the title of each figure. The continuity index of every radargram was discontinues with $\psi < 0.22$.

Karlsson, N. B., Rippin, D. M., Bingham, R. G., and Vaughan, D. G. (2012). A "continuity-index" for assessing ice-sheet dynamics from radar-sounded internal layers. Earth Planet. Sci. Lett. 335–336, 88–94. doi:10.1016/j.epsl.2012.04.034.

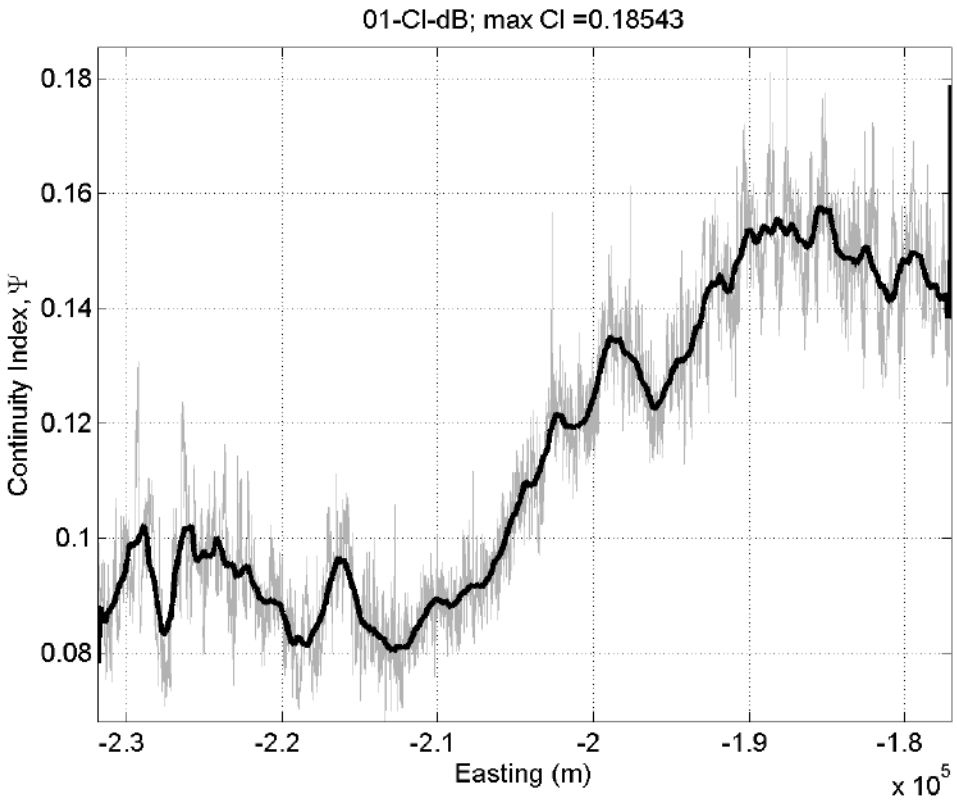
01-CI-dB; max CI =0.18543
Continuity Index, Ψ
0.18
0.16
0.14
0.12
0.1
0.08
-2.3
-2.2
-2.1
-2
-1.9
-1.8
Easting (m)
x 10^5

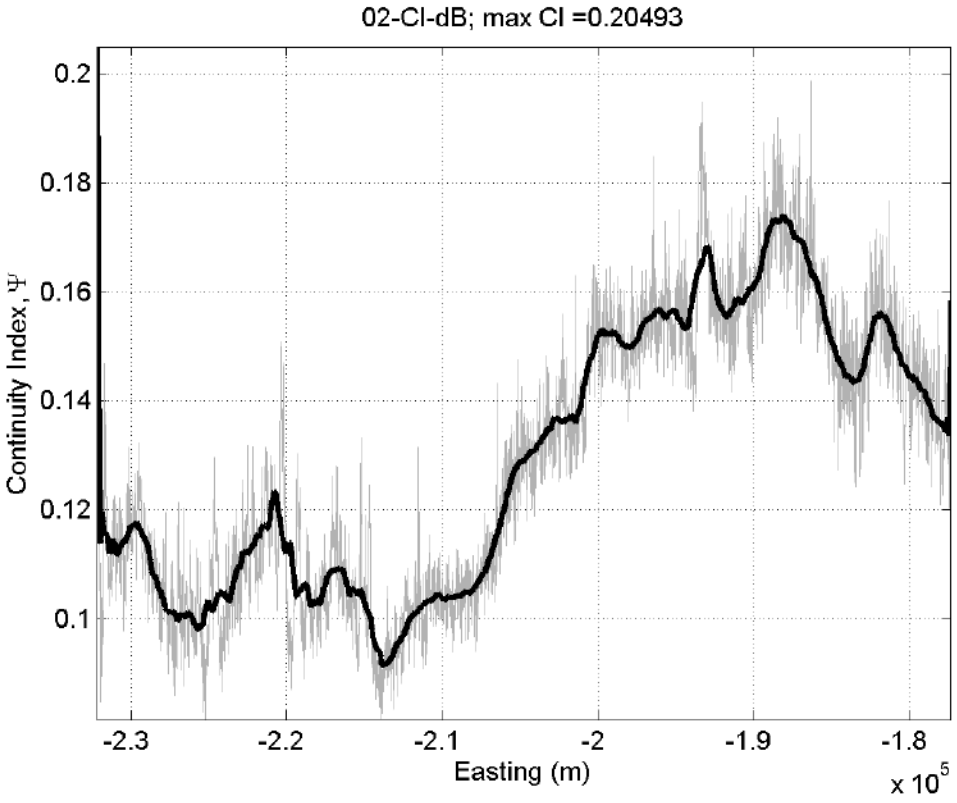
02-CI-dB; max CI =0.20493
Continuity Index, Ψ
0.2
0.18
0.16
0.14
0.12
0.1
-2.3
-2.2
-2.1
-2
-1.9
-1.8
Easting (m)
x 10^5

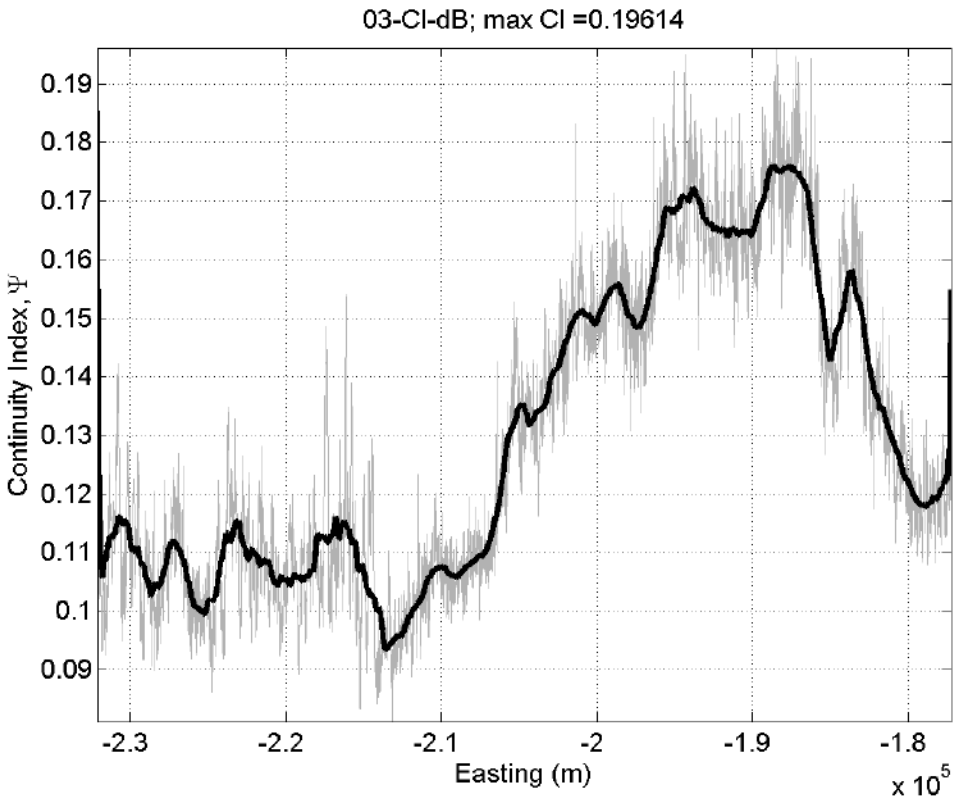
03-CI-dB; max CI =0.19614
Continuity Index, Ψ
0.19
0.18
0.17
0.16
0.15
0.14
0.13
0.12
0.11
0.1
0.09
-2.3
-2.2
-2.1
-2
-1.9
-1.8
Easting (m)
x 10^5

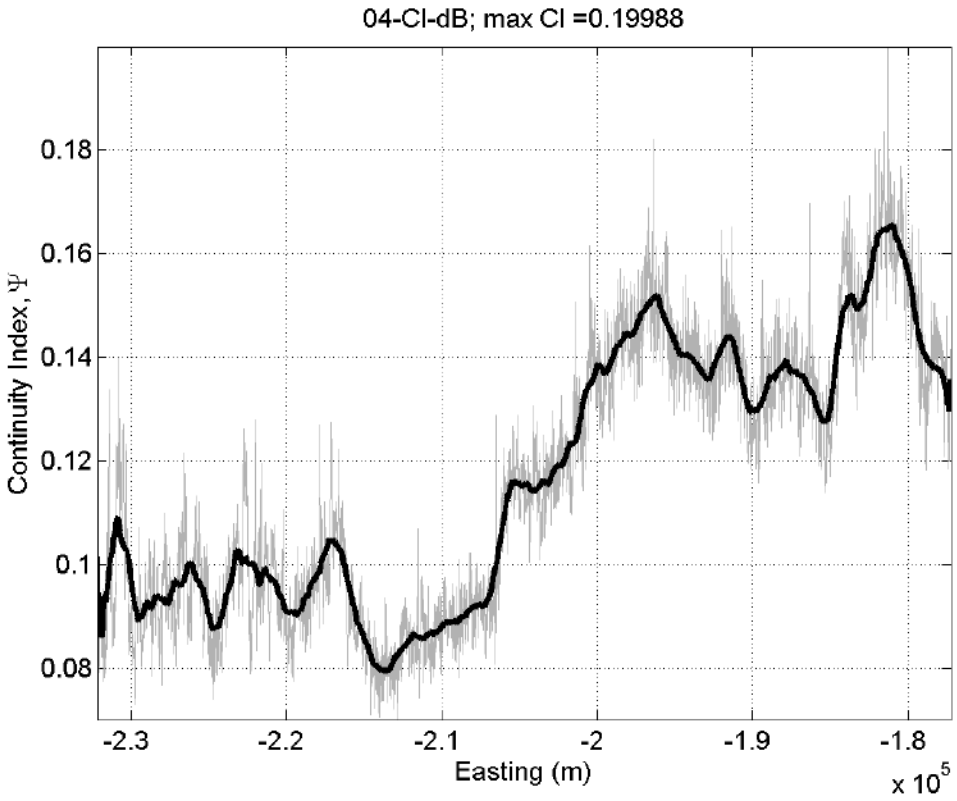
04-CI-dB; max CI =0.19988
Continuity Index, Ψ
0.18
0.16
0.14
0.12
0.1
0.08
-2.3
-2.2
-2.1
-2
-1.9
-1.8
Easting (m)
x 10^5

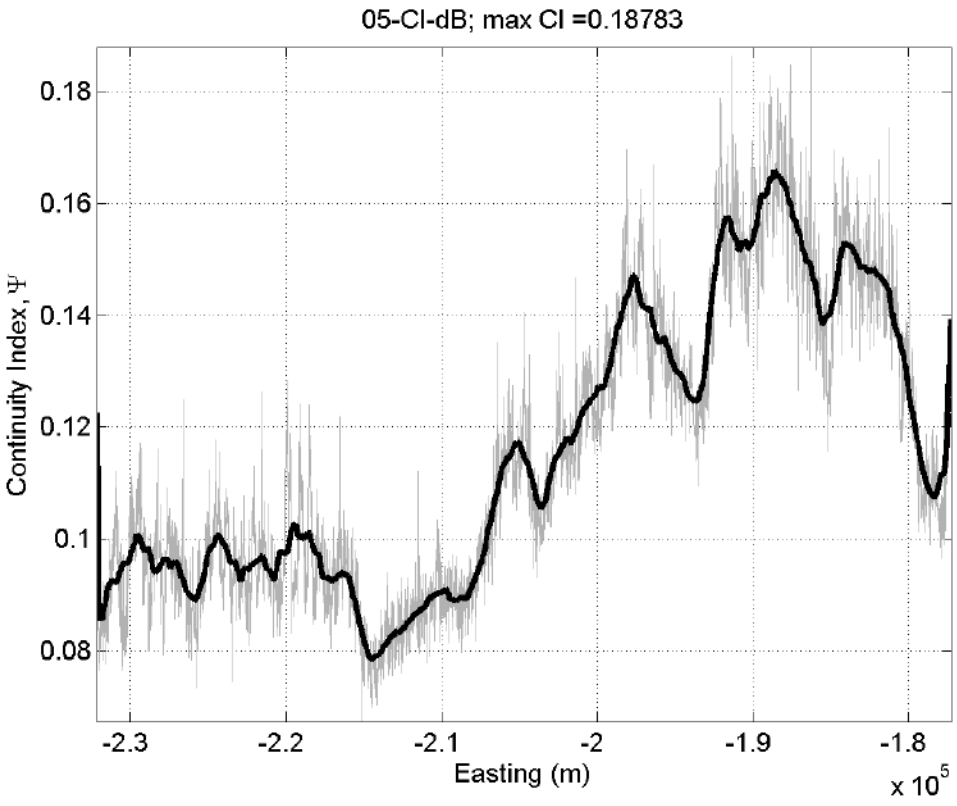
05-CI-dB; max CI =0.18783
Continuity Index, Ψ
0.18
0.16
0.14
0.12
0.1
0.08
-2.3
-2.2
-2.1
-2
-1.9
-1.8
Easting (m)
x 10^5

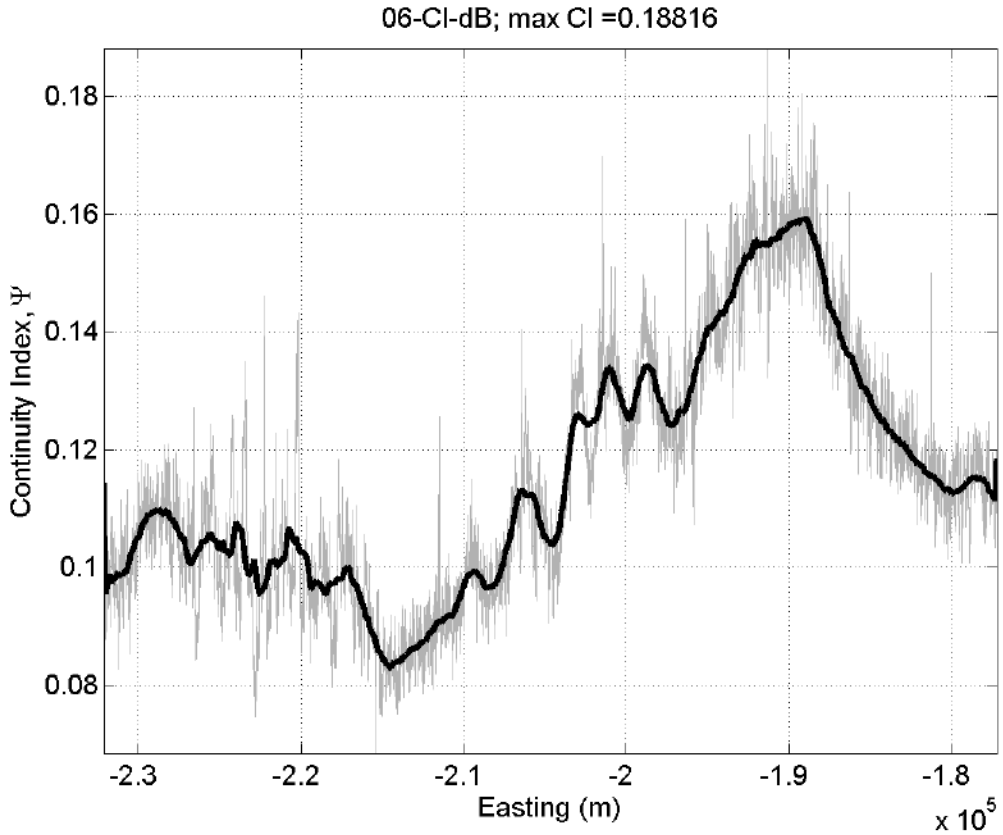
06-CI-dB; max CI =0.18816
Continuity Index, Ψ
0.18
0.16
0.14
0.12
0.1
0.08
-2.3
-2.2
-2.1
-2
-1.9
-1.8
Easting (m)
x 10^5

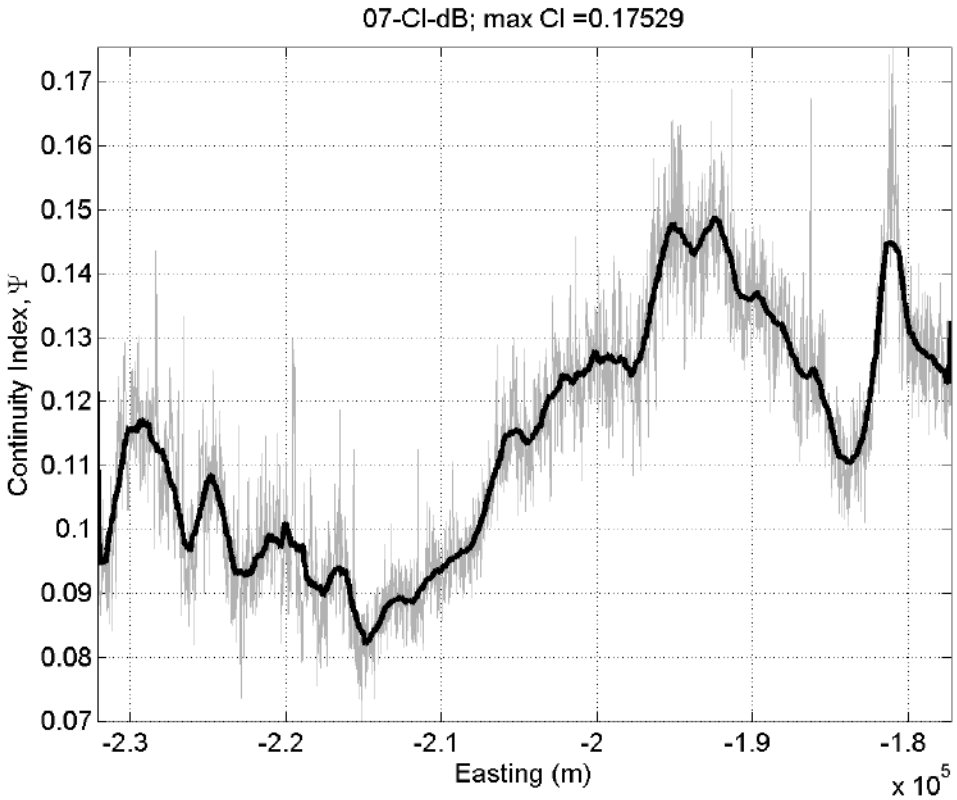
07-CI-dB; max CI =0.17529
Continuity Index, Ψ
0.17
0.16
0.15
0.14
0.13
0.12
0.11
0.1
0.09
0.08
0.07
-2.3
-2.2
-2.1
-2
-1.9
-1.8
Easting (m)
x 10^5

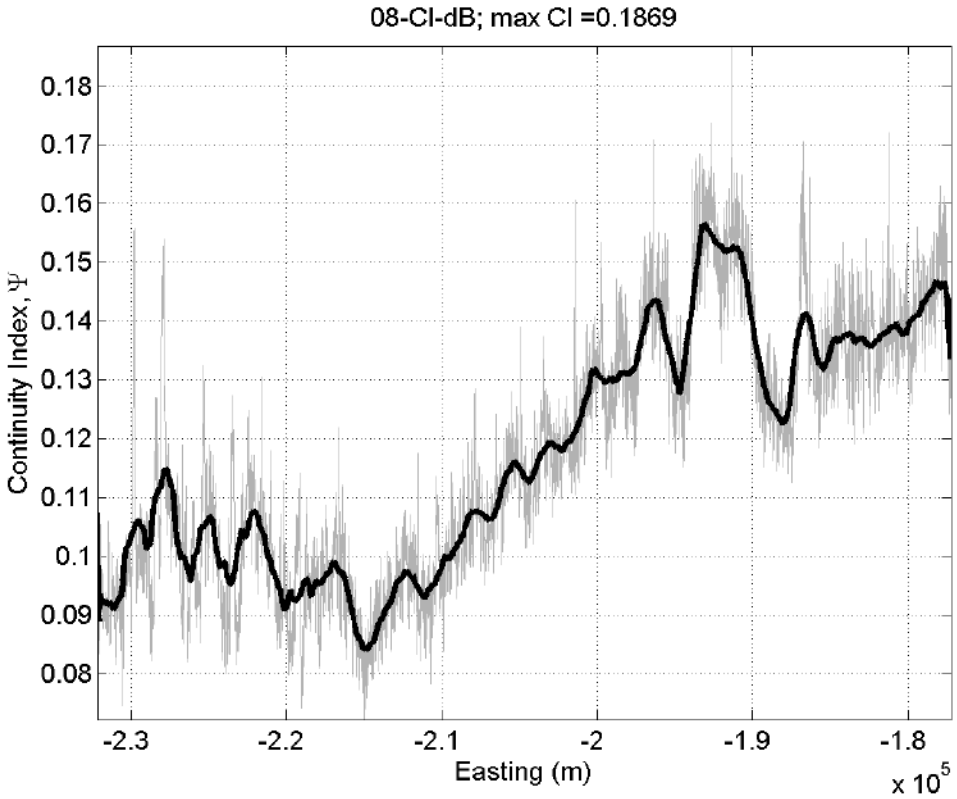
08-CI-dB; max CI =0.1869
Continuity Index, Ψ
0.18
0.17
0.16
0.15
0.14
0.13
0.12
0.11
0.1
0.09
0.08
-2.3
-2.2
-2.1
-2
-1.9
-1.8
Easting (m)
x 10^5

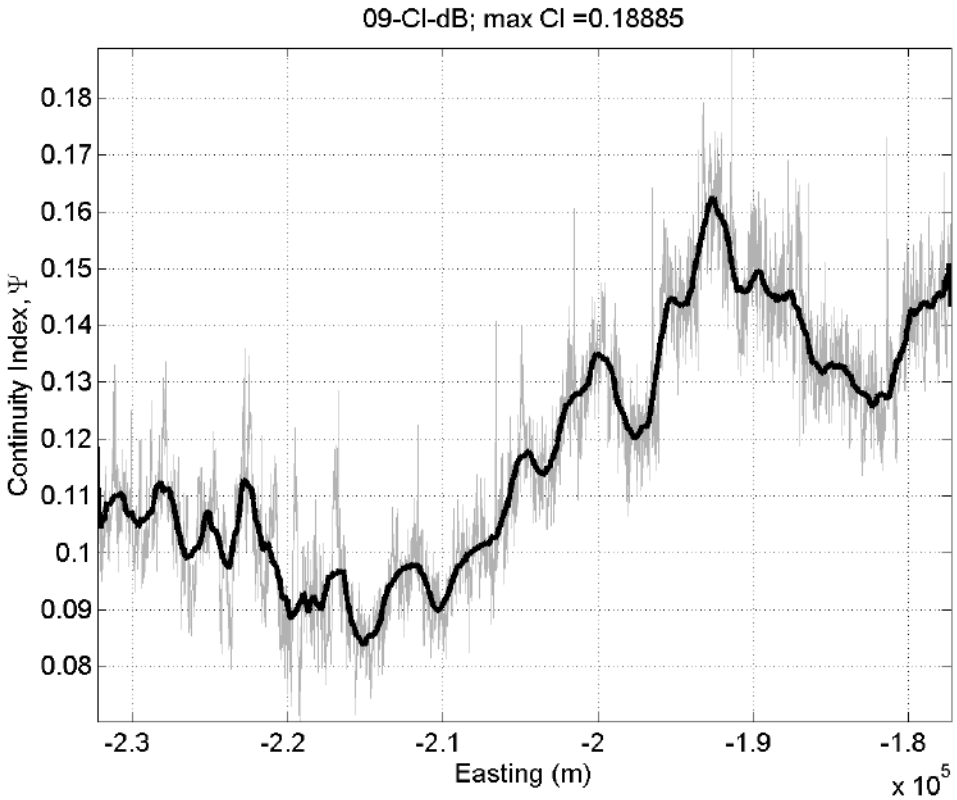
09-CI-dB; max CI =0.18885
Continuity Index, Ψ
0.18
0.17
0.16
0.15
0.14
0.13
0.12
0.11
0.1
0.09
0.08
-2.3
-2.2
-2.1
-2
-1.9
-1.8
Easting (m)
x 10^5

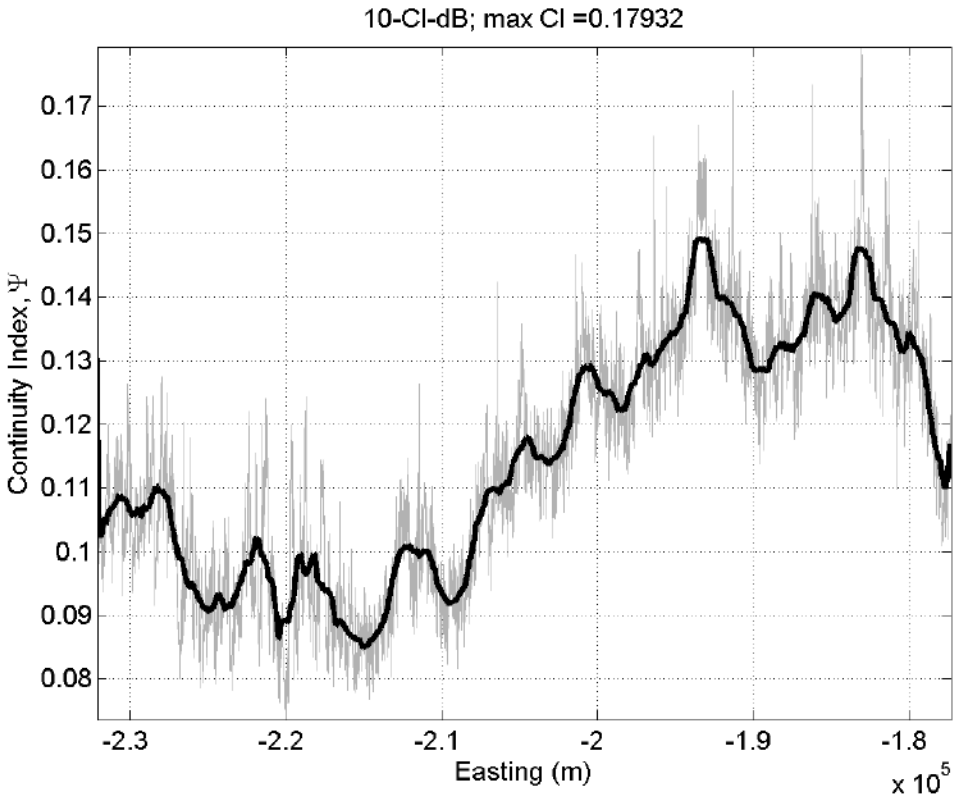
10-CI-dB; max CI =0.17932
Continuity Index, Ψ
0.17
0.16
0.15
0.14
0.13
0.12
0.11
0.1
0.09
0.08
-2.3
-2.2
-2.1
-2
-1.9
-1.8
Easting (m)
x 10^5

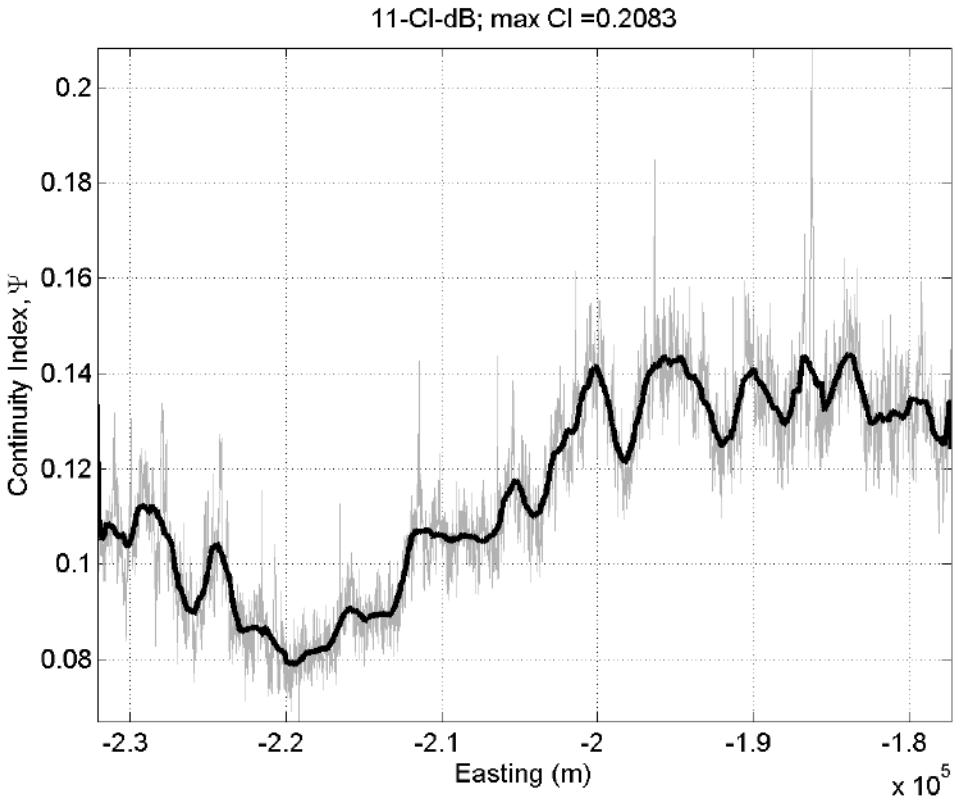
11-CI-dB; max CI =0.2083
Continuity Index, Ψ
0.2
0.18
0.16
0.14
0.12
0.1
0.08
-2.3
-2.2
-2.1
-2
-1.9
-1.8
Easting (m)
x 10^5

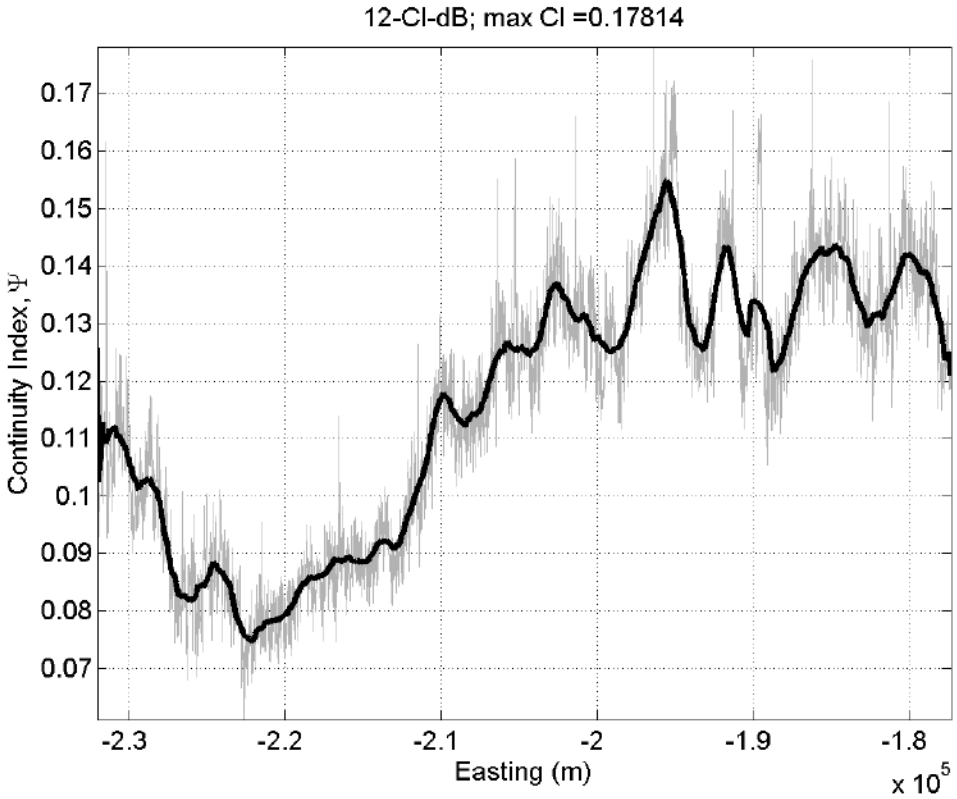
12-CI-dB; max CI =0.17814
Continuity Index, Ψ
0.17
0.16
0.15
0.14
0.13
0.12
0.11
0.1
0.09
0.08
0.07
-2.3
-2.2
-2.1
-2
-1.9
-1.8
Easting (m)
x 10^5

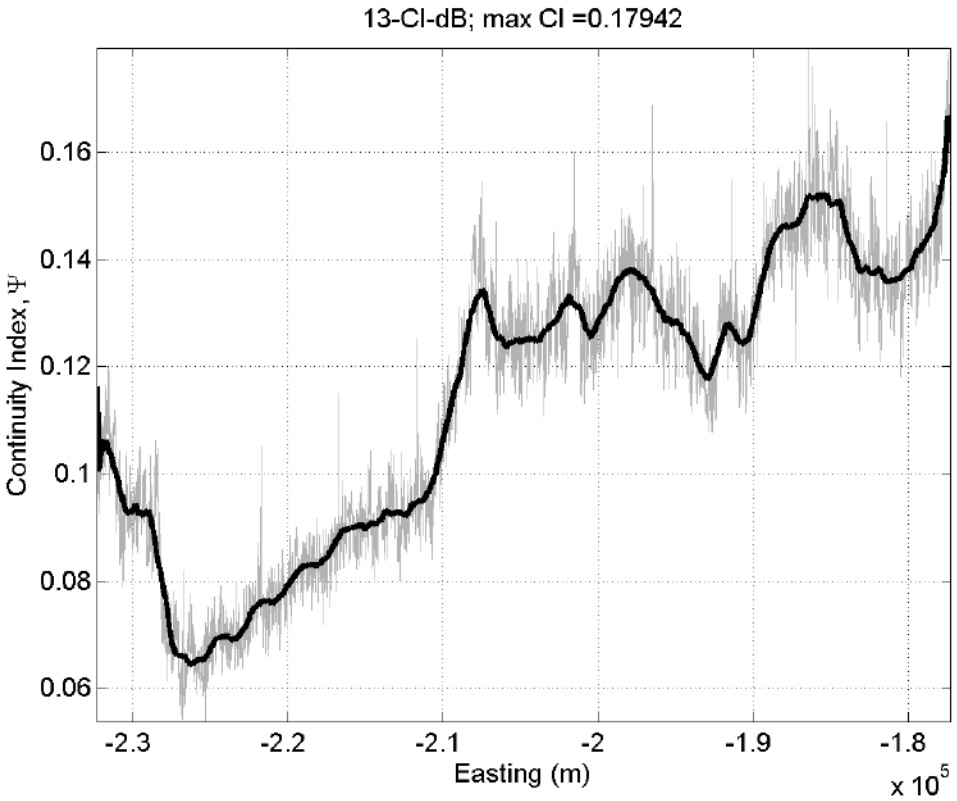
13-CI-dB; max CI =0.17942
Continuity Index, Ψ
0.16
0.14
0.12
0.1
0.08
0.06
-2.3
-2.2
-2.1
-2
-1.9
-1.8
Easting (m)
x 10^5

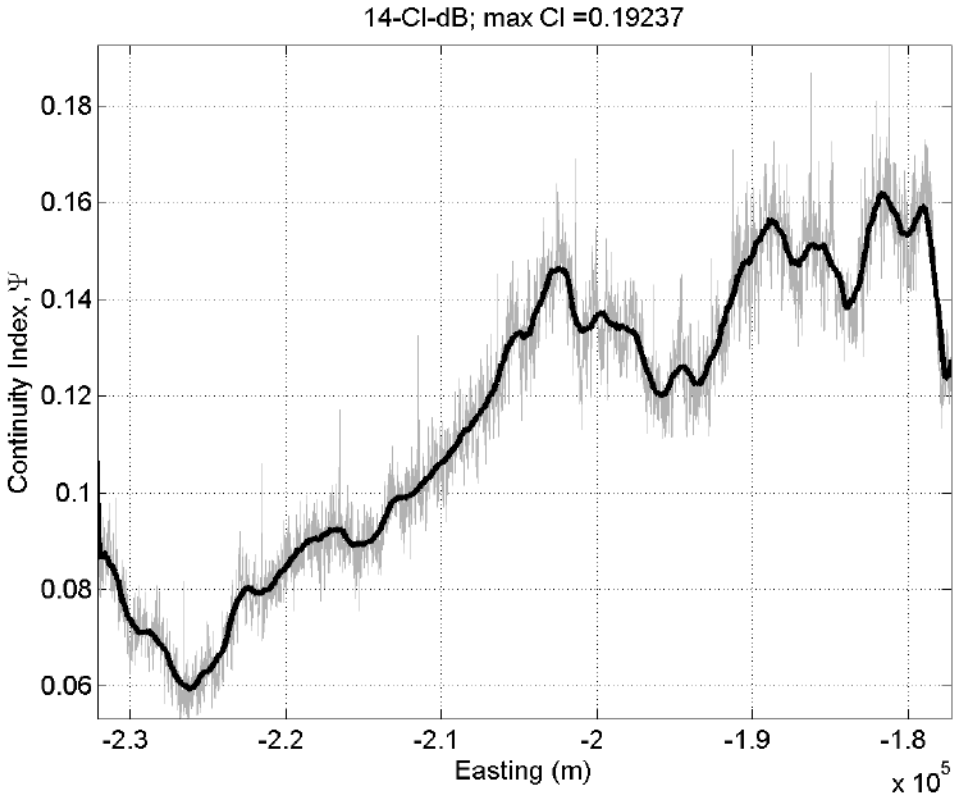
14-CI-dB; max CI =0.19237
Continuity Index, Ψ
0.18
0.16
0.14
0.12
0.1
0.08
0.06
-2.3
-2.2
-2.1
-2
-1.9
-1.8
Easting (m)
x 10^5

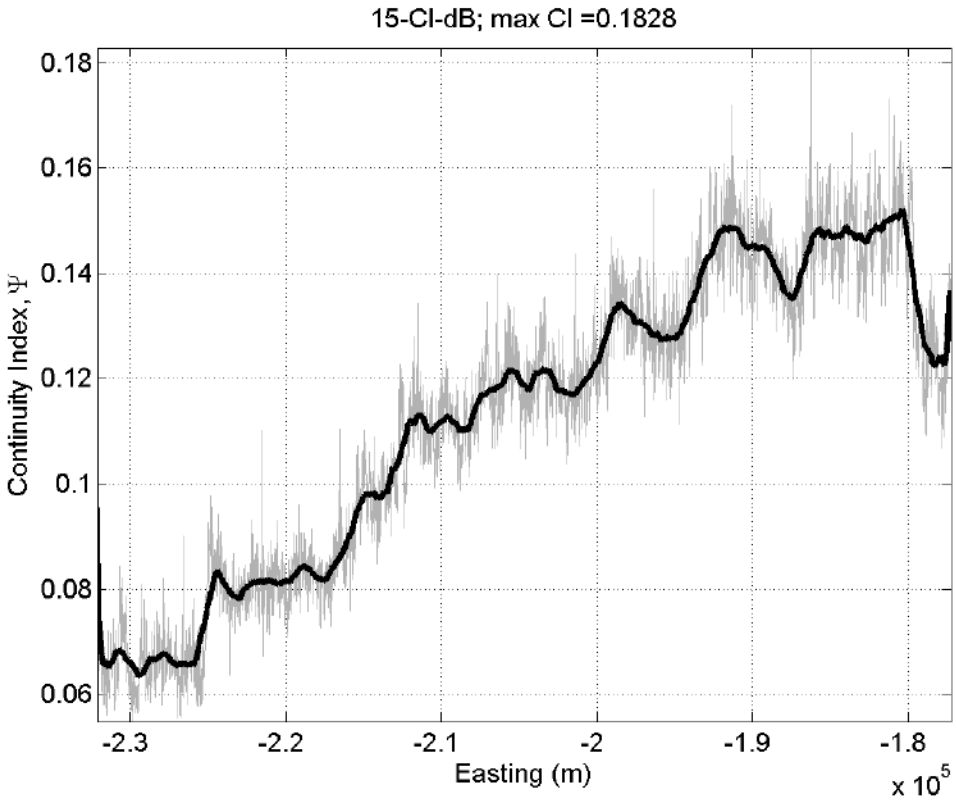
15-CI-dB; max CI =0.1828
Continuity Index, Ψ
0.18
0.16
0.14
0.12
0.1
0.08
0.06
-2.3
-2.2
-2.1
-2
-1.9
-1.8
Easting (m)
x 10^5

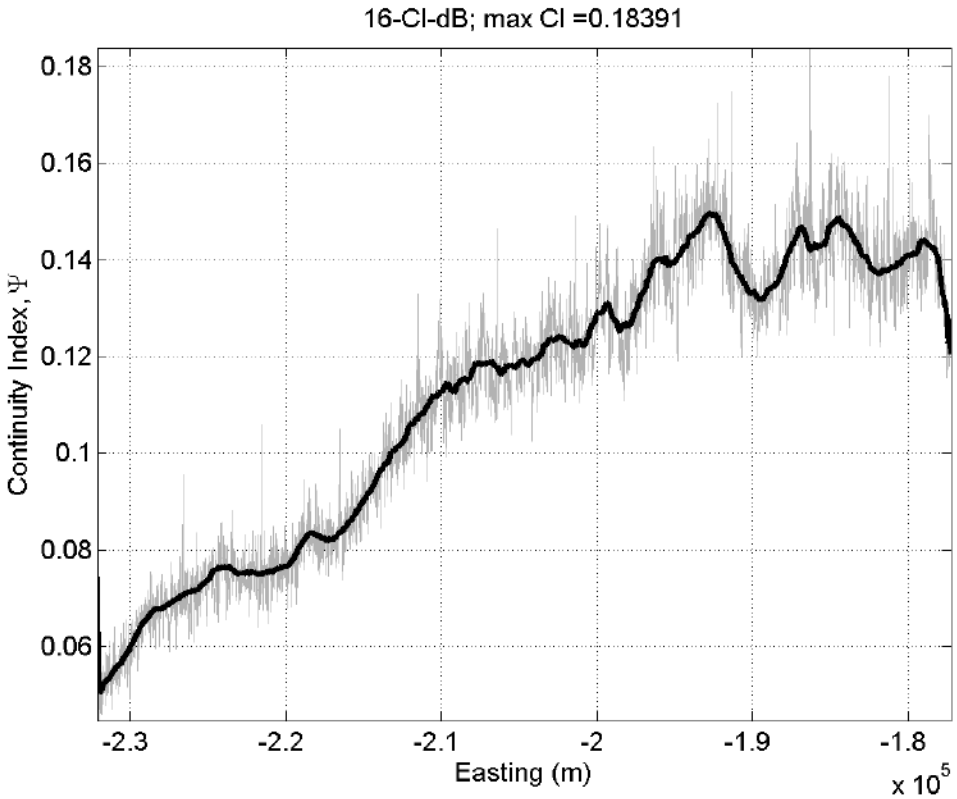
16-CI-dB; max CI =0.18391
Continuity Index, Ψ
0.18
0.16
0.14
0.12
0.1
0.08
0.06
-2.3
-2.2
-2.1
-2
-1.9
-1.8
Easting (m)
x 10^5

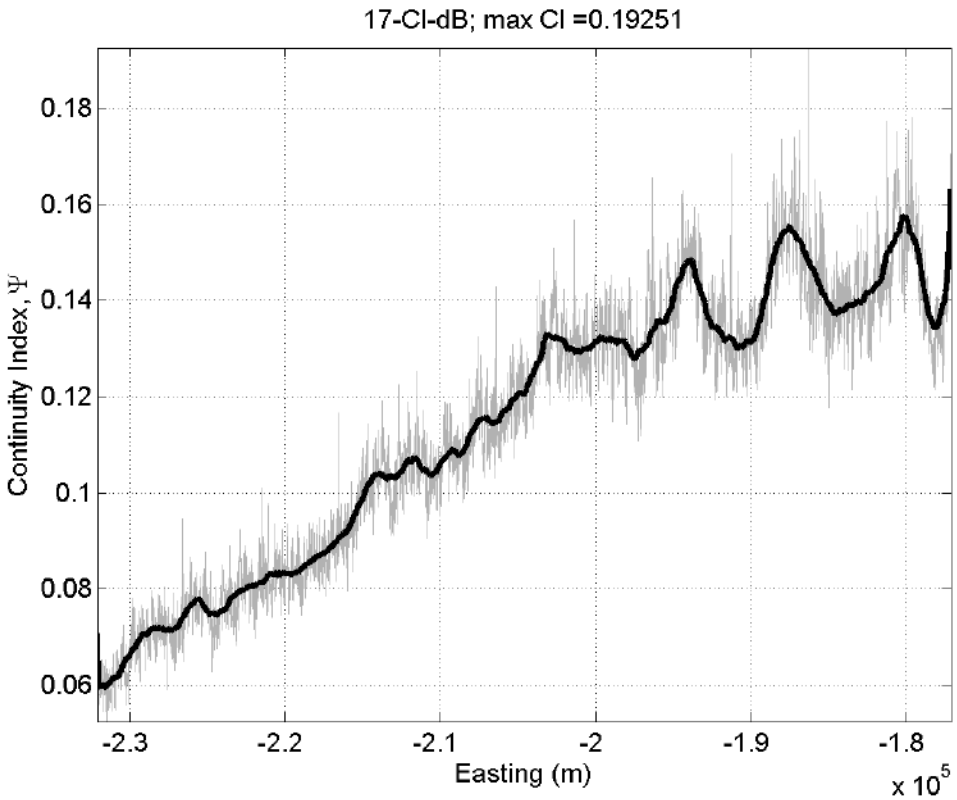
17-CI-dB; max CI =0.19251
Continuity Index, Ψ
0.18
0.16
0.14
0.12
0.1
0.08
0.06
-2.3
-2.2
-2.1
-2
-1.9
-1.8
Easting (m)
x 10^5

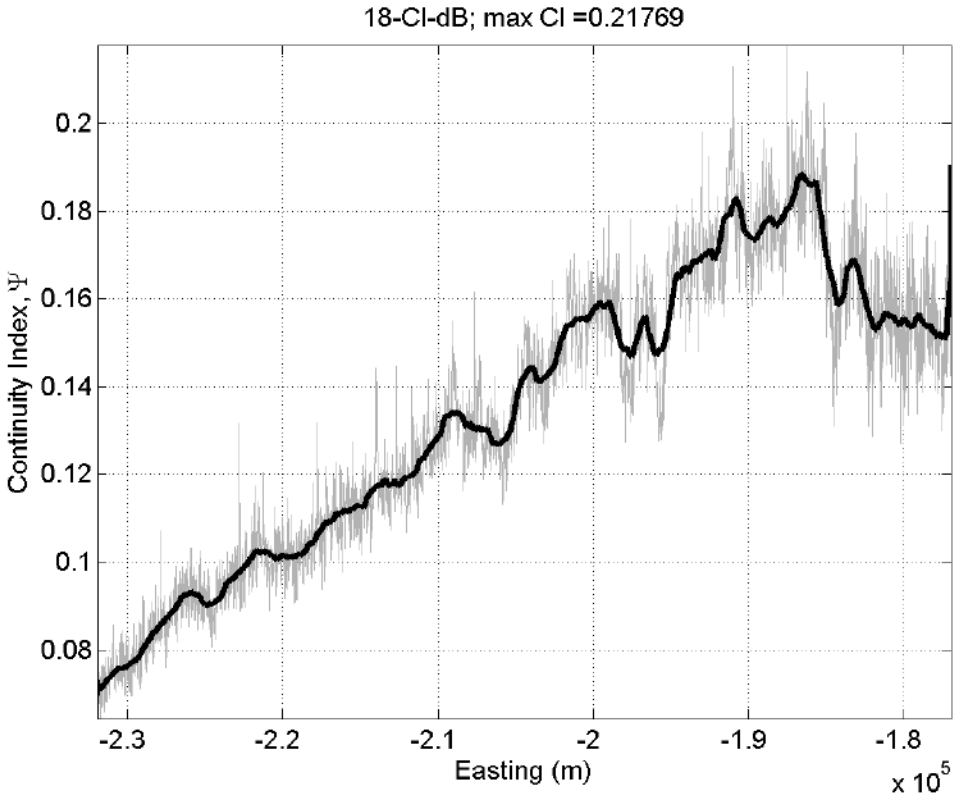
18-CI-dB; max CI =0.21769
Continuity Index, Ψ
0.2
0.18
0.16
0.14
0.12
0.1
0.08
-2.3
-2.2
-2.1
-2
-1.9
-1.8
Easting (m)
x 10^5

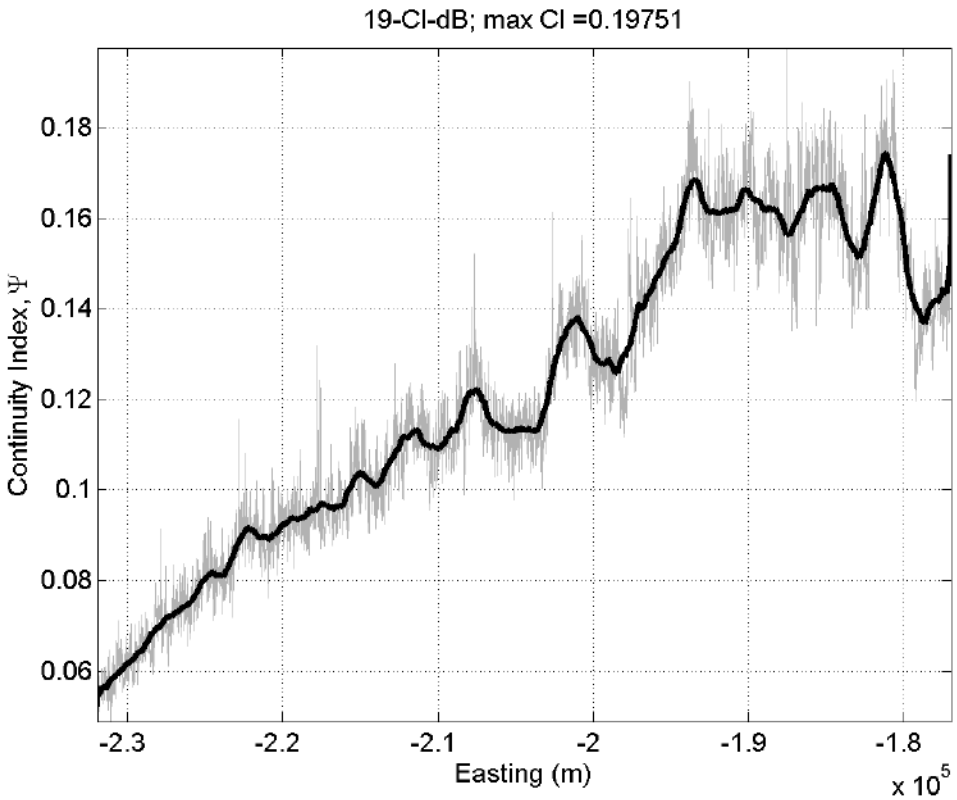
19-CI-dB; max CI =0.19751
Continuity Index, Ψ
0.18
0.16
0.14
0.12
0.1
0.08
0.06
-2.3
-2.2
-2.1
-2
-1.9
-1.8
Easting (m)
x 10^5

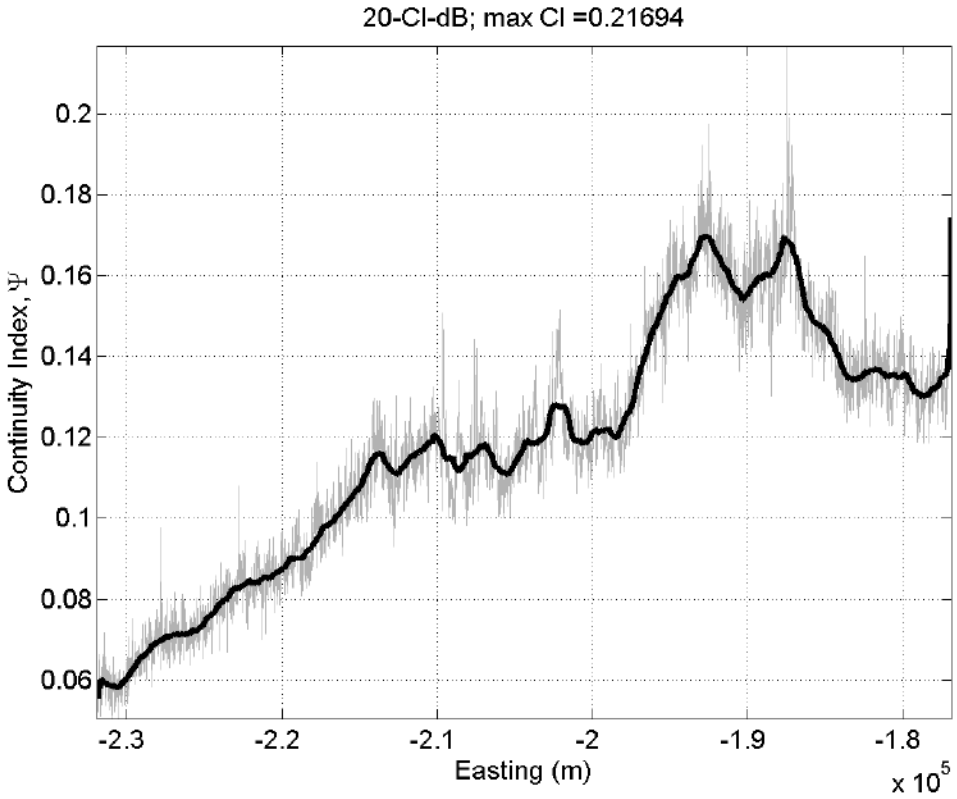
20-CI-dB; max CI =0.21694
Continuity Index, Ψ
0.2
0.18
0.16
0.14
0.12
0.1
0.08
0.06
-2.3
-2.2
-2.1
-2
-1.9
-1.8
Easting (m)
x 10^5

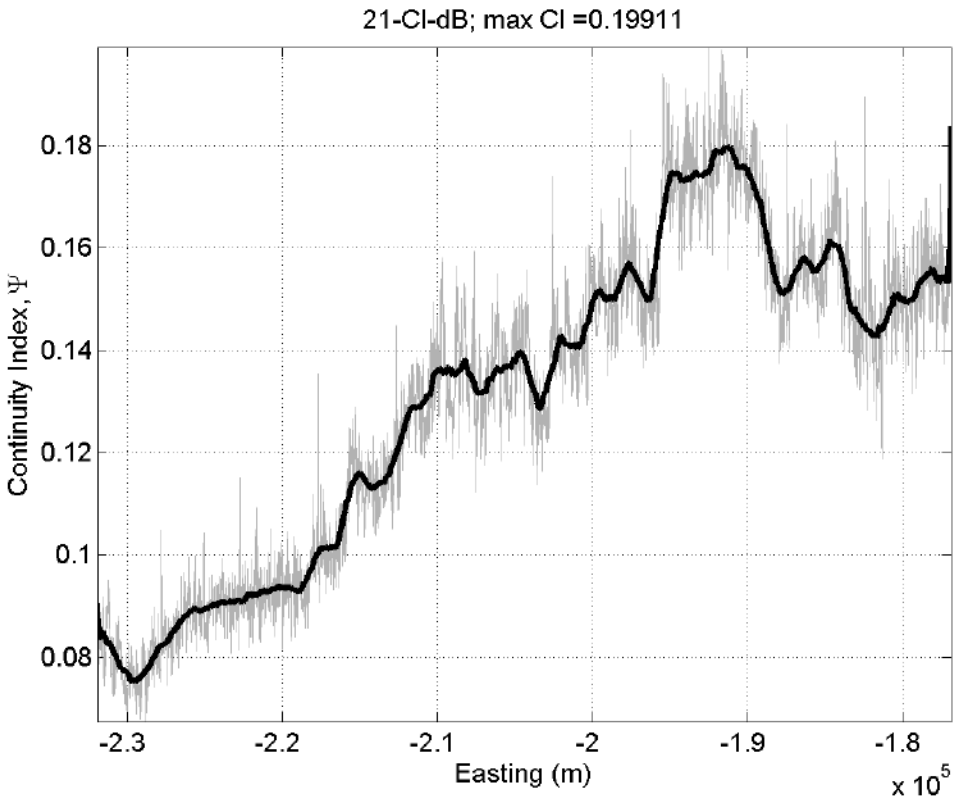
21-CI-dB; max CI =0.19911
Continuity Index, Ψ
0.18
0.16
0.14
0.12
0.1
0.08
-2.3
-2.2
-2.1
-2
-1.9
-1.8
Easting (m)
x 10^5

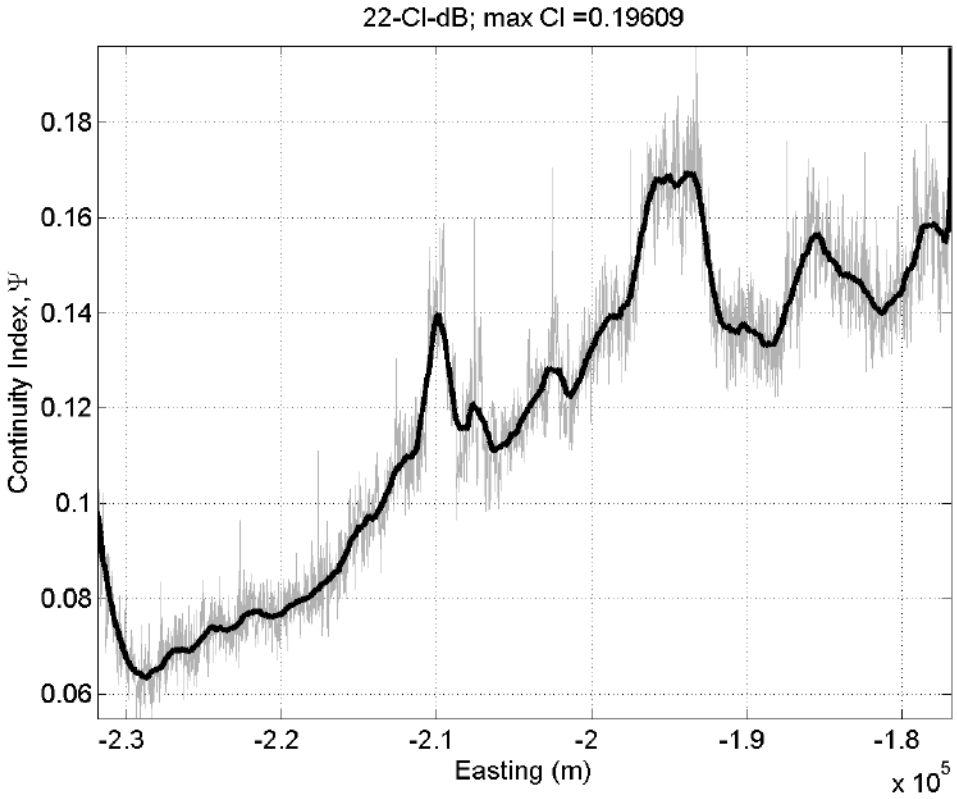
22-CI-dB; max CI =0.19609
Continuity Index, Ψ
0.18
0.16
0.14
0.12
0.1
0.08
0.06
-2.3
-2.2
-2.1
-2
-1.9
-1.8
Easting (m)
x 10^5

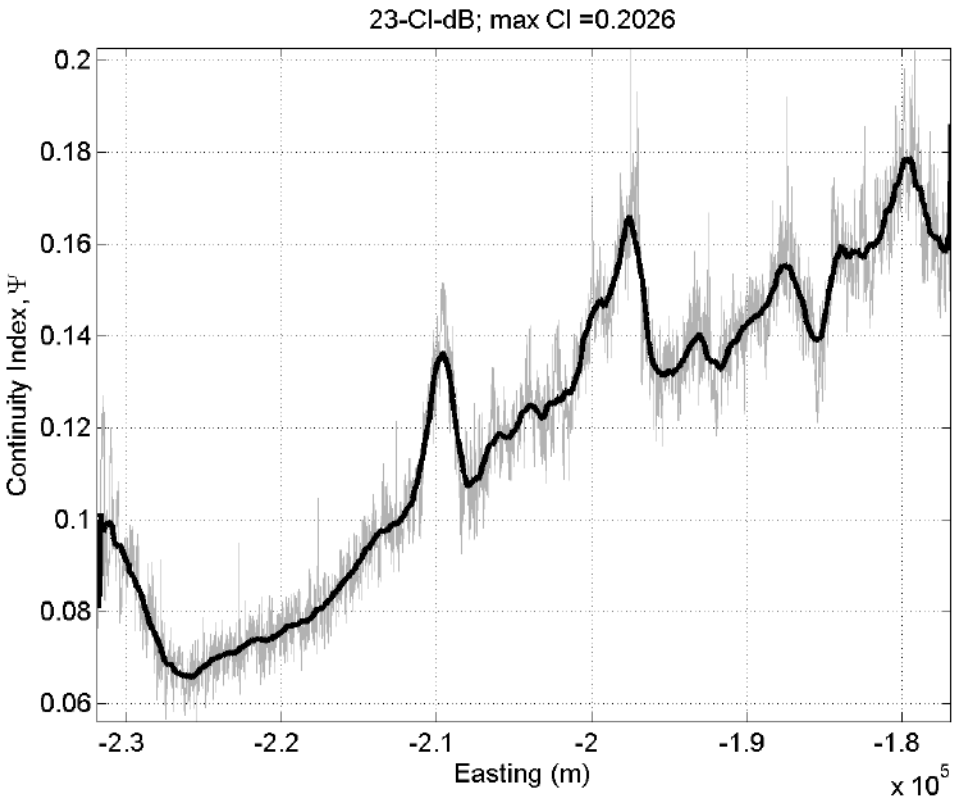
23-CI-dB; max CI =0.2026
Continuity Index, Ψ
0.2
0.18
0.16
0.14
0.12
0.1
0.08
0.06
-2.3
-2.2
-2.1
-2
-1.9
-1.8
Easting (m)
x 10^5

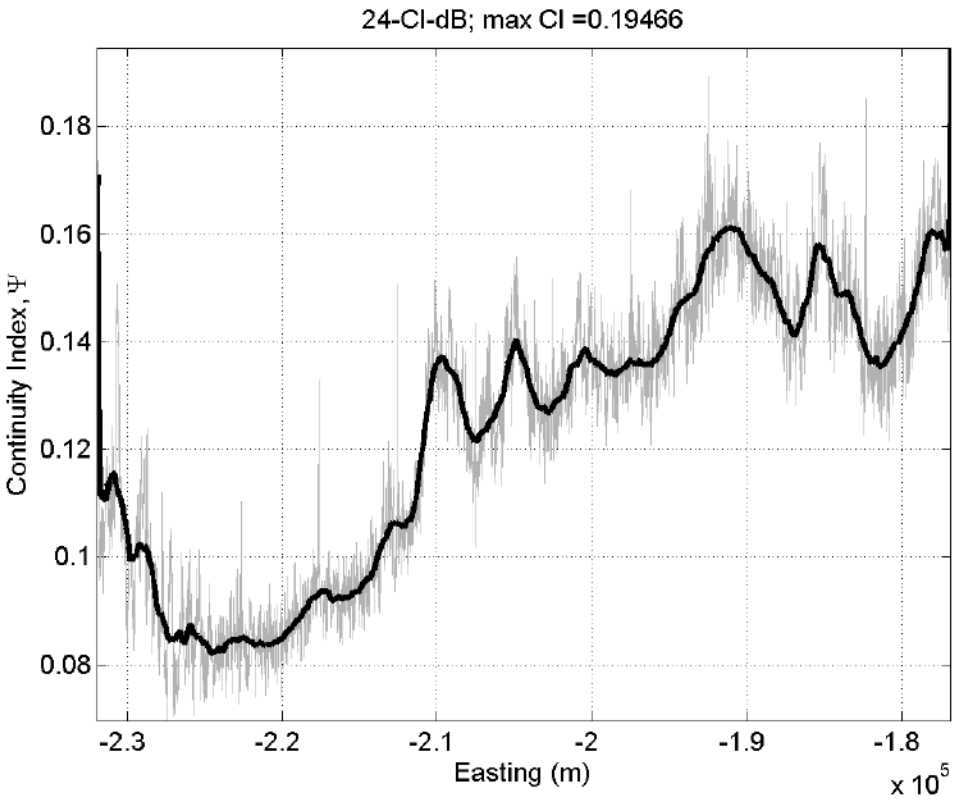
24-CI-dB; max CI =0.19466
Continuity Index, Ψ
0.18
0.16
0.14
0.12
0.1
0.08
-2.3
-2.2
-2.1
-2
-1.9
-1.8
Easting (m)
x 10^5

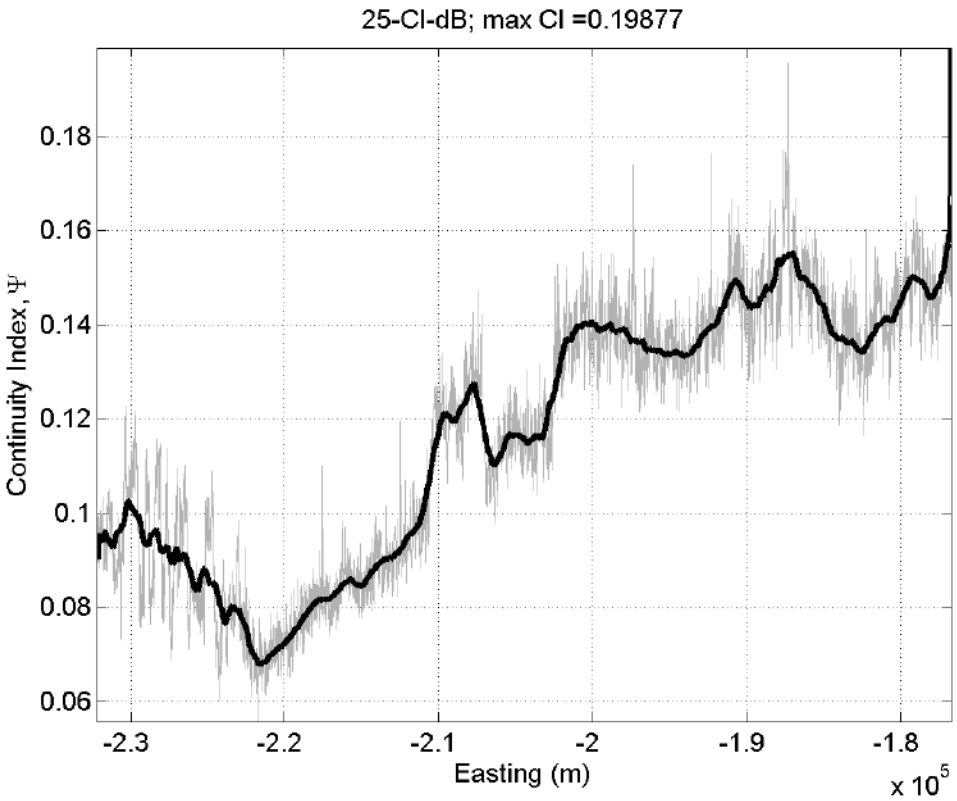
25-CI-dB; max CI =0.19877
Continuity Index, Ψ
0.18
0.16
0.14
0.12
0.1
0.08
0.06
-2.3
-2.2
-2.1
-2
-1.9
-1.8
Easting (m)
x 10^5

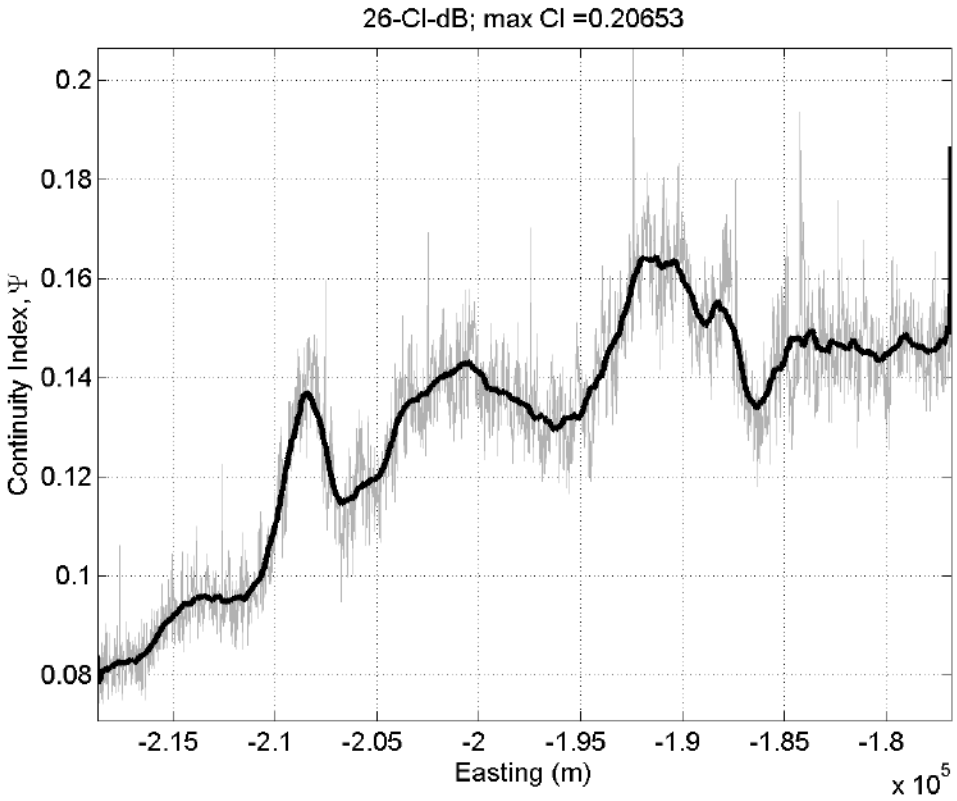
26-CI-dB; max CI =0.20653
Continuity Index, Ψ
0.2
0.18
0.16
0.14
0.12
0.1
0.08
-2.15
-2.1
-2.05
-2
-1.95
-1.9
-1.85
-1.8
Easting (m)
x 10^5

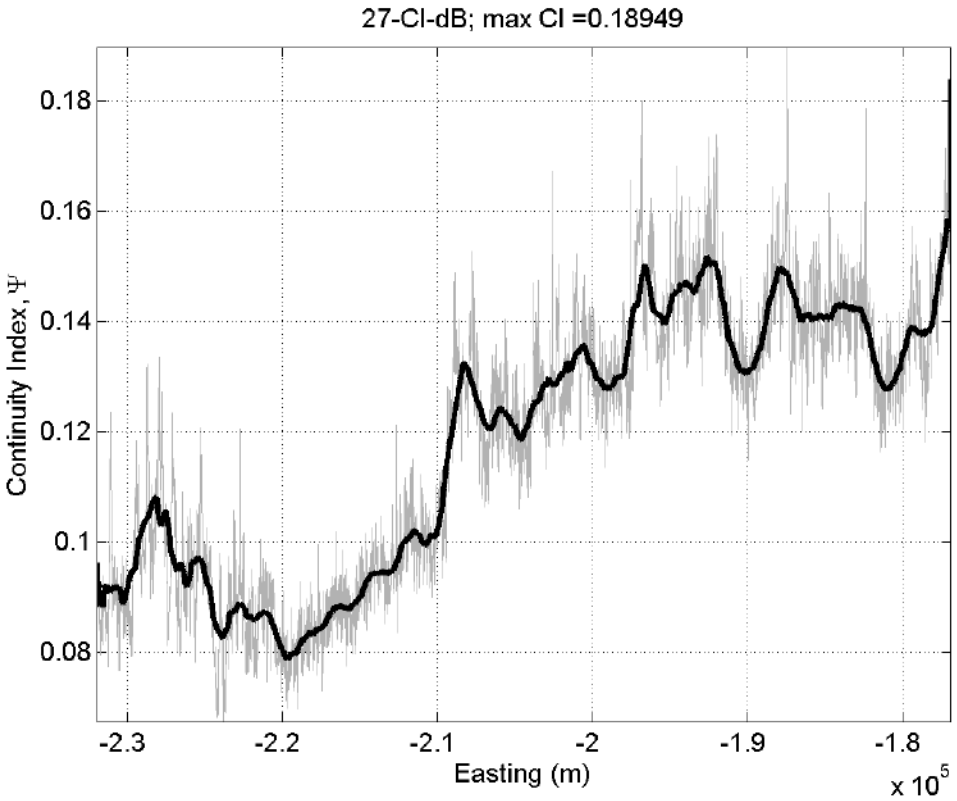
27-CI-dB; max CI =0.18949
Continuity Index, Ψ
0.18
0.16
0.14
0.12
0.1
0.08
-2.3
-2.2
-2.1
-2
-1.9
-1.8
Easting (m)
x 10^5

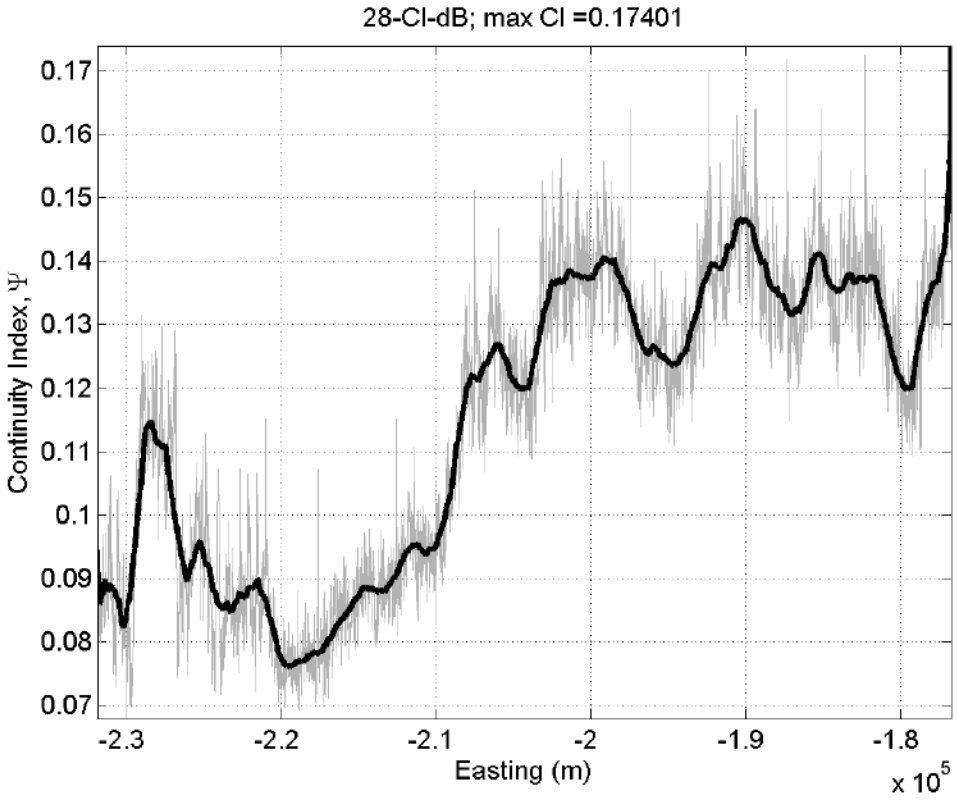
28-CI-dB; max CI =0.17401
Continuity Index, Ψ
0.17
0.16
0.15
0.14
0.13
0.12
0.11
0.1
0.09
0.08
0.07
-2.3
-2.2
-2.1
-2
-1.9
-1.8
Easting (m)
x 10^5

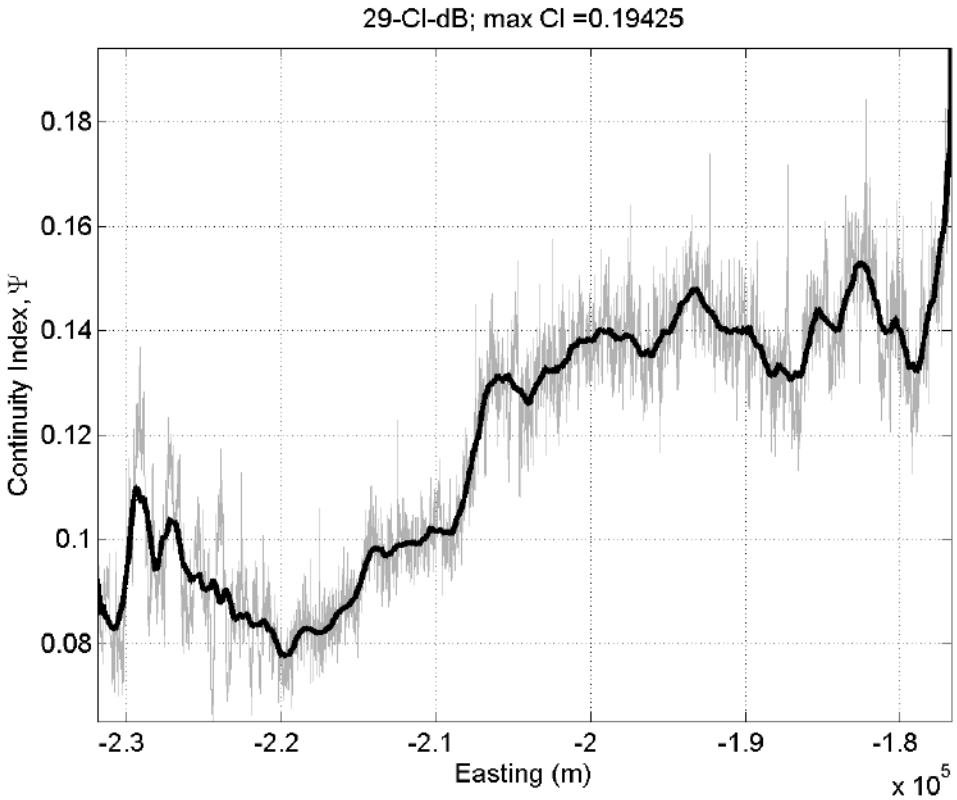
29-CI-dB; max CI =0.19425
Continuity Index, Ψ
0.18
0.16
0.14
0.12
0.1
0.08
-2.3
-2.2
-2.1
-2
-1.9
-1.8
Easting (m)
x 10^5

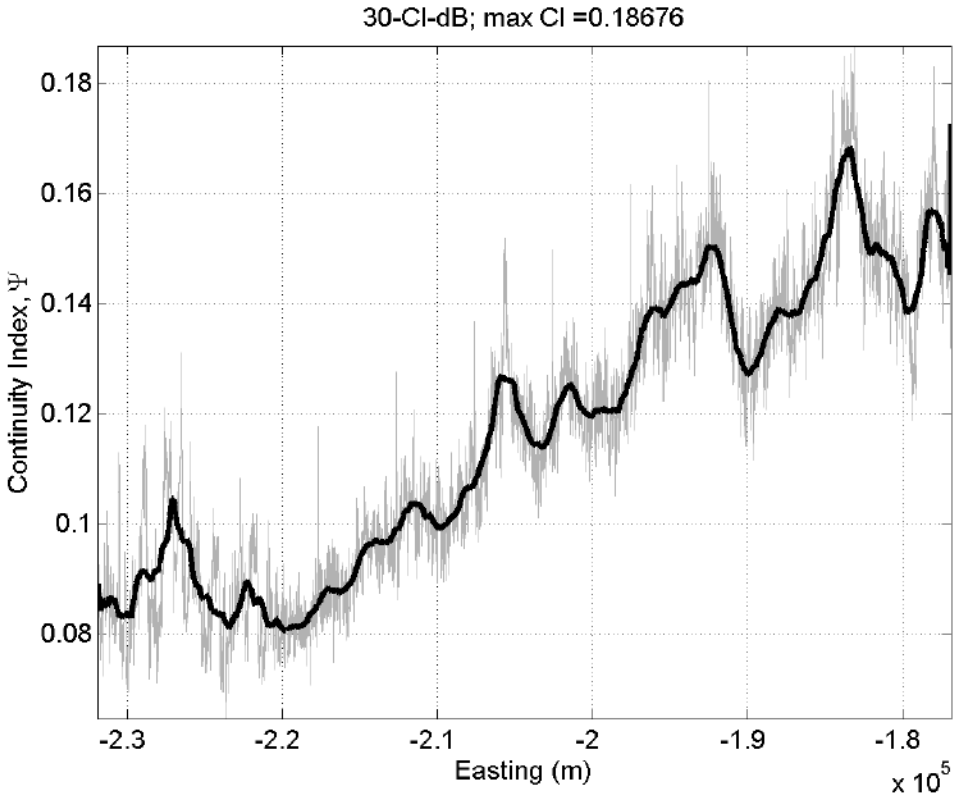
30-CI-dB; max CI =0.18676
Continuity Index, Ψ
0.18
0.16
0.14
0.12
0.1
0.08
-2.3
-2.2
-2.1
-2
-1.9
-1.8
Easting (m)
x 10^5

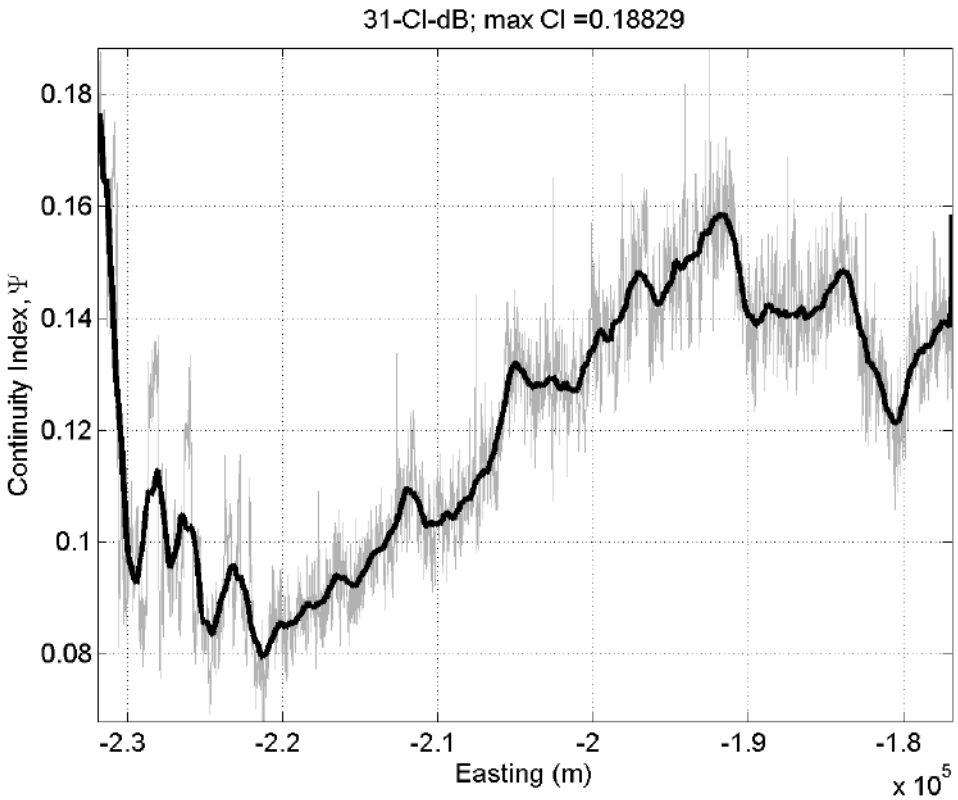
31-CI-dB; max CI =0.18829
Continuity Index, Ψ
0.18
0.16
0.14
0.12
0.1
0.08
-2.3
-2.2
-2.1
-2
-1.9
-1.8
Easting (m)
x 10^5

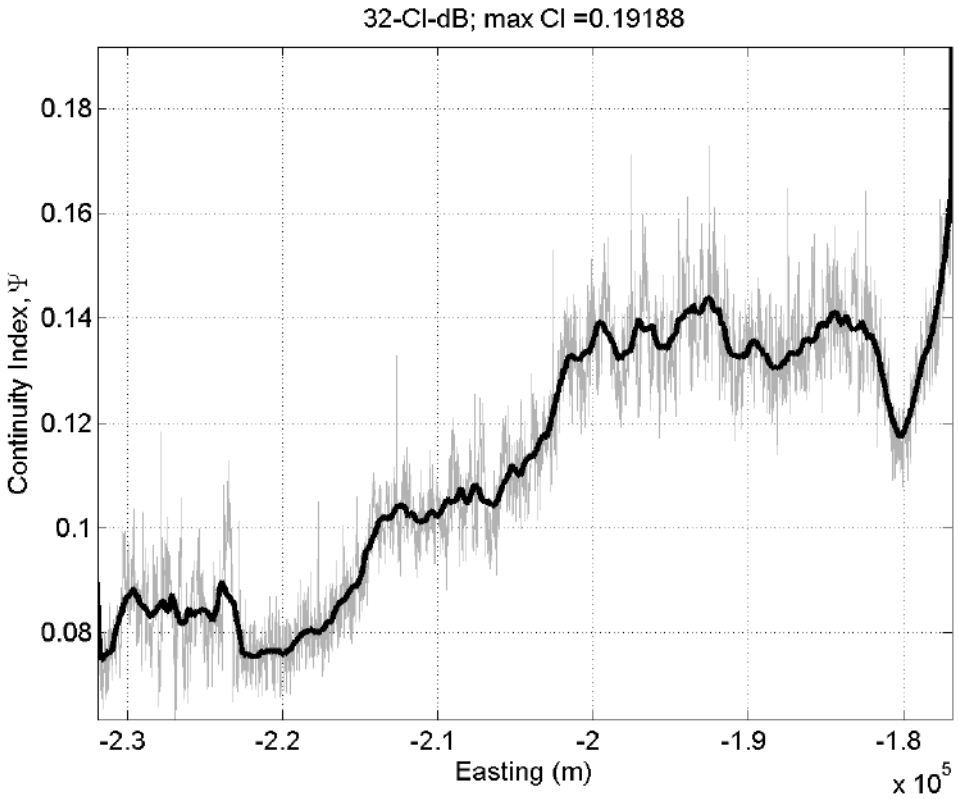
32-CI-dB; max CI =0.19188
Continuity Index, Ψ
0.18
0.16
0.14
0.12
0.1
0.08
-2.3
-2.2
-2.1
-2
-1.9
-1.8
Easting (m)
x 10^5

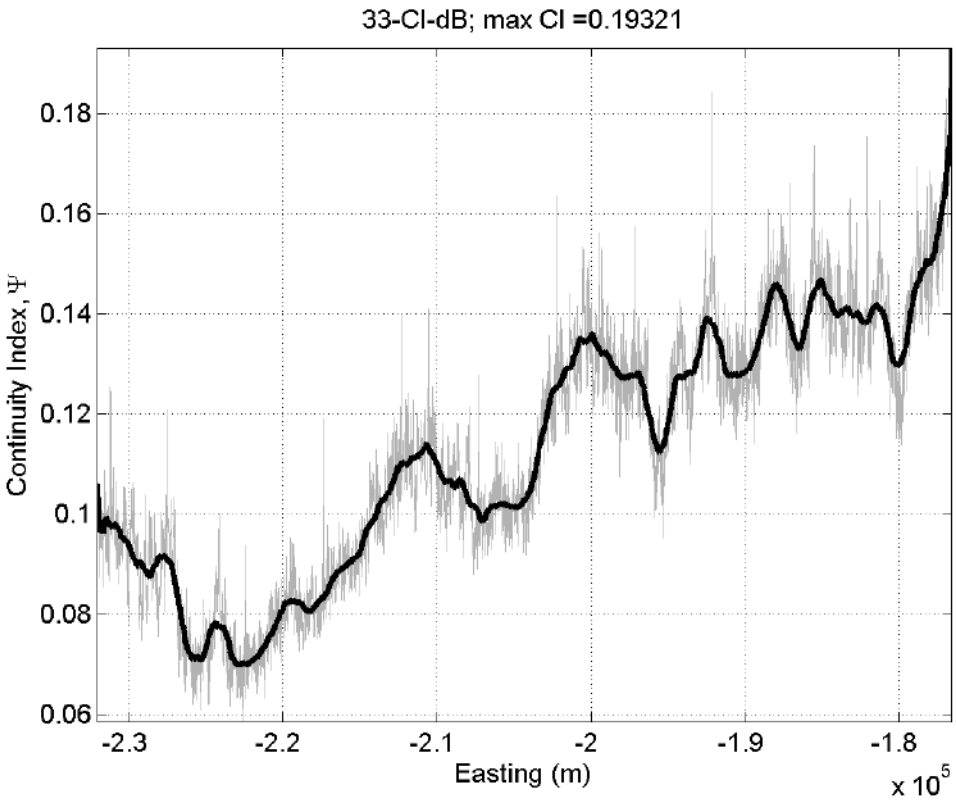
33-CI-dB; max CI =0.19321
Continuity Index, Ψ
0.18
0.16
0.14
0.12
0.1
0.08
0.06
-2.3
-2.2
-2.1
-2
-1.9
-1.8
Easting (m)
x 10^5

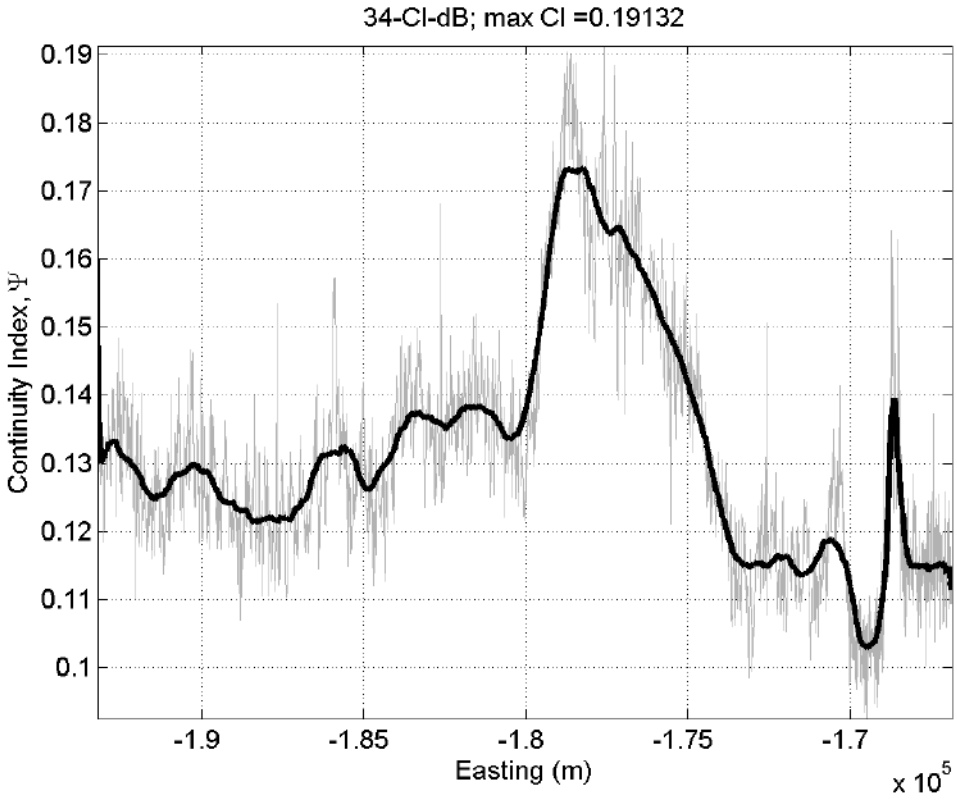
34-CI-dB; max CI =0.19132
Continuity Index, Ψ
0.19
0.18
0.17
0.16
0.15
0.14
0.13
0.12
0.11
0.1
-1.9
-1.85
-1.8
-1.75
-1.7
Easting (m)
x 10^5

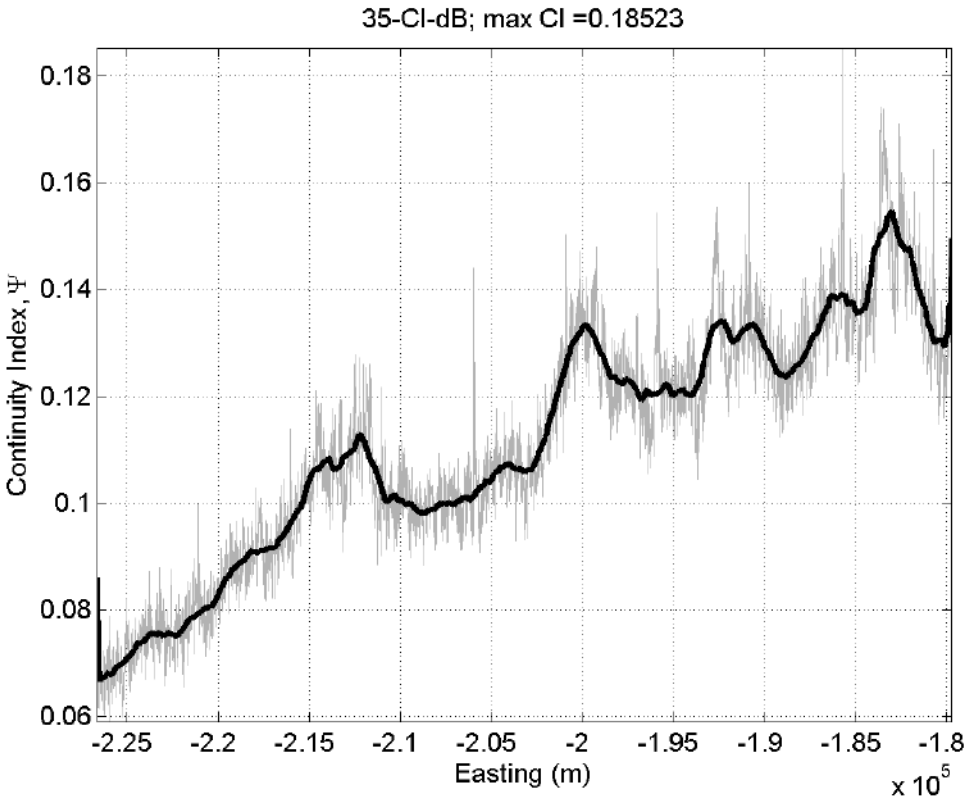
35-CI-dB; max CI =0.18523
Continuity Index, Ψ
0.18
0.16
0.14
0.12
0.1
0.08
0.06
-2.25
-2.2
-2.15
-2.1
-2.05
-2
-1.95
-1.9
-1.85
-1.8
Easting (m)
x 10^5

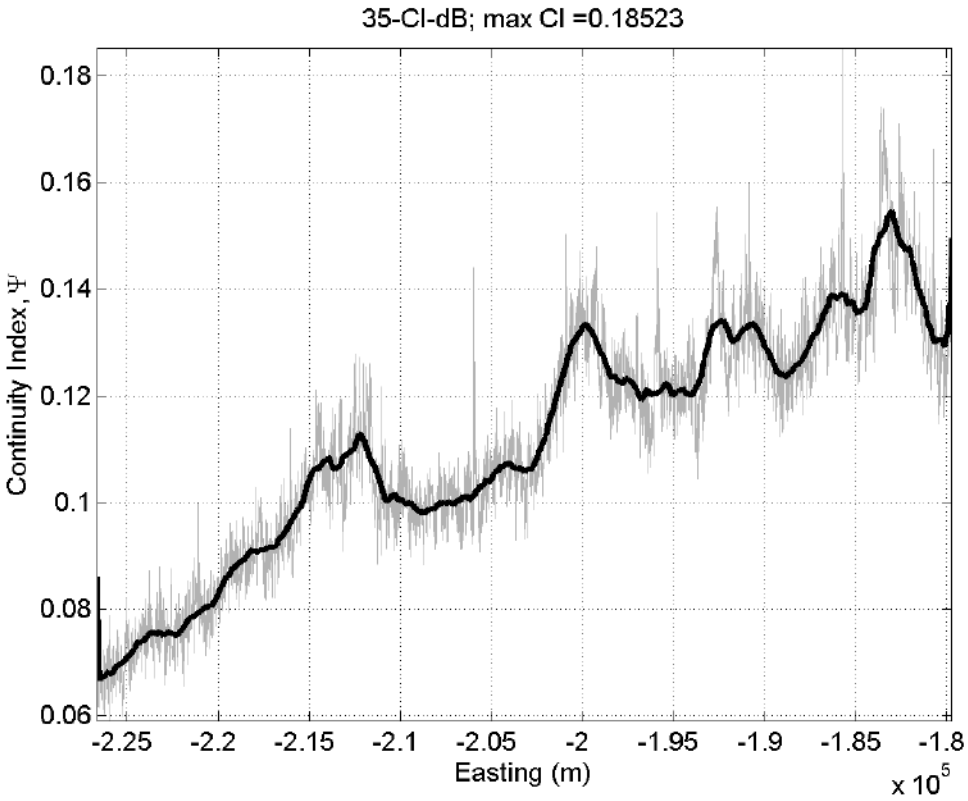
35-CI-dB; max CI =0.18523
Continuity Index, Ψ
0.18
0.16
0.14
0.12
0.1
0.08
0.06
-2.25
-2.2
-2.15
-2.1
-2.05
-2
-1.95
-1.9
-1.85
-1.8
Easting (m)
x 10^5

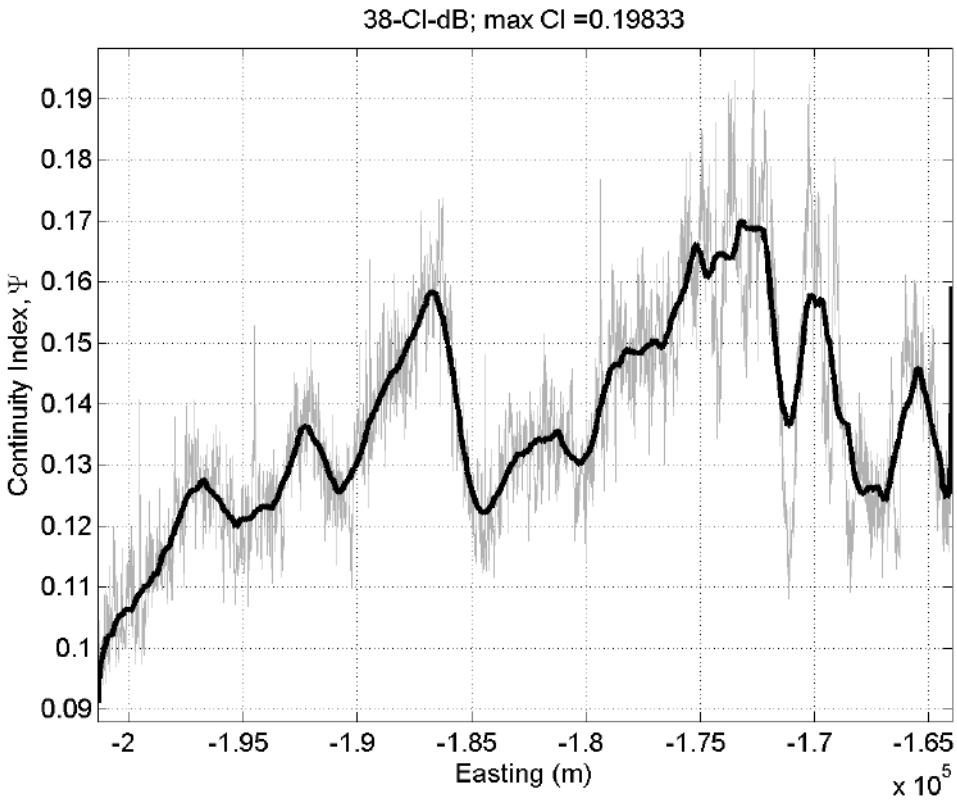
38-CI-dB; max CI =0.19833
Continuity Index, Ψ
0.19
0.18
0.17
0.16
0.15
0.14
0.13
0.12
0.11
0.1
0.09
-2
-1.95
-1.9
-1.85
-1.8
-1.75
-1.7
-1.65
Easting (m)
x 10^5

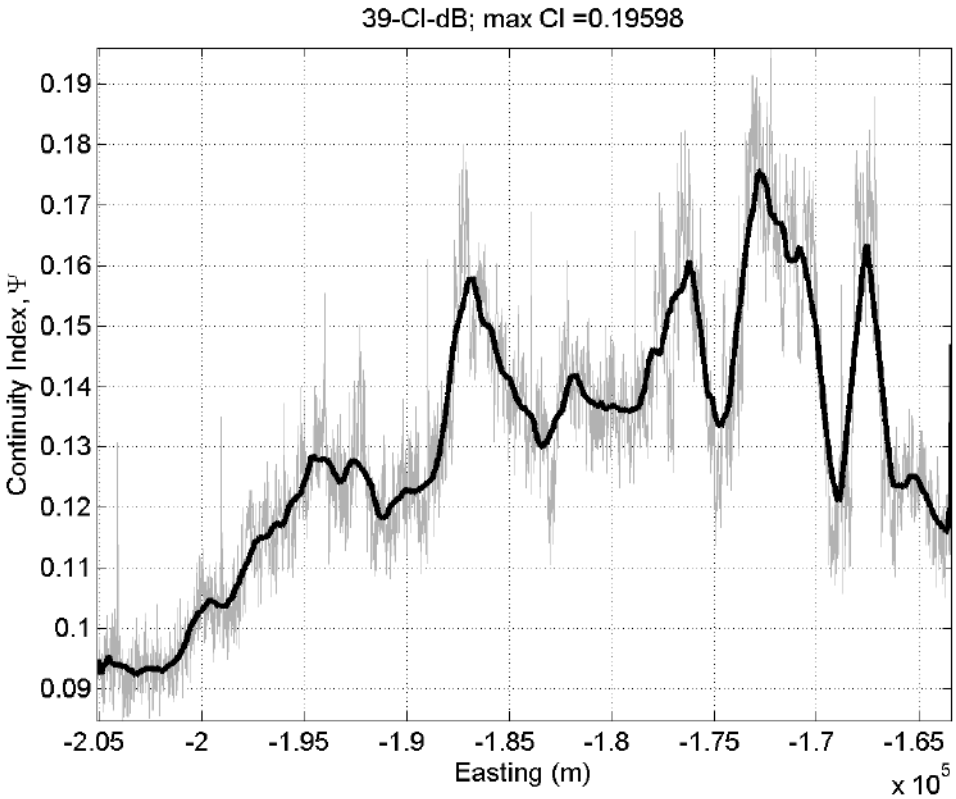
39-CI-dB; max CI =0.19598
Continuity Index, Ψ
0.19
0.18
0.17
0.16
0.15
0.14
0.13
0.12
0.11
0.1
0.09
-2.05
-2
-1.95
-1.9
-1.85
-1.8
-1.75
-1.7
-1.65
Easting (m)
x 10^5

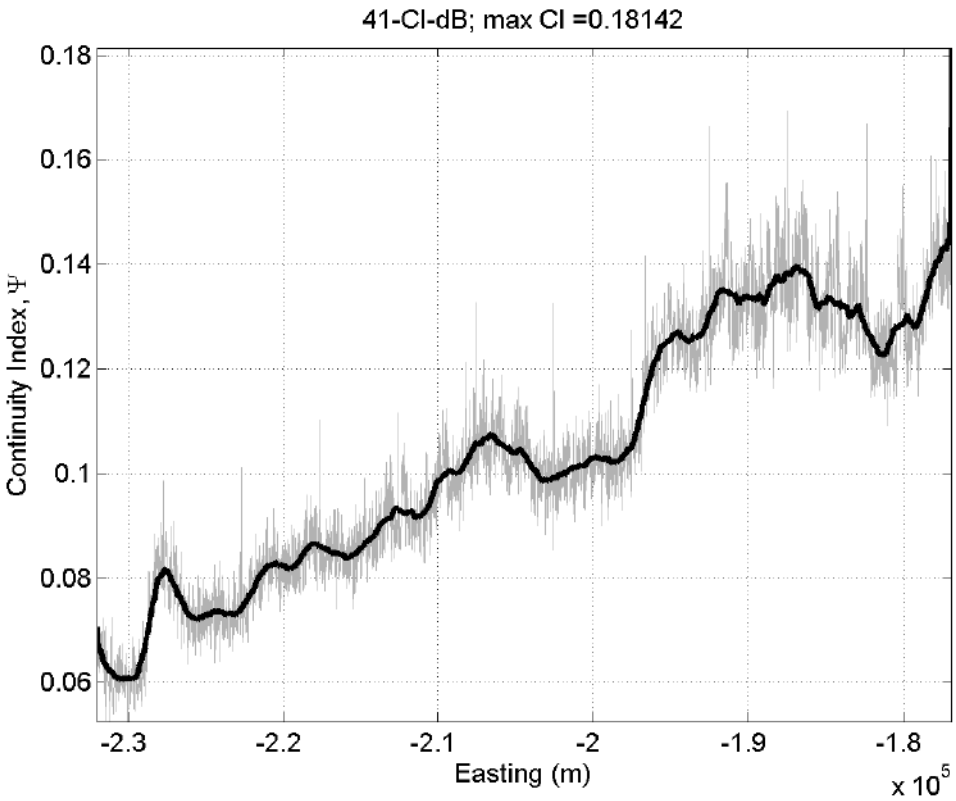
41-CI-dB; max CI =0.18142
Continuity Index, Ψ
0.18
0.16
0.14
0.12
0.1
0.08
0.06
-2.3
-2.2
-2.1
-2
-1.9
-1.8
Easting (m)
x 10^5

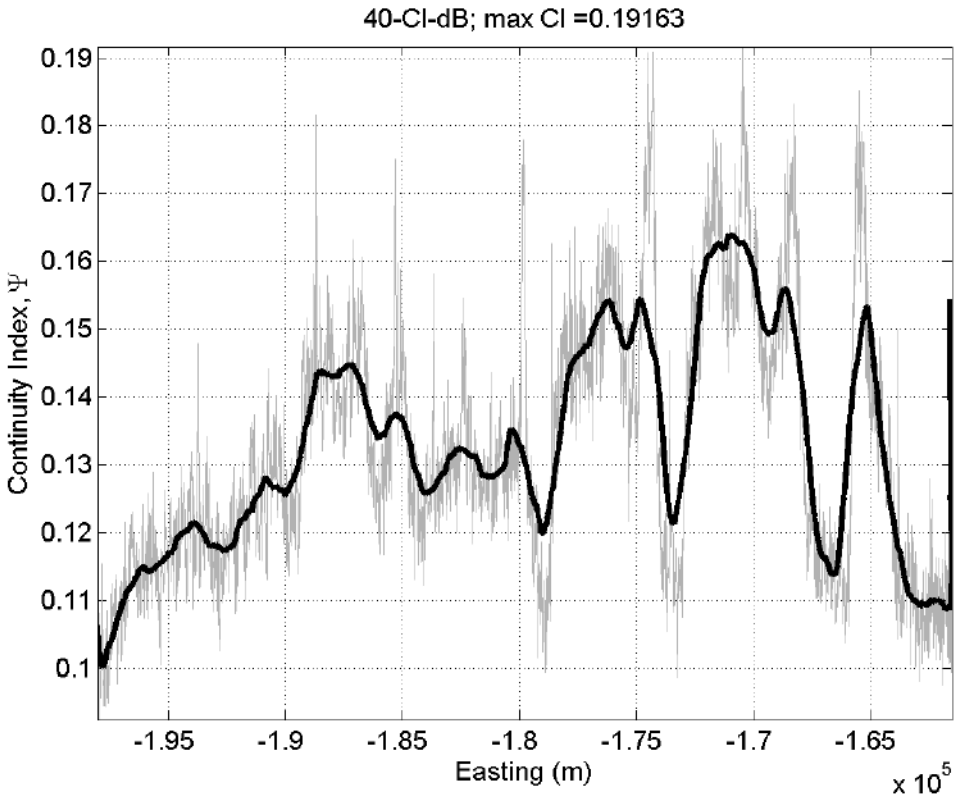
40-CI-dB; max CI =0.19163
Continuity Index, Ψ
0.19
0.18
0.17
0.16
0.15
0.14
0.13
0.12
0.11
0.1
-1.95
-1.9
-1.85
-1.8
-1.75
-1.7
-1.65
Easting (m)
x 10^5

APPENDIX C

HINDMARSH TEST

This appendix presents results from an additional test for alignment between englacial streamlines and layers. Hindmarsh et al. (2006) found that modelled, accumulation zone isochrones (same age layers depicted in radiostratigraphy) and streamlines are closely related when bed topography wavelength divided by ice thickness is small compared to ice velocity divided by accumulation rate, i.e. layers approximate particle paths where $|{}^{u}/_{\dot{a}}| > {}^{\lambda}/_{H}$. Ice velocity ($u$) was defined by data from Joughin et al. (2010), surface mass balance ($|\dot{a}|$) was defined by data from Ettema et al. (2009), I defined bedrock topography wavelength (λ) by measuring the horizontal distance between peaks in bedrock terrain depicted in radargrams, and ice thickness (H) was defined by differencing ice surface from bedrock elevations from the radargram (Leuschen, 2011). For every radargram, on the western portion of the flightline where radar layers were traced, $|{}^{u}/_{\dot{a}}| > {}^{\lambda}/_{H}$.

Ettema, J., Van Den Broeke, M. R., Van Meijgaard, E., Van De Berg, W. J., Bamber, J. L., Box, J. E., et al. (2009). Higher surface mass balance of the Greenland ice sheet revealed by high-resolution climate modeling. Geophys. Res. Lett. 36, 1–5. doi:10.1029/2009GL038110.

Hindmarsh, R. C. A., Leysinger Vieli, G. J. M. C., Raymond, M. J., and Gudmundsson, G. H. (2006). Draping or overriding: The effect of horizontal stress gradients on internal layer architecture in ice sheets. J. Geophys. Res. Earth Surf. 111, 1–17. doi:10.1029/2005JF000309.

Joughin, I., Smith, B. E., Howat, I. M., Scambos, T., and Moon, T. (2010). Greenland flow variability from ice-sheet-wide velocity mapping. J. Glaciol. 56, 415–430. doi:10.3189/002214310792447734.

Leuschen, C. (2011). IceBridge MCoRDS L1B Geolocated Radar Echo Strength Profiles, Version 2, Boulder, Colorado USA, NASA Snow and Ice Data Center Distributed Active Archive Center. doi:http://dx.doi.org/10.5067/90S1XZRBAX5N.

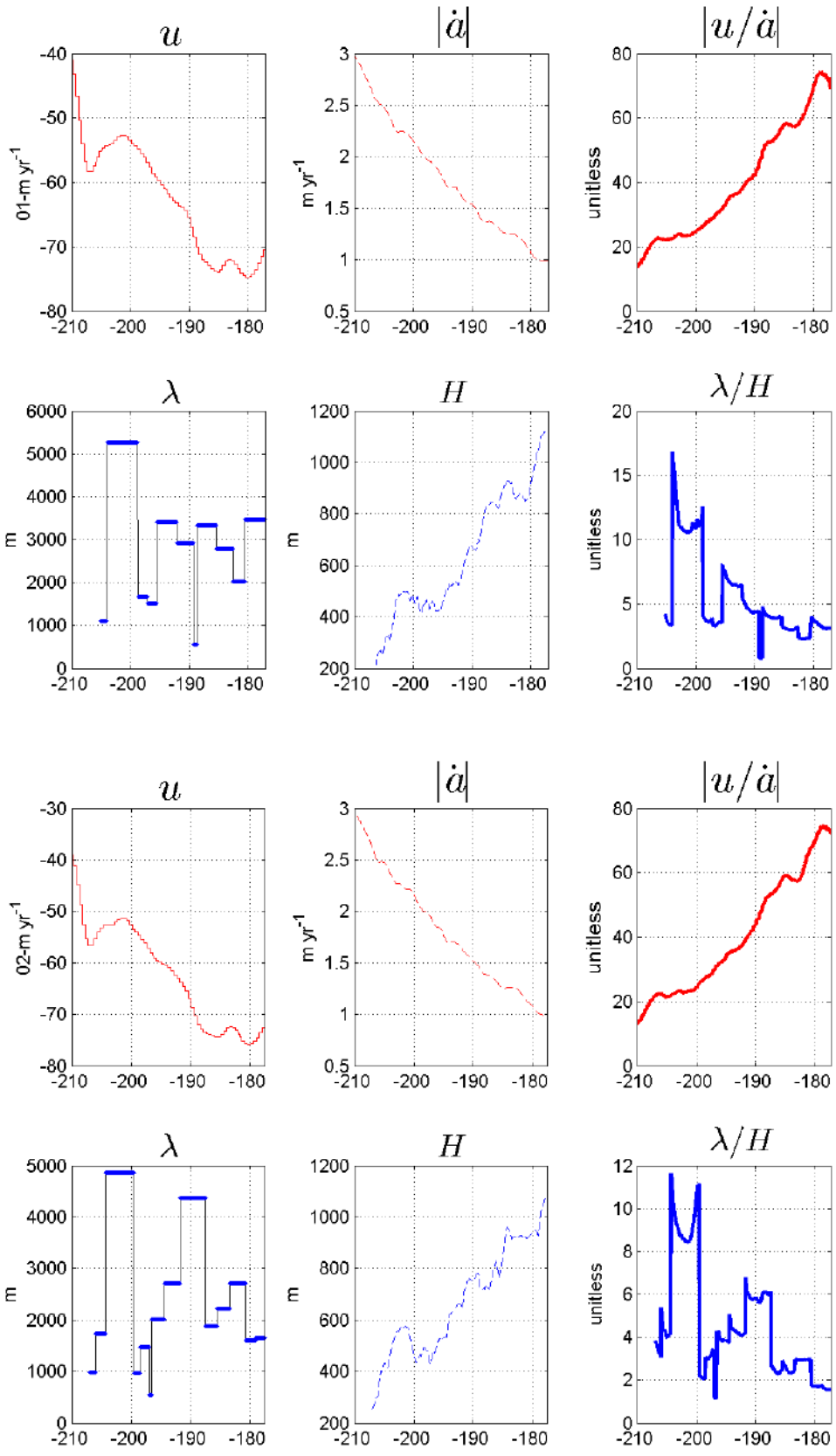
u
$|\dot{a}|$
$|u/\dot{a}|$
01-m yr^{-1}
m yr^{-1}
unitless
λ
H
λ/H
m
m
unitless
u
$|\dot{a}|$
$|u/\dot{a}|$
02-m yr^{-1}
m yr^{-1}
unitless
λ
H
λ/H
m
m
unitless

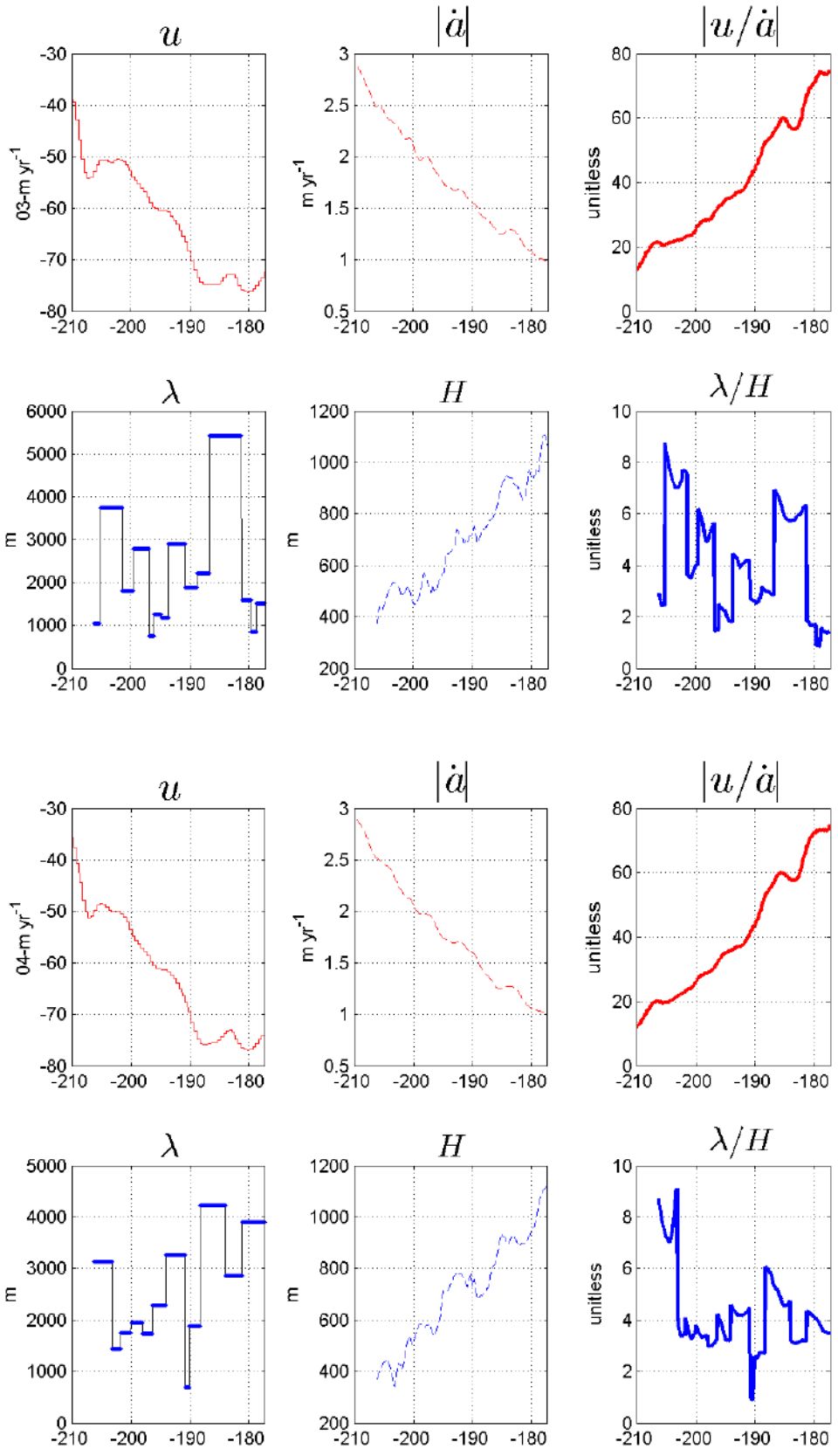
u
$|\dot{a}|$
$|u/\dot{a}|$
03-m yr^{-1}
m yr^{-1}
unitless
λ
H
λ/H
m
m
unitless
u
$|\dot{a}|$
$|u/\dot{a}|$
04-m yr^{-1}
m yr^{-1}
unitless
λ
H
λ/H
m
m
unitless

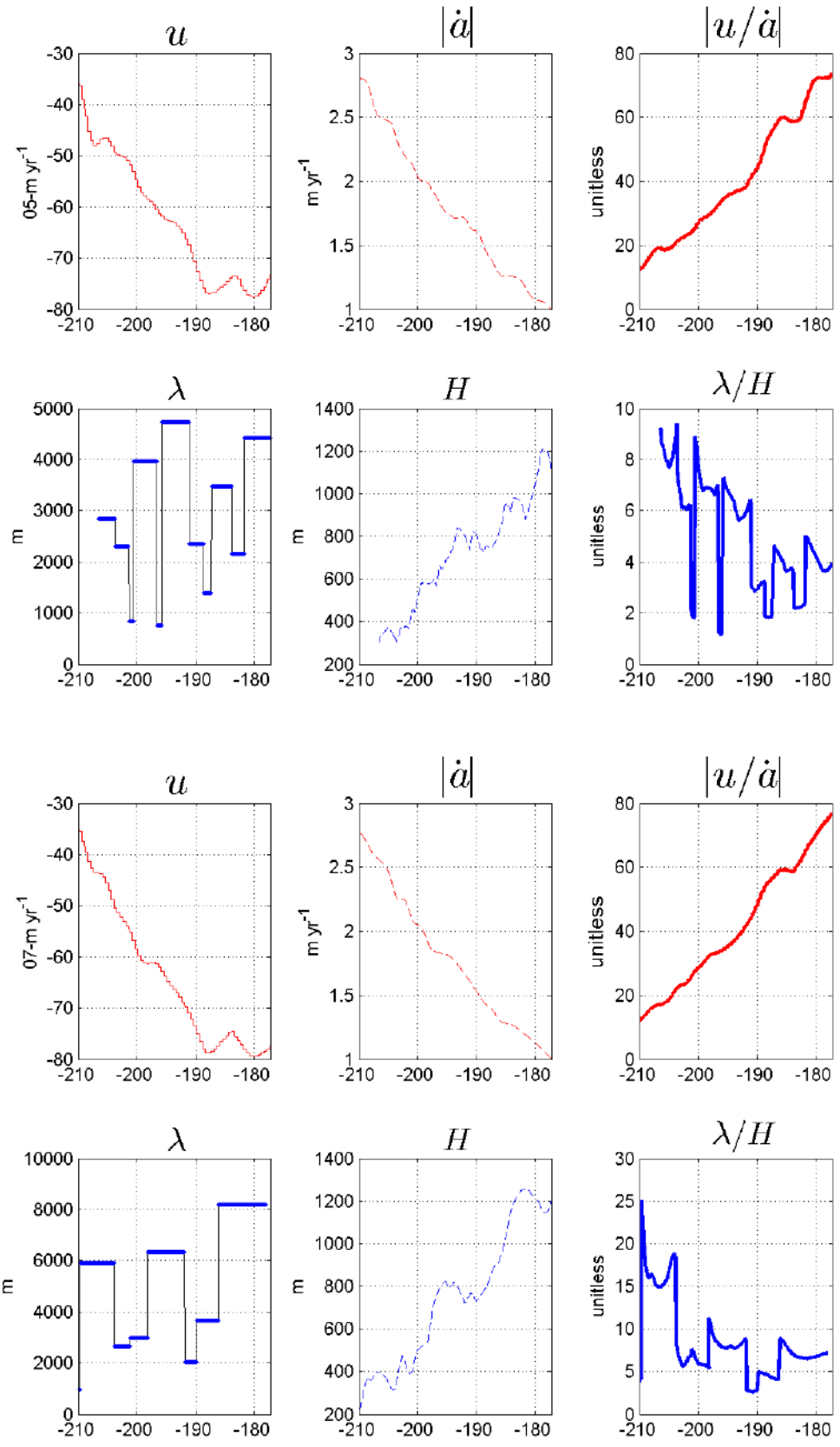
u
$|\dot{a}|$
$|u/\dot{a}|$
05-m yr^{-1}
m yr^{-1}
unitless
λ
H
λ/H
m
m
unitless
u
$|\dot{a}|$
$|u/\dot{a}|$
07-m yr^{-1}
m yr^{-1}
unitless
λ
H
λ/H
m
m
unitless

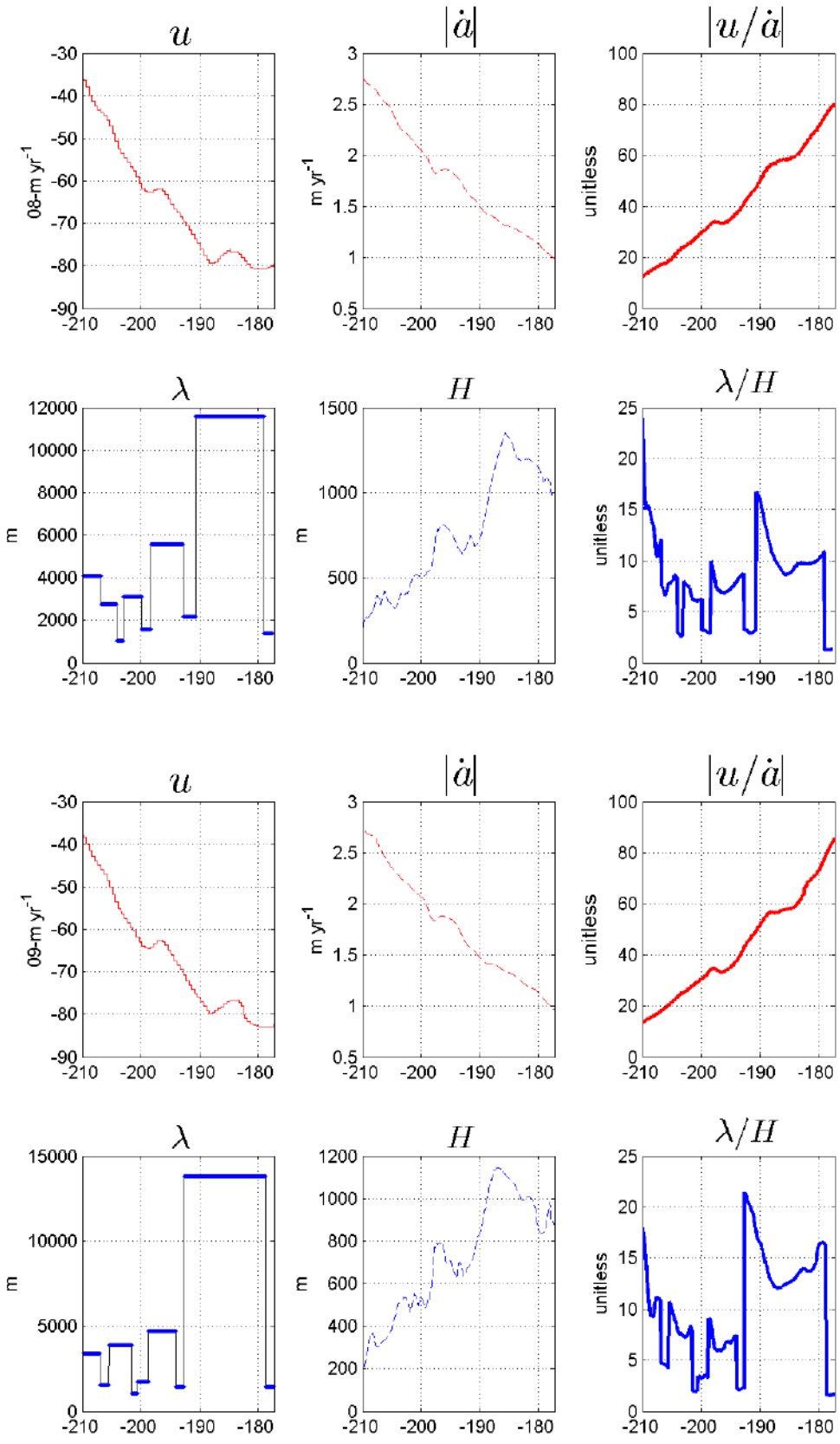
u
$|\dot{a}|$
$|u/\dot{a}|$
08-m yr^{-1}
m yr^{-1}
unitless
λ
H
λ/H
m
m
unitless
u
$|\dot{a}|$
$|u/\dot{a}|$
09-m yr^{-1}
m yr^{-1}
unitless
λ
H
λ/H
m
m
unitless

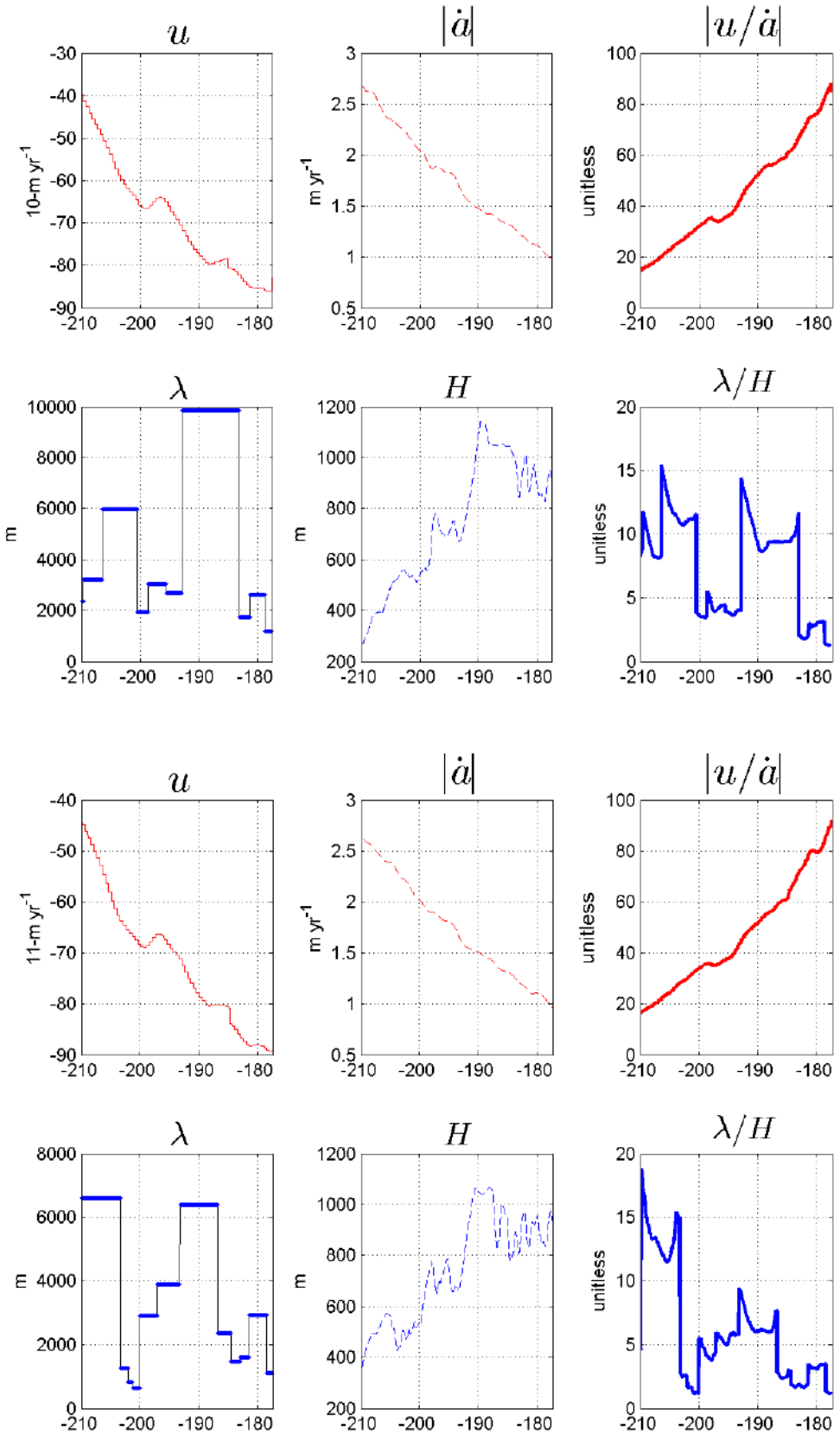
u
10-m yr^{-1}
$|\dot{a}|$
m yr^{-1}
$|u/\dot{a}|$
unitless
λ
m
H
m
λ/H
unitless
u
11-m yr^{-1}
$|\dot{a}|$
m yr^{-1}
$|u/\dot{a}|$
unitless
λ
m
H
m
λ/H
unitless

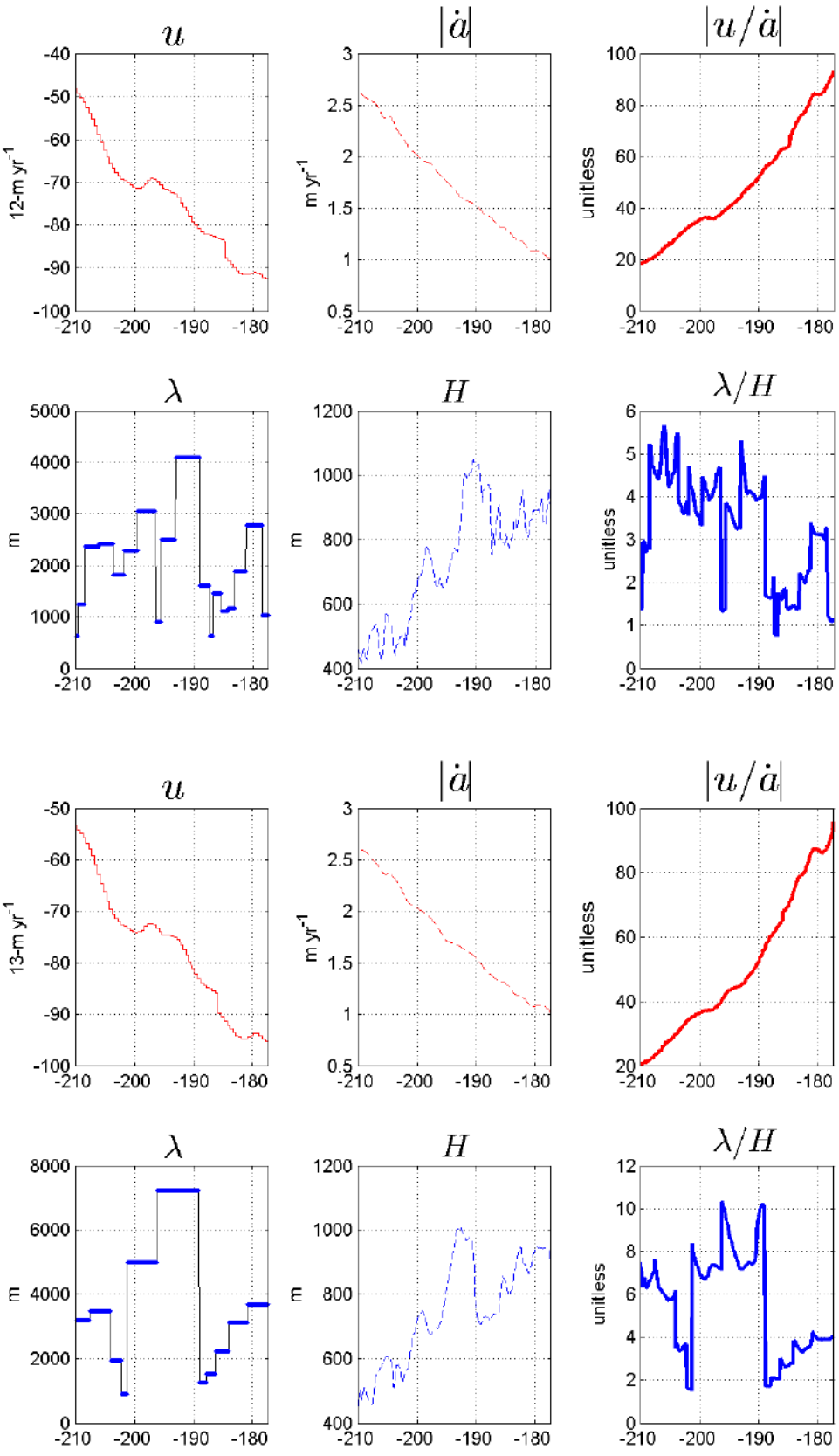
u
$|\dot{a}|$
$|u/\dot{a}|$
12-m yr^{-1}
m yr^{-1}
unitless
λ
H
λ/H
m
m
unitless
u
$|\dot{a}|$
$|u/\dot{a}|$
13-m yr^{-1}
m yr^{-1}
unitless
λ
H
λ/H
m
m
unitless

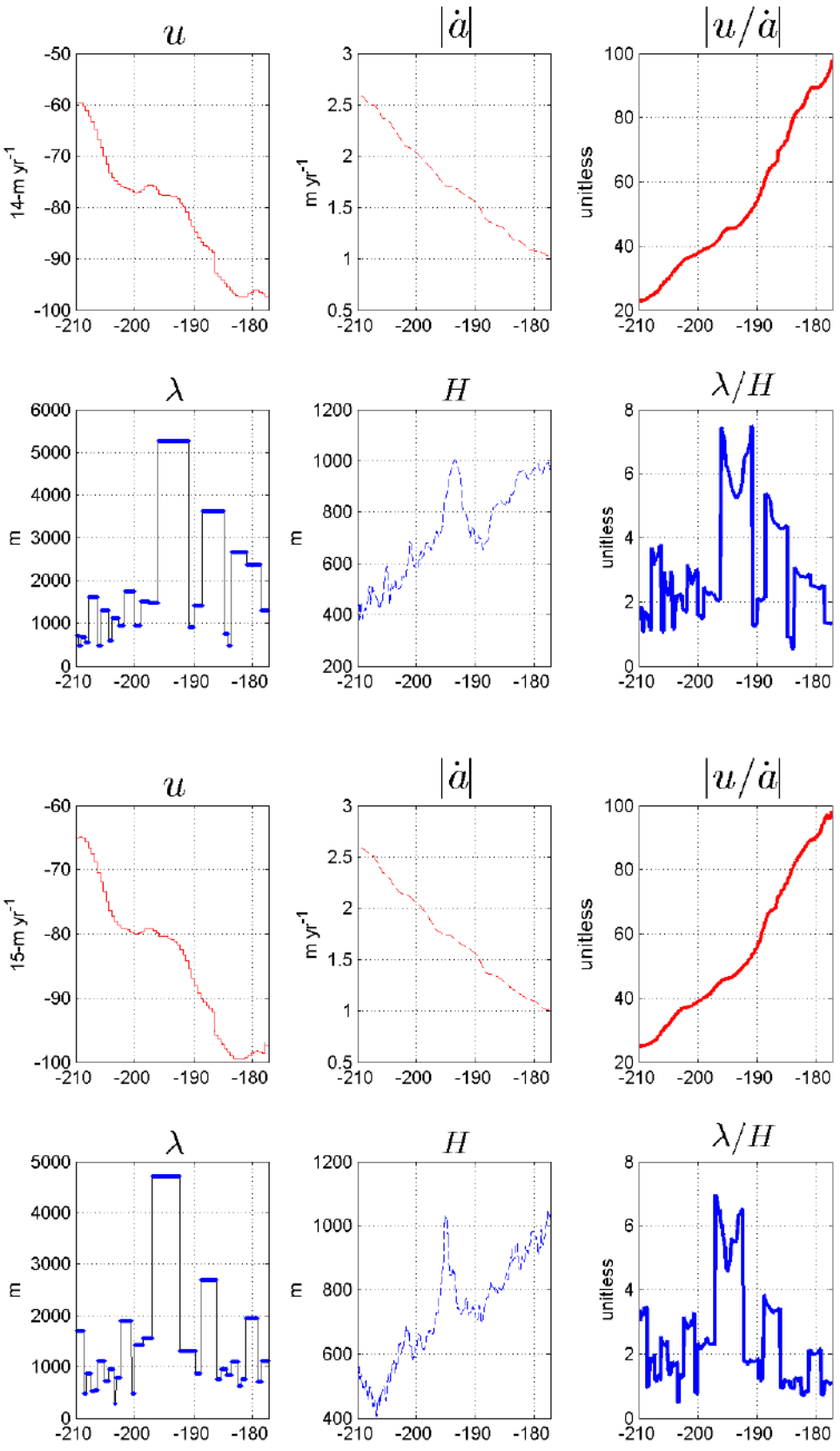
u
$|\dot{a}|$
$|u/\dot{a}|$
14-m yr^{-1}
m yr^{-1}
unitless
λ
H
λ/H
m
m
unitless
u
$|\dot{a}|$
$|u/\dot{a}|$
15-m yr^{-1}
m yr^{-1}
unitless
λ
H
λ/H
m
m
unitless

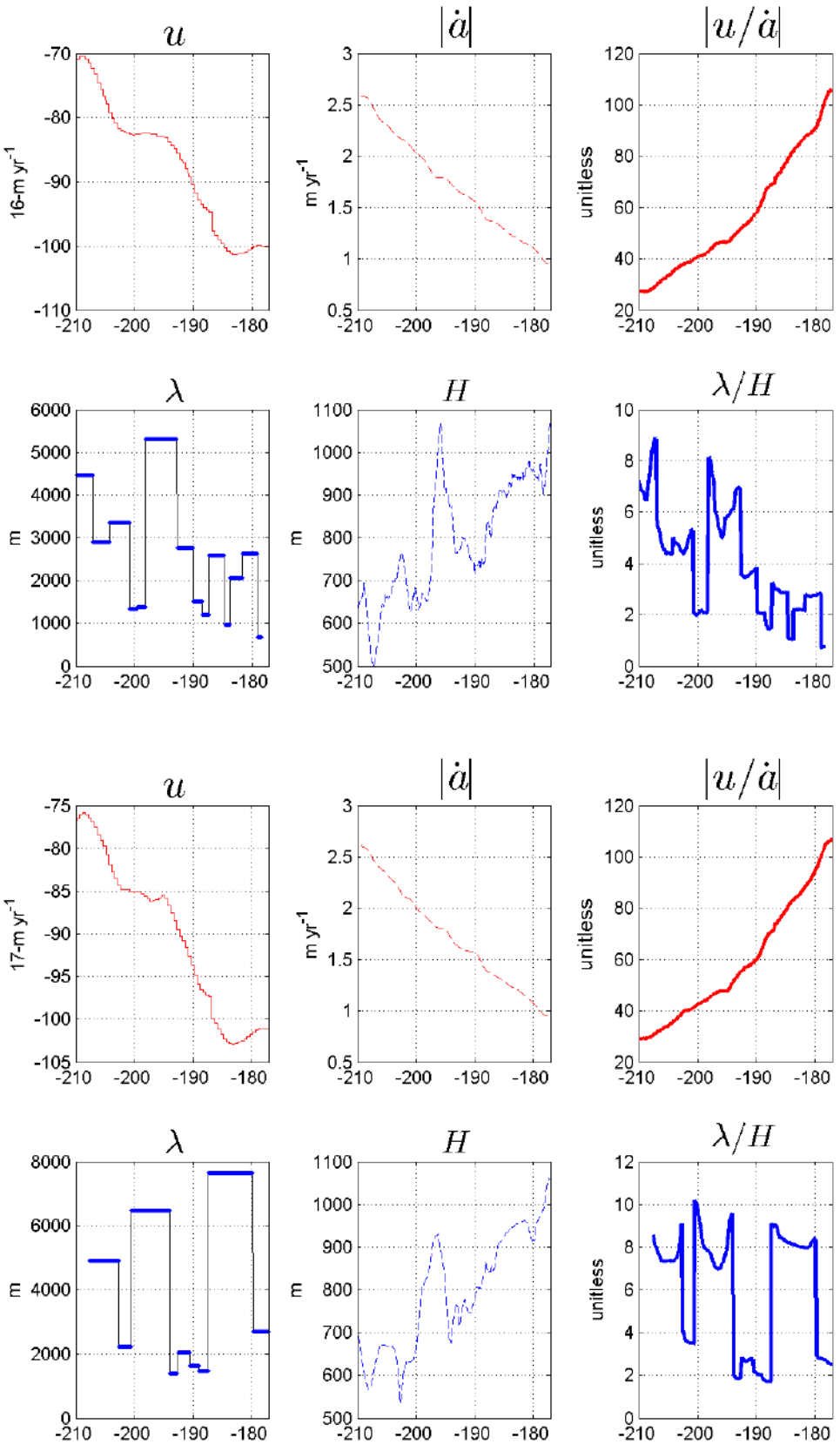
u
16-m yr^{-1}
-70
-80
-90
-100
-110
$|\dot{a}|$
m yr^{-1}
3
2.5
2
1.5
1
0.5
$|u/\dot{a}|$
unitless
120
100
80
60
40
20
λ
m
6000
5000
4000
3000
2000
1000
0
H
m
1100
1000
900
800
700
600
500
λ/H
unitless
10
8
6
4
2
0
-210
-200
-190
-180
u
17-m yr^{-1}
-75
-80
-85
-90
-95
-100
-105
$|\dot{a}|$
m yr^{-1}
$|u/\dot{a}|$
unitless
λ
m
8000
6000
4000
2000
0
H
m
λ/H
unitless
12

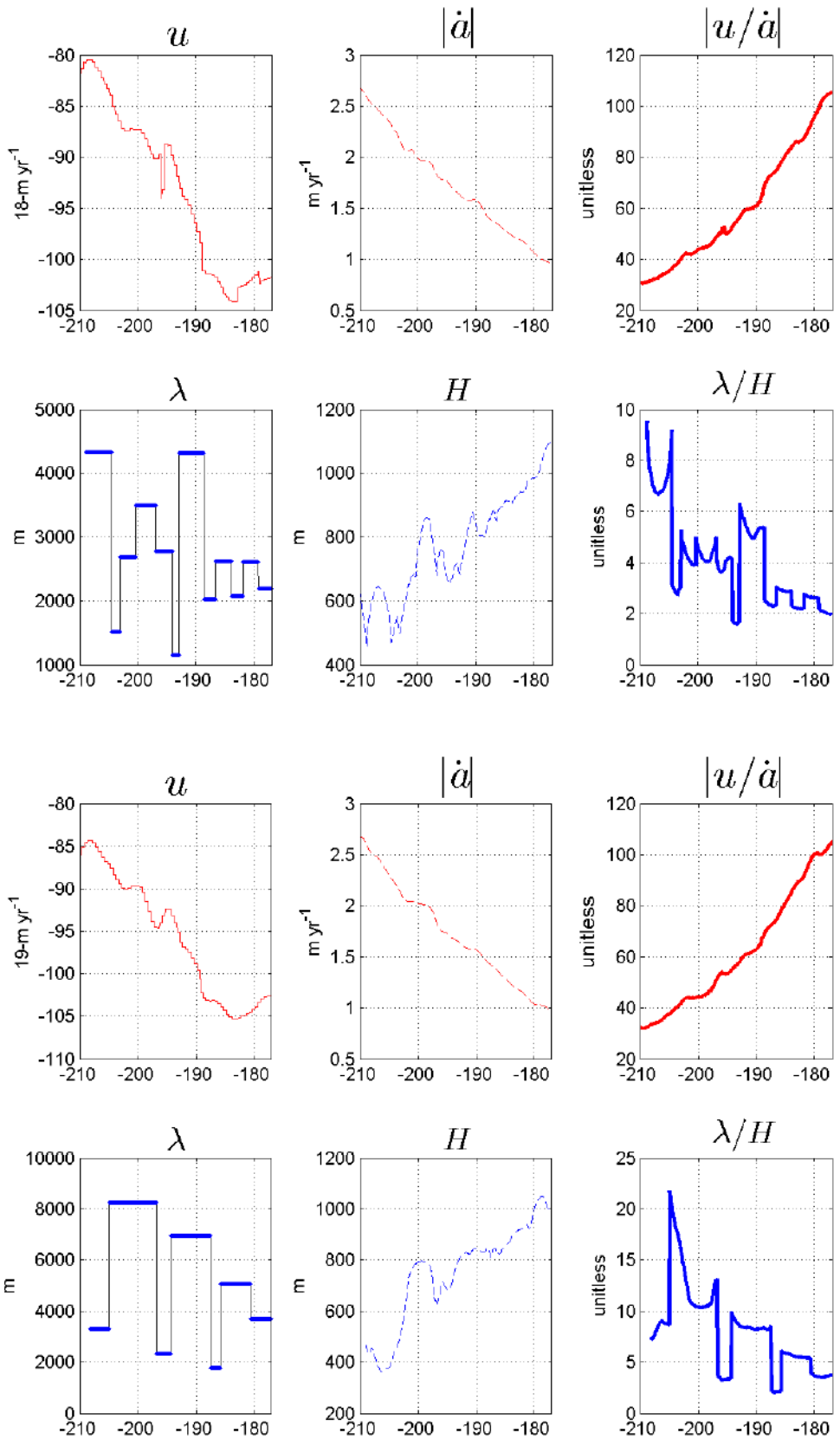
u
$|\dot{a}|$
$|u/\dot{a}|$
18-m yr^{-1}
m yr^{-1}
unitless
λ
H
λ/H
m
m
unitless
u
$|\dot{a}|$
$|u/\dot{a}|$
19-m yr^{-1}
m yr^{-1}
unitless
λ
H
λ/H
m
m
unitless

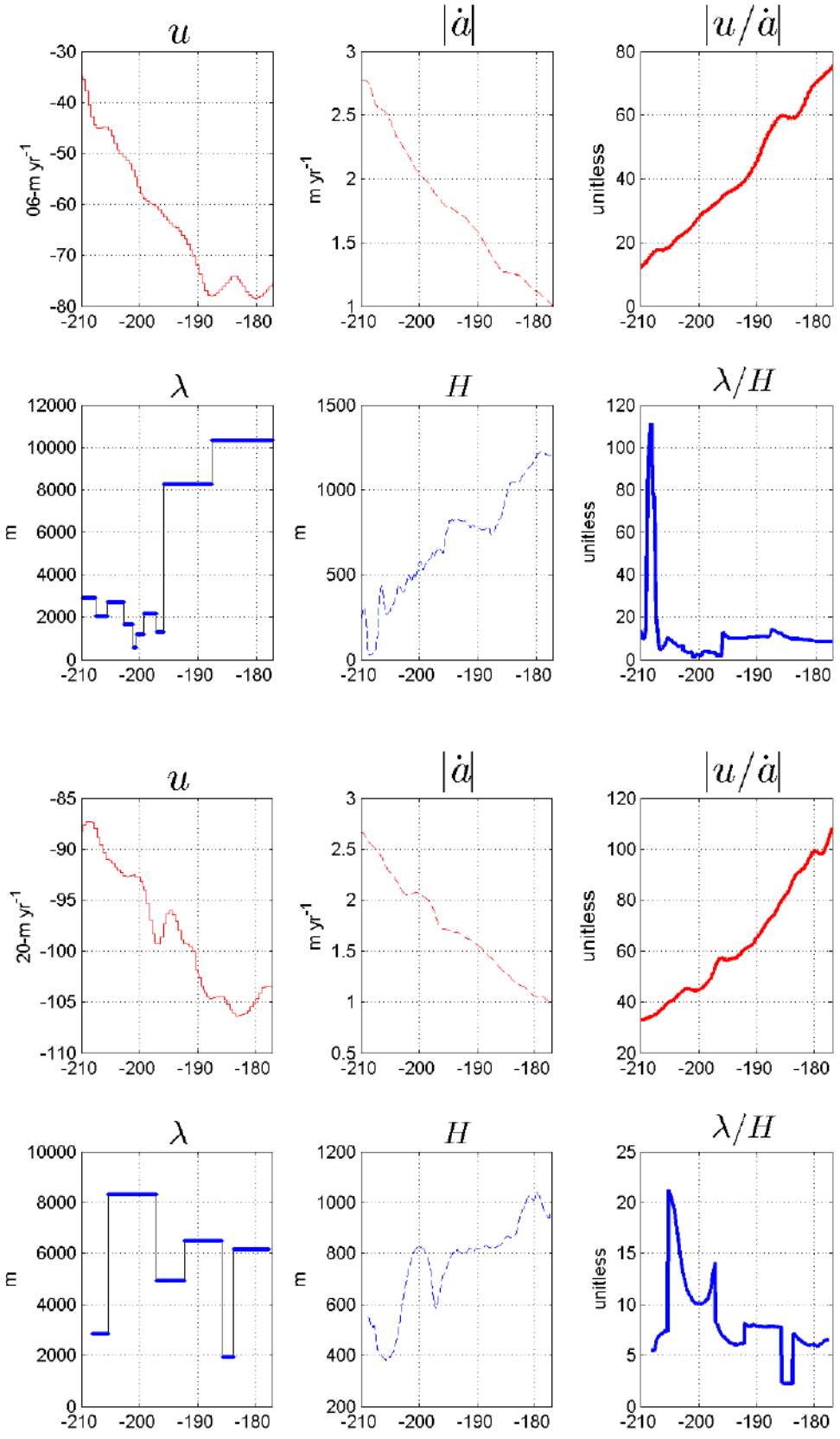
u
$|\dot{a}|$
$|u/\dot{a}|$
06-m yr^{-1}
m yr^{-1}
unitless
λ
H
λ/H
m
m
unitless
u
$|\dot{a}|$
$|u/\dot{a}|$
20-m yr^{-1}
m yr^{-1}
unitless
λ
H
λ/H
m
m
unitless

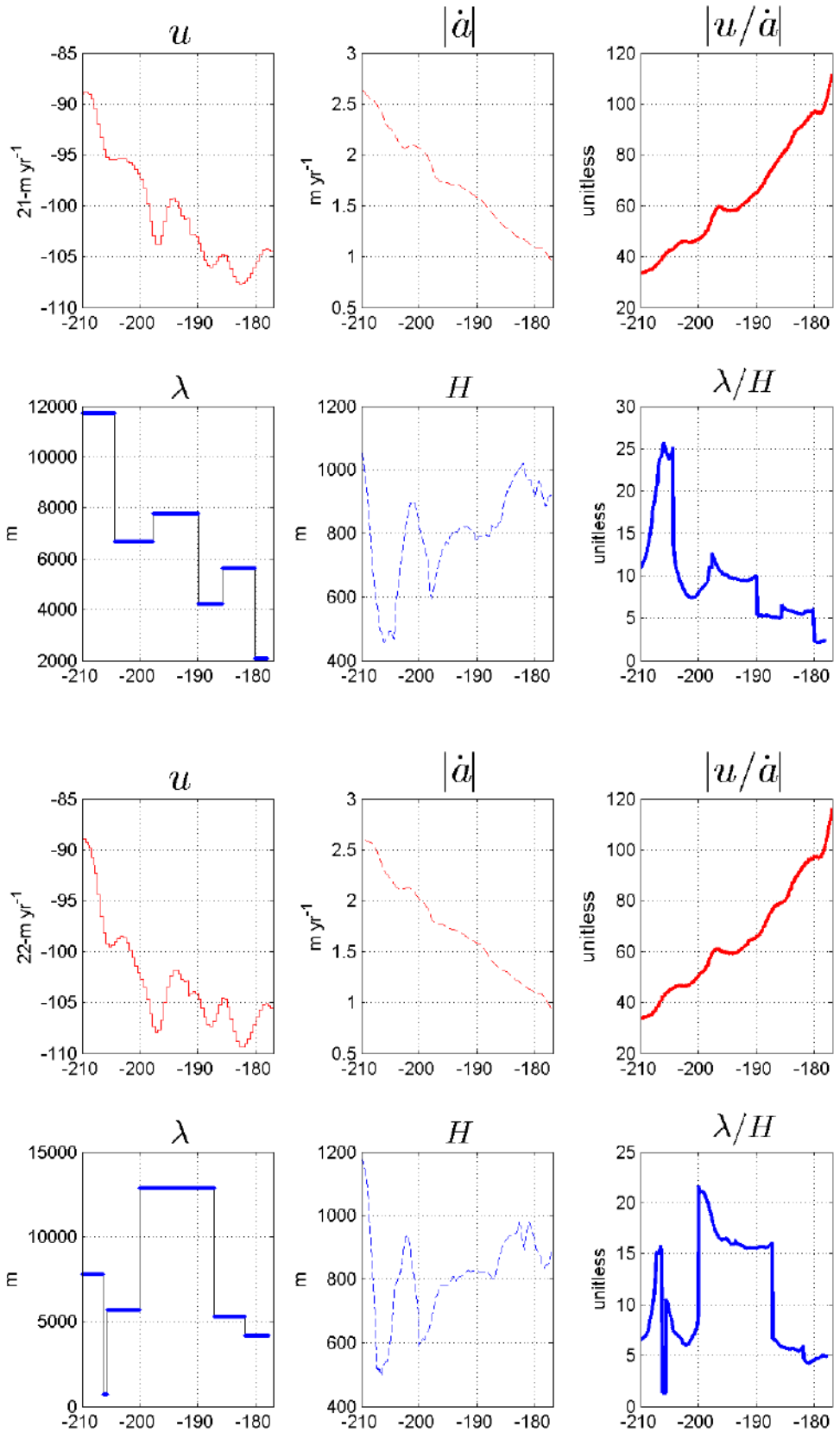
u
21-m yr^{-1}
$|\dot{a}|$
m yr^{-1}
$|u/\dot{a}|$
unitless
λ
m
H
m
λ/H
unitless
u
22-m yr^{-1}
$|\dot{a}|$
m yr^{-1}
$|u/\dot{a}|$
unitless
λ
m
H
m
λ/H
unitless

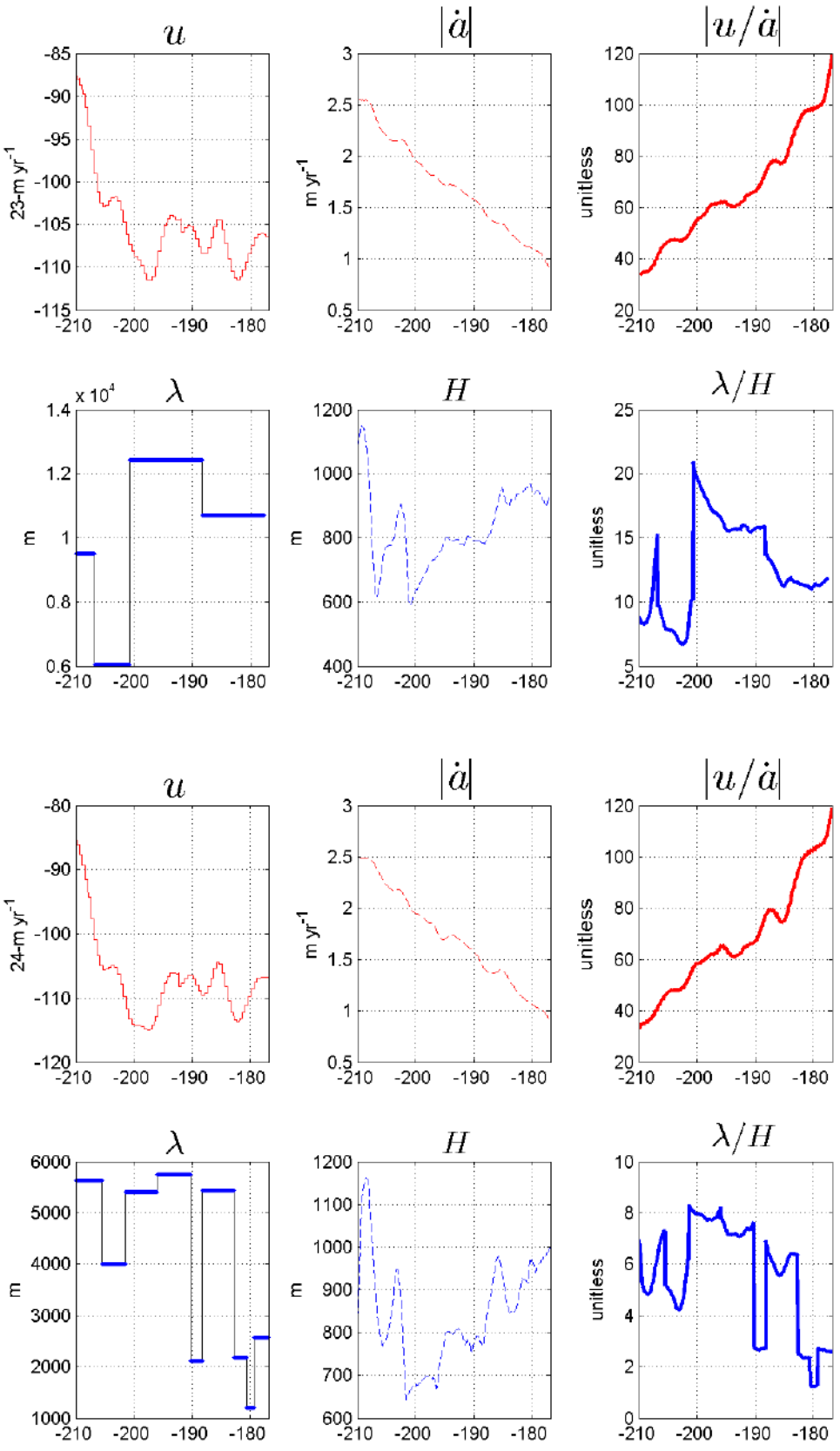
u
$|\dot{a}|$
$|u/\dot{a}|$
23-m yr^{-1}
m yr^{-1}
unitless
x 10^4
λ
H
λ/H
m
m
unitless
u
$|\dot{a}|$
$|u/\dot{a}|$
24-m yr^{-1}
m yr^{-1}
unitless
λ
H
λ/H
m
m
unitless

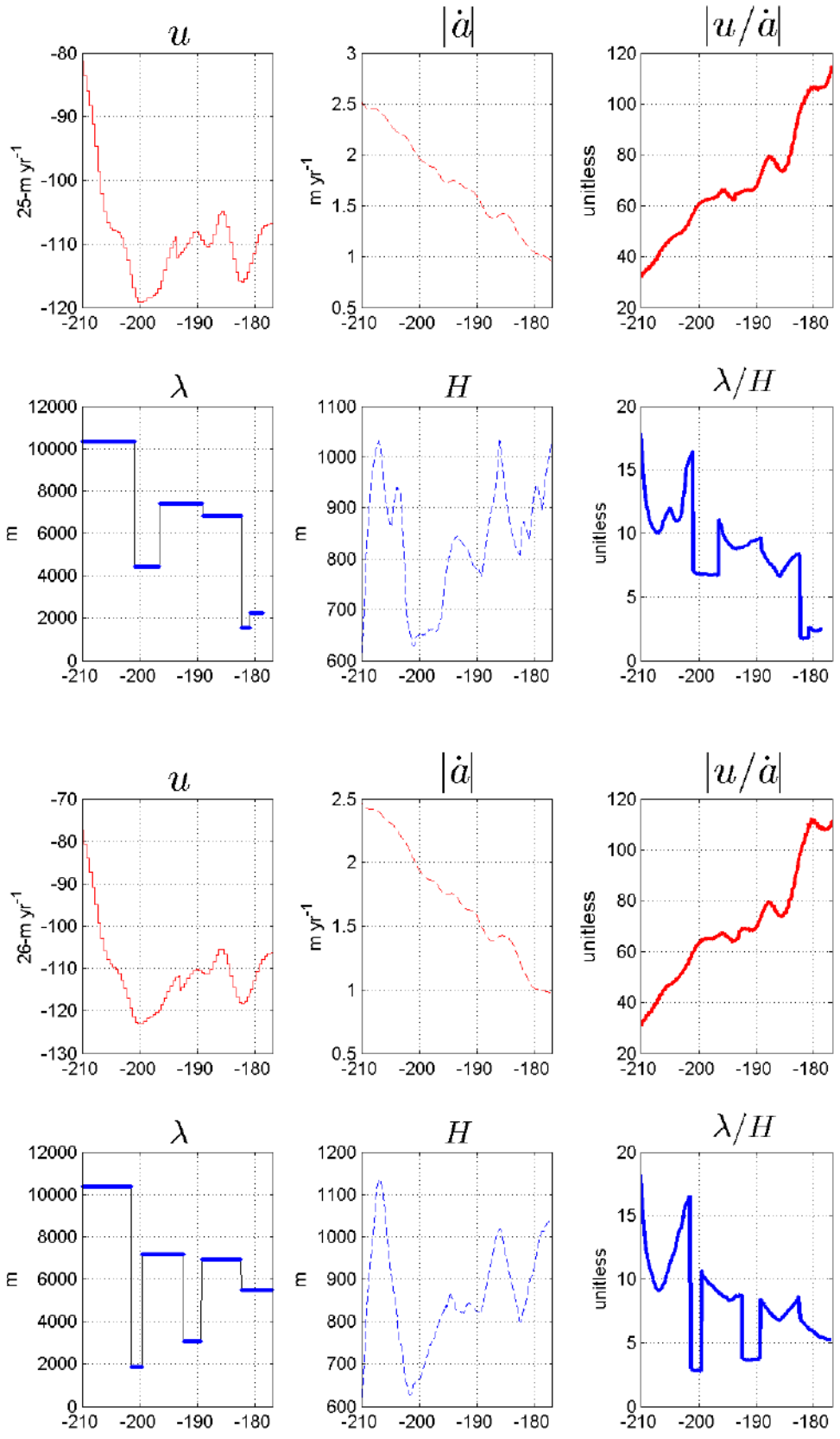
u
$|\dot{a}|$
$|u/\dot{a}|$
25-m yr^{-1}
m yr^{-1}
unitless
λ
H
λ/H
m
m
unitless
u
$|\dot{a}|$
$|u/\dot{a}|$
26-m yr^{-1}
m yr^{-1}
unitless
λ
H
λ/H
m
m
unitless

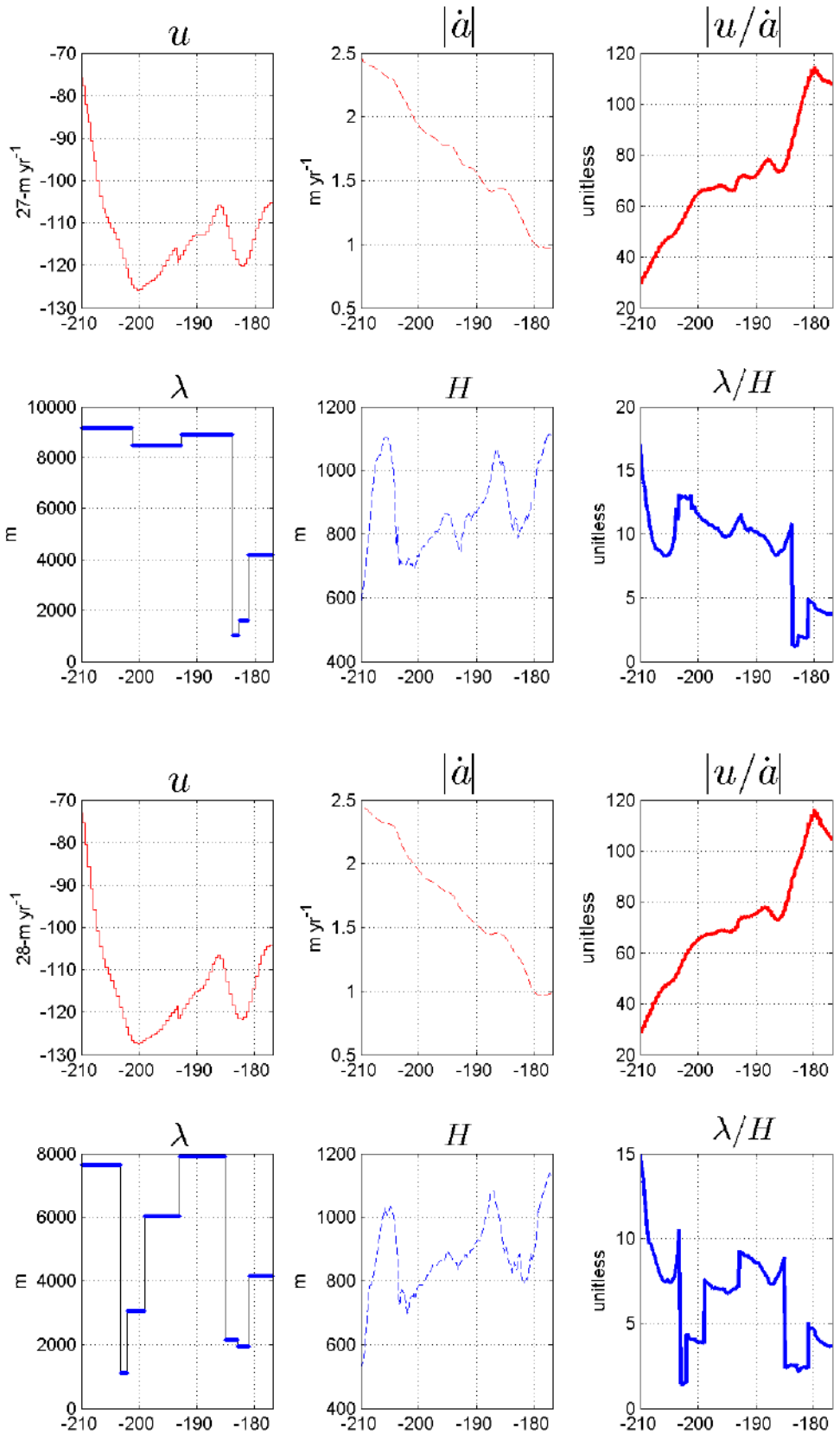
u
$|\dot{a}|$
$|u/\dot{a}|$
27-m yr^{-1}
m yr^{-1}
unitless
λ
H
λ/H
m
m
unitless
u
$|\dot{a}|$
$|u/\dot{a}|$
28-m yr^{-1}
m yr^{-1}
unitless
λ
H
λ/H
m
m
unitless

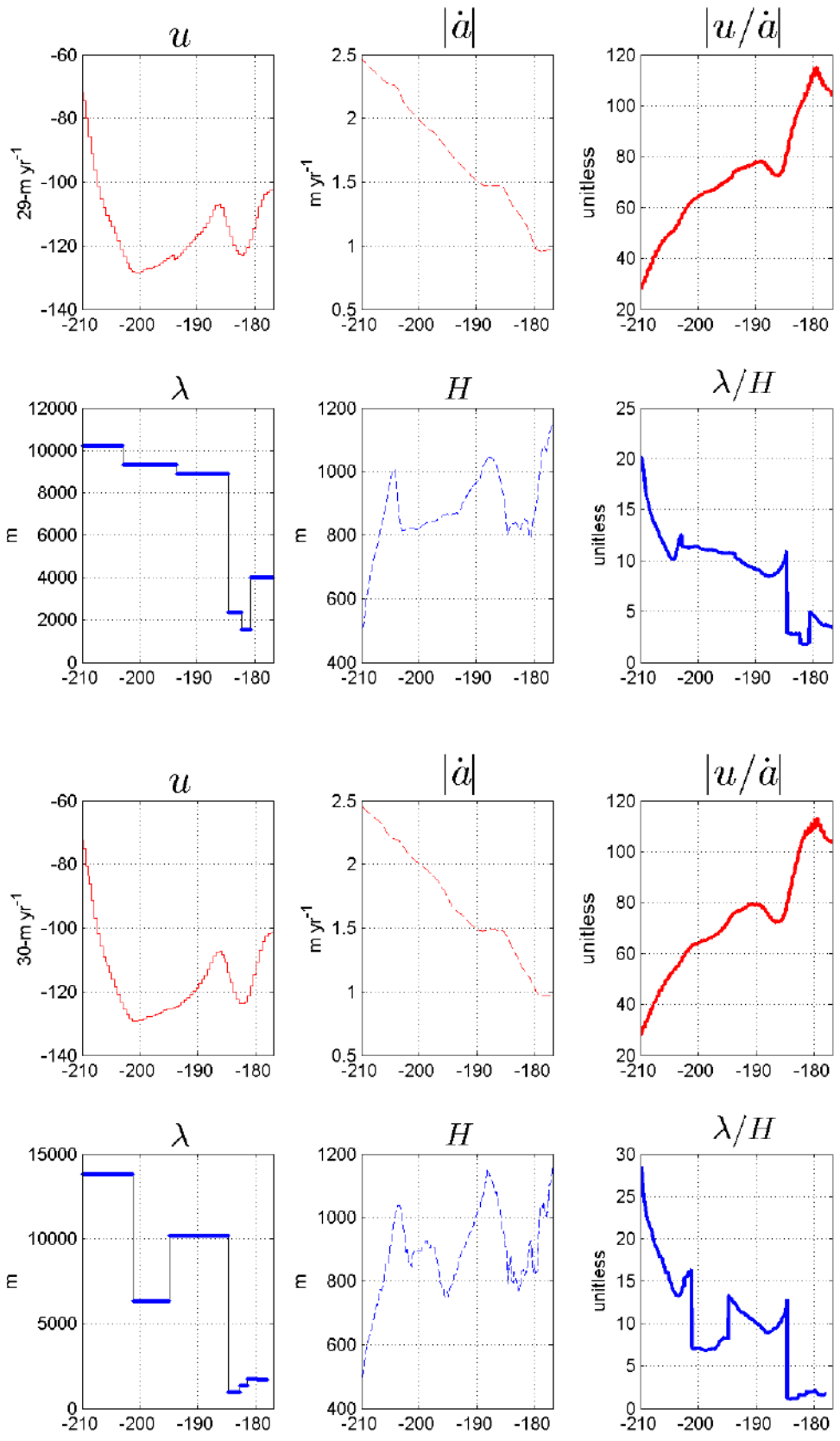
u
$|\dot{a}|$
$|u/\dot{a}|$
29-m yr^{-1}
m yr^{-1}
unitless
λ
H
λ/H
m
m
unitless
u
$|\dot{a}|$
$|u/\dot{a}|$
30-m yr^{-1}
m yr^{-1}
unitless
λ
H
λ/H
m
m
unitless

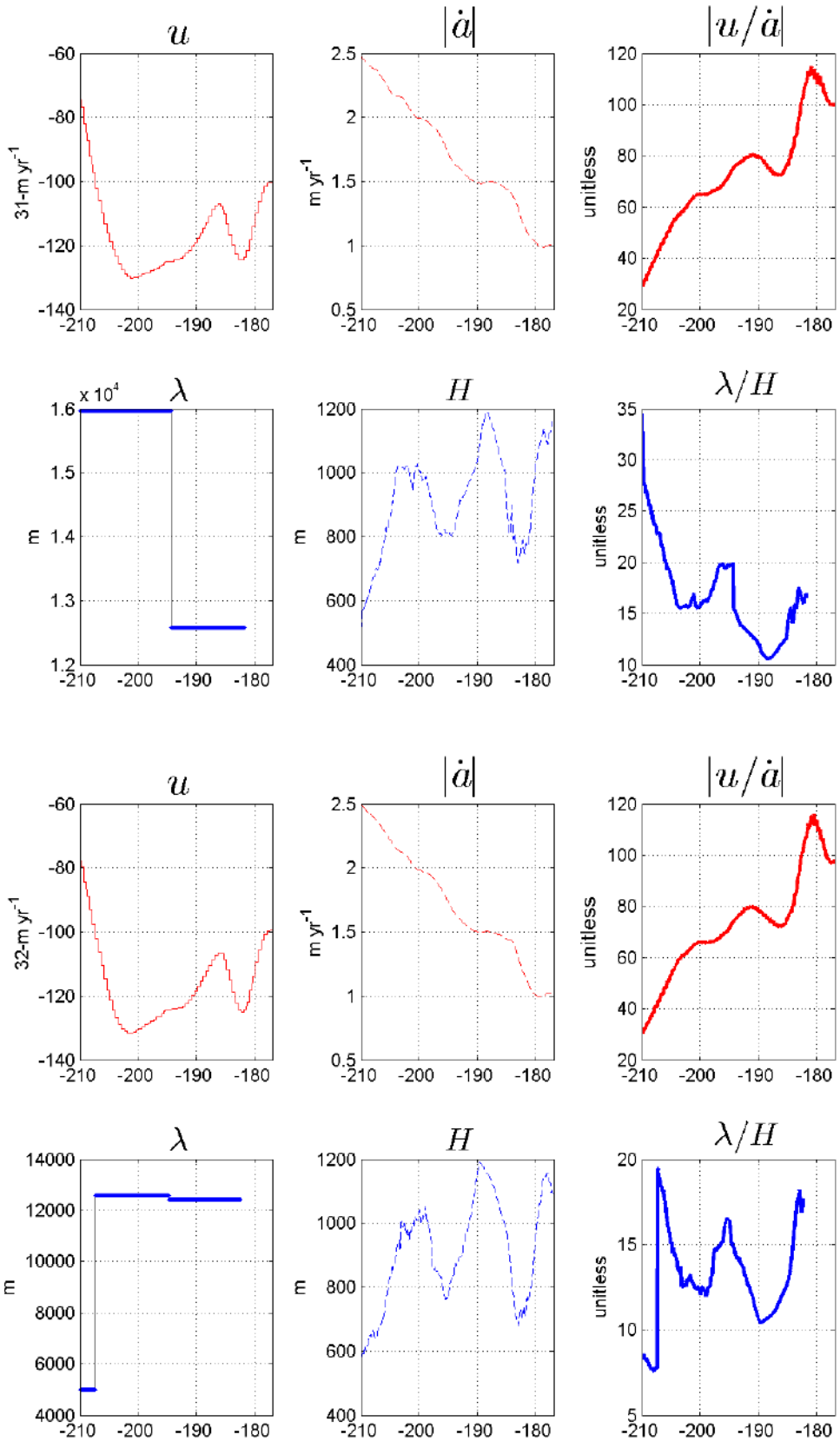
u
$|\dot{a}|$
$|u/\dot{a}|$
31-m yr^{-1}
m yr^{-1}
unitless
x 10^4
λ
H
λ/H
m
unitless
u
$|\dot{a}|$
$|u/\dot{a}|$
32-m yr^{-1}
m yr^{-1}
unitless
λ
H
λ/H
m
unitless

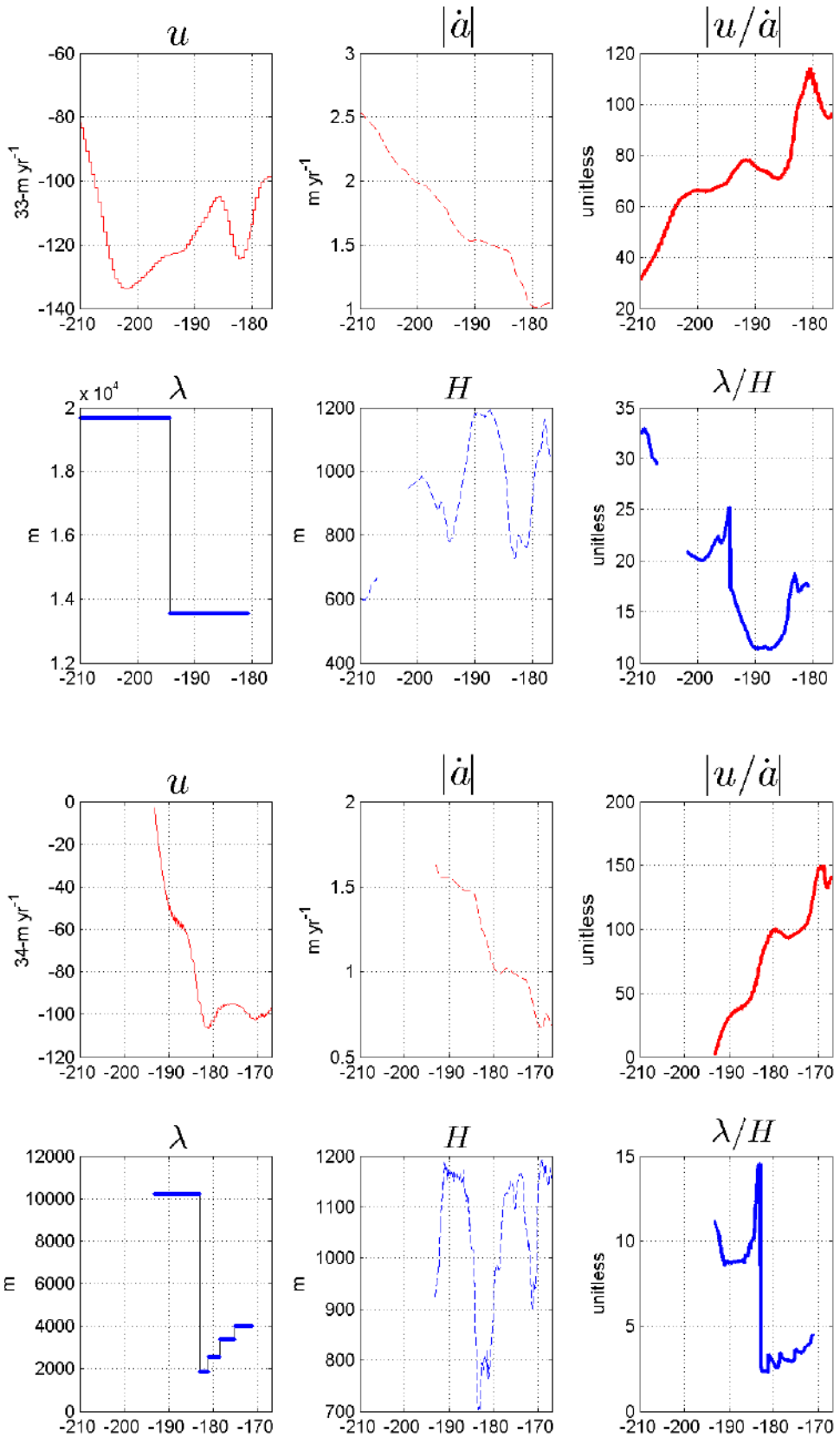
u
33-m yr^{-1}
$|\dot{a}|$
m yr^{-1}
$|u/\dot{a}|$
unitless
x 10^{4}
λ
m
H
m
λ/H
unitless
u
34-m yr^{-1}
$|\dot{a}|$
m yr^{-1}
$|u/\dot{a}|$
unitless
λ
m
H
m
λ/H
unitless

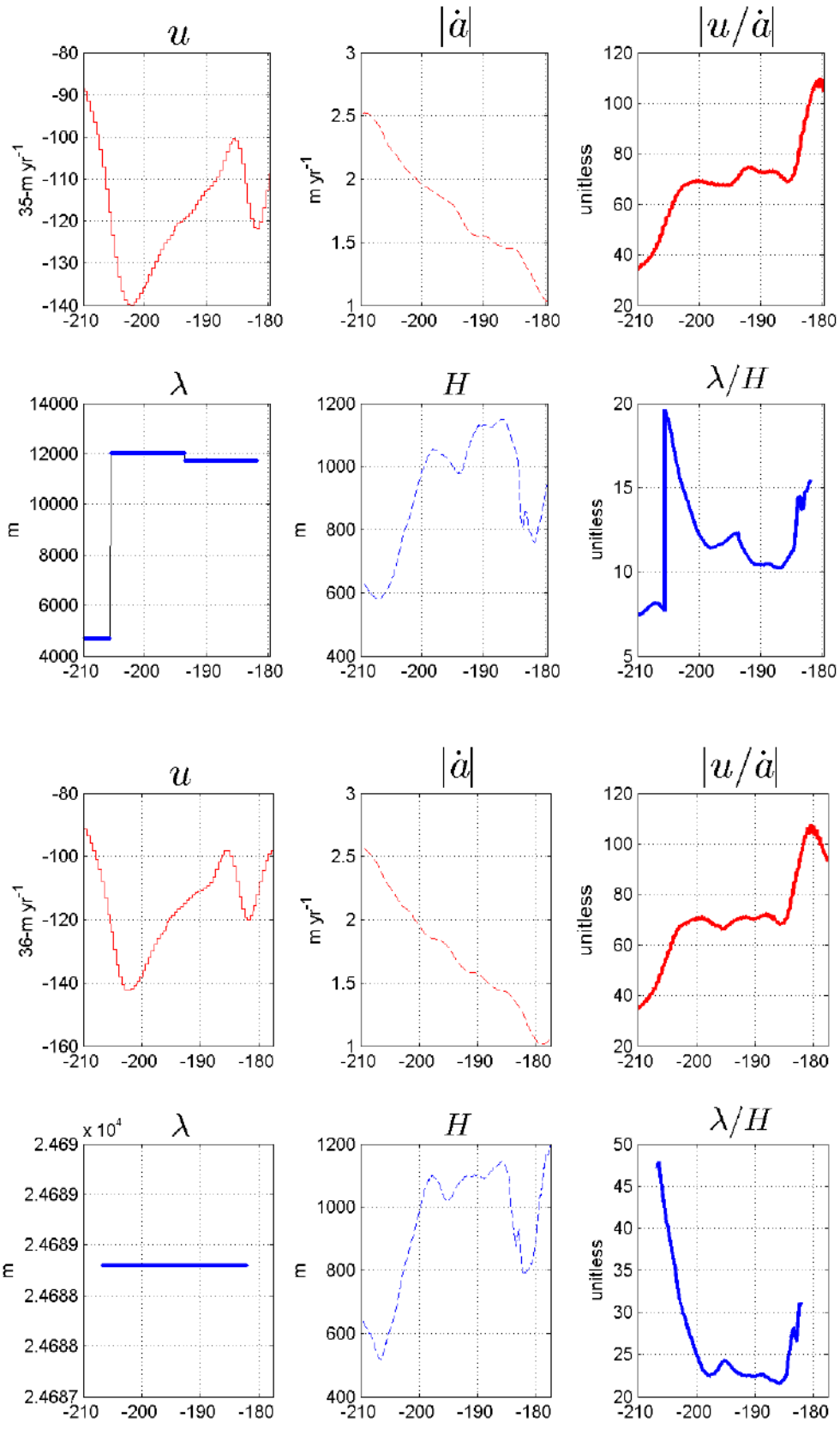
u
35-m yr^{-1}
$|\dot{a}|$
m yr^{-1}
$|u/\dot{a}|$
unitless
λ
m
H
m
λ/H
unitless
u
36-m yr^{-1}
$|\dot{a}|$
m yr^{-1}
$|u/\dot{a}|$
unitless
x 10^4
λ
m
H
m
λ/H
unitless

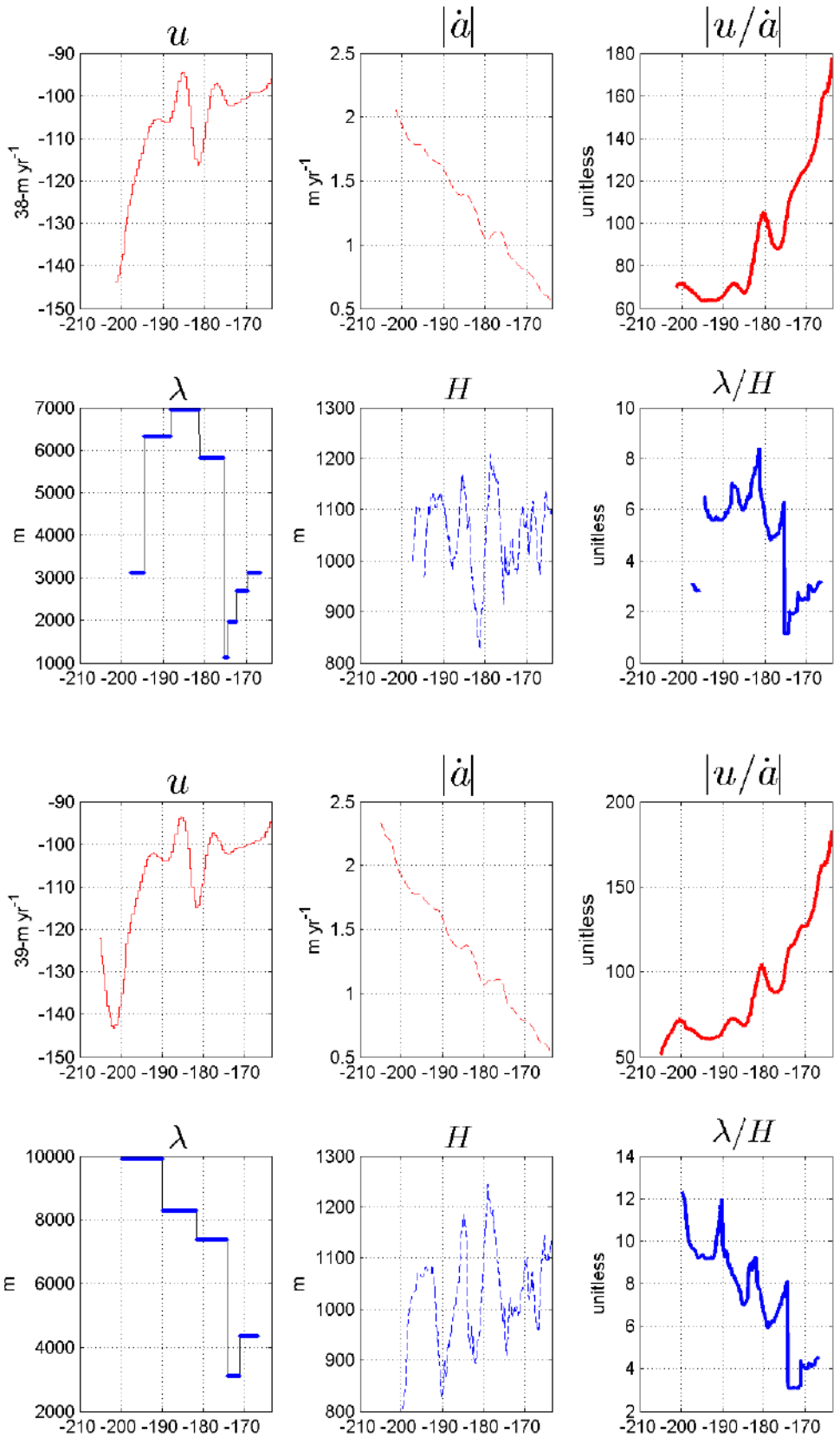
u
38-m yr^{-1}
-90
-100
-110
-120
-130
-140
-150
-210 -200 -190 -180 -170
$|\dot{a}|$
m yr^{-1}
2.5
2
1.5
1
0.5
-210 -200 -190 -180 -170
$|u/\dot{a}|$
unitless
180
160
140
120
100
80
60
-210 -200 -190 -180 -170
λ
m
7000
6000
5000
4000
3000
2000
1000
-210 -200 -190 -180 -170
H
m
1300
1200
1100
1000
900
800
-210 -200 -190 -180 -170
λ/H
unitless
10
8
6
4
2
0
-210 -200 -190 -180 -170
u
39-m yr^{-1}
-90
-100
-110
-120
-130
-140
-150
-210 -200 -190 -180 -170
$|\dot{a}|$
m yr^{-1}
2.5
2
1.5
1
0.5
-210 -200 -190 -180 -170
$|u/\dot{a}|$
unitless
200
150
100
50
-210 -200 -190 -180 -170
λ
m
10000
8000
6000
4000
2000
-210 -200 -190 -180 -170
H
m
1300
1200
1100
1000
900
800
-210 -200 -190 -180 -170
λ/H
unitless
14
12
10
8
6
4
2
-210 -200 -190 -180 -170

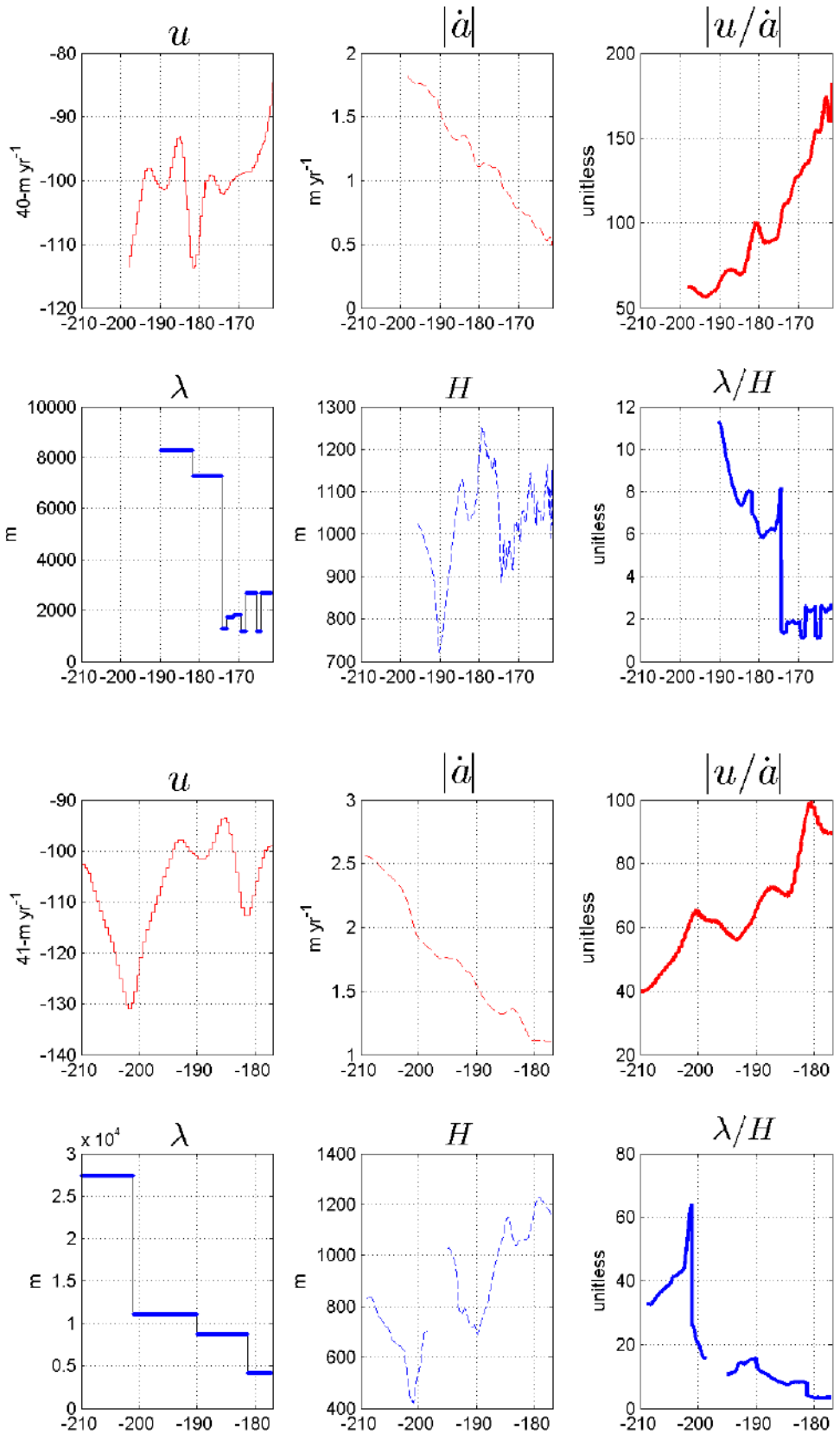
u
40-m yr^{-1}
$|\dot{a}|$
m yr^{-1}
$|u/\dot{a}|$
unitless
λ
m
H
m
λ/H
unitless
u
41-m yr^{-1}
$|\dot{a}|$
m yr^{-1}
$|u/\dot{a}|$
unitless
x 10^4
λ
m
H
m
λ/H
unitless